frontiers | Research Topics

Key technologies for hybrid energy system planning and operation

Edited by
Chengguo Su, Imr Fattah, Zhong-kai Feng,
Jianjian Shen and Yongxin Xiong

Published in
Frontiers in Energy Research

ISSN 1664-8714
ISBN 978-2-8325-4901-8
DOI 10.3389/978-2-8325-4901-8

About Frontiers

Frontiers is more than just an open access publisher of scholarly articles: it is a pioneering approach to the world of academia, radically improving the way scholarly research is managed. The grand vision of Frontiers is a world where all people have an equal opportunity to seek, share and generate knowledge. Frontiers provides immediate and permanent online open access to all its publications, but this alone is not enough to realize our grand goals.

Frontiers journal series

The Frontiers journal series is a multi-tier and interdisciplinary set of open-access, online journals, promising a paradigm shift from the current review, selection and dissemination processes in academic publishing. All Frontiers journals are driven by researchers for researchers; therefore, they constitute a service to the scholarly community. At the same time, the *Frontiers journal series* operates on a revolutionary invention, the tiered publishing system, initially addressing specific communities of scholars, and gradually climbing up to broader public understanding, thus serving the interests of the lay society, too.

Dedication to quality

Each Frontiers article is a landmark of the highest quality, thanks to genuinely collaborative interactions between authors and review editors, who include some of the world's best academicians. Research must be certified by peers before entering a stream of knowledge that may eventually reach the public - and shape society; therefore, Frontiers only applies the most rigorous and unbiased reviews. Frontiers revolutionizes research publishing by freely delivering the most outstanding research, evaluated with no bias from both the academic and social point of view. By applying the most advanced information technologies, Frontiers is catapulting scholarly publishing into a new generation.

What are Frontiers Research Topics?

Frontiers Research Topics are very popular trademarks of the *Frontiers journals series*: they are collections of at least ten articles, all centered on a particular subject. With their unique mix of varied contributions from Original Research to Review Articles, Frontiers Research Topics unify the most influential researchers, the latest key findings and historical advances in a hot research area.

Find out more on how to host your own Frontiers Research Topic or contribute to one as an author by contacting the Frontiers editorial office: frontiersin.org/about/contact

Key technologies for hybrid energy system planning and operation

Topic editors

Chengguo Su — Zhengzhou University, China
Imr Fattah — University of Technology Sydney, Australia
Zhong-kai Feng — Hohai University, China
Jianjian Shen — Dalian University of Technology, China
Yongxin Xiong — Aalborg University, Denmark

Citation

Su, C., Fattah, I., Feng, Z.-K., Shen, J., Xiong, Y., eds. (2024). *Key technologies for hybrid energy system planning and operation*. Lausanne: Frontiers Media SA.
doi: 10.3389/978-2-8325-4901-8

Table of contents

04 Editorial: Key technologies for hybrid energy system planning and operation
Chengguo Su, Jianjian Shen, Zhong-kai Feng, IMR Fattah and Yongxin Xiong

07 A safety check method to maximize the effective reserve by optimizing the power of the tie-line in the power market
Yang Wu, Xingxing Wanyan, Xiangyang Su, Wentao Zou, Xinchun Zhu, Shuangquan Liu and Qizhuan Shao

16 A multi-objective optimization model for the coordinated operation of hydropower and renewable energy
Benxi Liu, Zihan Peng, Shengli Liao, Tengyuan Liu and Jia Lu

30 Flexible torque control for wind turbines considering frequency response under wind speed crossing region
Yingwei Wang, Yufeng Guo, Yilin Du and Weimao Xu

42 Optimal configuration and operation of the regional integrated energy system considering carbon emission and integrated demand response
Xianqiang Zeng, Jin Wang, Yun Zhou and Hengjie Li

60 Mid-term scheduling and trading decisions for cascade hydropower stations considering multiple variable uncertainties
Jia Lu, Yaxin Liu, Hui Cao, Yang Xu, Haoyu Ma, Zheng Zhang, Tao Wang and Yuqi Yang

72 Market bidding method for the inter-provincial delivery of cascaded hydroelectric plants in day-ahead markets considering settlement rules
Xu Han, Jianjian Shen and Chuntian Cheng

86 Deep learning integration optimization of electric energy load forecasting and market price based on the ANN–LSTM–transformer method
Bin Zhong

103 An ensemble model for short-term wind power prediction based on EEMD-GRU-MC
Peilin Wang, Chengguo Su, Li Li, Wenlin Yuan and Chaoyu Guo

120 A runoff-based hydroelectricity prediction method based on meteorological similar days and XGBoost model
Yang Wu, Yigong Xie, Fengjiao Xu, Xinchun Zhu and Shuangquan Liu

frontiers | Frontiers in Energy Research

TYPE Editorial
PUBLISHED 06 May 2024
DOI 10.3389/fenrg.2024.1413951

OPEN ACCESS

EDITED AND REVIEWED BY
Ellen B. Stechel,
Arizona State University, United States

*CORRESPONDENCE
IMR Fattah,
rizwanul.buet@gmail.com

RECEIVED 08 April 2024
ACCEPTED 22 April 2024
PUBLISHED 06 May 2024

CITATION
Su C, Shen J, Feng Z-k, Fattah IMR and Xiong Y (2024), Editorial: Key technologies for hybrid energy system planning and operation. *Front. Energy Res.* 12:1413951. doi: 10.3389/fenrg.2024.1413951

Editorial: Key technologies for hybrid energy system planning and operation

Chengguo Su[1], Jianjian Shen[2], Zhong-kai Feng[3,4], IMR Fattah[5]* and Yongxin Xiong[6]

[1]School of Hydraulic Science and Engineering, Zhengzhou University, Zhengzhou, China, [2]Institute of Hydropower and Hydroinformatics, Dalian University of Technology, Dalian, China, [3]College of Hydrology and Water Resources, Hohai University, Nanjing, China, [4]The National Key Laboratory of Water Disaster Prevention, Hohai University, Nanjing, China, [5]School of Civil and Environmental Engineering, Faculty of Engineering and IT, University of Technology Sydney, Ultimo, NSW, Australia, [6]State Key Laboratory of Advanced Electromagnetic Engineering and Technology, School of Electrical and Electronics Engineering, Huazhong University of Science and Technology, Wuhan, China

KEYWORDS

energy forecasting, power grid optimization, wind turbine control, short-term prediction models, optimization algorithms, ensemble forecasting, hydro-wind-solar scheduling, market decision-making methods

Editorial on the Research Topic
Key technologies for hybrid energy system planning and operation

This Research Topic addresses the growing demand for clean and reliable energy in the face of rising electricity consumption and environmental concerns. Traditional fossil fuels dominate power generation, but their accelerated use creates pollution problems. Wind and solar power offer promising renewable alternatives, but their widespread adoption presents challenges. These sources are highly variable and difficult to control due to their dependence on weather conditions. Large-scale integration of wind and solar power can destabilize power grids and threaten their safe operation.

The research presented here explores solutions for integrating these renewable sources effectively. A key approach involves combining wind and solar with controllable power sources like hydropower, thermal power, and battery storage to create hybrid energy systems. Accurate prediction of new energy power generation is crucial for such hybrid systems' reliable and secure operation.

This collection features nine research articles investigating various aspects of hybrid energy systems:

- Techniques for controlling wind turbines
- Decision-making methods for markets dominated by hydropower
- Optimization models for regional energy integration
- Short-term wind power prediction models
- Decision-making methods for hydropower-dominated markets

The original research by Y. Wang et al. proposed a flexible torque control method for wind turbines participating in frequency regulation. It addresses the issue of transient torque fluctuations during wind speed transitions. The method divides the transition region between operating speeds into sub-regions. It then employs dynamic deloading and flexible

torque control within these sub-regions to ensure smooth generator torque transfer. This is achieved without requiring additional sensors, making it simple to implement. The effectiveness of the proposed method is verified through simulations. The study demonstrates that this method can mitigate transient torque fluctuations and improve the overall reliability and efficiency of wind turbine systems.

The original research by Zeng et al. introduced a novel double-layer optimization model tailored for a regional integrated energy system (RIES), emphasizing the integration of concentrating solar power (CSP) stations, carbon emissions management, and integrated demand response (IDR). The primary objective is to minimize both annual planning costs and net pollutant emissions while ensuring optimal system operation. The model operates on two distinct layers: the upper layer employs an enhanced NSGA-II algorithm to configure capacities, focusing on minimizing annual planning costs and net emissions, while the lower layer utilizes a mixed-integer linear programming (MILP) solver to minimize annual operating costs and optimize device output and load curves. Notably, the model encompasses the entire carbon emissions process, including capture, utilization, and trading, and incorporates flexible loads for electricity, heat, cooling, and gas. Simulation results, compared against conventional approaches, underscore several key advantages of the proposed methodology. CSP station integration is found to enhance coordinated optimization, while the improved NSGA-II algorithm demonstrates superior convergence over its conventional counterpart. Furthermore, considering the entirety of carbon emissions alongside IDR leads to reductions in annual operating costs and net carbon emissions. Overall, this innovative approach fosters a more economically viable and environmentally sustainable RIES.

The original research by Liu et al. presented a pioneering approach to coordinated scheduling for hydro-wind-solar power systems, taking into account both peak shaving and navigation objectives. With the rapid expansion of wind and solar energy, grid stability faces challenges due to their intermittent nature. Although hydropower offers flexibility, its conventional operation might clash with other functionalities like navigation. To tackle these challenges, the proposed model incorporates uncertainty quantification via a Gaussian mixture model for wind and solar power forecasts. This integration enables the model to effectively manage the inherent variability of these renewable sources. Additionally, the model utilizes the ε-constraint method to achieve Pareto optimality, effectively balancing the conflicting goals of peak shaving and navigation. Key contributions of this study include the development of a multi-objective hydro-wind-solar scheduling model that accounts for both peak shaving and navigation, uncertainty quantification of wind and solar power forecasts using a Gaussian mixture model, and the transformation of chance constraints into solvable linear constraints through error bounds. The model's effectiveness is demonstrated through a real-world application on the Jinghong-Ganlanba cascade hydropower system, with further analysis conducted on the impact of wind and solar factors on its performance. This research provides valuable insights for power grid operators aiming to integrate renewable energy sources while upholding system reliability and addressing navigation requirements.

The methods paper by Wu et al. proposed a novel safety check method for the electricity spot market that optimizes tie-line power to maximize effective reserve resources within the power system. This approach aims to ensure the stability of the market and the safety of regional power grids. The key challenge addressed is the difficulty of accurately evaluating effective reserves in the current spot market environment. This is due to factors like limited real-time data and the impact of new energy sources with fluctuating power generation. The proposed method tackles this challenge by incorporating a safety check during the optimization process. This check considers tie-line equipment limitations, reserve capacity, and various constraints of the spot market clearing model. The model itself is linear, facilitating practical implementation in power-dispatching applications.

Th original research article by Zhong investigated the application of deep learning for improved power load forecasting and market price prediction in the face of complex energy systems and market volatility. Deep learning has emerged as a powerful tool for time series forecasting, and this research proposes a novel framework that integrates and optimizes multiple deep learning models to achieve superior prediction accuracy and reliability. The proposed framework leverages the strengths of three distinct deep learning architectures: Artificial Neural Networks (ANNs), Long Short-Term Memory (LSTM) networks, and transformers. ANNs provide a versatile foundation for the model, while LSTMs, known for their proficiency in sequence modeling, generate initial predictions. The framework further incorporates transformers, specifically their self-attention mechanism, to capture long-range dependencies within the data. This combined approach significantly enhances the overall model performance. The effectiveness of the proposed framework is evaluated through experiments using various public datasets. The performance is compared to both traditional forecasting methods and a single-model deep learning approach. The results conclusively demonstrate that the integrated framework surpasses other methods in predicting both power load and market prices.

The methods article by Wu et al. proposed a novel method for predicting hydroelectricity generation using a combination of meteorological similar days and the XGBoost machine learning model. Accurate prediction of hydroelectricity supply and demand is crucial for efficient resource management, reliable power supply, and minimizing the impact of natural disasters. The proposed method leverages historical meteorological and runoff data to identify days with weather patterns similar to the current day. These "similar days" form a dataset used to train an XGBoost model. The trained model then predicts future runoff based on the current meteorological data, which can be used to estimate future hydroelectricity generation. The effectiveness of the proposed method is evaluated using data from a hydroelectricity cluster in Yunnan, China. The results demonstrate high prediction accuracy and stability, highlighting its potential as a valuable tool for hydroelectricity prediction.

The original article by P. Wang et al. proposed a novel ensemble model for short-term wind power prediction that addresses the challenges posed by the high randomness and volatility of wind power. The model leverages a combination of three techniques:

Ensemble Empirical Mode Decomposition (EEMD), Gated Recurrent Unit (GRU), and Markov Chain (MC). Initially, the EEMD algorithm decomposes historical wind power sequences into stationary subsequences, reducing the impact of random fluctuations and noise. Subsequently, the GRU model predicts each subsequence, and the aggregated predicted values yield preliminary forecasts. Finally, the MC is employed to refine the prediction accuracy. Extensive numerical experiments, particularly on the ZMS wind farm's spring dataset, demonstrate the superiority of the proposed EEMD-GRU-MC model over six benchmark models in terms of various evaluation metrics. Notably, the model achieves a mean absolute error (MAE) of 1.37 MW, a root mean square error (RMSE) of 1.97 MW, and a mean absolute percentage error (MAPE) of 1.76%. Moreover, the model exhibits high computational efficiency, requiring an average of approximately 35 min for accurate daily wind power prediction after 30 iterations. Thus, the ensemble model based on EEMD-GRU-MC holds promise for short-term wind power forecasting.

The Policy and practice review article by Han et al. proposed a new scheduling method for large hydropower plants in China's evolving electricity market. The method addresses challenges caused by complex factors like uncertain electricity prices, diverse settlement rules, and inter-provincial transmission lines. It incorporates Latin hypercube sampling and K-means clustering to account for electricity price fluctuations. The study also establishes a performance measure for priority electricity considering settlement rules and proposes methods to handle inter-regional transmission connections and hydraulic coupling in cascaded hydropower plants. The complex non-linear problem is then transformed into a solvable mixed-integer linear programming model using the Big M method.

Cascade hydropower producers face two risks in medium- and long-term electricity markets: bidding risks during bidding and operational risks during scheduling due to uncertain water flow and market prices. The methods article by Lu et al. proposed a new decision-making method for such producers in a hydropower-dominated market in Southwest China. The method combines Joint Information Gap Decision Theory (IGDT) and Prospect Theory to address these risks. IGDT is used in a robust optimization model to find the maximum allowable variation in water flow and market prices while meeting expected revenue targets. Prospect Theory is then used to consider producer risk tolerance when developing bidding strategies. To avoid accuracy Research Topic caused by curve fitting in traditional solvers, the paper employs a nonlinear programming method combined with an improved stepwise optimization algorithm. The effectiveness of the method is verified using a real-world cascade hydropower station example. The results show that the method can determine the acceptable range of variation for water flow and market prices under different revenue targets and can be used to develop bidding and operation plans that consider producer risk tolerance.

Author contributions

CS: Writing–review and editing. JS: Writing–review and editing. Z-kF: Writing–review and editing. IF: Writing–original draft. YX: Writing–review and editing.

Conflict of interest

The authors declare that the research was conducted in the absence of any commercial or financial relationships that could be construed as a potential conflict of interest.

Publisher's note

frontiers | Frontiers in Energy Research

TYPE Methods
PUBLISHED 17 April 2023
DOI 10.3389/fenrg.2023.1162122

OPEN ACCESS

EDITED BY
IMR Fattah,
University of Technology Sydney,
Australia

REVIEWED BY
Dejian Yang,
Northeast Electric Power University,
China
Narottam Das,
Central Queensland University, Australia

*CORRESPONDENCE
Xingxing Wanyan,
wanyan163@foxmail.com
Shuangquan Liu,
Liushuangquan@yn.csg.cn

SPECIALTY SECTION
This article was submitted to Process and Energy Systems Engineering, a section of the journal Frontiers in Energy Research

RECEIVED 09 February 2023
ACCEPTED 29 March 2023
PUBLISHED 17 April 2023

CITATION
Wu Y, Wanyan X, Su X, Zou W, Zhu X, Liu S and Shao Q (2023), A safety check method to maximize the effective reserve by optimizing the power of the tie-line in the power market.
Front. Energy Res. 11:1162122.
doi: 10.3389/fenrg.2023.1162122

A safety check method to maximize the effective reserve by optimizing the power of the tie-line in the power market

Yang Wu[1], Xingxing Wanyan[2]*, Xiangyang Su[2], Wentao Zou[2], Xinchun Zhu[1], Shuangquan Liu[1]* and Qizhuan Shao[1]

[1]Yunnan Power Dispatching and Control Center, Yunnan Power Grid Co., Ltd., Kunming, China, [2]Beijing Tsintergy Technology Co., Ltd., Beijing, China

To ensure the stability of the electricity spot market and the safety of the provincial and regional power systems, a safety check method is proposed to maximize the effective reserve resources in the power system by optimizing the power of each tie-line. This safety check method accurately models the tie-line equipment and the effective reserve resources and is coupled with each constraint of the electricity spot market clearing model to form a safety check algorithm to optimize the power of tie-line power. The model involved in this paper is a linear model, which has a clear implementation method in practical dispatching applications. Through this method, the power configuration scheme of each tie-line to meet the electricity spot market constraints can be obtained, and the safety check results have the executability of the power market. The rationality and feasibility of the safety check algorithm results are verified by simulating the provincial-scale electricity spot market. According to the simulation results, this method can release effective reserve resources and provide more guarantees for the safe operation of the power grid. In addition, this method can save up to 4.9% of the total operation cost of the power system and improve the dispatching economy of the power system. This method is of great significance to ensure the safe operation of the power system and the day-ahead market and real-time market scheduling in the actual power spot system. In addition, this method also has great guiding significance for the analysis of the actual reserve situation of the power market after the event.

KEYWORDS

power market, safety checks, effective reserve, tie-line optimization, power grid congestion

1 Introduction

With the increase in power consumption load and the large-scale integration of new energy into the grid, the safety and economic operation of the power system is facing severe challenges (Li et al., 2020). With the rapid construction of a new power system with new energy as the main body, the penetration rate of new energy is increasing, which puts forward new requirements for the adequacy of power system operation (Chen et al., 2022). Large-scale new energy integration brings a large amount of clean energy to the power grid and great challenges to the power system reserve (Yang et al., 2020).

With the large-scale construction of provincial and regional electricity spot markets, the current progress of power market construction in various provinces is different, and regional

grid security verification requires coordination between provincial markets and regional dispatching (Cai et al., 2022). When there is a breakthrough in power grid security constraints, the correction strategy needs to consider the stable operation of the market, which poses new challenges to the traditional security check mode.

Safety check refers to the process of analyzing the safety and power balance of the power system from the perspective of power system operation safety (Bao et al., 2022). The safety check of electricity spot energy market transactions is carried out simultaneously with market clearance, and the market clearance results must strictly meet the national and industry policies and standard requirements and, at the same time, meet the requirements of safe and stable operation of the power grid, power balance, and clean energy consumption.

In addition, China adopts UHVDC (ultra-high-voltage direct current) transmission technology to transport surplus energy in the western region to the load center in the central and eastern regions over long distances, which breaks the reverse distribution of energy resources and energy consumption in China (Fang et al., 2022), where power is usually transmitted between regions through multiple inter-provincial AC/DC channels. At present, the provincial government of the inter-provincial AC and DC channels usually signs an inter-provincial power transmission framework agreement to agree on the annual power transmission scale (Zhou et al., 2022), generally including the annual power transmission, transmission load, and peak-to-valley ratio, but it is difficult to stipulate the specific power transmission curve throughout the year with the inter-provincial power transmission framework agreement. The daily output curve of the tie-line is determined by the decomposition mechanism, and the contract power decomposition curve obtained by different decomposition mechanisms may be different. Since the framework agreement between the provinces connected by the transmission tie-line usually needs to be physically implemented, especially the inter-provincial priority power generation plan needs to be cleared first according to the decomposition curve to ensure implementation, the daily output curve of the tie-line determined by the decomposition mechanism forms the constraint of the spot market model (Peng et al., 2020); that is, the provincial electricity spot market usually takes the power of the tie-line as the boundary data of the spot market clearance.

In the electricity spot market, adjusting the transmission power of the tie-line needs to consider the safety of the regional collaborative power grid, the fairness of the market, and the rationality of the clearing results. In the actual operation of the power grid, the power replacement of the tie-line occurs from time to time in real-time scheduling, and the change of the tie-line power is bound to affect the blocking of the section and line. Therefore, based on the results of the day-ahead electricity spot market, it is necessary to optimize the power of the tie-line for the safety check, which can further ensure the stability of the power market and the safety of the provincial and regional power systems.

The operation reserve of the power system refers to the additional active capacity that can be called up at any time to cope with load forecast errors, unexpected equipment outages, unit power generation failures, renewable energy power fluctuations, etc., in the arrangement of power system operation mode and real-time dispatch operation. In actual grid operation, it is difficult to evaluate the actual available operational reserve (Duan et al., 2022). This article refers to this reserve as an effective reserve, which refers to the spare capacity of the unit that the system can call up in time. However, the evaluation of effective reserve in the current stage of research is often localized in the calculation problem of production applications, such as in the work of Zhang et al. (2020) and Wenhuan et al. (2022). The literature classifies effective reserve evaluation as a production application problem and only a *post hoc* calculation and deduction method, which cannot cope with the needs of real-time scheduling in the spot market environment. It is difficult to accurately calculate the effective reserve of the system in real-time scheduling, which brings great security risks to the system. In addition, due to changes in boundary conditions, the day-ahead clearing results may not meet the demand for an effective reserve of the system in the real-time market, especially in the new power system, where the effect of the new energy forecast is particularly significant. In the new power system, relevant research on the difficulty of reserve evaluation caused by the deviation of new energy prediction includes the probability evaluation method (Chen et al., 2022; Liu et al., 2023), random optimization (Xu et al., 2023), and robust optimization (Ran et al., 2022; Wang et al., 2022). The probabilistic evaluation method and stochastic optimization method are too dependent on the probabilistic accuracy of boundary data prediction in the day-ahead electricity spot market and cannot meet the actual scheduling demand in the day-ahead and real-time electricity spot market. The solution results of the robust optimization method are too conservative and cannot be applied to the actual electricity spot market clearing model.

At present, it is also difficult to assess the effective reserve in the day-ahead electricity spot market; if the proportion of effective reserve components in the operating reserve is relatively low, it will mislead the dispatcher, give the dispatcher the illusion of sufficient effective reserve, and bring serious hidden dangers to the safety of the power system.

The factors affecting the effective reserve capacity of the power system can be divided into the following three levels: first, at the level of power system power grid security, the power flow limit of the section or line will affect the effective reserve space provided by the unit; for example, when the section exceeds the limit in the forward/reverse direction, the unit with a positive/negative generation shift distribution factor (GSDF) relationship with the section cannot provide the corresponding reserve at this time, and the marketization of power spot may cause transmission congestion to be more obvious and compress the effective reserve space. Second is the multi-energy coupling in energy interconnection (Wu et al., 2019; Hou et al., 2022). At this level, the primary energy supply can also affect the effective reserve, such as the coal storage limit of the coal turbine, the natural gas supply limit of the gas engine, the reservoir capacity limit of the pumped storage unit, the water level limit of the hydropower unit, and the cascade hydropower limited by the basin hydraulic limit, which will affect the effective reserve that the unit can provide. Third, at the time coupling level of the power system, the constraints of the climbing rate of the unit and the maximum energy of the unit in a dispatching cycle make the spare capacity of the unit unable to be called by the system in time and unable to provide an effective reserve.

Therefore, by optimizing the power of the tie-line in the safety check link, alleviating the congestion of the power grid, and releasing more effective reserve in the system, the overall reserve and peak regulation

capabilities of the system can be guaranteed, and safe, stable, and economical operation of the power grid can be guaranteed.

The preparation and verification of the tie-line plan is a key link affecting the scheduling and transaction organization of multi-level coordination, so it is necessary to reasonably evaluate the transmission power of inter-provincial channels to ensure the security of the power grid in the whole region.

From the level of safety check of the power system, it is a very novel research point to optimize the power of the tie-line to release effective reserve of the system.

2 Safety check method

The safety check of spot energy market transactions is carried out simultaneously with market clearance, and the results of market clearance must strictly meet the national and industry policies and standards and the requirements of safe and stable operation of the power grid, power balance, and clean energy consumption.

The clearing model of the electricity spot market includes the security-constrained unit commitment (SCUC) and the security-constrained economic dispatch (SCED). The specific clearing model is shown in the Supplementary Material's SCUC model and SCED model (Fang et al., 2020). Among them, the tie-line planned power is used as a boundary condition and does not participate in market optimization.

Among them, the security check has been completed simultaneously in the process of solving SCUC and SCED, the power grid security check is completed by the power grid security constraint in the clearing model, and the load balance check is completed by the system balance constraint in the clearing model.

The consideration of positive and negative reserves of the system in the spot market clearance is completed by the system reserve capacity constraint. However, this constraint is relatively extensive in considering reserve, and usually, the positive reserve of the system is based on the proportion of the total system load forecast, or the positive reserve demand is set according to the maximum capacity of a single unit.

The safety check method proposed in this paper is to modify the day-ahead electricity spot market clearing model under the condition that the unit power is determined. For details of the modification, see the safety check model in Section 3 of this article.

3 Safety check model

The safety check model is a transformation of the SCUC model (the SCUC model is shown in Supplementary Material), which mainly includes the following four points:

1. The objective function of the safety check model is to maximize the effective reserve
2. Model the effective reserve
3. Model the DC tie-line
4. Modify the constraints that affect the effective reserve of the system

3.1 Objective function: effective reserve maximization

$$\max \sum_{i=1}^{N} \sum_{t=1}^{T} PR_{i,t}. \tag{1}$$

Here, $PR_{i,t}$ indicates the maximum effective reserve that the unit i can provide at the time t; N indicates the total number of units; and T is the total number of periods.

3.2 DC tie-line model

DC tie-line power has the characteristics of controllability, which can be optimized as a flexible resource to promote the optimal allocation of resources. For DC tie-lines, its power can be freely controlled, so it can be optimized by constructing variables separately, and its sending and receiving ends are used as node loads and node injections, respectively (Peng et al., 2020).

Although the DC tie-line power can be flexibly adjusted, in actual operation, it is not possible to make frequent adjustments, except in emergencies, in which the action of AC filters and converter transformers is an important limiting factor (Shen et al., 2020).

Therefore, the tie-line power constraint includes the following five items.

3.2.1 Limits of tie-line power

The upper and lower limit constraints of tie-line power mean that the transmission power of the tie-line should be within its maximum and minimum technical output range, which can be described as

$$TL_{j,t}{}^{\min} \le TL_{j,t} \le TL_{j,t}{}^{\max}, \tag{2}$$

where $TL_{j,t}$ is the tie-line j power at the time t. $TL_{j,t}{}^{\min}$ and $TL_{j,t}{}^{\max}$ are the tie-line j minimum and maximum power transmission limits of the time t, respectively. This article simulates the power of the tie-line sent out, and $TL_{j,t}{}^{\min}$ there will not be less than 0, so in this article, we set $TL_{j,t}{}^{\min} = 0$.

3.2.2 Tie-line adjustment time limit

The DC tie-line adjustment limit constraint means that the number of power changes of the tie-line throughout the day must be within a certain range, which can be described as

$$\begin{cases} x_{j,t}^{u} + x_{j,t}^{d} \le 1 \\ \sum_{t=1}^{T} x_{j,t}^{u} + x_{j,t}^{d} \le NTL_{j}{}^{\max} \end{cases}, \tag{3}$$

where $x_{j,t}^{u}$ and $x_{j,t}^{d}$ are 0–1 integer variables. $x_{j,t}^{u} = 1$ indicates the tie-line j is adjusted up at the time t; $x_{j,t}^{u} = 0$ indicates the tie-line is not adjusted up at the time t; $x_{j,t}^{d} = 1$ indicates the tie-line is adjusted down at the time t; and $x_{j,t}^{d} = 0$ indicates the tie-line is not adjusted down at the time t. $NTL_{j}{}^{\max}$ is the maximum number of changes in the power of the tie-line throughout the day.

3.2.3 Tie-line adjacent periods cannot be reversed

The power of the tie-line cannot be first up and then down or first down and then up in adjacent periods, which can be described as

$$\begin{cases} x_{j,t}^{u} + x_{j,t+1}^{d} \le 1 \\ x_{j,t+1}^{u} + x_{j,t}^{d} \le 1 \end{cases}. \tag{4}$$

3.2.4 Tie-line power adjustment rate constraints

DC tie-line climbing constraint refers to the up/down adjustment of DC tie-line power, which must meet the climbing rate requirements, which can be described as

$$\begin{cases} TL_{j,t} - TL_{j,t-1} \le x_{j,t}^{u} \cdot \Delta TL_{j}^{U} \\ TL_{j,t-1} - TL_{j,t} \le x_{j,t}^{d} \cdot \Delta TL_{j}^{D} \end{cases}, \tag{5}$$

where ΔTL_j^U and ΔTL_j^D are the tie-line j maximum upward and downward adjustment rates.

3.2.5 Tie-line channel constraints

In medium- and long-term transactions, the planned power of each tie-line channel has been confirmed, and it is prioritized in the spot market according to the contract power decomposition curve. This model focuses on the safety check after the day-ahead electricity spot market clearing, so it does not change the total power curve of the tie-line channel, only optimizes the power of the tie-line contained in the channel, and the total transmission power of each tie-line is consistent with the total power of the channel, which can be described as

$$\sum_{j \in q} TL_{j,t} = TL_{q,t}, \tag{6}$$

where $TL_{q,t}$ is the planned power of the tie-line channel q during the time t.

3.3 Effective reserve-related constraints

3.3.1 Coupling constraint between the unit operating status and effective reserve variables

When the unit is down, it cannot provide any effective reserve, so effective reserve variables should be a coupling relationship with the operating state of the unit:

$$0 \le PR_{i,t} \le \alpha_{i,t} P_{i,t}^{\max}. \tag{7}$$

A binary variable $\alpha_{i,t}$ is used to describe whether the unit i is on at the time t. $\alpha_{i,t} = 0$ indicates the unit is shut down, and $\alpha_{i,t} = 1$ indicates the unit is turned on; $P_{i,t}^{\max}$ is the maximum power limit of the unit i at the time t.

In addition, the effective reserve variables' upper limit should be less than the difference between the maximum adjustable output of the unit and the actual output of the unit, that is, the following constraint should be met:

$$PR_{i,t} \le P_{i,t}^{\max} - P_{i,t}, \tag{8}$$

where $P_{i,t}$ indicates the power of the unit i at the time t.

Constraints (7) and (8) can be written together as follows:

$$0 \le PR_{i,t} \le \alpha_{i,t} P_{i,t}^{\max} - P_{i,t}. \tag{9}$$

3.3.2 Unit climbing constraint coupled with effective reserve

At the time coupling level, constrained by the climbing rate of the unit, the effective reserve is the output of the unit that can be called at the next period, and the climbing constraint of the unit coupled with the effective reserve is shown as follows:

$$\begin{aligned} P_{i,t} + PR_{i,t} - P_{i,t-1} \le \Delta P_i^U \alpha_{i,t-1} + P_{i,t}^{\min}\left(\alpha_{i,t} - \alpha_{i,t-1}\right) \\ + P_{i,t}^{\max}\left(1 - \alpha_{i,t}\right), \end{aligned} \tag{10}$$

where ΔP_i^U is the maximum uphill climbing rate of the unit i and $P_{i,t}^{\min}$ is the minimum power limit of the unit i at the time t.

3.3.3 Unit energy constraint coupled with effective reserve

Due to the limitation of the primary energy supply of thermal power units and the limitation of the water level and storage capacity of hydropower units, the effective reserve that can be provided by the unit is limited, and the following energy constraint is used:

$$T_0 \sum_{t=1}^{T} \left(P_{i,t} + PR_{i,t}\right) \le Q_i^{\max}, \tag{11}$$

where T_0 is the length of a period; if 96 periods are considered per day, each period is 15 min, $T_0 = 0.25$ (hours); $Q_i^{\max}$ is the maximum energy of the unit i.

To ensure the solution speed of the model, the modeling of hydropower units is linearized: the water level water consumption rate curve and the water level reservoir capacity curve of the hydropower plant are linearized in segments and converted into electricity constraints after external linearization treatment. The water level reservoir capacity curve of hydropower plants is the curve of the relationship between the reservoir level of hydropower plants and its corresponding reservoir capacity. The water level water consumption rate curve is the curve of the relationship between the water head and water level of the hydropower plant and its corresponding water consumption rate.

3.3.4 Power grid security constraint with effective reserve coupling

Reserve, that is, subject to power grid security constraints, using line safety constraints as an example, as shown in the formula (12), the same applies to section safety constraints:

$$\begin{aligned} -P_l^{\max} \le \sum_{i=1}^{N} G_{l-i}\left(P_{i,t} + PR_{i,t}\right) + \sum_{j=1}^{NT} G_{l-j} TL_{j,t} - \sum_{k=1}^{K} G_{l-k} D_{k,t} - SL_l^{+} \\ + SL_l^{-} \le P_l^{\max}, \end{aligned} \tag{12}$$

where $P_l^{\max}$ it is the power transmission limit of the line l; G_{l-i} is the GSDF between the node where the unit i is located and the line l; G_{l-j} is the GSDF between the node where the tie-line j is located and the line l; G_{l-k} is the GSDF between the node k and the line l; K is the number of nodes in the system; $D_{k,t}$ is the bus load value for the node

k at the period t; and SL_l^+、 SL_l^- are the positive and negative flow relaxation variables of the line l.

The coupling of the slack variable and the effective reserve variable of power grid security constraint has the constraint relation of formula (13). When the line crosses the limit, the unit with the corresponding positive sensitivity cannot provide the corresponding reserve. When the line crosses the limit, the unit with the corresponding positive GSDF cannot provide the corresponding reserve. When the line reverses the limit, the unit with the corresponding negative GSDF cannot provide the corresponding reserve:

$$\begin{cases} SL_l^+ > 0 \& G_{l-i} > 0 \Rightarrow PR_i = 0 \\ SL_l^- > 0 \& G_{l-i} < 0 \Rightarrow PR_i = 0 \end{cases}. \tag{13}$$

3.3.4.1 Constraint linearization

To facilitate the implementation of model engineering and ensure the speed of model solving, the formula is linearized as follows:

$$\begin{cases} SL_l^+ + SL_l^- > -H(1-\tau_l) \\ PR_i \le H(1-\tau_l) \end{cases}, \tag{14}$$

where τ_l is a 0–1 integer variable. When $\tau_l = 1$, it represents that the line crosses the limit. When $\tau_l = 0$, it means that the line has not exceeded the limit. Since no single machine capacity in the market currently exceeds 2,000 MW, H can be set to 2000.

4 Case analysis

This paper simulates the provincial-scale power grid data of tie-line power sent out of the province, and the generator sets are mainly composed of clean energy.

4.1 Boundary data analysis

In the boundary data, the proportion of each type of unit by capacity is shown in Table 1.

In this case, only thermal-type and hydropower-type units can provide reserve capacity, while wind-type and photovoltaic-type units do not provide reserve capacity.

In the case simulation in this paper, the number of nodes is 1,641, the number of branches is 2,081, and the number of tie-lines is 21, of which the power of the tie-line is all the sending power, and the power grid nodes on the 21 tie-lines are seven. In this paper, for the convenience of description, the power grid nodes of the tie-line are the same, called a tie-line group.

TABLE 1 The proportion of capacity of each type of unit.

Unit type	Number of units	Capacity/MW	Percentage/%
Thermal	34	13,600	26
Hydropower	88	27,672	54
Wind power	91	8,105	16
Photovoltaic	51	2,208	4

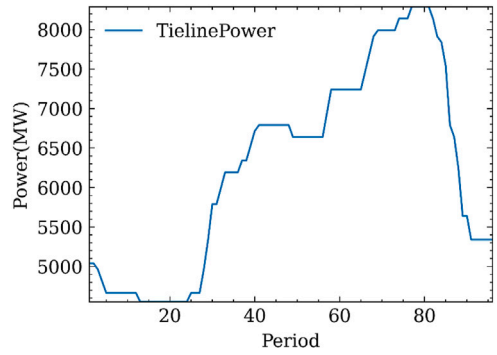

FIGURE 1
Total power curve of the whole system tie-line.

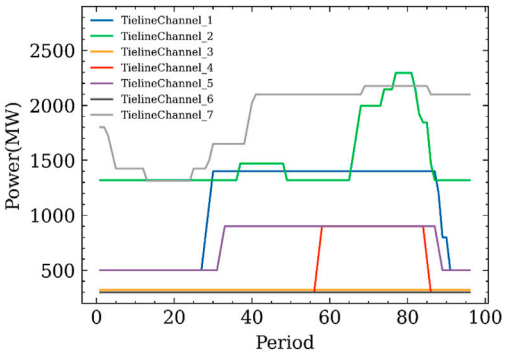

FIGURE 2
Power curve of seven tie-line groups.

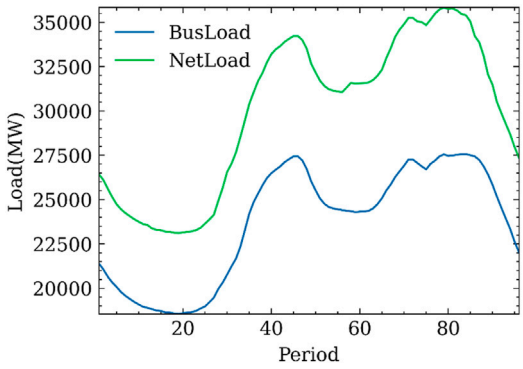

FIGURE 3
Net load and bus load of the whole system.

The total power of the tie-line at each period is shown in Figure 1. In the period 13–24, the minimum power of the tie-line is 4,552.5 MW, and in the period 77–81, the maximum power of the tie-line is 8,290 MW.

The power curve of seven tie-line groups at each period is shown in Figure 2. The power of TielineChannel_3 and TielineChannel_

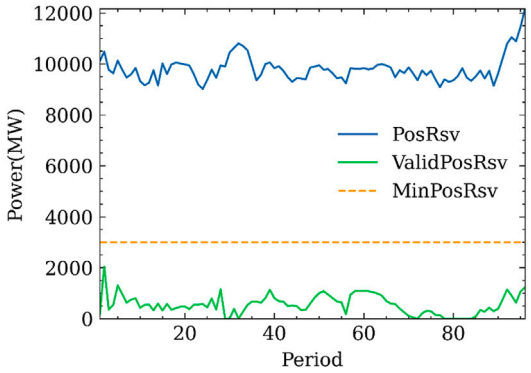

FIGURE 4
Comparison diagram of system positive reserve, effective positive reserve, and positive reserve demand.

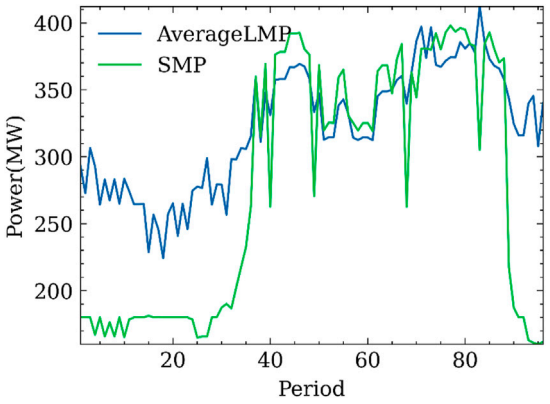

FIGURE 5
Comparison diagram of average LMP and SMP.

4 for 96 periods in the whole day is the same, and no power adjustment occurs. The power of other tie-line groups is not adjusted for 96 periods in the whole day.

The net load and bus load for each period are shown in Figure 3. In this figure, the bus load of the system represents the total load of the whole grid, and the net load of the system represents the total load of the whole grid minus the load of the tie-line. The net load of the system and the total bus load have the same variation trend. The 20 period (4:45) is the load valley, and the 80 period (19:45) is the load peak.

The reserve demand value is about 8.5% of the maximum net load, that is, 3,000 MW.

The solver used to solve this model is CPLEX 12.8.0. The computer processor for the solution environment is Intel(R) Core(TM) i7-8565U CPU @ 1.80 GHz 1.99 GHz, the memory space is 16GB, and the operating system is Windows 10.

After simulation of all types of unit quotation, the results of solving the SCUC model (Fang et al., 2020) are as follows: the MIPGap value converges to 0.00997%, the objective function value is 495,417,627, and the solution time is 3,299 s.

In the SCUC clearing results, no lines have crossed the limit, and the safety constraints are met; 20 lines reach the boundary, and 117 lines are heavy load. Reaching the boundary means that the line power flow is equal to the line capacity. Heavy load means that the current flow of the line reaches more than 80% of the line capacity but does not reach the boundary.

The reserve and effective reserve pairs of the system are shown in Figure 4. PosRsv represents the reserve that can be provided by the system at each period, ValidPosRsv represents the effective reserve that can be provided by the system at each period, and MinPosRsv represents the positive reserve demand value of each period of the system. As shown in the figure, the effective reserve that the unit can provide during the 80 period and its vicinity is 0. The system load is maximum during this period. Although the system can provide positive and reserve values much higher than the reserve requirement of 3,000 MW, the effective reserve at 29, 30, 32, 72, 78, 79, 80, 81,82, 83, and 84 periods are 0. It shows that although the positive reserve constraint is met in the results of day-ahead electricity spot market clearing, the effective reserve is very low, and if the dispatcher sees that the positive reserve capacity that the system can provide is much higher than the capacity demand of 3,000 MW, but the actual effective reserve is very low, it brings great safety risks to the power system dispatching operation.

The system marginal price is shown in Figure 5. Average LMP represents the average locational marginal price (LMP) in each period of the system, and SMP represents the system marginal price (SMP), that is, the price of energy.

When the whole power grid is not blocked, the LMP of all nodes in the whole power grid is the same, which is the marginal cost of the marginal generator set. When the power grid is blocked, the LMP of the nodes of the whole power grid is different. Figure 5 mainly illustrates the existence of the congestion situation, so the average LMP and SMP of the results of day-ahead electricity spot market clearing are inconsistent.

4.2 Results of safety checks

After the safety check of the tie-line power optimization, it has a positive impact on the power grid congestion situation. A total of 16 lines reached the boundary, 115 lines were overloaded, no line exceeded the limit, and the safety constraint was met. The line congestion was alleviated to a certain extent.

After the safety check of the tie-line power optimization, the impact on the effective reserve is shown in Figure 6. ValidPosRsv_befor represents the effective reserve of day-ahead electricity spot market clearing, ValidPosRsv_after represents the effective reserve that can be provided by the system after optimizing the tie-line power, and MinPosRsv represents the positive reserve demand value for each period in the system. As shown in Figure 6, the effective reserve value of the system is significantly improved after the optimization of the tie-line power, and the minimum positive reserve demand value of the system is met for most of the period. In the original model, the effective reserve at 29, 30, 32, 72, 78, 79, 80, 81, 82, 83, and 84 periods are 0. After the optimization of the power of the tie-line power, the effective reserve in these periods is significantly improved. Among them, the effective reserve

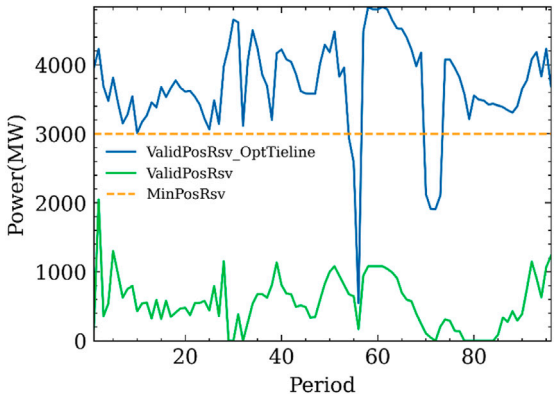

FIGURE 6
Comparison diagram of the effective positive reserve before and after optimizing the power of the tie-line.

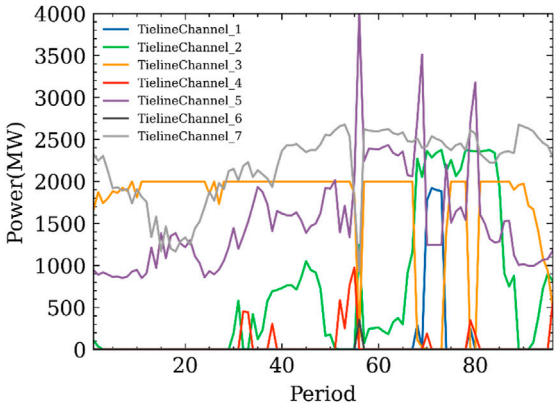

FIGURE 7
Power curve of seven tie-line groups after optimizing the power of the tie-line.

value in the load peak 80 period (3,553.7 MW) is greater than the minimum positive reserve demand value (3,000 MW).

In summary, after the safety check optimizing the tie-line power, the system power grid congestion situation is alleviated, and the effective reserve is significantly released.

Compared with Figures 2, 7, it can be seen that after optimization the power of the tie-line changes more frequently with periods. However, this change has a positive impact on the safety of the whole system operation.

4.3 Safety check and clearance model iteration

After the safety check of tie-line power optimization, a new tie-line power curve is obtained, which is used as new boundary data, and the original SCED model (Fang et al., 2020) is optimized under the condition of fixed unit start and stop. The clearing results are as follows: the objective function value is 471,042,162, which is 4.9%

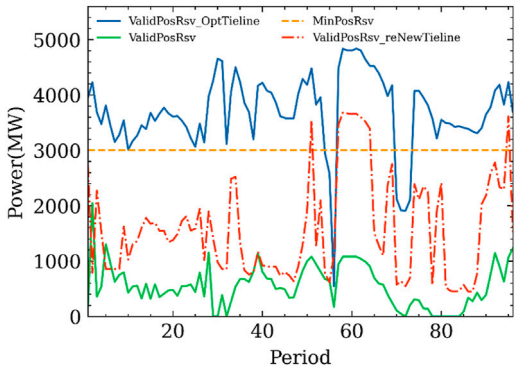

FIGURE 8
Comparison diagram of the effective positive reserve.

lower than the total cost of the output curve of the original tie-line power. This shows that the safety check method to optimize the power of the tie-line has a positive impact on the economy of the whole system operation. System power grid congestion: 31 lines reach the boundary, and 132 lines are overloaded. The power grid congestion is worse than the original tie-line power. By comparing the results of the actual day-ahead electricity spot market clearing optimization model, it is found that although the power grid congestion situation is slightly aggravated, there is no line exceeding the limit. The most important thing is that the economy of the operation cost is objectively improved.

The effective reserve situation of the system is shown in Figure 8, where ValidPosRsv represents the effective reserve of day-ahead electricity spot market clearing, ValidPosRsv_OptTieline represents the effective reserve that the system can provide after optimizing the tie-line, MinPosRsv represents the positive reserve demand of each period of the system, and ValidPosRsv_reNewTieline represents the effective reserve that the units can provide after the SCED model clears when the new tie-line power replaces the tie-line power of the original boundary data. It can be seen from Figure 8 that after the iteration of the optimized tie-line power and the SCED model, the effective reserve for most of the period has been significantly improved. Although the effective reserve did not exceed the positive reserve requirement value of 3,000 MW for many periods, there was no period when the effective reserve was 0.

Figure 9 is a comparison chart of positive reserve and effective positive reserve in the SCED model clearing results as a boundary, and it can be seen from Figures 4, 9 that the effective reserve has been significantly released. In Figure 9, there are not only all periods that can provide effective reserves but also periods 83 and 87 that provide the lowest effective reserve, and the lowest effective reserve value is 450 MW.

The average LMP and SMP are shown in Figure 10. The average LMP and SMP of the results of day-ahead electricity spot market clearing are inconsistently illustrating the existence of the congestion situation.

For the power grid with heavy congestion, the reserve deduction method (Zhang et al., 2020; Wenhuan et al., 2022) will lead to clearing failure. However, the method provided in this paper will not only affect the normal clearing process but also improve the effective reserve resources, which not only ensures the safety of the power grid but also improves the economy of power system dispatching. For the new power system with a high proportion of new energy, compared with the

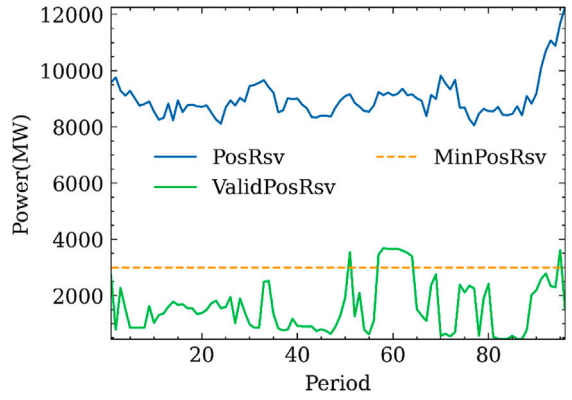

FIGURE 9
Comparison diagram of system positive reserve, effective positive reserve, and positive reserve demand.

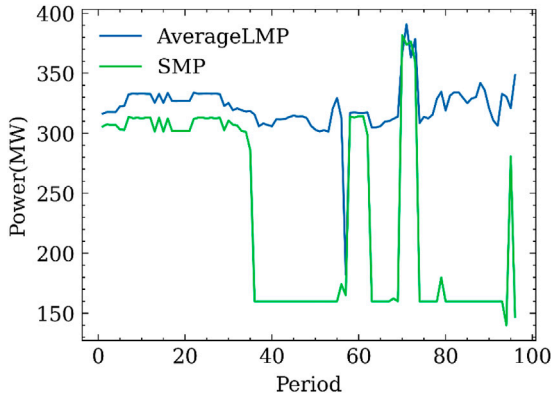

FIGURE 10
Comparison diagram of average LMP and SMP.

probabilistic evaluation method (Chen et al., 2022; Liu et al., 2023) and random optimization (Xu et al., 2023), the method provided in this paper has better real-time performance and certainty, can meet the actual power scheduling requirements, and can be directly applied to the engineering algorithm of power spot market clearing.

5 Summary

In this paper, a safety check method is proposed to optimize the power of each tie-line to maximize the effective reserve resources in the power system. Through the simulation analysis of the provincial-scale power system, by optimizing the power of 21 tie-lines, it is proved that the use of this safety check method has a significant effect on the effective reserve resources of the system, and the optimized tie-line power as a new boundary brings positive impact on the operation safety and system economy of the whole system. However, from the perspective of regional safety check, the effect of changes in the power of the transmission tie-line in the province on other provinces or regions requires the regional dispatching agency to re-evaluate from the regional safety check level.

This safety check method is deeply coupled with the day-ahead electricity spot market clearing model and takes into account all constraints of the electricity spot market. This security check method has high clearance efficiency and is of great significance in connecting the real day-ahead electricity spot market with the real-time electricity spot market. This security check method has a clear implementation path, which is convenient for engineering applications.

The safety check optimization results are reasonable and reliable and have extremely high practical significance. The safety check optimization results of the tie-line power are executable for power dispatching and can provide a reasonable and reliable dispatching scheme for real-time dispatching staff to cope with the sudden increase in reserve demand.

This safety check method is also of great guiding significance for the post-event analysis of the real reserve situation of the power market. In addition, this method is of positive significance to improve the difficulty of effective reserve assessment of the electricity spot market.

Data availability statement

The original contributions presented in the study are included in the article/Supplementary Material; further inquiries can be directed to the corresponding authors.

Author contributions

YW: contributing to the core ideas of the article; XW: article writing, model conception, and algorithm development; XS: providing effective reserve model ideas; WZ: providing tie-line model ideas; XZ: core idea discussion, validation, and revision; SL: providing the core issues and power spot clearing process modification suggestions; and QS: providing data, data processing, related works.

Conflict of interest

YW, XZ, SL, and QS were employed by the company Yunnan Power Grid Co., Ltd.

XW, XS, and WZ were employed by the company Beijing Tsintergy Technology Co., Ltd.

Publisher's note

Supplementary material

The Supplementary Material for this article can be found online at: https://www.frontiersin.org/articles/10.3389/fenrg.2023.1162122/full#supplementary-material

References

Bao, Y., Xinyuan, L., Huiping, Z., Zhi, C., Han, B., and Xiaojing, H. (2022). "Electricity spot market design considering accurate security check," in *2022 4th international conference on power and energy technology (ICPET)* (IEEE).

Cai, Z., Zhang, G., Wang, M., Zhang, C., Sun, Y., and Sun, Y. (2022). Collaborative security check and correction of regional and provincial power grids under the environment of power market[J]. *Proc. CSEE*, 1–11.

Chen, Y., Fan, X. U., Zhang, W., and Wang, C. (2022). Research on reserve allocation of novel power system facing energy security and the corresponding preservation criterion[J]. *Proc. CSU-EPSA* 34 (4), 32–40.

Duan, Q., Xie, X., Tang, X., and Zhu, C. (2022). Multi-stage robust clearing model considering renewable energy output uncertainty and unit effective reserve calculation in electricity market[J]. *Front. Energy Res.* 10, 1–2.

Fang, K., Ke, D., Sun, Y., Wu, H., Shen, Y., and Gong, L. (2022). Grid optimal dispatching model considering stability constraints of large-scale HVDC infeed[J]. *South. Power Syst. Technol.* 16 (7), 1–9.

Fang, X., Yang, Z., Yu, J., Zou, P., Zhao, W., and Lai, X. (2020). Theoretical analysis and extension of locational marginal price[J]. *Proc. CSEE* 40 (2), 379–390.

Fang, X., Yang, Z., Yu, J., Zou, P., Zhao, W., and Lai, X. (2020). Theoretical Analysis and Extension of Locational Marginal Price[J]. *Proceedings of the CSEE* 40 (2), 379–390.

Hou, Y., Ding, Y., Bao, M., Liang, Z., Song, Y., and Guo, C. (2022). Analysis of Texas blackout from the perspective of electricity-gas coupling and its enlightenment to the development of China's new power system[J]. *Proc. CSEE*.

Li, L., Lin, W., Yang, Z., Yu, J., Xia, S., and Wang, Y. (2020). Characterizing a tie-line transfer capacity region considering time coupling in day-ahead multi-period dispatch [J]. *Power Syst. Prot. Control* 48 (23), 64–72.

Liu, S., Yan, Y. A. N. G., Yang, Z., and Chen, Q. (2023). Reserve capacity determination and its cost allocation considering stochastic characteristics of renewable energy[J]. *Automation Electr. Power Syst.* 47 (4), 10–18.

Peng, C., Gu, H., Zhu, W., Xu, D., Zhao, W., Xia, Q., et al. (2020). Study on spot market clearing model of regional power grid considering AC/DC hybrid connection[J]. *Power Syst. Technol.* 44 (1), 323–331.

Ran, L. I., Wang, M., Yang, M., Wang, M., and Wang, W. (2022). Robust-stochastic reserve optimization considering uncertainties of failure probability and net load[J]. *Automation Electr. Power Syst.* 46 (6), 20–29.

Shen, J., Zhang, H., and Chen, Z. (2020). Optimization model of HVDC tie-line power considering reactive power control equipment action times[J]. *South. Power Syst. Technol.* 14 (12), 17–24.

Wang, J., Hao, L., Cai, Y., Shao, Y., and Song, Z. (2022). Day-ahead joint clearing model of electric energy and reserve auxiliary service considering flexible load[J]. *Front. Energy Res.* 10, 1–2.

Wenhuan, H. A. O., Chen, Yefu, Qiu, D., Meng, Z., Yu, Z., Dong, K., et al. (2022). Research on deduction algorithm for limited power system reserve capacity network[J]. *Electr. Eng.* (9), 12–14.

Wu, K., Wang, J., Wei, L. I., and Zhu, Y. (2019). Research on the operation mode of new generation electric power system for the future energy internet[J]. *Proc. CSEE* 39 (4), 966–979.

Xu, D., Huang, H., Cheng, Q., Hu, X., and Tang, J. (2023). Generation-reserve two-staged joint optimization model for interconnected power grid considering security risks[J]. *Power Syst. Technol.* 47 (2), 624–637.

Yang, X., Luo, J., Chen, Y. U., Xie, D., Ge, R., and Feng, C. (2020). Review of power system reserve configuration and optimization for large-scale renewable energy integration[J]. *Electr. Power Eng. Technol.* 39 (1), 63. 10-20.

Zhang, Q., Zhang, L., Xiao, Y., Dai, X., and Lai, X. (2020). Design of south China (starting from guangdong province) power reserve market[J]. *Electr. Power* 53 (9), 28–37.

Zhou, Q., Jin, L., and Lv, Q. (2022). Research on China's new energy cross-provincial marketization mechanism under the background of"Double carbon"[J]. *Front. Energy Res.* 10, 1–2.

frontiers | Frontiers in Energy Research

TYPE Original Research
PUBLISHED 10 May 2023
DOI 10.3389/fenrg.2023.1193415

OPEN ACCESS

EDITED BY
Yongxin Xiong,
Aalborg University, Denmark

REVIEWED BY
Shichang Cui,
Huazhong University of Science and Technology, China
Wei Gan,
Cardiff University, United Kingdom

*CORRESPONDENCE
Benxi Liu,
benxiliu@dlut.edu.cn

RECEIVED 24 March 2023
ACCEPTED 25 April 2023
PUBLISHED 10 May 2023

CITATION
Liu B, Peng Z, Liao S, Liu T and Lu J (2023), A multi-objective optimization model for the coordinated operation of hydropower and renewable energy. *Front. Energy Res.* 11:1193415. doi: 10.3389/fenrg.2023.1193415

A multi-objective optimization model for the coordinated operation of hydropower and renewable energy

Benxi Liu[1]*, Zihan Peng[1], Shengli Liao[1], Tengyuan Liu[1] and Jia Lu[2]

[1]Institute of Hydropower and Hydroinformatics, Dalian University of Technology, Dalian, China, [2]Hubei Key Laboratory of Intelligent Yangtze and Hydroelectric Science, China Yangtze Power Co Ltd, Yichang, Hubei, China

The rapid growth of wind and solar energy sources in recent years has brought challenges to power systems. One challenge is surging wind and solar electric generation, understanding how to consume such generation is important. Achieving the complementarity of hydropower and renewable energies such as wind and solar power by utilizing the flexible regulation performance of hydropower is helpful to provide firm power to help renewable energy consumption. However, the multi-energy complementary operation mode will change the traditional hydropower operation mode, causing challenges to the comprehensive utilization of hydropower. In this paper, a multi-objective optimal scheduling model is built by considering coordinated hydro-wind-solar system peak shaving and downstream navigation. First, the Gaussian mixture model is adopted to quantify the uncertainty of wind and solar power. Then, a hydro-wind-solar coordinated model was built to obtain the standard deviation of the residual load and the standard deviation of the downstream water level. Finally, the ε-constraint method is used to solve for the Pareto optimality. The results demonstrate the following: 1) The proposed model can effectively determine hydropower output schemes that can coordinate wind and solar power output to reconcile peak shaving and navigation; 2) The downstream hydropower stations' reverse regulation of the upstream hydropower station is a positive factor in reconciling conflicts; and 3) Reasonable planning of wind power and solar power is helpful for hydro-wind solar power complement operation.

KEYWORDS

hydro-wind-solar, generation scheduling, multi-objective, peak shaving, navigation

1 Introduction

With the explosive growth of wind and solar power sources, grid-integrated variable renewable energy (VRE) has become a key part of achieving the "Carbon Peaking and Carbon Neutrality Goals" in China (Department of Resource Conservation and Environmental Protection, 2021). However, the inherent intermittent and random characteristics of wind and solar power seriously challenge the safety and reliability operation of power systems (Albadi and El-Saadany, 2010; Shivashankar et al., 2016; Jabir et al., 2017; Asiaban et al., 2021). Using flexible power sources to mitigate renewable intermittency is a key solution (Shivashankar et al., 2016). Hydropower is a flexible power source that has developed technology, a large scale, and a low cost. Thus, hydropower that complements VREs is important to support the wide-ranging integration of

VREs such as wind and solar. However, hydropower that operates in unison with reservoirs usually serves multiple purposes. It not only needs to meet the demand for electricity generation, but also serves navigation, flood control, irrigation, ecological protection, and other comprehensive utilization tasks. Using hydropower to complement VREs will significantly change the operation mode of hydropower, and directly affect the power output, water level, and discharge flow of the reservoir. This may conflict with comprehensive utilization tasks (Jian et al., 2012; Shang et al., 2017). Therefore, exploring a reasonable operation method that considers the hydro-wind-solar complementation mode and comprehensive hydropower utilization is very significant for multi-energy complementation and the large-scale consumption of wind and solar.

Research on the operation of hybrid hydro-wind-solar systems, include studies (Zhu et al., 2018; Hu et al., 2021) that have evaluated the complementarity and united operation reliability of hydro-wind-solar power; moreover, various models suitable for different needs are established. In the literature (Liu et al., 2019a), a united operation strategy of hydro-wind-solar power, which can effectively suppress the intermittency of wind and solar output, is proposed by considering the natural complementarity of wind and solar power. The literature (Xie et al., 2021) shows that the introduction of spinning reserve and regulating reserve in the model can effectively deal with intermittent wind and solar power and improve the practical application ability of the hybrid hydro-wind-solar system. The literature (Jin et al., 2022) shows that properly developed wind and solar power can effectively utilize complementarity and reducing hydropower output fluctuations on multiple time scales. The literature (Wang et al., 2019b) simplifies the system by dividing the subsystems that can be coordinated to operate, and obtains the long-term scheduling scheme of the hydro-wind-solar power complementary system based on the whole basin. The literature (Chen et al., 2019) predicts wind and solar output through environmental conditions such as wind speed, radiation intensity, and temperature. On this basis, a hydro-wind-solar short-term complementary model that minimizes residual load fluctuations and maximizes VRE output is established.

However, with the rapid growth of integrated VREs, problems such as the risk of power output curtailment and the safe operation of high-proportion clean energy systems have become increasingly evident (Ding et al., 2016; Cheng et al., 2017; Luo et al., 2018), and scholars are constantly looking for solutions. The literature (Zhang et al., 2018) aimed to minimize the amount of curtailed wind and solar power and to maximize the stored energy in cascade hydropower stations and then established a short-term optimal scheduling model of hydro-wind-solar power. The literature (Liu et al., 2020) controlled the amount of curtailed wind and solar power by quantifying the uncertainty. The literature (Li et al., 2018) established an expansion planning method for a large-scale hybrid wind-solar multi-objective transmission network, which effectively reduced the amount of abandoned wind and solar energy in the power grid. The literature (Xi'an Jiaotong University et al., 2019) proposed a system for testing the reliability of large-scale renewable electricity integration and long-distance transmission. The literature (Ming et al., 2019) established a water-solar complementary long-term optimization model for large-scale solar power participation, and deduced a scheduling scenario that is superior to traditional rules in terms of energy production and power supply reliability.

Research on multi-energy complementarity with hydropower mostly regards hydropower stations as power production units. However, hydropower stations with reservoirs can also provide multiple benefits, such as ecological protection, irrigation, and navigation. Moreover, existing studies have shown that the participation of hydropower in peak regulation has adverse effects on the comprehensive benefits of reservoirs (Pérez-Díaz and Wilhelmi, 2010; Wan et al., 2020; Halleraker et al., 2022). Therefore, the reasonable operation of hydropower stations must also consider the conflict between different tasks. The literature (Li et al., 2020) used non-dominated sorting genetic algorithm to find the hydropower station scheduling scenario that considered the ecological needs of fish and hydropower generation. The literature (Niu et al., 2016) established a dual-objective model that takes both peak shaving and navigation under the background of demand conflict. The literature (Liu et al., 2019b) established multi-objective optimal dispatching model that considers the power generation of hydropower stations, power generation stability and ecological requirements of downstream rivers. The literature (Wang et al., 2019a) proposes a hydropower station dispatching plan that meets the requirements of hydropower compensation for wind power generation and daily water storage targets during the reservoir storage period.

It can be seen from the above studies that most of the studies regard hydro-wind-solar multi-energy complementary and hydropower multi-objective optimal scheduling as two independent research directions at present. For the power grid companies or power dispatching departments, in the context of the increasing demand for renewable energy consumption, when developing power generation plans for hydropower stations with navigational requirements, they need to consider not only the demand for renewable energy consumption and peak regulation of the power grid, but also the navigational requirements of the hydropower stations. For this situation, the main contributions of this paper are as follows:

(1) This paper proposed a hydro-wind-solar coordinated operation model. In which, two objectives, peak shaving and navigation, are considered.
(2) The model uses Gaussian mixture model to estimate the forecast output error considering the uncertainty of wind and solar output. Using the upper and lower limits of the forecast output error, the chance constraints are transformed into linear constraints that are easy to solve.
(3) The real-world applications are applied to illustrate the effectiveness and applicability of the proposed model, and the influence of wind and solar output on the model is analyzed from the aspects of uncertainty and installed capacity.

The rest of this paper is structured as follows. In Section 2, the analysis method of wind-solar uncertainty and the composition of the multi-objective hydro-wind-solar collaborative scheduling model are described. In Section 3, the Gaussian mixture model, which is used to address uncertainty, and the ε-constraint method, which is used to solve the dual-objective model, are introduced. In Section 4, the model is applied to the Jinghong-Ganlanba cascade

hydropower system that complements wind and solar power. In Section 5, the influence of wind and solar factors on the model results are analyzed. The main conclusions of the model analysis are given in Section 6.

2 Methodology

2.1 Uncertainty analysis of wind and solar power

It is challenging to forecast the power generation of wind and solar power due to the inherent intermittency, which is affected by environmental factors such as wind speed and light intensity. The literatures (Lingfors and Widén, 2016; Gholami et al., 2017) shows that the wind and solar output will tend to smooth out with the increase in the cluster scale of wind and solar stations. In this paper, since power stations in the same area usually send power via the same transmission channels, all wind stations in the same area are combined into a virtual wind power plant (VWP) and all solar power stations are combined into a virtual solar power plant (VSP).

$$P_t^{AW} = \sum_{i=1}^{NW} P_{i,t}^{W} \tag{1}$$

$$P_t^{AS} = \sum_{j=1}^{NS} P_{j,t}^{S} \tag{2}$$

where NW is the number of wind power stations. NS is the number of solar power stations. t is the period number, $t = 1, 2, ..., T$. T is the number of time periods. i is the wind power station number, $i = 1, 2, ..., NW$. j is the solar power station number, $j = 1, 2, ..., NS$. Moreover, P_t^{AW} is the output of the virtual wind plant in period t, MW; P_t^{AS} is the output of the virtual solar power plant in period t, MW; $P_{i,t}^{W}$ is the output of wind power stations i in period t, MW; and $P_{j,t}^{S}$ is the output of solar power station i in period t, MW.

The forecast output error of the wind power plant and solar power plant is converted into the output error coefficient.

$$\varepsilon_t^{AW} = \frac{P_t^{AW,a} - P_t^{AW,f}}{P_t^{AW,f}} \tag{3}$$

$$\varepsilon_t^{AS} = \frac{P_t^{AS,a} - P_t^{AS,f}}{P_t^{AS,f}} \tag{4}$$

where ε_t^{AW} and ε_t^{AS} are the forecast output error coefficients of the wind power and solar power at time t, respectively; $P_t^{AW,a}$ and $P_t^{AS,a}$ are the actual output of wind power and solar power at time t, respectively; and $P_t^{AW,f}$ and $P_t^{AS,f}$ are the forecast output of wind power and solar power at time t, respectively.

Describing the uncertainty of wind and solar output reasonably is important for building a hybrid hydro-wind-solar complementary model. The Gaussian mixture model (GMM) is a kind of non-parametric estimation method. Compared with the parameter estimation method, it can theoretically describe any distribution. Compared with the kernel density estimation method, the GMM can avoid the bandwidth setting effect on the accuracy of the results. Therefore, in this paper, the GMM is adopted to describe the output uncertainty of wind and solar power. Given a random variable x, the expression for the Gaussian distribution is:

$$f(x \mid \mu, \sigma) = \frac{1}{\sqrt{2\sigma^2\pi}} e^{-\frac{(x-\mu)^2}{2\sigma^2}} \tag{5}$$

The essence of the GMM is a simple linear combination of multiple Gaussian distributions, and its expression can be described as:

$$p(x) = \sum_{n=1}^{N} \omega_n \varphi(x \mid \mu_n, \sigma_n) \tag{6}$$

where $p(x)$ is the probability distribution of x. ω_n is the weight coefficient, $\sum_{n=1}^{N} \omega_n = 1$. Using the maximum likelihood estimation method, the parameters ω_n, μ_n, and σ_n can be determined.

2.2 Objective

With large-scale integration, the intermittent wind and solar power and the anti-peaking characteristics of wind power will challenge the peak shaving of the system. To meet the peak shaving requirements and balance the influence of wind and solar uncertainty, the flexible adjustment of hydropower output will cause frequent changes in downstream outflows and water level, which will directly affect navigation. Therefore, in this paper, peak shaving is considered the target of the hybrid hydro-wind-solar hybrid system:

$$minF(x) = [f_1(x), f_2(x)]^T \tag{7}$$

$f_1(x)$ represents the peak shaving target. Under certain conditions of incoming water, the goal of the hydro-wind-solar coordinate peak-shaving operation is to minimize the fluctuation of the residual load so that the residual load can be as smooth as possible. Therefore, the mathematical expression of the peak shaving target can be set to minimize the residual load variance:

$$f_1(x) = \min\left\{\frac{\sum_{t=1}^{T}(R_t - \bar{R})^2}{T}\right\} \tag{8}$$

$$R_t = C_t - P_t \tag{9}$$

$$\bar{R} = \frac{\sum_{t=1}^{T} R_t}{T} \tag{10}$$

$$P_t = \sum_{m=1}^{M} P_{m,t}^{H} + P_t^{AW,f} + P_t^{AS,f} \tag{11}$$

$$P_{m,t}^{H} = g(H_{m,t}, q_{m,t}) \tag{12}$$

where R_t is the residual load in the t period, MW. C_t is the original load of the grid. $\bar{R}$ is the average residual load. P_t is the sum of the output of the hybrid hydro-wind-solar system at Period t. $P_t^{AW,f}$ is the predicted output of the virtual wind plant at period t., MW. $P_t^{AS,f}$ is the predicted output of the virtual solar power plant at period t. $P_{m,t}^{H}$ is the output of the m hydropower station at period t. m is the serial number of hydropower station, $m = 1, 2, \ldots, M$. $H_{m,t}$ is the water head of hydropower station m at period t. $q_{m,t}$ is the power generation flow of hydropower station m at period t. $g(\cdot)$ is the output calculation function of the hydropower station.

$f_2(x)$ is the navigation target. The goal of navigation focuses on the elevation and variation in the downstream water level. Therefore, the minimum of the downstream water level change variance is taken as the objective function:

$$f_2(x) = \min\left\{\frac{\sum_{t=1}^{T}\left(Z_{down,t} - \bar{Z}_{down}\right)^2}{T}\right\} \tag{13}$$

where $Z_{down,t}$ is the downstream water level of the downstream hydropower station m at period t, m. $\bar{Z}_{down}$ is the mean value of the downstream water level of the downstream hydropower station.

2.3 Constraints

2.3.1 System constraints

a) Constraints of hydro-wind-solar complementarity

Since wind and solar power are uncertain and difficult to forecast accurately, chance constraints are introduced to use hydropower flexibility to complement wind and solar power output uncertainty.

$$\Pr\left\{\sum_{m=1}^{M} P_{m,t}^{H,max} - \sigma^{*}C_t + P_t^{AW,a} + P_t^{AW,a} \geq P_t\right\} \geq \vartheta_1 \tag{14}$$

$$\Pr\left\{\sum_{m=1}^{M} P_{m,t}^{H,min} + \sigma^{*}C_t + P_t^{AW,a} + P_t^{AW,a} \leq P_t\right\} \geq \vartheta_2 \tag{15}$$

Eqs 14, 15 represent positive and negative output complement constraints, respectively. In these equations, Pr $\{\cdot\}$ represents the probability, and $P_{m,t}^{H,max}$ is the upper output limit of hydropower station m at period t. $P_{m,t}^{H,min}$ is the lower output of hydropower station m at period t. ϑ_1 and ϑ_2 are confidence levels.

b) Hybrid system reserve capacity requirements are satisfied with hydropower and can be expressed as a percentage of the power demand:

$$\sum_{m=1}^{M}\left(P_{m,t}^{H,max} - P_{m,t}^{H}\right) \geq \sigma \times C_t \tag{16}$$

$$\sum_{m=1}^{M} P_{m,t}^{H} \geq \sigma \times C_t \tag{17}$$

where σ is the reserve capacity percentage factor.

2.3.2 Hydropower constraints

a) Mass balance constraints:

$$V_{m,t+1} = V_{m,t} + \left(S_{m-1,t-\tau_m} + Q_{m,t} - S_{m,t}\right) \times \Delta t \tag{18}$$

$$S_{m,t} = q_{m,t} + d_{m,t} \tag{19}$$

where $V_{m,t}$ is the storage of hydropower station m at period t. $Q_{m,t}$, $S_{m,t}$, $q_{m,t}$, and $d_{m,t}$ are the natural incremental inflow, total discharge, turbine discharge and spillage of hydropower station m at period t respectively. τ_m is the water transportation time from reservoir $m-1$ to m. Δt is the time period duration.

b) Simultaneous regulation constraints:

For all hydropower stations in the same cascade hydropower system, the output in each period usually has the same trend of change.

$$\left(P_{m,t+1}^{H} - P_{m,t}^{H}\right)\left(P_{j,t+1}^{H} - P_{j,t}^{H}\right) \geq 0 \tag{20}$$

c) Reservoir storage constraints:

$$V_{-m,t} \leq V_{m,t} \leq V_{+m,t} \tag{21}$$

where $V_{-m,t}$ and $V_{+m,t}$ are the lower and upper storage bounds of hydropower station m at period t, respectively.

d) Total discharge constraints:

$$S_{-m,t} \leq S_{m,t} \leq S_{+m,t} \tag{22}$$

where $S_{-m,t}$ and $S_{+m,t}$ are the lower and upper bounds of the total discharge of hydropower station m at period t.

e) Turbine discharge constraints:

$$q_{-m,t} \leq q_{m,t} \leq q_{+m,t} \tag{23}$$

where $q_{-m,t}$ and $q_{+m,t}$ are the lower and upper bounds of the turbine discharge of hydropower station m at period t.

f) Initial storage and expected final storage and constraints:

$$V_{m,T} \geq V_{m,end} \tag{24}$$

$$V_{m,0} = V_{m,beg} \tag{25}$$

where $V_{m,end}$ is the initial storage volume of hydropower station m. $V_{m,beg}$ is the initial storage volume of hydropower station m.

g) Navigation constraints:

$$\left|Z_{m,t}^{down} - Z_{m,t+1}^{down}\right| \leq \omega_1, t = 1, 2, \ldots, T-1 \tag{26}$$

$$\max_{1\leq t\leq T}\left\{Z_{m,t}^{down}\right\} - \min_{1\leq t\leq T}\left\{Z_{m,t}^{down}\right\} \leq \omega_2 \tag{27}$$

$$Z_{m,t}^{down} \geq Z_{m}^{down} \tag{28}$$

where $Z_{m,t}^{down}$ is the downstream water level of the hydropower station at period t, m. Z_{m}^{down} is the minimum downstream water level of the downstream hydropower station specified by the navigation requirements, m; ω_1 and ω_2 are fixed values selected according to the downstream waterway standard.

h) Water level-storage capacity function:

$$Z_{m,t}^{up} = f_m^{ZV}\left(V_{m,t}\right) \tag{29}$$

where $f_m^{ZV}(\cdot)$ represents the water level-storage capacity calculation function. $Z_{m,t}^{up}$ is the water level of hydropower station m at period t.

i) Downstream water level-discharge function:

$$Z_{m,t}^{down} = f_m^{ZS}\left(S_{m,t}\right) \tag{30}$$

where $f_m^{ZS}(\cdot)$ represents the downstream water level-discharge function.

3 Solution method

3.1 Hydro-wind-solar complementary constraint processing

In this paper, the GMM is used to analyze the distribution of output error coefficients of wind power and solar power plants. The Gaussian mixture model (GMM) is a kind of non-parametric estimation method, it can theoretically describe any distribution. Literature (Pöthkow and Hege, 2013) compared the extract

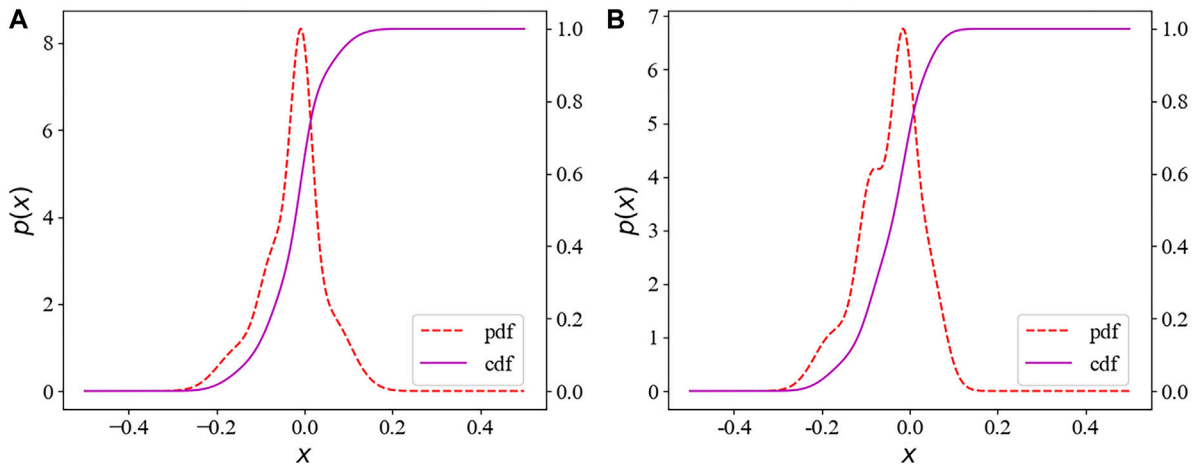

FIGURE 1
The PDF of the wind power plant output forecast error **(A)** and solar power plant output forecast error **(B)** of a typical period.

uncertainty contour line effects of the non-parametric models with Gaussian, and observed that Non-parametric models have good feasibility for various data sets. Therefore, it has widely used in uncertainty description for diverse applications (Potter et al., 2009; Mihai and Westermann, 2014), and compactly model relatively complex distributions (Liu et al., 2012).With the historical forecast and actual output coefficient data of the solar and wind power plant, the deviation value between the actual and the forecasted output coefficient can be calculated. The GMM is used to fit the deviation value data of the output coefficient, and the probability density function (PDF) $p(x)$ of the output error coefficient x is obtained as shown in Figure 1.

From the PDF graph of the output errors of the solar power plant and the wind power plant, the output coefficient deviation value can be obtained given the confidence interval [0.05, 0.95]. $\rho_t^{AW,min}$, $\rho_t^{AW,max}$, $\rho_t^{AS,min}$, and $\rho_t^{AS,max}$ correspond to the endpoints of the confidence interval [0.05, 0.95] at each moment, and the upper/lower limit of the wind and solar output at each moment can be calculated:

$$P_t^{AW,min} = \left(1 + \rho_t^{AW,min}\right)^* P_t^{AW,f} \tag{31}$$

$$P_t^{AW,max} = \left(1 + \rho_t^{AW,max}\right)^* P_t^{AW,f} \tag{32}$$

$$P_t^{AS,min} = \left(1 + \rho_t^{AS,min}\right)^* P_t^{AS,f} \tag{33}$$

$$P_t^{AS,max} = \left(1 + \rho_t^{AS,max}\right)^* P_t^{AS,f} \tag{34}$$

where $P_t^{AW,min}$, $P_t^{AW,max}$, $P_t^{AS,min}$, and $P_t^{AS,max}$ are the lower limit of the wind power output range, the upper limit of the wind power output range, the lower limit of the solar output range and the upper limit of the solar output range during period t, respectively.

Confidence in chance constraints (14) and (15) represents the probability that the power gird can consume all the wind and solar power, and whether the constraints are established is affected by the wind and solar forecast error. The chance constraint (14) means that when the hydropower is at its maximum value, the probability that the actual output of the hydro-wind-solar system is greater than the forecast output should be greater than the confidence. If the actual output of the wind and solar power is too small, the constraint may be destroyed. Therefore, the minimum output $P_t^{AW,min}$ of wind power and the minimum output $P_t^{AS,min}$ of solar power within the confidence level ϑ_1 can be found through the CDF of wind and solar power forecast error. The opportunity constraint (14) can be transformed into that when the sum of wind power and solar power output is $P_t^{AW,min} + P_t^{AS,min}$, the output of the hydro-wind-solar system meets the requirements:

$$\sum_{m=1}^{M} P_m^{H,max} - \sigma \times C_t + P_t^{AW,min} + P_t^{AS,min} \geq P_t \tag{35}$$

The chance constraint (15) means that when the hydropower is at the minimum value, the probability that the actual output of the hydro-wind-solar system is less than the forecast output should be greater than the confidence. If the actual output of scenery is too large, the constraint may be destroyed. Similarly, the opportunity constraint (15) can be transformed into that when the sum of wind power and photovoltaic output is $P_t^{AW,max} + P_t^{AS,max}$, the output of the hydro-wind-solar system meets the requirements:

$$\sum_{m=1}^{M} P_m^{H,min} + \sigma \times C_t + P_t^{AW,max} + P_t^{AS,max} \leq P_t \tag{36}$$

3.2 ε – *constraint* method

The ε – *constraint* method simplifies the problem by retaining only one primary objective function and transforming the remaining objective functions into constraints (Mavrotas, 2009; De Santis et al., 2022); moreover, this method has been widely used in the solution of multi-objective models (Biswas et al., 2018; Fathipour and Saidi-Mehrabad, 2018). Compared with the weighted method, the ε – *constraint* method has a smaller search range and better performance in efficiently finding the Pareto front solution. Regarding the dual-objective optimization problem of finding the minimum value, its mathematical description is as follows:

$$\begin{cases} \min \ (f_1(x), f_2(x)) \\ s.t. \quad Ax \le b \end{cases} \tag{37}$$

where A is a matrix of appropriate dimensions; and b is a column vector of appropriate dimensions.

For the dual objective, if Objective $f_1(x)$ can be regarded as the primary objective function, then Objective $f_2(x)$ is transformed into the constraints of $f_1(x)$. The specific operation steps are as follows:

Take $f_1(x)$ as the objective function, find its minimum value f_1^{min} under the original constraints, and find the value of $f_2(x)$ at this time, which is regarded as the feasible maximum value f_2^{min} of $f_2(x)$. The solution model required for this step is:

$$\begin{cases} \min f_1(x) \\ s.t. \quad Ax \le b \end{cases} \tag{38}$$

Take $f_2(x)$ as the objective function, and find the minimum value f_2^{min} of $f_2(x)$ under the original constraints. The range of $f_2(x)$ is $[f_2^{min}, f_2^{max}]$. The solution model required for this step is:

$$\begin{cases} \min f_2(x) \\ s.t. \quad Ax \le b \end{cases} \tag{39}$$

Take K points ε_k (k $\in$ 1, 2, . . . , K) in $[f_2^{min}, f_2^{max}]$, and generate K new constraints: $f_2(x) \le \varepsilon_k$.

Take $f_1(x)$ as the objective function and add the new constraints to the constraints. After the calculation is performed, K result arrays (f_{11}, f_{21})、$(f_{12}, f_{22}) \ldots (f_{1k}, f_{2k})$ can be obtained, that is, the approximate Pareto maximum excellent Frontier. The solution model required for this step is:

$$\begin{cases} min\, f_1(x) \\ s.t. \quad Ax \le b \\ f_2(x) \le \varepsilon_k \end{cases} \tag{40a}$$

4 Case study

4.1 Background information

Yunnan Province is located in southwest China. In this region, with sufficient rainfall occurs, and several large rivers travels through, can be found. Yunnan province is endowed with abundant hydropower resources. In late 2022, the hydropower installed capacity in this region surged to 78.02 GW. This value is close to the hydropower installed capacity of Canada, which is the world's third largest hydropower capacity. In addition, Yunnan Province is rich in renewable energy. In late 2022, wind power and solar power has surged to 8.83 and 4.17 GW respectively. However, there is very large potential for expanding wind and solar power resources, since the developed capacity accounts for only 5% of the developable capacity. According to the "New Energy Construction Plan of Yunnan Province in 2022" issued by Yunnan Province, Yunnan will accelerate the development of wind and solar power in the next few years. Since wind and solar power generation is depend on the weather, Yunnan is facing challenges of broad-scale renewable energy consumption and power grid peak shaving brought by the broad-scale integration of VREs. Therefore, using the flexibility of hydropower to achieve the multi-energy complementation of hydro-wind-solar power is one of the best ways for Yunnan to achieve large-scale consumption of VREs.

As shown in Figure 2, the Jinghong hydropower station and the Ganlanba hydropower station are both located in Jinghong City, Xishuangbanna Prefecture, Yunnan Province. They are the last two hydropower stations in the Lancang/Mekong River before flow out of China. Due to Jinghong's rated flow and the restriction of downstream channel conditions, Jinghong's adjustment of power generation flow will cause large fluctuations in downstream water level and flow, which will adversely affect navigation. To solve this problem, the main development task of the yet-to-be-constructed Ganlanba hydropower station is to provide reverse regulation for the Jinghong hydropower station to meet the downstream navigation requirements. Therefore, the Jinghong-Ganlanba cascade hydropwer station must undertake complex comprehensive utilization tasks. Considering Yunnan's ever-increasing renewable energy construction plan, this cascade system will also undertake the severe task of VRES complementarity. Therefore, it is required to find a reasonable operation mode considering the conflicting objectives of generation and navigation. In this paper, the Jinghong-Ganlanba cascade hydropower stations are taken as the background. The load curve, interval runoff, initial and final water levels, and other conditions involved in the calculation process refer to the actual operating data of the power grid and power station, as shown in Supplementary Table S1.

In this paper, a non-linear model is built, where a quadratic polynomial fitting function is used to express the water level-storage function and tail water level-discharge function. The model was solved using Lingo18.0.

According to Section 2.1, all wind power plants in the same region are considered as one wind power plant with the installed capacity of 208.5 MW and a solar power plant with the installed capacity of 300 MW. Figure 3 illustrates the typical wind and solar power daily output during the dry season (January, February, and March) of the lower reaches of the Lancang River, which were chosen to evaluate the scheduling situation of cascade hydropower stations under difficult conditions.

4.2 Analysis of the results

Since Ganlanba has not been constructed, three cases are considered to analyze the impact of the construction of the Ganlanba on the overall results and the impact of the navigation requirements on the separate operation of the Jinghong hydropower station: 1) Case 1: only the Jinghong hydropower plant is considered in the hybrid hydro-wind-solar complement operation model, but does not take navigation constraints into account; 2) Case 2: only the Jinghong hydropower plant is considered and takes navigation constraints into account and 3) Case 3: both Jinghong and Ganlanba are considered, and navigational constraints are also taken into account.

Figure 4 and Supplementary Table S2 show the distribution and range of the Pareto front for the three cases which reflect the conflict between the two objective functions. The rectangular area in Figure 4 marks solutions at the turning part of the Pareto front, which are hydropower output processes that can better meet the requirements of peak shaving and navigation at the same time. Under the

FIGURE 2
Schematic diagram of the hydropower station locations.

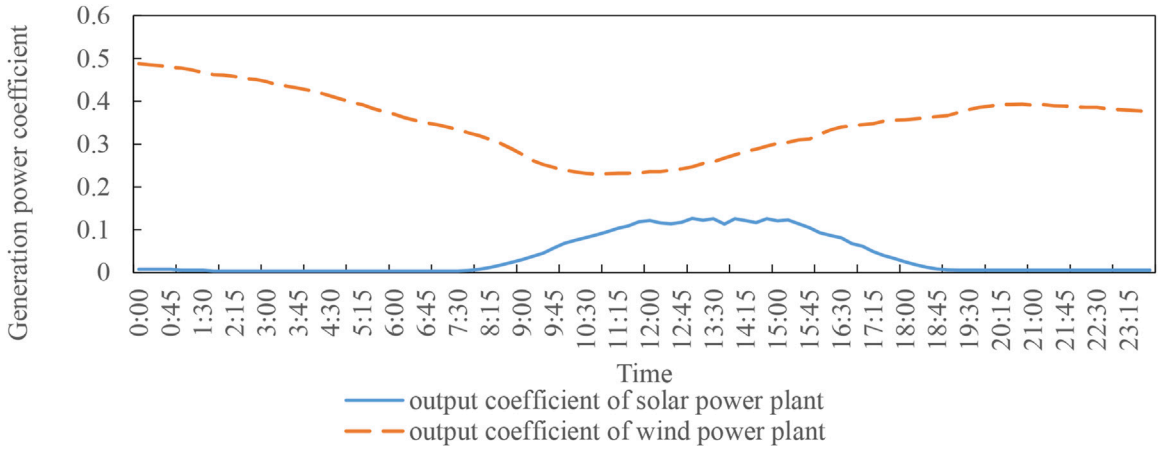

FIGURE 3
The typical time output coefficient of solar and wind power plant.

experimental conditions, the Pareto front turning of the cascade solution is more obvious, indicating that it can moderate the conflict more effectively. Because the navigation constraints limit the output of Jinghong, the range of feasible solutions is reduced, and even some solutions with good peak-shaving effects turn into infeasible solutions.

Figure 5 illustrate the differences of solutions on the Pareto front for Case1 and show the changes in the output and water abandonment under Case1, respectively, by selecting different downstream water level variance limits (f_2 = 1.4, 1.0, 0.6, 0.2, 0.01, 0.0001). When the target requirements for f_2 tighten, Jinghong's discharge adjustment ability is restricted, which result in Jinghong abandoning water for peak shaving. For Case1, the peak shaving and navigation task requirements cannot be achieved at the same time.

In the Pareto front of Case 1, three scenarios of f_2 = 1, f_2 = 0.5, and f_2 = 0.01 are selected as the solution that prefers a better peak shaving effect, the neutral case, and the solution that prefers a better navigation effect, respectively. These three points can effectively compare the gaps in peak regulation and navigation between these cases, as shown in Supplementary Table S3.

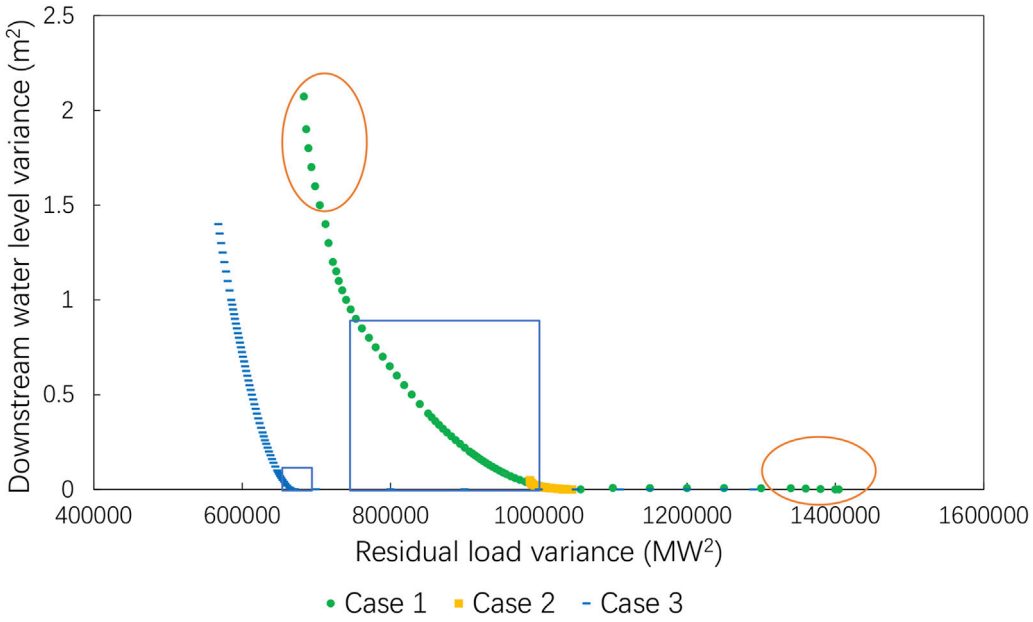

FIGURE 4
Comparison of the Pareto front in different cases.

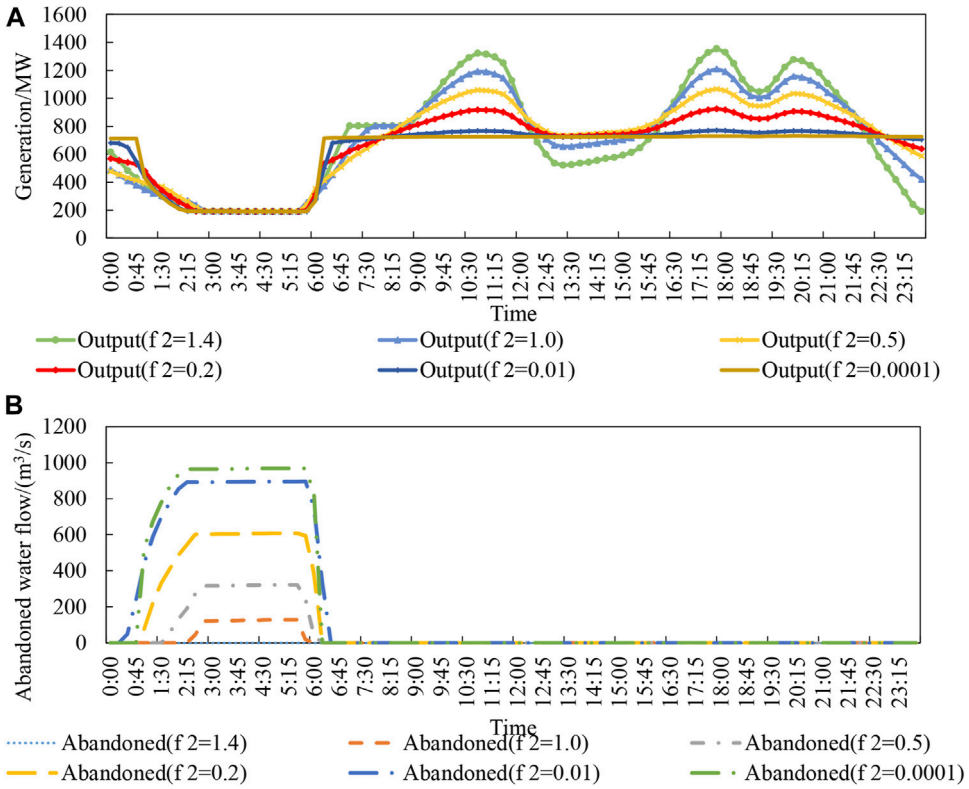

FIGURE 5
Comparison of **(A)** Jinghong's output and **(B)** abandoned water without navigation constraint.

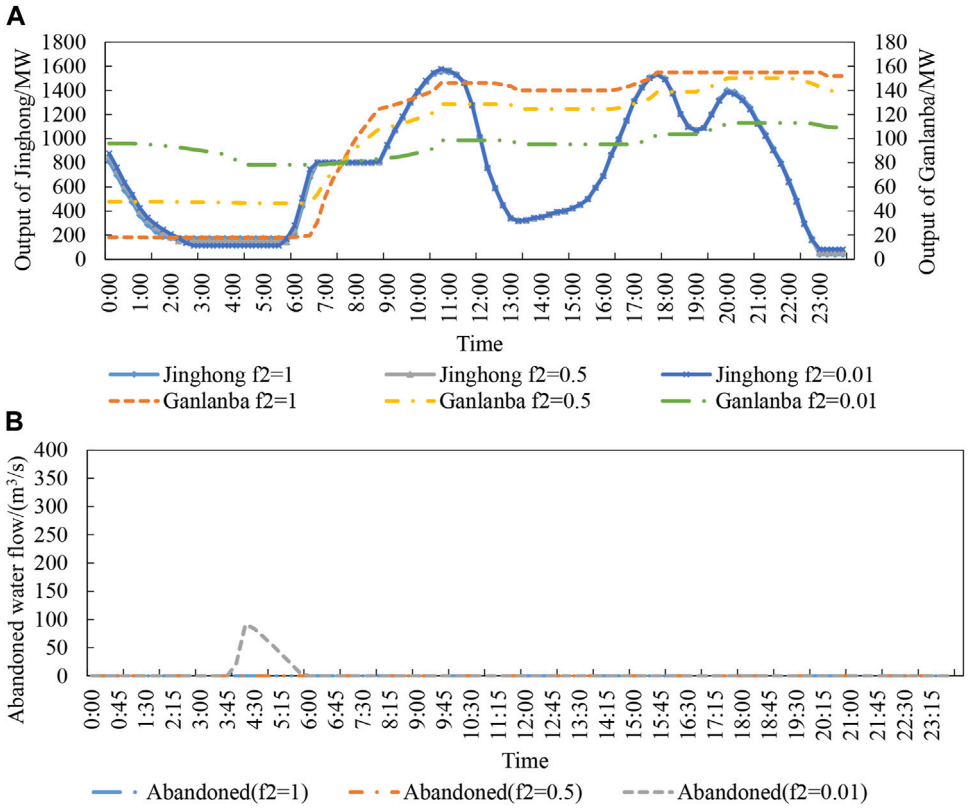

FIGURE 6
Cascade **(A)** hydropower station output and **(B)** abandoned water flow under different downstream water level variance targets.

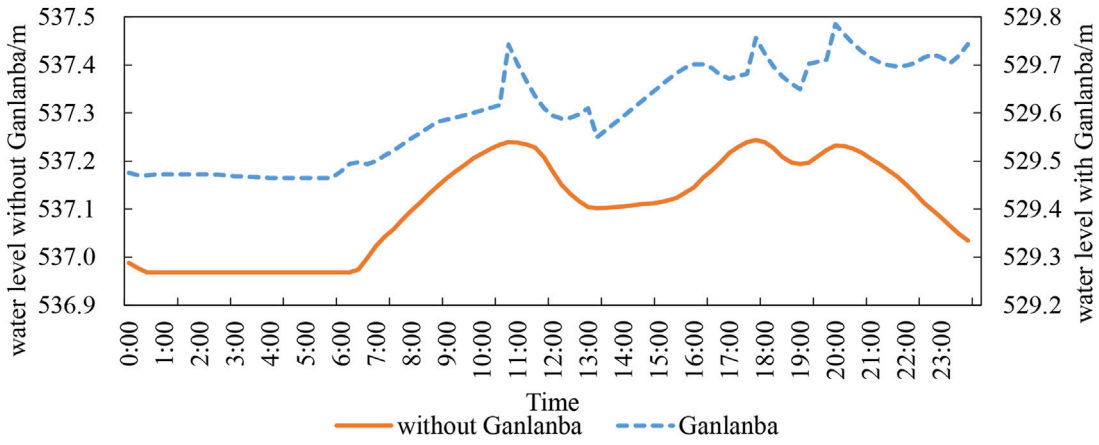

FIGURE 7
Comparison of the downstream water level (navigation) when f_2 = 0.01.

Supplementary Table S3 summarizes the eigenvalues of each case. It is obvious that under the same f_2, Case 3's peak shaving impact is superior based on the peak-to-valley difference of the residual load. Since the target f_1 tends to reduce the hydropower output at the load valley, the hydroelectric plant can only supply reserve capacity at the load valley leaving a constant minimum load at 6178.285 MW. Figure 6 show the output and water abandonment of Case 3 under three f_2 conditions. From Figure 5, 6, it can be concluded that: 1) in Figure 6, the output of Ganlanba slightly changes under different f_2 conditions, which indicates that

Ganlanba has a weak adjustment ability and is mainly responsible for navigation tasks. Therefore, Figure 5, 6 show that with the addition of Ganlanba, Jinghong's adjustment capacity can be unleashed, and a better result can be obtained. 2) Figure 5, 6 also show that Ganlanba's participation can significantly reduce the abandoned water for peak shaving, which may successfully address conflicting objectives of peak shaving and navigation.

Figure 7 shows the downstream water levels before and after the addition of Ganlanba and displays the affected navigation due to Ganlanba's involvement. When the downstream water level variance is set to 0.01, the corresponding solution of Case 3 is located at the turning point of the Pareto front. In Figure 7, the Pareto front of Case 2 also has a corresponding solution, which can be compared. Without Ganlanba, the navigable water level is maintained at 537 m for 1/3 of the time, which indicates that the downstream channel barely meets the navigation requirements. For Case 3, the Ganlanba's addition lowers the expense of maintaining navigation, and it maintains the navigation target's ideal value between 529.45 m and 529.78 m. The safety of downstream navigation has been further assured compared to the minimum water level requirement of 525 m downstream of the Ganlanba.

In conclusion, the Ganlanba hydropower plant can successfully reduce the tension between peak shaving and navigation, address the issue of water abandonment for peak shaving, and raise the level of safety for downstream navigation.

5 Impact analysis of the wind and solar output

Due to the randomness and uncontrollability of the wind and solar output, in actual operation, the real output of wind and solar power usually deviates from the predicted value. In this section, to analyze the influence of wind and solar power uncertainty on scheduling, 1) the residual load under various wind and solar output conditions is compared to analyze the influence of with/without considering hydro-wind-solar complementary constraints on the calculation results of the dual-objective model. 2) The hydropower output under various wind and solar capacity scenarios is evaluated to examine the impact of wind and solar power scale on the calculations of the dual-objective model. Therefore, 1,000 wind and solar output scenarios were generated by using the Monte Carlo method. Among the seven cases selected in Section 4.2, Case 3 ($f_2 = 0.01$) works best. Thus, $f_2 = 0.01$ in the cascade system is taken as an example.

5.1 Influence of the wind and solar uncertainty on the peak shaving effect

Literature (Shen et al., 2021) proposes that the load fluctuation coefficient can be used to evaluate the peak shaving effect, and the revised index mainly reflects the overall smoothness of the load curve, which is better than the visualization effect of the residual load mean square error. Therefore, in this paper, this index is used to reflect the peak shaving effect in different scenarios:

$$\alpha = \frac{\sqrt{\frac{1}{T}\sum_{t=1}^{T}\left(R_{r,t} - \overline{R_r}\right)^2}}{\overline{R_r}} \tag{40b}$$

where, $R_{r,t}$ is the residual load of the scenario at the period t; and $\overline{R_r}$ is the average residual load of the scenario r, with $r = 1, 2, \ldots, 1000$.

In Case 3, the actual operation of the cascade is simulated under two conditions: one condition with complementary constraints for the solar and wind output (Eqs 33, 34) and the other condition without such constraints. When there is no hydro-wind-solar complement constraint, the residual load in each scenario is:

$$R_{r,t} = C_t - \sum_{m=1}^{M} P_{m,t}^{H} - P_{r,t} \tag{41}$$

$$P_{r,t} = P_{r,t}^{AW} + P_{r,t}^{AS} \tag{42}$$

where, $R_{r,t}$ is the residual load of the r th scenario at period t without hydro-wind-solar complement constraints; $P_{m,t}^{H}$ is the output of hydropower station m at period t; $P_{r,t}$ is the wind and solar power output of the scenario r at period t; $P_{r,t}^{AW}$, $P_{r,t}^{AS}$ represent the wind and solar power output of scenario r at period t respectively.

When considering the hydro-wind-solar complementary constraint, here are the residual loads for each scenario:

$$R_{r,t} = \begin{cases} R_t, P_{r,t} < P_{r,t}^{max} \text{ and } P_{r,t} > P_{r,t}^{min} \\ R_t + \left(P_{r,r} - P_{r,t}^{max}\right), P_{r,t} > P_{r,t}^{max} \\ R_t + \left(P_{r,t} - P_{r,t}^{min}\right), P_{r,t} < P_{r,t}^{min} \end{cases} \tag{43}$$

$$P_t^{max} = P_t^{AW,max} + P_t^{AS,max} \tag{44}$$

$$P_t^{min} = P_t^{AW,min} + P_t^{AS,min} \tag{45}$$

where $P_t{}^{max}$ is the upper limit of the range for the sum output of wind and solar; and $P_t{}^{min}$ is the lower limit of the range for the sum output of wind and solar.

Through Eqs 40–45, the residual load under 1,000 simulation scenarios was carried out, and the distribution of the load fluctuation coefficients is shown in Figure 8. It is obvious that considering hydro-wind-solar complementarity can effectively control the residual load fluctuation in real operation where actual wind and solar power deviate from the forecast value. In summary, hydro-wind-solar complement operation can effectively reduce the adverse impact of wind and solar uncertainty on the peak shaving results.

5.2 Influence of the wind and solar uncertainty on the navigation

Under the condition of fixed hydropower output and without providing wind and solar reserve capacity, the navigation effect will not be affected by VRE when actual wind and solar output deviate from the forecast value. In the case of hydro-wind-solar complement operation, the part of the output deviation between the upper and lower limits of the reserve capacity needs to be absorbed by changing the hydropower output. Due to the small adjustment capacity of Ganlanba, in this situation, Jinghong is required to undertake the adjustment tasks. Since the navigation is determined by the discharge of Ganlanba, the picture A of Figure 9 shows the maximum and minimum water levels of the Ganlanba reservoir

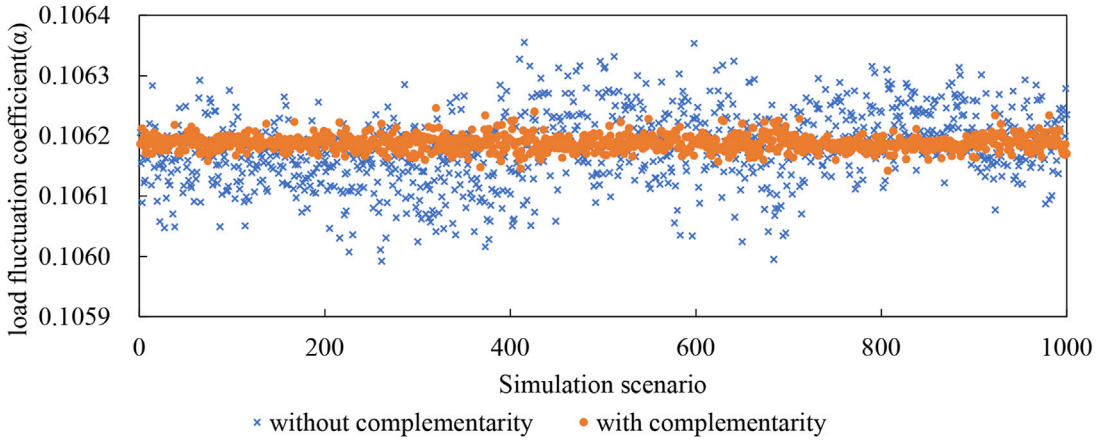

FIGURE 8
Comparison of the residual load fluctuation coefficient under different scenarios.

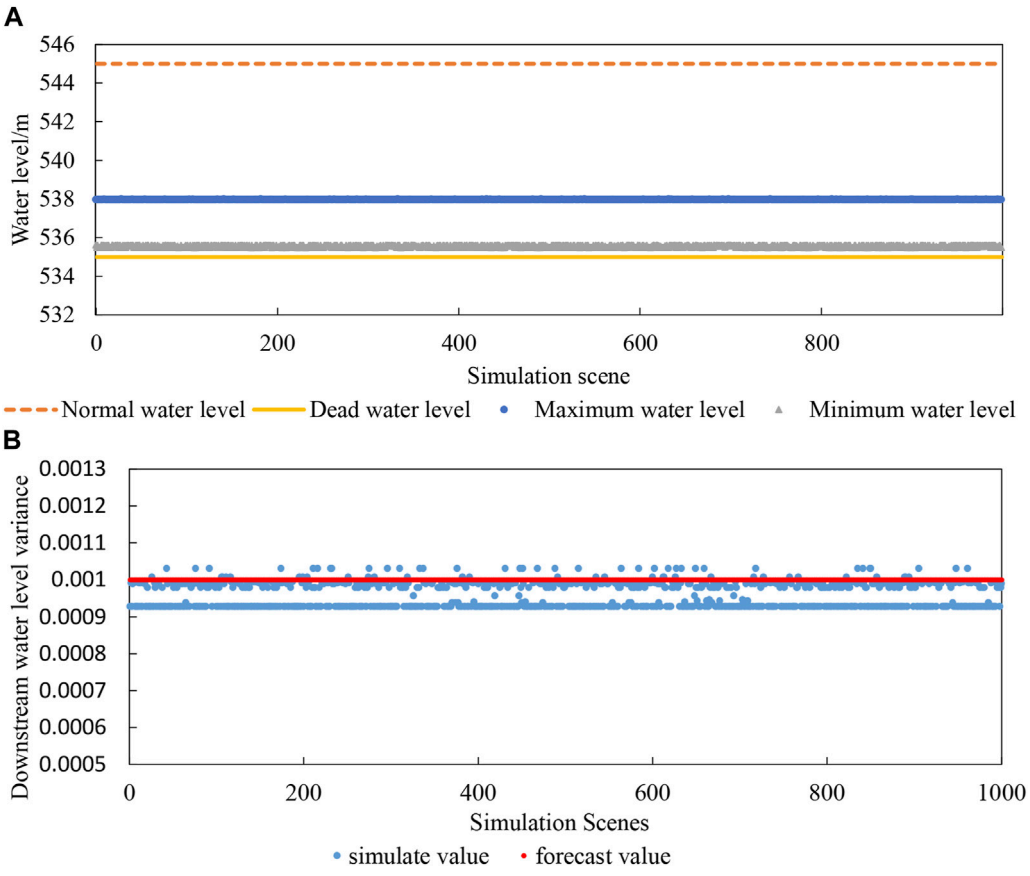

FIGURE 9
(A) Water level extremum and **(B)** downstream water level variance of the Ganlanba reservoir.

and the upper limit and lower limit water levels of the Ganlanba reservoir under 1,000 scenarios. In all scenarios, Ganlanba reservoir's water level will not exceed its limit, which means that when wind and solar forecast errors cause the upper reservoir outflow to change, Ganlanba has sufficient adjustment capacity to address it. The picture B of Figure 9 shows the downstream water level variance of Ganlanba Reservoir under 1,000 scenarios. The mean square deviations of the downstream water level in most scenarios are smaller than the predicted situation, and a few are slightly larger than the predicted situation. However, the difference

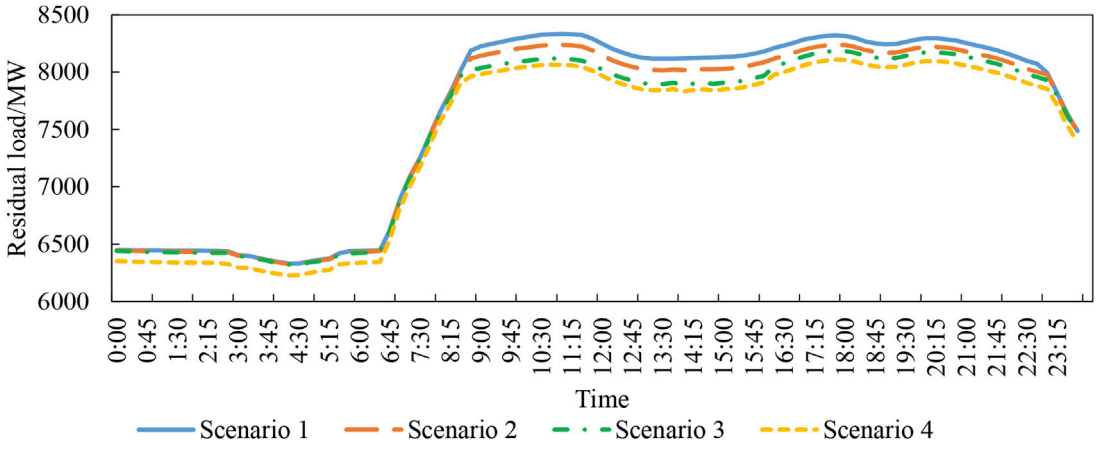

FIGURE 10
Residual load of scenarios.

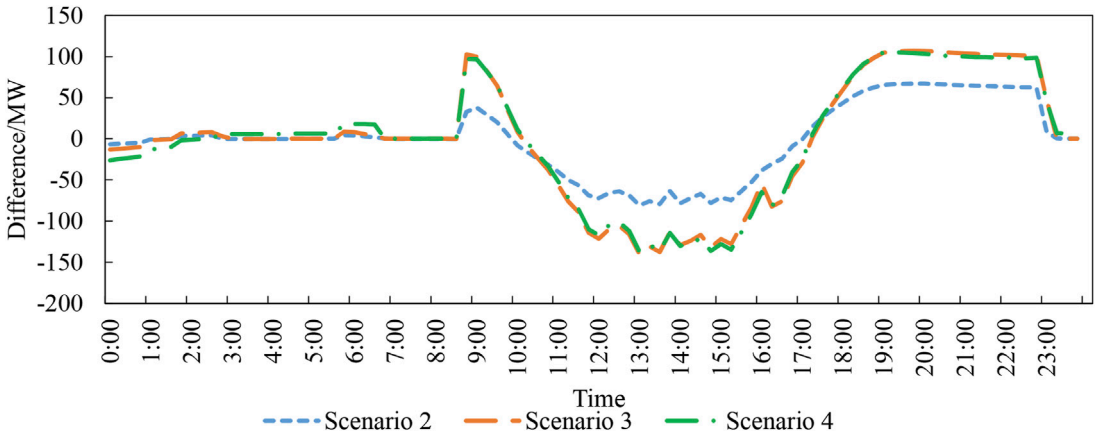

FIGURE 11
Hydropower output difference between scenarios 2,3,4 and 1.

is small and negligible. This demonstrates that Ganlanba can maintain navigational conditions despite VREs' forecast errors.

That is, wind and solar uncertainties have little effect on navigation.

5.3 The influence of the expanding wind power and solar power scale on hydro-wind-solar complementarity

In this section, different wind and solar power installed capacity scales are selected to explore their impact on the simulation results. There shows four wind and solar power scales. Scenario 1 elects solar power scales of 300 MW and wind power scales of 208.5 MW, which are the wind and solar installed capacity in 2020. Referring to the "List of New Energy Projects in the 14th Five-Year Plan of Yunnan Province," Xishuangbanna will add 1.43 GW of solar power during the "14th Five-Year Plan" period. However, no wind power projects are planned. Scenario 2 sets the estimated installed capacity of solar and wind power in 2025 as 1730 and 208.5 MW. Scenario 3 sets the projected installed solar and wind capacity in 2030 as 3160 and 208.5 MW, and the growth rate is consistent with that in Scenario 2. Scenario 4 doubles the wind-power capacity installed based on Scenario 3, and sets the estimated installed capacity of solar and wind power as 3160 and 417 MW.

Figure 10 shows the residual load curves of each scenario, and Figure 11 shows the hydropower output gap between Scenario 1 and Scenario 2, 3 and 4, in which a negative value indicates that hydropower output will decrease as solar/wind power output increases, while a positive value indicates the opposite. As shown in these two figures, for Scenario 2 and 3, when solar power output increases, the residual load reduce from 8:30 to 20:00, and hydropower will reduce output during the load saddle periods and uses the saved water to increase the output during the load

peak periods. This is because solar power is mainly generated during the daytime which is the load saddle, and hydropower adapts to achieve hydro-solar complementarity and improve the peak shaving effect. The simulation results of Scenarios 2 and 3 in Supplementary Table S4 also prove that increasing the output of solar power has a positive effect on the peak shaving of the model.

As shown in Table 4, the peak-to-valley difference of the residual load increases from Scenario 3 to Scenario 4. This is because hydropower has reached the best peak shaving performance in Scenario 3. When the wind power capacity is increased from Scenario 3 to Scenario 4, the hydropower output changes little with the change of reserve capacity, as shown in Figure 11, and helps little in further peak shaving. Therefore, with the increase in wind power capacity, although both the residual peak load and valley load decrease, as the anti-peak characteristic of wind power shows in Figure 3., the peak-valley difference will increase.

Figure 11 shows that the hydropower output changes little, which means that the outflow of hydropower changes little. From Scenario 1 to Scenario 4, the increase in wind power and solar power scale will not have a large negative impact on navigation.

In summary, during the dry season, the increase in the scale of solar power output has a positive impact on the peak shaving of the hydro-wind-solar complementarity system; in contrast, wind power tends to have a negative impact on peak shaving.

6 Conclusion

Grid-connected VRE can be effectively solved by a coordinated development of hydro-wind-solar. However, there are conflicting relationships among the multiple tasks undertaken by hydropower stations. To ease the contradiction between multi-energy complementarity and comprehensive utilization tasks of hydropower stations, a hydro-wind-solar coordination scheduling model that takes both peak shaving and navigation objectives into account is established in this study. Conclusions can be drawn through the verification and analysis of an actual case study:

1) A Pareto front that considers the objectives of peak shaving and navigation is developed by applying the model to Jinghong-Ganlanba cascade hydropower station dispatching. The case study results show that there is an obvious turning point in the Pareto front of the cascade hydropower station, where the solution has a better effect of reconciling contradictions, which means that the conflict between the complement operation with VRE and comprehensive utilization can be reconciled or relieved with an appropriate method.
2) Hydropower station cooperation is very important for achieving multiple objectives. The case studies show that only Jinghong is unable to cope with task conflicts, and it is prone to the problem of water abandonment for peak shaving. The addition of Ganlanba not only eases task conflicts and Jionghong's peak shaving ability but also helps reduce water abandonment.
3) Reasonable planning of wind power and solar power is important to make full use of hydro-wind-solar power complementary ability. The case study shows that, within the range of hydropower that can offer enough complement reserve capacity for wind and solar power, an increase in the solar power capacity has a positive impact on peak shaving, while an increase in wind power has a negative impact. To reconcile the needs of peak regulation and navigation, the development of wind and solar power within the range of complementary reserve capacity offered by hydropower is very important.

Data availability statement

The original contributions presented in the study are included in the article/Supplementary Material, further inquiries can be directed to the corresponding author.

Author contributions

BL: Conceptualization, Methodology, Software, Funding acquisition, Supervision, and Resources. ZP: Software, Visualization, and Writing—original draft. SL: Supervision and Investigation. TL: Data curation and Software. JL: Formal analysis. All authors contributed to the article and approved the submitted version.

Funding

This study is supported by the National Natural Science Foundation of China (Grant No. 51979023) and the Open Research Fund of Hubei Key Laboratory of Intelligent Yangtze and Hydroelectric Science (Grant No. ZH2102000108).

Conflict of interest

Author JL is employed by China Yangtze Power Co Ltd.

The remaining authors declare that the research was conducted in the absence of any commercial or financial relationships that could be construed as a potential conflict of interest.

Publisher's note

Supplementary material

The Supplementary Material for this article can be found online at: https://www.frontiersin.org/articles/10.3389/fenrg.2023.1193415/full#supplementary-material

References

Albadi, M. H., and El-Saadany, E. F. (2010). Overview of wind power intermittency impacts on power systems. *Electr. Power Syst. Res.* 80, 627–632. doi:10.1016/j.epsr.2009.10.035

Asiaban, S., Kayedpour, N., Samani, A. E., Bozalakov, D., De Kooning, J. D. M., Crevecoeur, G., et al. (2021). Wind and solar intermittency and the associated integration challenges: A comprehensive review including the status in the Belgian power system. *Energies* 14, 2630. doi:10.3390/en14092630

Biswas, P. P., Suganthan, P. N., Qu, B. Y., and Amaratunga, G. A. J. (2018). Multiobjective economic-environmental power dispatch with stochastic wind-solar-small hydro power. *Energy* 150, 1039–1057. doi:10.1016/j.energy.2018.03.002

Chen, S., Fang, G., Huang, X., and Yan, M. (2019). A joint optimal dispatching method of wind-solar-hydro generation system. *IOP Conf. Ser. Earth Environ. Sci.* 227, 032004. doi:10.1088/1755-1315/227/3/032004

Cheng, C., Yan, L., Mirchi, A., and Madani, K. (2017). China's booming hydropower: Systems modeling challenges and opportunities. *J. Water Resour. Plann. Manage.* 143, 02516002. doi:10.1061/(ASCE)WR.1943-5452.0000723

De Santis, M., Eichfelder, G., and Patria, D. (2022). On the exactness of the ε-constraint method for biobjective nonlinear integer programming. *Operations Res. Lett.* 50, 356–361. doi:10.1016/j.orl.2022.04.007

Department of Resource Conservation and Environmental Protection (2021). *Action plan for carbon dioxide peaking before 2030*. Available at: https://en.ndrc.gov.cn/policies/202110/t20211027_1301020.html.

Ding, M., Xu, Z., Wang, W., Wang, X., Song, Y., and Chen, D. (2016). A review on China's large-scale PV integration: Progress, challenges and recommendations. *Renew. Sustain. Energy Rev.* 53, 639–652. doi:10.1016/j.rser.2015.09.009

Fathipour, F., and Saidi-Mehrabad, M. (2018). A multi-objective energy planning considering sustainable development by a TOPSIS-based augmented e-constraint. *J. Renew. Sustain. Energy* 10, 034901. doi:10.1063/1.5008545

Gholami, M., Fathi, S. H., Milimonfared, J., Chen, Z., and Deng, F. "The effect of turbulence and wake on the power fluctuation in the wind farms," in 2017 Iranian Conference on Electrical Engineering (ICEE), Tehran, Iran, March, 2017 (IEEE), 1148–1153. doi:10.1109/IranianCEE.2017.7985214

Halleraker, J. H., Kenawi, M. S., L'Abée-Lund, J. H., Bakken, T. H., and Alfredsen, K. (2022). Assessment of flow ramping in water bodies impacted by hydropower operation in Norway – is hydropower with environmental restrictions more sustainable? *Sci. Total Environ.* 832, 154776. doi:10.1016/j.scitotenv.2022.154776

Hu, W., Wang, Y., Sun, Y., Nie, Q., Ding, R., and Zhang, X. "Research on comprehensive complementary characteristics evaluation technology of wind-solar-hydro combined power generation system," in 2021 International Conference on Power System Technology (POWERCON), Haikou, China, September, 2021 (IEEE), 1017–1022. doi:10.1109/POWERCON53785.2021.9697711

Jabir, M., Azil Illias, H., Raza, S., and Mokhlis, H. (2017). Intermittent smoothing approaches for wind power output: A review. *Energies* 10, 1572. doi:10.3390/en10101572

Jian, Z., Shiqiang, Z., and Xizhang, C. (2012). Impact upon navigation conditions of river reach between the two dams by peak shaving at three gorges hydropower station. *Procedia Eng.* 28, 152–160. doi:10.1016/j.proeng.2012.01.698

Jin, X., Liu, B., Liao, S., Cheng, C., Li, G., and Liu, L. (2022). Impacts of different wind and solar power penetrations on cascade hydroplants operation. *Renew. Energy* 182, 227–244. doi:10.1016/j.renene.2021.10.022

Li, F.-F., Wang, H.-R., Wu, Z.-G., and Qiu, J. (2020). Maximizing both the firm power and power generation of hydropower station considering the ecological requirement in fish spawning season. *Energy Strategy Rev.* 30, 100496. doi:10.1016/j.esr.2020.100496

Li, H., Gao, H., Zhang, Y., and Ai, X. (2018). Expansion planning of large scale hybrid wind\-photovoltaic transmission network considering correlation. *Power Syst. Technol.* 42, 2120–2127. doi:10.13335/j.1000-3673.pst.2018.0144

Lingfors, D., and Widén, J. (2016). Development and validation of a wide-area model of hourly aggregate solar power generation. *Energy* 102, 559–566. doi:10.1016/j.energy.2016.02.085

Liu, B., Lund, J. R., Liao, S., Jin, X., Liu, L., and Cheng, C. (2020). Optimal power peak shaving using hydropower to complement wind and solar power uncertainty. *Energy Convers. Manag.* 209, 112628. doi:10.1016/j.enconman.2020.112628

Liu, J., Shen, W., Yang, H., Su, K., and Zhou, H. "Operation strategy of a combined system consists of multi-type hydropower and wind-solar," in 2019 IEEE 3rd Conference on Energy Internet and Energy System Integration (EI2), Changsha, China, November, 2019a (IEEE), 369–374. doi:10.1109/EI247390.2019.9062166

Liu, S., Levine, J. A., Bremer, P., and Pascucci, V. (2012). "Gaussian mixture model based volume visualization," in *IEEE symposium on large data analysis and visualization (LDAV)* (Seattle, WA: IEEE), 196, 73–77. doi:10.1109/LDAV.2012.6378978

Liu, W., Zhu, F., Chen, J., Wang, H., Xu, B., Song, P., et al. (2019b). Multi-objective optimization scheduling of wind–photovoltaic–hydropower systems considering riverine ecosystem. *Energy Convers. Manag.* 196, 32–43. doi:10.1016/j.enconman.2019.05.104

Luo, G., Dan, E., Zhang, X., and Guo, Y. (2018). Why the wind curtailment of northwest China remains high. *Sustainability* 10, 570. doi:10.3390/su10020570

Mavrotas, G. (2009). Effective implementation of the ε-constraint method in multi-objective mathematical programming problems. *Appl. Math. Comput.* 213, 455–465. doi:10.1016/j.amc.2009.03.037

Mihai, M., and Westermann, R. (2014). Visualizing the stability of critical points in uncertain scalar fields. *Computers & Graphics* 41, 13–25. doi:10.1016/j.cag.2014.01.007

Ming, B., Liu, P., Guo, S., Cheng, L., and Zhang, J. (2019). Hydropower reservoir reoperation to adapt to large-scale photovoltaic power generation. *Energy* 179, 268–279. doi:10.1016/j.energy.2019.04.209

Niu, W., Shen, J., Cheng, C., Wu, X., Feng, Z., and Guo, Y. (2016). A hybrid search method for multi-objective optimization operations of cascaded hydropower plants with peak load regulation and navigation demands. *Proc. Chin. Soc. Electr. Eng.* 36, 2331–2341. doi:10.13334/j.0258-8013.pcsee.2016.09.003

Pérez-Díaz, J. I., and Wilhelmi, J. R. (2010). Assessment of the economic impact of environmental constraints on short-term hydropower plant operation. *Energy Policy* 38, 7960–7970. doi:10.1016/j.enpol.2010.09.020

Pöthkow, K., and Hege, H.-C. (2023). Nonparametric models for uncertainty visualization. *Computer Graphics Forum* 32, 131–140. doi:10.1111/cgf.12100

Potter, K., Wilson, A., Bremer, P.-T., Williams, D., Doutriaux, C., Pas, V., et al. (2009). Ensemble-vis: a framework for the statistical visualization of ensemble data," in. *2009 IEEE international conference on data mining workshops* (Miami, FL: IEEE), 233–240. doi:10.1109/ICDMW.2009.55

Shang, Y., Li, X., Gao, X., Guo, Y., Ye, Y., and Shang, L. (2017). Influence of daily regulation of a reservoir on downstream navigation. *J. Hydrol. Eng.* 22, 05017010. doi:10.1061/(ASCE)HE.1943-5584.0001522

Shen, J., Chen, G., Wei, W., Cheng, C., and Wang, L. (2021). Short-term optimal scheduling model with multiple peak shaving indexes based on linkage analysis. *Journal of Hydraulic Engineering* 52, 936–947.

Shivashankar, S., Mekhilef, S., Mokhlis, H., and Karimi, M. (2016). Mitigating methods of power fluctuation of photovoltaic (PV) sources – a review. *Renew. Sustain. Energy Rev.* 59, 1170–1184. doi:10.1016/j.rser.2016.01.059

Wan, Z., Li, Y., Wang, X., An, J., Dong, B., and Liao, Y. (2020). Influence of unsteady flow induced by a large-scale hydropower station on the water level fluctuation of multi-approach channels: A case study of the three gorges project, China. *Water* 12, 2922. doi:10.3390/w12102922

Wang, X., Virguez, E., Kern, J., Chen, L., Mei, Y., Patiño-Echeverri, D., et al. (2019a). Integrating wind, photovoltaic, and large hydropower during the reservoir refilling period. *Energy Convers. Manag.* 198, 111778. doi:10.1016/j.enconman.2019.111778

Wang, X., Virguez, E., Xiao, W., Mei, Y., Patiño-Echeverri, D., and Wang, H. (2019b). Clustering and dispatching hydro, wind, and photovoltaic power resources with multiobjective optimization of power generation fluctuations: A case study in southwestern China. *Energy* 189, 116250. doi:10.1016/j.energy.2019.116250

Xi'an Jiaotong UniversityWang, J., Wei, J., Xi'an Jiaotong UniversityZhu, Y., Xi'an Jiaotong University, et al. (2019). The reliability and operation test system of power grid with large-scale renewable integration. *CSEE JPES*. doi:10.17775/CSEEJPES.2017.01300

Xie, J., Zheng, Y., Pan, X., Zheng, Y., Zhang, L., and Zhan, Y. (2021). A short-term optimal scheduling model for wind-solar-hydro hybrid generation system with cascade hydropower considering regulation reserve and spinning reserve requirements. *IEEE Access* 9, 10765–10777. doi:10.1109/ACCESS.2021.3049280

Zhang, X., Ma, G., Huang, W., Chen, S., and Zhang, S. (2018). Short-term optimal operation of a wind-PV-hydro complementary installation: Yalong river, sichuan province, China. *Energies* 11, 868. doi:10.3390/en11040868

Zhu, Y., Chen, S., Huang, W., Wang, L., and Ma, G. (2018). Complementary operational research for a hydro-wind-solar hybrid power system on the upper Jinsha River. *J. Renew. Sustain. Energy* 10, 043309. doi:10.1063/1.5027758

frontiers | Frontiers in Energy Research

TYPE Original Research
PUBLISHED 30 May 2023
DOI 10.3389/fenrg.2023.1181996

OPEN ACCESS

EDITED BY
Yongxin Xiong,
Aalborg University, Denmark

REVIEWED BY
Jianyu Zhou,
Aalborg University, Denmark
Liansong Xiong,
Xi'an Jiaotong University, China

*CORRESPONDENCE
Yufeng Guo,
guoyufenghit@163.com

RECEIVED 08 March 2023
ACCEPTED 15 May 2023
PUBLISHED 30 May 2023

CITATION
Wang Y, Guo Y, Du Y and Xu W (2023), Flexible torque control for wind turbines considering frequency response under wind speed crossing region.
Front. Energy Res. 11:1181996.
doi: 10.3389/fenrg.2023.1181996

Flexible torque control for wind turbines considering frequency response under wind speed crossing region

Yingwei Wang[1], Yufeng Guo[1]*, Yilin Du[1] and Weimao Xu[2]

[1]School of Electrical Engineering and Automation, Harbin Institute of Technology, Harbin, China, [2]Technical and Economic Center of Economic and Technological Research Institute, Liaoning Electric Power Co., Ltd., Shenyang, China

The operational range of a wind turbine is typically divided into two regions based on wind speed: below and above the rated wind speed. The turbine switches between these two regions depending on the prevailing wind speed; however, during the transition, the generator may undergo transient shocks in torque, which can negatively impact both the mechanical load of the turbine and the reliability of the power system. This article presents a flexible torque control method for wind turbines, specifically designed to handle the transition between wind speed regions when the turbine is participating in frequency regulation. First, the anomalies in generator torque caused by traditional torque control methods during frequency response scenarios are analyzed. Next, two methods—dynamic deloading and flexible torque control—are developed to address these issues. The developed methods set transition regions based on generator speed, which helps to reduce the impact of transient changes in generator torque. Importantly, the addition of transition regions does not require additional feedback, making the controller easy to implement. The response characteristics of the proposed methods are then analyzed under different deloading factors and wind speeds using model linearization. Simulation studies are presented to verify the effectiveness of the proposed methods. Overall, this study demonstrates the potential value of flexible torque control methods for wind turbines, which can help to mitigate the negative impact of torque shocks and improve the reliability and efficiency of wind power systems.

KEYWORDS

flexible torque control, frequency response, wind turbine control, deloading control, frequency regulation

1 Introduction

With the increasing integration of wind energy, the frequency stability of power systems has been falling (Wang et al., 2023; Xue et al., 2022). However, the participation of wind turbines in frequency response through overspeed control can significantly improve frequency stability (Xiong et al., 2022a; Yang et al., 2022). Due to the randomness of wind speed and system frequency, and the increase in complexity of the control system with the introduction of the frequency control loop, the control system plays a significant role in wind energy conversion systems (Boyle et al., 2021; Xiong et al., 2023). In terms of wind turbine control without consideration of frequency response, the control system includes constant power control above the rated wind speed, power tracking control below the rated

wind speed, and regional switching control under the prevailing wind speed (Suna et al., 2020; Xiong et al., 2022b). However, the introduction of a frequency response control loop makes the traditional switching control inapplicable, which causes abnormal fluctuations of generator torque and increases mechanical load. In addition, this causes abnormal output power fluctuations and damages the frequency stability of the system (Wang et al., 2020). Therefore, flexible torque control of wind turbines requires investigation, considering frequency response under wind speeds that cross the regions of operation.

Whether the wind speed is above or below the rated wind speed, the wind turbine control and corresponding frequency response methods proposed by scholars can allow for stable operation of the wind turbine. When the wind speed is lower than the rated wind speed, a control approach has been proposed to provide an emulated inertial response when the wind turbine is operating at the maximum power point. The proposed method mitigates the antagonistic interaction between maximum power point tracking (MPPT) control and inertia control (Bastiani and Vasques de Oliveira, 2021). An inertial power-based perturb and observe method has been proposed for MPPT control of wind turbines. The dynamical performance is increased by accurately identifying the maximum power point with high performance, either in the transient or in the steady state (Karabacak, 2019). A robust finite-time controller based on the Lyapunov function has been proposed to improve the transient performance of wind turbine speed-tracking and the robustness of the controlled system (Shotorbania et al., 2019). Finally, sliding mode control has been proposed to control MPPT, with aerodynamic torque being observed to mitigate the vibrations of the wind turbine (Pan and Shao, 2020).

When the wind speed is above the rated wind speed, a gain scheduled pitch controller has been designed by solving linear matrix inequalities and is used for stability control of the wind turbine (Bundi et al., 2020). An application of neural network-based model predictive control is presented to offer a stable response to frequency changes and significantly enhance the capability of reference tracking of the wind turbine (Kayedpour et al., 2022). In addition, the two-degree-of-freedom robust individual pitch controller is proposed to reduce loads in the above-rated region (Tang et al., 2022).

When the wind speed is around the rated wind speed (prevailing wind speed), the current model of switching control does not consider the frequency response of the system. The stability criteria for the switching operation of wind turbines are analyzed using second-order linear systems under the non-linear control framework (Palejiya et al., 2015). A bumpless transfer scheme has been presented to reduce the associated power fluctuation and fatigue loading (Chen et al., 2016). A method has been proposed to protect the wind turbine against the impulses and intense oscillations involved in switching between the different regions (Ali and Moradi, 2020). A method for adaptive envelope protection control of wind turbines under varying operational conditions has been proposed by Sahin and Yavrucuk (2022). A linear parameter-varying anti-windup controller has also been proposed to improve the transition between low- and high-wind speed operations (Inthamoussou et al., 2014). Additionally, it has been proposed that the dynamic switching transient be driven by predefined wind speed crossing events in order to mitigate step generator torque fluctuation (Xing et al., 2019). It can be noted that these recently proposed switching control methods focus only on a model of wind turbine control that does not participate in and is not applicable to frequency response.

To enable the application of switching control to frequency response, this article proposes a flexible torque control method for wind speed crossing regions. First, the phenomenon in which the traditional method for frequency regulation causes transient shocks to generator torque in the wind speed crossing region is analyzed. Next, the region around the prevailing wind speed is divided into transition regions of operation. Dynamic deloading and flexible torque control methods are proposed to allow flexible generator torque transfer at wind speeds around the prevailing wind speed. Finally, the dynamic characteristics of the proposed method are analyzed through linearization of the model and the effectiveness of the proposed method is verified by simulation.

The main contribution of this article is the proposal of a control scheme that provides flexible switching control under the wind crossing region, which is suitable for frequency regulation. Unlike conventional switching control methods, under this approach, generator torque is unaffected by the wind speed crossing region and frequency response. Wind turbines can provide stable generator and power output, which mitigates wind turbine vibration and improves frequency stability.

The remainder of this paper is organized into five sections. Section 2 provides an overview of conventional frequency regulation methods and discusses the abnormal torque fluctuation caused by the conventional method. Section 3 presents the proposed dynamic deloading and flexible torque control scheme, which overcomes the problems associated with conventional frequency control when applied under the wind speed crossing region. The results of the case studies are presented and analyzed in Section 4. Finally, Section 5 presents the conclusions drawn from the findings and identifies avenues for future research.

2 Problem description

In this section, the dynamic model of wind turbines is first described, the traditional torque and pitch control methods are introduced, and the frequency response method based on traditional torque control is also introduced. Finally, the problem is introduced, namely, that the frequency response of wind turbines under the conventional control method causes transient shocks to generator torque.

2.1 Dynamic modeling and control of wind turbines

The mechanical energy captured by the wind turbine is evaluated by Eq. 1. The rotor and generator are defined as in Eqs 2, 3.

$$P_{\mathrm{mec}} = 0.5\rho\pi R^2 v^3 C_{\mathrm{P}}(\omega_{\mathrm{r}}, v, \theta), \tag{1}$$

$$\dot{\omega}_{\mathrm{r}} = \frac{1}{J_{\mathrm{r}}}\left(T_{\mathrm{a}} - \eta_{\mathrm{g}} T_{\mathrm{g}}\right), \tag{2}$$

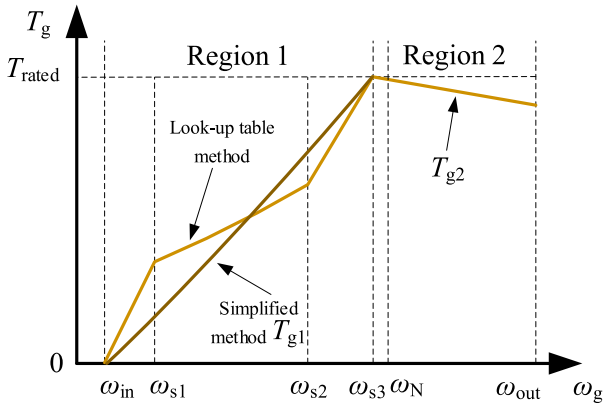

FIGURE 1
Generator torque control under different regions [ω_{s1}, ω_{s2}, and ω_{s3} are the set generator speed (rad/s)].

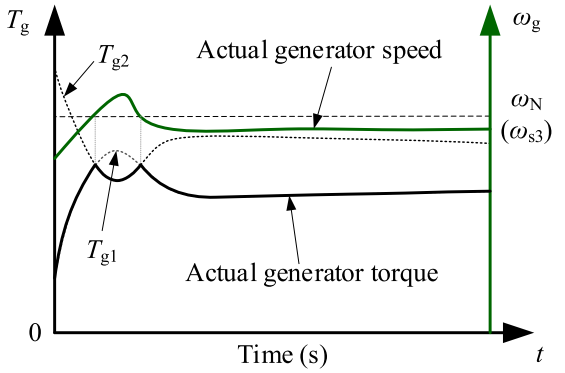

FIGURE 2
Generator speed and torque during the transitions between various operating regions.

$$\omega_g = \eta_g \omega_r, \tag{3}$$

where P_{mec} is the mechanical power (W), ρ is the air density (kg/m^3), v is the wind speed (m/s), R is the length of the blade (m), ω_r is the rotor speed (rad/s), ω_g is the generator speed (rad/s), C_p is the power coefficient, θ is the pitch angle (deg), T_a is the rotor torque (Nm), T_g is the generator torque (Nm), and η_g is the gearbox ratio.

To ensure that the wind turbine runs stably and to maximize the power output, many control methods have been proposed. Torque control (short for generator torque control of the wind turbine) can be divided into two regions according to wind speed, as shown in Figure 1. This torque control method is well-used and has been reported on by many scholars (Grunnet et al., 2010; Zhao et al., 2015; Zhao et al., 2017; Zhang et al., 2018; Wang et al., 2021; Wang et al., 2022). Region 1 is defined as the region where wind speed is below the rated wind speed, referred to as the partial-load region. In this region, the most commonly used control method in engineering is the look-up table method, employed to ensure that the wind turbine runs stably while processing MPPT. For simplification for the purpose of this study, the look-up table method can be simplified to Eq. 4. Region 2 is that the region where wind speed is above the rated wind speed, referred to as the full-load region. In this region, the main objective of torque control is maintaining a constant output power. The control method is expressed in Eq. 5. Furthermore, to limit the capture of wind energy in region 2, pitch control is activated, as determined by Eq. 6.

$$T_{g1} = k_{opt}\omega_g^2, \tag{4}$$

$$T_{g2} = \frac{P_{rated}}{\omega_g}, \tag{5}$$

$$\theta_{ref} = \max\left(\frac{180}{\pi}\frac{\left(k_p + \frac{k_i}{s}\right)\left(\omega_g - \omega_{gN}\right)}{k_{a1}\theta_{ref} + k_{a2}}, 0\right), \tag{6}$$

where k_{opt} is the generator control factor; P_{rated} is the rated power (W); T_{rated} is the rated generator torque (Nm); θ_{ref} is the reference pitch angle (deg); k_p and k_i are the proportional and integral gains of the PI controller, respectively; ω_{gN} is the rated generator speed (rad/s); and k_{a1} and k_{a2} are gain coefficients related to the pitch angle.

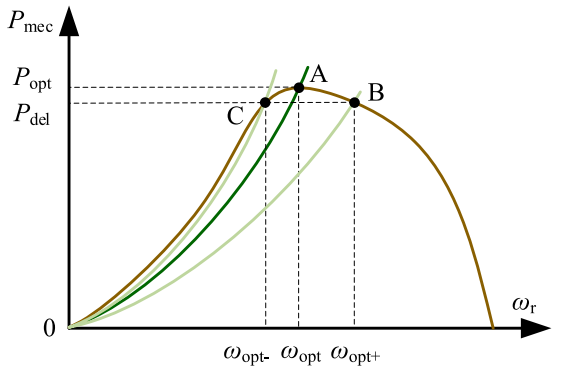

FIGURE 3
Mechanical power at different rotor speeds at zero-pitch angles.

It is worth noting that transition between the torque control regions is mainly judged based on the generator speed, but is also related to the captured power and pitch angle. The switching generator speed is set to speed ω_{s3} instead of the rated speed, as shown in Figure 1, which can enable advanced integration of the pitch angle to maximize the operational stability of the wind turbine. It can be seen that torque control is divided into two regions: Eqs 4, 5. In the conversion between regions, judgment of the generator speed is significant, and the set speed ω_{s3} is usually slightly lower than the rated speed. Figure 2 depicts the speed and torque of the generator during the transition between various operating regions of the wind turbine if the set speed ω_{s3} is the rated rotational speed, and in the absence of frequency response. It can be seen that when the generator speed crosses the set point, the generator torque crosses between different operating regions. Since the problem of transition in generator torque crossing is considered in the design of the traditional control method, the actual output generator torque shown in Figure 2 is smooth.

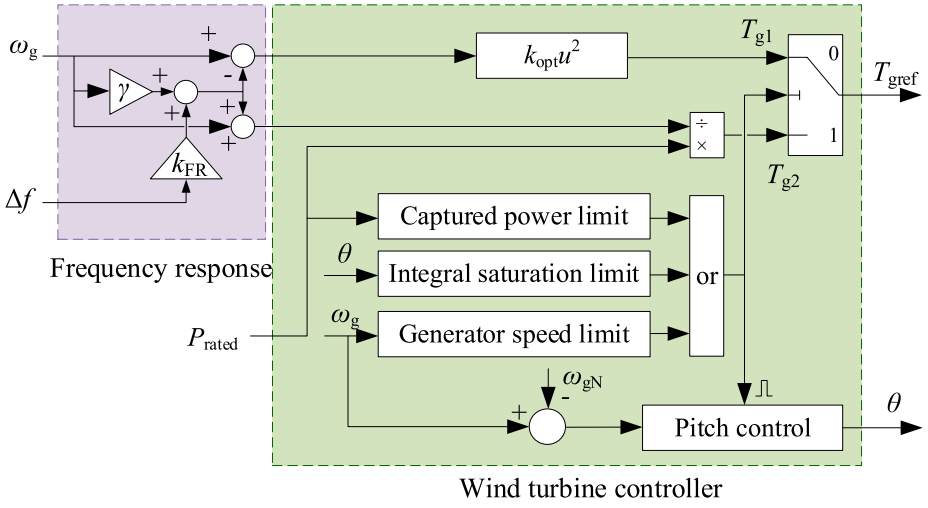

FIGURE 4
Block diagram ffor the frequency response method based on overspeed control.

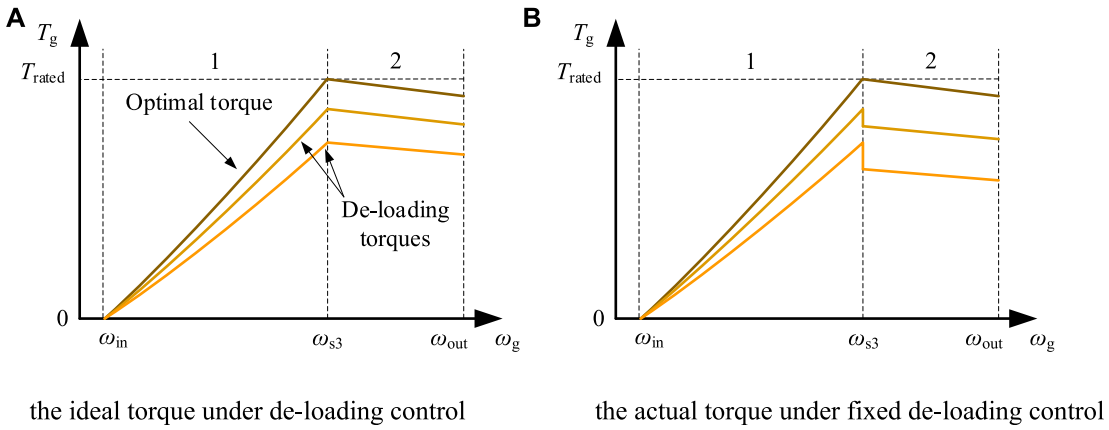

FIGURE 5
Generator torque under deloading control. **(A)** Ideal torque under deloading control. **(B)** Actual torque under fixed deloading control.

2.2 Frequency response method based on speed control

Adjustment of wind turbine speed can change the power captured. Figure 3 shows the mechanical power captured at different rotor speeds at a zero pitch angle. It can be seen that the wind turbine attains maximum power (P_{opt}) only when the rotor reaches a specific speed (ω_{opt}). In order to retain the capacity for frequency response, the wind turbine does not operate at the optimal power point A but rather at a suboptimal power point B or C through deloading control. In addition, reducing the generator speed under the same output power would increase the generator torque, which is not conducive to reducing the fatigue load. Thus, point B is the optimal choice for deloading control, that is, overspeed control.

The frequency response method, which utilizes overspeed control, is presented in block diagram form in Figure 4. Frequency response methods based on different methods of torque control are shown in Eqs 7, 8.

$$T_{g1}\left(\omega_g, \Delta f\right) = k_{opt}\left((1-\gamma)\omega_g - k_{FR}\Delta f\right)^2, \tag{7}$$

$$T_{g2}\left(\omega_g, \Delta f\right) = \frac{P_{rated}}{(1+\gamma)\omega_g + k_{FR}\Delta f}, \tag{8}$$

where γ is the deloading factor, k_{FR} is the frequency response gain (p.u.), k_{OPT} is the torque control gain (p.u.), and Δf is the frequency deviation of the power system (p.u.).

2.3 Transient shocks to generator torque caused by conventional methods

Generator torque under ideal deloading control can be simplified as shown in Figure 5A. Overspeed control (deloading torque) can reduce

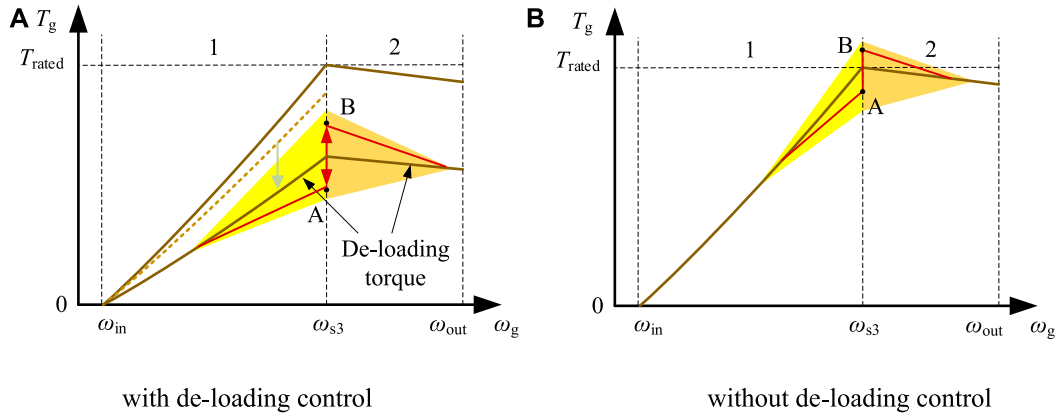

FIGURE 6
Generator torque when the wind turbine participates in frequency response by employing deloading control: **(A)** with deloading control; **(B)** without deloading control.

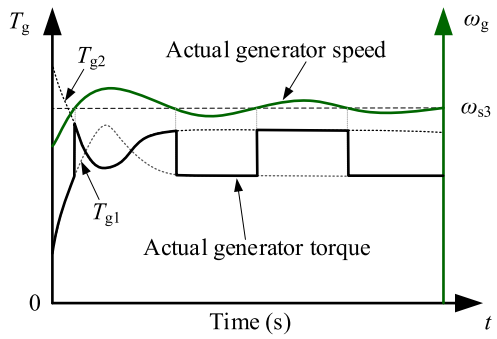

FIGURE 7
Transient shocks to generator torque fluctuations.

generator torque at the same speed. However, since the deloading factor is fixed under conventional control methods, generator torque undergoes shocks under region switching, as shown in Figure 5B. Moreover, generator torque cannot be transitioned smoothly between regions 1 and 2, which causes significant transient shocks and a significant increase in mechanical load.

Generator torque can be smoothed by regulating the deloading factor, which can be represented by the process from the dotted line to the solid line in Figure 6A. However, the generator torque participating in the frequency response is related not only to the generator speed but also to system frequency deviation. Figure 6A shows the generator torque when the wind turbine participates in frequency response by employing deloading control. If system frequency deviation were introduced into the torque control loop, generator torque would fall within the solid line of deloading torque and the yellow area. Since the system frequency is random to the wind turbine, the feedback of frequency deviation causes generator torque to vary irregularly within a specific range (the yellow-shaded parts of the two regions). There exist alternative techniques for regulating the frequency of a wind turbine, such as controlling the rotor speed to release kinetic energy, without requiring deloading. If a wind turbine is not subjected to de-rating control, its deloading factor can be deemed to be zero. Even in the absence of de-rating control, transient oscillations in generator torque may occur in the yellow region illustrated in Figure 6B, owing to frequency response dynamics.

The frequency response can cause frequent switching of generator torque between points A and B, resulting in unavoidable transient shocks to the generator torque fluctuations in the crossing region, as depicted in Figure 7. Due to the shift in the optimal operating point caused by overspeed control and frequency response, the generator torque values in regions 1 and 2 under the set speed are unequal, leading to abnormal fluctuations of generator torque in the crossing region. Connections between the generator, gearbox, and spindle can increase the drive train load due to transient fluctuation of the generator torque. The drive train dynamic equation is shown in Eqs 9–11.

$$T_s = \left(\frac{K}{s} + B\right)\left(\omega_r - \frac{\omega_g}{\eta_g}\right), \tag{9}$$

$$J_g\dot{\omega}_g = \frac{1}{\eta_g}T_s - T_g, \tag{10}$$

$$J_r\dot{\omega}_r = T_a - T_s, \tag{11}$$

where T_s is the shaft torque (Nm), J_g is the generator mass (kg·m^2), J_r is the rotor mass (kg·m^2), K is the shaft spring constant (Nm/rad), B is the shaft viscous friction (Nm·s/rad), and T_a is the rotor torque (Nm).

In summary, the current frequency response method has two main problems: transient shocks to generator torque caused by a fixed deloading factor, and transient shocks to generator torque caused by frequency regulation.

3 Proposed flexible torque

Dynamic deloading and flexible generator torque control methods are proposed here to address the challenges described in

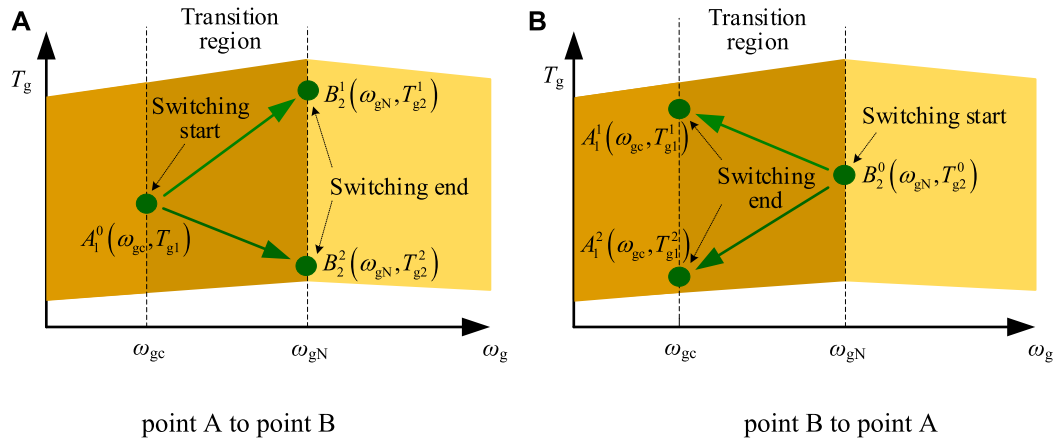

FIGURE 8
Generator torque crossing between different points: **(A)** point A to point B; **(B)** point B to point A.

the previous section. The response characteristics of the control scheme are also analyzed.

3.1 Proposed dynamic deloading method

Under a fixed deloading factor, generator torque cannot smoothly cross the set speed, resulting in step fluctuation in generator torque. However, when the deloading factor is not fixed, generator torque at the set speed can be equalized by adjusting the deloading factor. In other words, when frequency deviation is not considered, Eqs 7, 8 can be equalized to obtain the deloading factor of region 1. The deloading factor for region 1 is calculated by Eq. 12.

$$\gamma_1 = 1 - \frac{\sqrt{\frac{P_{rated}}{k_{opt}(1+\gamma_2)}}\omega_{gN}}{\omega_{gN}} \tag{12}$$

where γ_1 and γ_2 are the deloading factors of regions 1 and 2, respectively. The determination of γ_2 is typically left to the discretion of the user. When setting the value of γ_2, careful consideration is given to achieving a balance between the available spare capacity and the capacity for frequency adjustment in the wind turbine. In practice, it is common for γ_2 to be set at either 5% or 10%.

3.2 Proposed method for flexible torque control

The introduction of frequency deviation to torque control systems has led to transient shocks to generator torque. Therefore, it is necessary to set the generator torque transition region so that the torque undergoes a smooth transition between different regions. The torque transition region is referred to as the $1\frac{1}{2}$ region (transition region).

The process of torque crossing between regions 1 and 2 can be divided into two scenarios: region 1 to region 2, and region 2 to region 1. Figure 8 shows the generator torque crossing process from different points. When the torque shifts from point A to point B, two scenarios exist for torque increase and decrease (A_1^0 to B_2^1 and A_1^0 to B_2^2, respectively). Irrespective of whether the torque applied to the generator is increased or decreased, the speed of the generator will correspondingly increase. This relationship allows for the determination of torque traversal based on the observed speed. The gradient of the torque change can be used to represent the change rate. Thus, the shift in generator torque from region 1 to region 2 can be calculated by the speed increase shown in Eq. 13. When the torque shifts from point B to point A, no matter how the torque changes, the speed is reduced. Therefore, gradients can exist in either case that represent the change in torque. Equation 13 can be used to calculate generator torque in the shift from region 2 to region 1.

$$T_{g1\frac{1}{2}}(\omega_g, \Delta f) = \begin{cases} \frac{T_{g1}(\omega_g, \Delta f) - T_{g2}(\omega_g, \Delta f)}{\omega_{gc} - \omega_{gN}}(\omega_g - \omega_{gc}) + T_{g1}(\omega_g, \Delta f) & \Delta\omega_g > 0, \\ \frac{T_{g2}(\omega_g, \Delta f) - T_{g1}(\omega_g, \Delta f)}{\omega_{gN} - \omega_{gc}}(\omega_g - \omega_{gN}) + T_{g2}(\omega_g, \Delta f) & \Delta\omega_g < 0, \end{cases} \tag{13}$$

where $T_{g1\frac{1}{2}}$ is the generator torque of the transition region and ω_{gc} is the transition speed of the transition region. When wind turbines are operated without frequency regulation, the transition area should generally be neither too large nor too small. An excessively large transition area can reduce the frequency regulation capability of the wind turbine, while a transition area that is too small cannot achieve the desired effect of flexible torque control. To determine the appropriate control parameters in this study, with reference to previous research on transitional control without frequency response, a value for ω_{gc} of 121.7 rad/s was selected (Wang et al., 2020; Wang et al., 2021; Wang et al., 2022; Wang et al., 2023).

The control block diagram is shown in Figure 9. Generator speed governs the torque control, as follows:

- If the generator speed is less than the transition speed, the torque control system adopts the control method shown in Eq. 7.
- If the speed is within the crossing area (between the transition speed and the rated speed), the torque control system adopts the control method shown in Eq. 13.

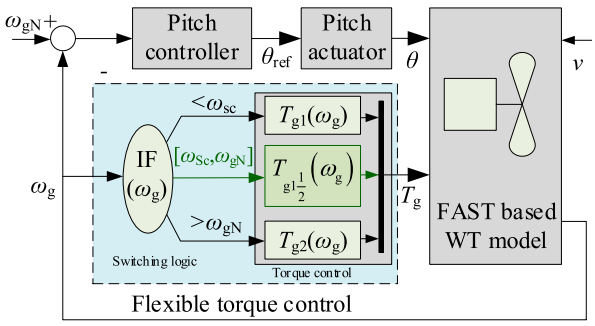

FIGURE 9
Control block diagram based on flexible torque control.

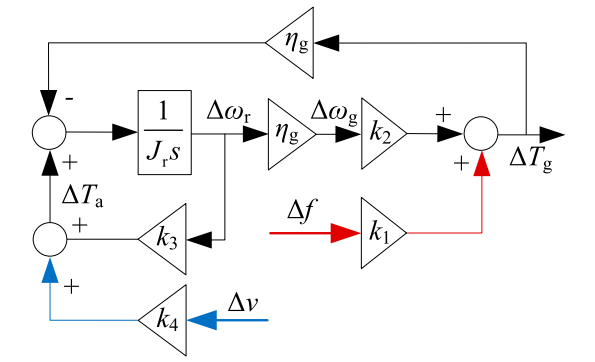

FIGURE 10
Closed-loop control block diagram.

- If the speed exceeds the rated speed, the torque control system adopts the control method shown in Eq. 8.

Note that the proposed flexible torque method only needs to detect the generator speed, which makes the method relatively easy to apply in engineering practice.

3.3 Dynamic analysis

A closed-loop control block diagram, as presented in Figure 10, was constructed to examine the response characteristics of the proposed method under different wind speeds and deloading factors For this purpose, error transfer functions were derived to analyze the response characteristics. The error transfer function for torque fluctuation and frequency fluctuation can be seen in Eq. 14; the error transfer function for torque fluctuation and wind speed fluctuation can be seen in Eq. 15.

$$\frac{\Delta T_g}{\Delta f} = \frac{k_1 (J_r s - k_3)}{J_r s - k_3 + k_2 \eta_g^2} \tag{14}$$

$$\frac{\Delta T_g}{\Delta v} = \frac{k_2 k_4 \eta_g}{J_r s - k_3 + k_2 \eta_g^2} \tag{15}$$

where $k_1 = \frac{\partial T_g}{\partial \Delta f}$, $k_2 = \frac{\partial T_g}{\partial \omega_g}$, $k_3 = \frac{\partial T_a}{\partial \omega_r}$, and $k_4 = \frac{\partial T_a}{\partial v}$.

The Bode diagram for Eq. 14 is shown in Figure 11A, in which the fluctuation of generator torque in the transition region is affected by wind speed. The impact mechanism is as follows: as the wind speed increases, torque fluctuations increase, and as the deloading factor increases, torque fluctuations increase. The Bode diagram for Eq. 15 is shown in Figure 11B, in which it can be seen that torque fluctuations increase with increased wind speed, while torque fluctuations decrease with an increase in deloading factor.

4 Case study

Different operating conditions were used as case studies to further illustrate the shortcomings of current control methods and to verify the effectiveness of the proposed method. Wind speed was generated using TurbSim (Kelley and Jonkman, 2006). The damage equivalent load was used to evaluate the fatigue loading of the wind turbine, which was calculated using the MCrunch package (Buhl, 2008).

4.1 Turbulent wind speed

The proposed flexible torque control system was first validated under turbulent wind speed conditions. In this scenario, the wind turbine only performs deloading control and does not participate in the frequency response. The average wind speed, as shown, was 10.68 m/s. The deloading factor γ_2 was 0.13. Figure 12 shows the generator speed, torque, and power output under different methods. FTC represents the proposed flexible torque control method and CON the conventional torque control method. Figure 12A shows the generator speed for each of the different methods; it can be seen that generator speed under the proposed FTC method is almost the same as that under the traditional method. Furthermore, under overspeed control, the generator speed of the wind turbine increases relative to that under MPPT. Based on the generator torque patterns shown in Figure 12B, it can be seen that generator speed under the traditional method fluctuates abnormally at certain moments, for the reason given in the above analysis. The proposed FTC method can avoid transient shocks, which greatly reduces the mechanical load of the wind turbine. Compared to generator torque under MPPT, generator torque under derating control is reduced.

The output power of the different methods is shown in Figure 12C. It can be seen that power output fluctuates abnormally under the traditional method (CON), which is not conducive to the frequency stability of the power system. The proposed method can produce smoother power output, which is beneficial to the stability of the power system. Furthermore, due to the implementation of deloading control, a portion of power (between 20 and 50 s) is reserved. Thus, the shaded region in Figure 12D displays the frequency response power that can be achieved. Wind turbines with sufficient power reserve can contribute to the frequency response of the system from 20 to 50 s. In the period from 50 to 80 s, wind turbines typically respond to frequency through the kinetic energy of the rotor due to insufficient wind speed.

In summary, the proposed method can provide the wind turbine with stable mechanical dynamics and power output under deloading control.

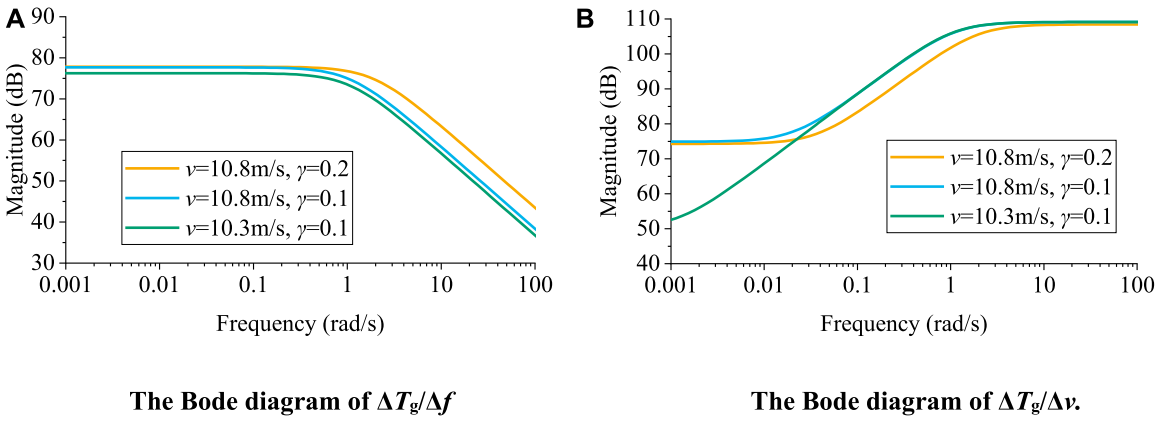

FIGURE 11
Bode diagrams for **(A)** $\Delta T_g/\Delta f$ and **(B)** $\Delta T_g/\Delta v$.

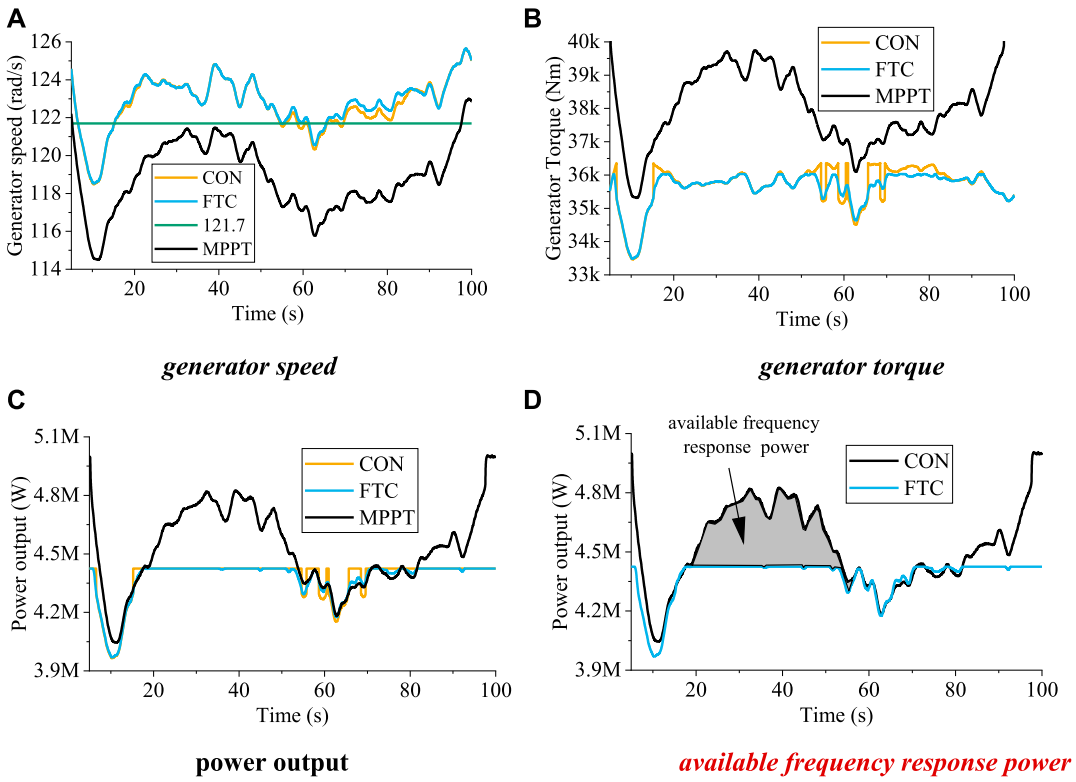

FIGURE 12
Operational states of the wind turbine under the different methods. In this scenario, the wind turbine only performs deloading control and does not participate in the frequency response. **(A)** Generator speed; **(B)** generator torque; **(C)** power output; **(D)** available frequency response power.

4.2 Participation in frequency regulation

In this scenario, the wind turbine engages in frequency response through dynamic deloading control. Generator speeds under the different methods are shown in Figure 13A. Similarly to the scenario with no participation in the frequency response, the differences in generator speed under the different methods are insignificant. Generator torque under the different methods is shown in Figure 13B. It can be seen that generator torque under the traditional method fluctuates abnormally at 35 s. Generator torque under the proposed method is smooth, which is beneficial for the mitigation of fatigue load and the stability of the power system. The output power of the different methods is shown in Figure 13C. It can be seen that output power fluctuates abnormally under the traditional method. If the frequency response is enacted according to the traditional method, system frequency may be negatively affected by

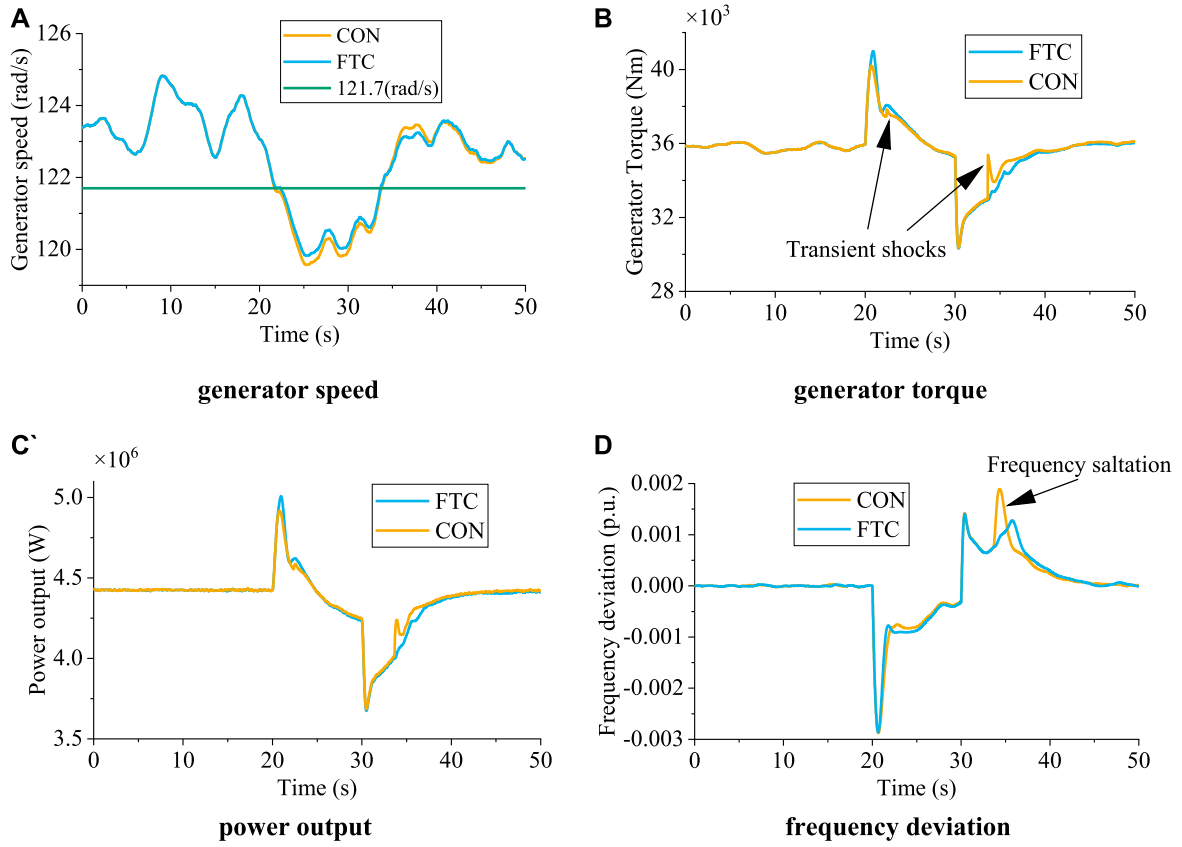

FIGURE 13
Operational states of the wind turbine under different methods under frequency regulation. **(A)** Generator speed; **(B)** generator torque; **(C)** power output; **(D)** frequency deviation.

TABLE 1 Comparison of fatigue load under the different methods under random system load.

	DEL (MNm)
CON	1.50
FTC	1.44
Percentage	−4%

the shock to power output in the transition region. The proposed method can smooth the output power and increase the power participating in the frequency response, which can significantly improve frequency stability and the profitability of the wind farm. The system frequency deviation under each of the different methods is shown in Figure 13D. It can be seen that frequency deviation under the conventional method shifts suddenly at 35 s due to transient shocks to generator torque. Under the proposed FTC scheme, saltation of frequency deviation caused by transient shocks can be avoided.

4.3 Performance under random system load

In this study, the long-term dynamics of the power system and mechanical load of wind turbines were analyzed to explain how the proposed FTC can reduce mechanical load and improve power system stability. The simulation used an average wind speed of 11.4 m/s, turbulence strength of 0.1, and random fluctuations in system load every 20 s, with an amplitude not exceeding 4% over a period of 600 s.

Figure 14A illustrates generator torque under various methods under random load conditions. The traditional approach results in frequent torque transients due to wind speed changes near the rated wind speed, leading to significant torque fluctuations, as evident in the local amplification diagram (360–400 s and 510–550 s). In contrast, the proposed FTC method effectively curbs abnormal torque fluctuations.

Figure 14B presents system frequency under different methods under random loads. The proposed FTC method successfully prevents abnormal frequency fluctuations caused by torque fluctuations and reduces the maximum frequency deviation to some extent, as evident in the locally enlarged images (180–200 s and 320–350 s). The drive train, which is directly connected to the generator, is the component most affected by transient fluctuations in generator torque.

As depicted in Figure 14C, abnormal generator torque fluctuations result in shaft torque abnormalities and increase twisting in the drive train, leading to gearbox damage. The local amplification diagrams (180–190 s and 316–328 s) clearly indicate

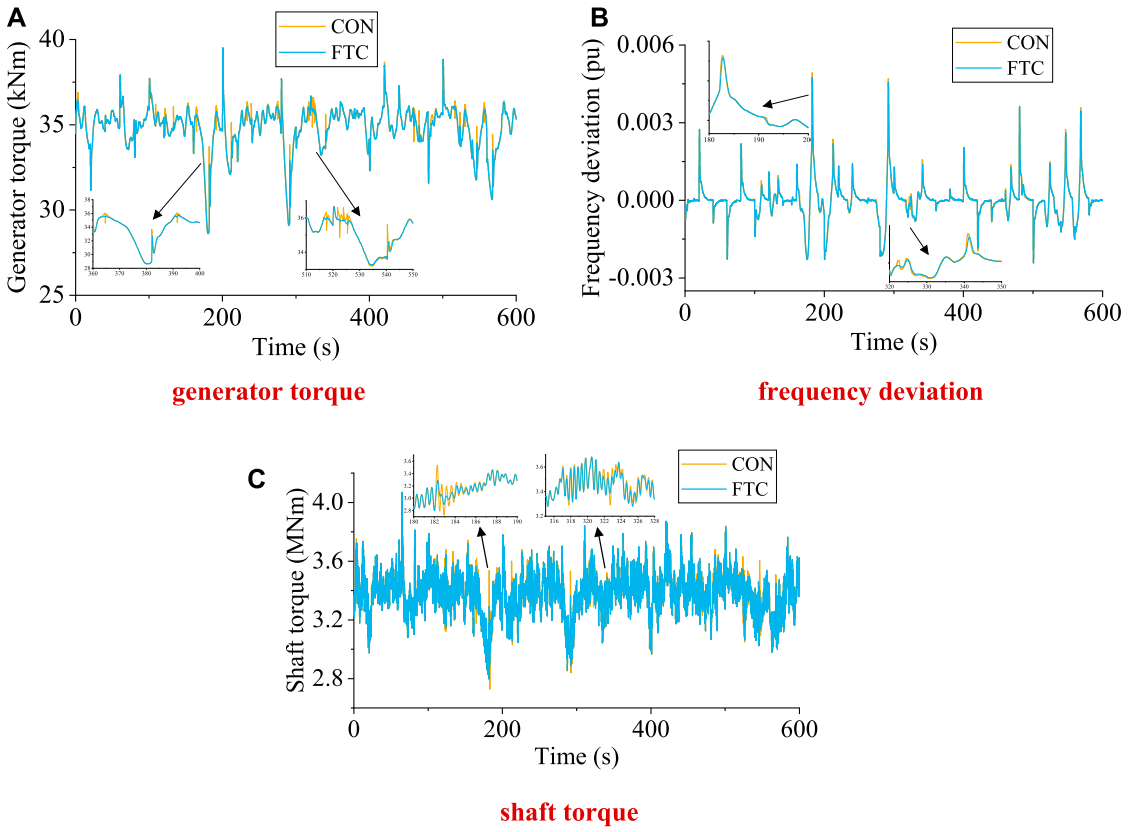

FIGURE 14
System frequency and wind turbine mechanical load for different methods under random load. **(A)** Generator torque; **(B)** frequency deviation; **(C)** shaft torque.

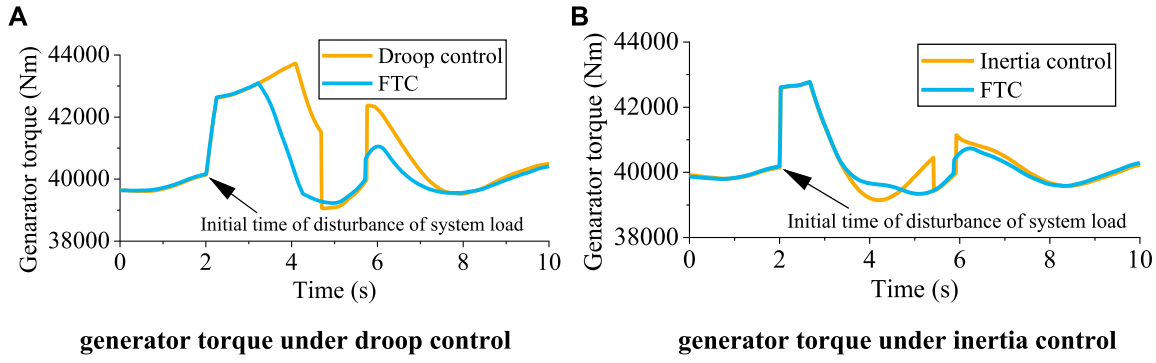

FIGURE 15
Generator torque of the wind turbine under frequency response with and without FTC. **(A)** Generator torque under droop control; **(B)** generator torque under inertia control.

these abnormalities, which aggravate fatigue load of the drive train and reduce the service life of the wind turbine. Table 1 displays the damage equivalent load (DEL) of the drive train torque under random load conditions for the different methods. DEL was 4% lower under the proposed FTC than under traditional methods. In summary, the proposed FTC method is advantageous in reducing mechanical load and improving power system stability, thereby enhancing the performance and durability of the wind turbine.

4.4 Performance under different frequency response methods

To illustrate the generality of the proposed FTC, we compared the generator torque under different frequency response methods. A rotor speed control method used in previous work was adoptedly, and primary frequency regulation, based on droop and inertia control, in turn based on power scheduling, was then tested (Wu et al., 2018). The initial

fluctuation time of system load was 2 s. Figure 15 shows the generator torque with and without FTC under droop control and inertia control. As shown from 3 to 8 s, it is clear that the proposed FTC can significantly reduce the fluctuation of generator torque. The above-described results show that the proposed method can be applied to different frequency response methods to reduce abnormal crossing of generator torque.

5 Conclusions and discussion

This paper has proposed a dynamic derating and flexible torque control method for frequency response in wind turbines within the wind speed crossing region. First, the abnormal torque ride-through phenomenon caused by fixed derating and traditional torque control methods under derating control were analyzed. Next, dynamic deloading and flexible torque control methods were proposed. The effectiveness of the proposed method was verified for turbulent wind with an average velocity near the rated wind speed. The results showed that the proposed method enables the system to avoid abnormal torque fluctuation and allows the wind turbine to operate with greater stability.

Data availability statement

The original contributions presented in the study are included in the article/Supplementary Material. Further inquiries can be directed to the corresponding author.

Author contributions

This article was completed collaboratively by the authors. YW, YG, and YD carried out the theoretical research, analyzed the data and the results, wrote the manuscript, and contributed constructive suggestions. WX revised the article. All authors contributed to the article and approved the submitted version.

Funding

This work was supported by Science and Technology projects managed by the headquarters of State Grid Corporation of China (grant 5108-202299259A-1-0-ZB). The study was funded by State Grid Corporation of China. The funder was not involved in the study design, data collection, analysis, interpretation, or in the writing of the article or the decision to submit it for publication.

Conflict of interest

Author WX was employed by the company Liaoning Electric Power Co., Ltd.

The remaining authors declare that the research was conducted in the absence of any commercial or financial relationships that could be construed as a potential conflict of interest.

Publisher's note

References

Ali, N., and Moradi, H. (2020). Smooth switching in power control of wind turbines using a combination strategy of hysteresis and modified middle regions. *Sustain. Energy Technol. Assessments* 37, 100585. doi:10.1016/j.seta.2019.100585

Bastiani, B. A., and Vasques de Oliveira, R. (2021). Adaptive MPPT control applied to virtual synchronous generator to extend the inertial response of type-4 wind turbine generators. *Sustain. Energy, Grids Netw.* 27, 100504. doi:10.1016/j.segan.2021.100504

Boyle, J., Littler, T., Muyeen, S. M., and Foley, A. M. (2021). An alternative frequency-droop scheme for wind turbines that provide primary frequency regulation via rotor speed control. *Int. J. Electr. Power Energy Syst.* 133, 107219. doi:10.1016/j.ijepes.2021.107219

Buhl, M. L. (2008) NREL/TP-500-45843139. Denver, CO, USA: Nat. Renew. Energy Lab. Mcrunch user's guide for version 1.00

Bundi, J. M., Ban, X., Wekesa, D. W., and Ding, S. (2020). Pitch control of small H-type Darrieus vertical axis wind turbines using advanced gain scheduling techniques. *Renew. Energy* 161, 756–765. doi:10.1016/j.renene.2020.05.184

Chen, Q., Li, Y., and John, E. (2016). Bumpless transfer-based inter-region controller switching of wind turbines for reducing power and load fluctuation. *IEEE Trans. Sustain. Energy* 7 (1), 23–31. doi:10.1109/tste.2015.2471104

Grunnet, J. D., Soltani, M., Knudsen, T., Kragelund, M. N., and Bak, T. (2010). "Aeolus toolbox for dynamics wind farm model simulation and control," in Proceedings of the European Wind Energy Conference and Exhibition, Brussels, Belgium, March, 2010, 3119–3129.

Inthamoussou, F. A., Bianchi, F. D., De Battista, H.´an, and Mantz, R. J. (2014). LPV wind turbine control with anti-windup features covering the complete wind speed range. *IEEE Trans. Energy Convers.* 29 (1), 259–266. doi:10.1109/tec.2013.2294212

Karabacak, M. (2019). A new perturb and observe based higher order sliding mode MPPT control of wind turbines eliminating the rotor inertial effect. *Renew. Energy* 133, 807–827. doi:10.1016/j.renene.2018.10.079

Kayedpour, N., Samani, A. E., JeroenDe Kooning, D. M., Vandevelde, L., and Crevecoeur, G. (2022). Model predictive control with a cascaded hammerstein neural network of a wind turbine providing frequency containment reserve. *IEEE Trans. Energy Convers.* 37 (1), 198–209. doi:10.1109/tec.2021.3093010

Kelley, N., and Jonkman, B. (2006). NREL/TP-500-3979. Denver, CO, USA: Nat. Renew. Energy Lab.,.Overview of the turbsim stochastic inflow turbulence simulator

Palejiya, D., Shaltout, M., Yan, Z., and Chen, D. (2015). L_2 stability of wind turbine switching control. *Int. J. Control* 88 (1), 193–203. doi:10.1080/00207179.2014.942883

Pan, L., and Shao, C. (2020). Wind energy conversion systems analysis of PMSG on offshore wind turbine using improved SMC and Extended State Observer. *Renew. Energy* 161, 149–161. doi:10.1016/j.renene.2020.06.057

Sahin, M., and Yavrucuk, I. (2022). Adaptive envelope protection control of wind turbines under varying operational conditions. *Energy* 247, 123544. doi:10.1016/j.energy.2022.123544

Shotorbania, A. M., Mohammadi-Ivatlooa, B., Wang, L., Marzband, M., and Sabahi, M. (2019). Application of finite-time control Lyapunov function in low-power PMSG wind energy conversion systems for sensorless MPPT. *Int. J. Electr. Power Energy Syst.* 106, 169–182. doi:10.1016/j.ijepes.2018.09.039

Suna, K., Xiaoa, H., Youa, S., Li, H., Pan, J., Li, K. J., et al. (2020). Frequency secure control strategy for power grid with large-scale wind farms through HVDC links. *Int. J. Electr. Power Energy Syst.* 117, 105706. doi:10.1016/j.ijepes.2019.105706

Tang, S., Tian, D., Wu, X., Huang, M., and Deng, Y. (2022). Wind turbine load reduction based on 2DoF robust individual pitch control. *Renew. Energy* 183, 28–40. doi:10.1016/j.renene.2021.10.086

Wang, H., Liu, Y., Wang, X., Guo, G., and Wang, L. (2023). Dynamic synthetic inertial control method of wind turbines considering fatigue load. *Front. Energy Res.* 10, 1–15. doi:10.3389/fenrg.2022.1067896

Wang, X., Wang, Y., and Liu, Y. (2020). Dynamic load frequency control for high-penetration wind power considering wind turbine fatigue load. *Int. J. Electr. Power Energy Syst.* 117, 105696. doi:10.1016/j.ijepes.2019.105696

Wang, Y., Guo, Y., Zhang, D., Liu, H., and Song, R. (2022). Analysis and mitigation of the drive train fatigue load for wind turbine with inertial control. *Int. J. Electr. Power & Energy Syst.* 136, 107698. doi:10.1016/j.ijepes.2021.107698

Wang, Y., Guo, Y., and Zhang, D. (2021). Optimal ancillary control for frequency regulation of wind turbine generator based on improved fatigue load sensitivity. *Int. J. Electr. Power & Energy Syst.* 17, 107751. doi:10.1016/j.ijepes.2021.107751

Wu, Z., Gao, W., Gao, T., Yan, W., Zhang, H., Yan, S., et al. (2018). State-of-the-art review on frequency response of wind power plants in power systems. *J. Mod. power Syst. clean energy* 6 (1), 1–16. doi:10.1007/s40565-017-0315-y

Xing, X., Meng, H., Xie, L., Yue, L., and Lin, Z. (2019). Switching performance improvement based on model-predictive control for wind turbine covering the whole wind speed range. *IEEE Trans. Sustain. Energy* 10 (1), 290–300. doi:10.1109/tste.2018.2833634

Xiong, Y., Yao, W., Lin, S., AiFang, J., Wen, J., and Cheng, S. (2022). Improved communication-free coordinated control of VSC-mtdc integrated offshore wind farms for onshore system frequency support. *IEEE Trans. Power Deliv.*, 1–13. doi:10.1109/tpwrd.2022.3184497

Xiong, Y., Yao, W., Shi, Z., Fang, J., Ai, X., Wen, J., et al. (2022). Adaptive dual droop control of MTDC integrated offshore wind farms for fast frequency support. *IEEE Trans. Power Syst.*, 1–13. doi:10.1109/TPWRS.2022.3179504

Xiong, Y., Yao, W., Yao, Y., Fang, J., Ai, X., Wen, J., et al. (2023). Distributed cooperative control of offshore wind farms integrated via MTDC system for fast frequency support. *IEEE Trans. Industrial Electron.* 70 (5), 4693–4704. doi:10.1109/tie.2022.3183355

Xue, L., Zhao, Y., Groß, D., and Liu, T. (2022). Receding horizon control based secondary frequency regulation for power systems with wind energy integration. *Int. J. Electr. Power Energy Syst.* 142, 108282. doi:10.1016/j.ijepes.2022.108282

Yang, D., Jin, Z., Zheng, T., and Jin, E. (2022). An adaptive droop control strategy with smooth rotor speed recovery capability for type III wind turbine generators. *Int. J. Electr. Power Energy Syst.* 135, 107532. doi:10.1016/j.ijepes.2021.107532

Zhang, B., Soltani, M., Hu, W., Hou, P., Huang, Q., and Chen, Z. (2018). Optimized power dispatch in wind farms for power maximizing considering fatigue loads. *IEEE Trans. Sustain. Energy* 9 (2), 862–871. doi:10.1109/tste.2017.2763939

Zhao, H., Wu, Q., Guo, Q., Sun, H., and Xue, Y. (2015). Distributed model predictive control of a wind farm for optimal active power control-Part II: Implementation with clustering-based piece-wise affine wind turbine model. *IEEE Trans. Sustain. Energy* 6 (3), 840–849. doi:10.1109/tste.2015.2418281

Zhao, H., Wu, Q., Huang, S., Shahidehpour, M., Guo, Q., and Sun, H. (2017). Fatigue load sensitivity based optimal active power dispatch for wind farms. *IEEE Trans. Sustain. Energy* 8 (3), 1247–1259. doi:10.1109/tste.2017.2673122

frontiers | Frontiers in Energy Research

TYPE Original Research
PUBLISHED 10 July 2023
DOI 10.3389/fenrg.2023.1218035

OPEN ACCESS

EDITED BY
Chengguo Su,
Zhengzhou University, China

REVIEWED BY
Guangsheng Pan,
Southeast University, China
Hongxun Hui,
University of Macau, China

*CORRESPONDENCE
Yun Zhou,
yun.zhou@sjtu.edu.cn

RECEIVED 06 May 2023
ACCEPTED 19 June 2023
PUBLISHED 10 July 2023

CITATION
Zeng X, Wang J, Zhou Y and Li H (2023), Optimal configuration and operation of the regional integrated energy system considering carbon emission and integrated demand response.
Front. Energy Res. 11:1218035.
doi: 10.3389/fenrg.2023.1218035

Optimal configuration and operation of the regional integrated energy system considering carbon emission and integrated demand response

Xianqiang Zeng[1], Jin Wang[1], Yun Zhou[2]* and Hengjie Li[1,2]

[1]School of Electrical and Information Engineering, Lanzhou University of Technology, Lanzhou, China, [2]Key Laboratory of Control of Power Transmission and Conversion, Ministry of Education, Shanghai Jiao Tong University, Shanghai, China

Under the "carbon peaking and carbon neutrality" development strategy, in order to suppress load fluctuations and promote renewable energy consumptions in the regional integrated energy system involving concentrating solar power stations, a double-layer optimization model based on the improved non-dominated sorting genetic algorithm-II (NSGA-II) and mixed integer linear programming (MILP) is proposed. The upper layer completes the capacity configuration process based on multiple objectives to minimize the annual planning cost and the net emission of pollutants. The lower layer is designed to minimize the annual operating cost and optimize the output of the devices and the load curves through the participation of the integrated demand response process for flexible loads and the whole process of carbon emission including carbon capture, carbon utilization, and carbon trading mechanisms to obtain the best operating plan. The final results indicate that the participation of concentrating solar power stations can improve the level of coordinated optimization, and the improved NSGA-II is stronger than the conventional one in convergence ability. Besides, considering the whole process of carbon emission and integrated demand response is capable of decreasing the annual operating cost and net carbon emission to improve the economy and environmental protection of the system significantly.

KEYWORDS

regional integrated energy system, concentrating solar power station, NSGA-II, the whole process of carbon emission, integrated demand response

1 Introduction

In recent years, environmental problems have become more serious, so the exploration of clean energy will become an inevitable trend in the future development (Fan et al., 2021). The regional integrated energy system (RIES) breaks the barrier between energy planning and operation, and its internal multi-energy coupling equipment can realize energy gradient utilization (Chen et al., 2022; Wang B. et al., 2022), which plays a huge part in realizing the goal of promoting economic and environmental benefits.

In the field of RIES low-carbon operation, relevant studies mostly focus on the regulatory means and economic mechanisms such as carbon capture, carbon storage, and carbon trading. In the work of Dong et al. (2022), a carbon capture model combined with power-to-gas and gas-fired units was installed, which effectively minimized the carbon cost of the total system through the improved energy hub formulation. In the work of Zhang D. et al. (2021), a carbon storage

device with pollutant treatments and carbon capture systems (CCSs) was regarded as the structure of an evolutionary IES, which significantly improved renewable energy penetration under different specifications. In the work of Yan et al. (2023), a seasonal-stepped carbon trading mechanism was introduced, and the impacts of economics on optimal dispatch are also considered comprehensively. However, few studies have been conducted on cost-effective carbon utilization processes compared with costly carbon storage processes.

Research on the participation of flexible loads in integrated demand response (IDR) is generally classified into price type, incentive type, and substitution type according to their guiding modes. Yang et al. (2020) divided the IDR into price-based and alternative parts with the process of rolling optimization and finally showed that the aforementioned method can restrain the fluctuation of the loads. Wang et al. (2021) put forward an uncertain model of the demand response through the energy coupling matrices to investigate the impact of price incentives under different scenarios in the RIES to realize the improvement in the load profile. Shao et al. (2019) promoted the IDR to smart buildings and then developed a real-time exchange market with the feasible region method to adjust energy consumption behaviors. Zhang et al. (2022) proposed a multi-objective model considering two-dimensional demand responses with spatiotemporal coupling characteristics to obtain the control strategy among different benefit weights. However, most research on IDR focuses on electricity and heat at present, while cool energy and gas energy are rarely considered.

In addition, with the steady development of concentrating solar power (CSP) in renewable energy, photothermal power generation has gradually attracted wide attention for its advantages of good controllability and high adjustability. Zhao et al. (2019) analyzed the influences of wind power uncertainty on optimal dispatch and put forward a stochastic model for the combination of the CSP stations and wind farms according to the simulation results. In the work of Zhang G. et al. (2021), CSP stations were introduced as cogenerated units and a multi-dispatch method for the RIES was proposed. The results show that the participation of CSP stations can reduce operating costs. On the premise of considering operating cost, Jiang et al. (2020) built an exchange model between CSP stations and energy markets to participate in DR programs, which significantly improved the energy operating efficiency through the price elasticity matrix of the electrical and the heat loads. However, the existing literature has generally ignored the potential of CSP stations operating in conjunction with the aforementioned CCS.

In view of the problems mentioned previously, the main contributions of this paper are shown as follows:

1) An energy hub (EH) with the participation of the CSP station and the whole process of carbon emission including carbon capture, carbon utilization, and carbon trading is established by considering the power-to-gas equipment.
2) The analysis includes flexible loads such as electricity, heat, cooling, and gas and successively elaborates them for the uncontrollable loads, transferable loads, curtailable loads, and fungible loads, which are refined to reflect the IDR.
3) A double-layer optimization model of improved NSGA-II and MILP is constructed. The upper layer takes the annual planning cost and net pollutant discharge as the target for device selection and capacity configuration through the improved NSGA-II, while the lower layer regards the annual operating cost as the target to optimize the output of each device through the Cplex solver.

This paper is organized as follows. In Section 2, the basic structure and the operating principle of the RIES are introduced. Section 3 is focused on the expression of the proposed CSP station, the whole process of carbon emission, and the IDR. In Section 4, a double-layer model considering the solving methods is developed to realize the optimized process. Case studies are conducted in Section 5, in which the proposed model is simulated

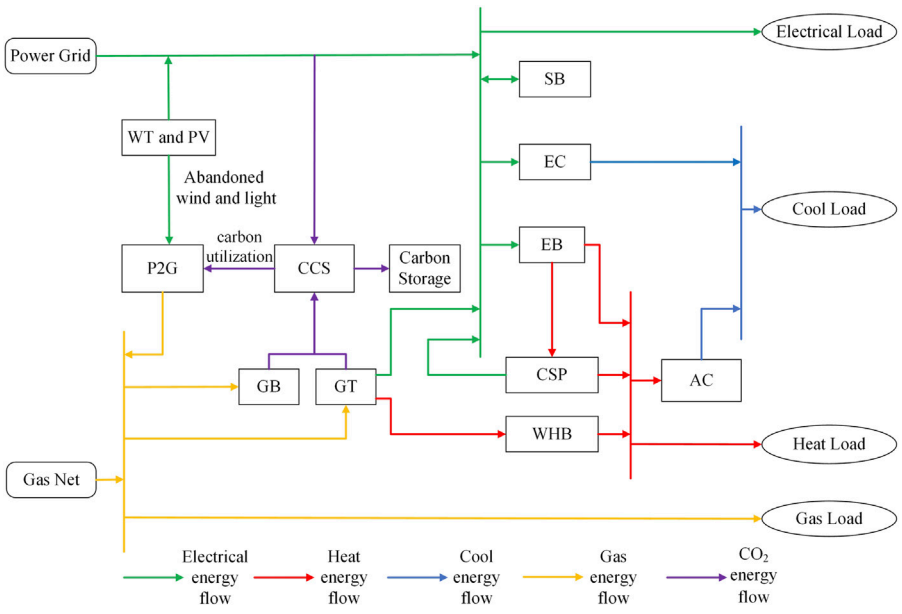

FIGURE 1
Structure diagram of the RIES.

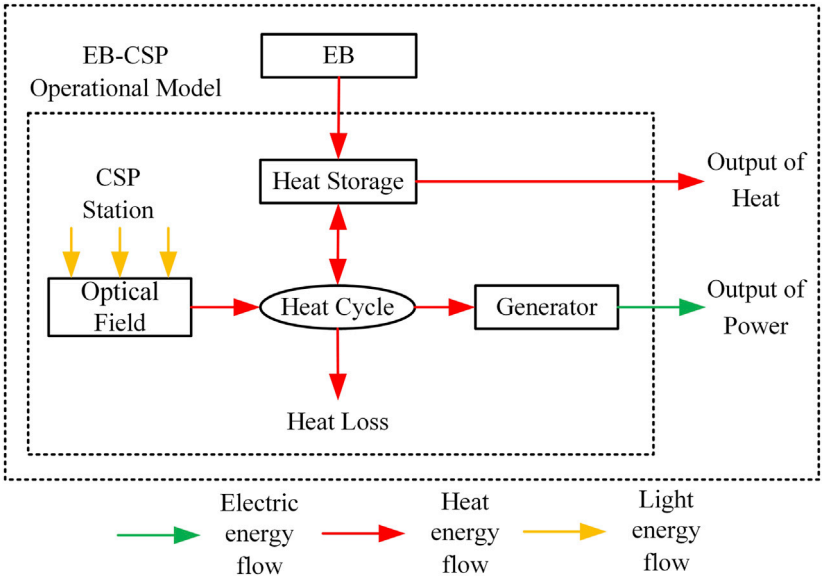

FIGURE 2
EB–CSP framework.

under different scenarios. At last, the conclusions are given in Section 6.

2 Basic structure of the RIES

This paper focuses on the RIES shown in Figure 1. The system includes the wind turbine (WT), photovoltaic (PV), CSP station, electric boiler (EB), electric chiller (EC), waste heat boiler (WHB), absorption chiller (AC), gas turbine (GT), gas boiler (GB), carbon capture system (CCS), power to gas (P2G), and storage battery (SB). The energy input sources of the RIES are electricity and natural gas, and the loads include electricity, heat, cooling, and gas. The CSP station can be regarded as cogenerated equipment. Similarly, GT consumes natural gas to generate heat, which can be recovered by WHB. For the CCS, the CO_2 captured is mainly from coal-fired plants in the power grid and gas-fired units (GT and GB) in the RIES. The power consumption of P2G can be supplied by abandoned wind and light, thus realizing the absorptive process of renewable energy. The entered electricity and natural gas of the EH can be purchased from power grid companies and natural gas companies, respectively, and then reasonably distributed to various energy conversion equipment and user-side loads.

3 The whole process of carbon emission and integrated demand response in the RIES

3.1 Conventional device model of the RIES

The conventional devices of the RIES mainly include gas-fired units, EB, EC, AC, and WHB. The models are shown as follows:

$$\begin{cases} P_t^{\mathrm{GT}} = P_t^{\mathrm{GT,e}} + P_t^{\mathrm{GT,h}}, \\ P_t^{\mathrm{GT,e}} = \eta_{\mathrm{GT,e}} H_{\mathrm{g}} Q_t^{\mathrm{GT}}, \\ P_t^{\mathrm{GT,h}} = \eta_{\mathrm{GT,h}} H_{\mathrm{g}} Q_t^{\mathrm{GT}}, \\ P_t^{\mathrm{GB,h}} = \eta_{\mathrm{GB,h}} H_{\mathrm{g}} Q_t^{\mathrm{GB}}, \\ P_t^{\mathrm{EB,h}} = \eta_{\mathrm{EB,h}} P_t^{\mathrm{e,EB}}, \\ P_t^{\mathrm{EC,c}} = \eta_{\mathrm{EC,c}} P_t^{\mathrm{e,EC}}, \\ P_t^{\mathrm{AC,c}} = \eta_{\mathrm{AC,c}} P_t^{\mathrm{h,AC}}, \\ P_t^{\mathrm{WHB,h}} = \eta_{\mathrm{WHB,h}} P_t^{\mathrm{GT,h}}, \end{cases} \tag{1}$$

where P_t^{GT}, $P_t^{\mathrm{GT,e}}$, and $P_t^{\mathrm{GT,h}}$ are the total output, electrical output, and thermal output of GT at time t, respectively; $P_t^{\mathrm{GB,h}}$, $P_t^{\mathrm{EB,h}}$, $P_t^{\mathrm{EC,c}}$, $P_t^{\mathrm{AC,c}}$, and $P_t^{\mathrm{WHB,h}}$ are the output of GB, EB, EC, AC, and WHB at time t, respectively; Q_t^{GT} and Q_t^{GB} are the amount of natural gas consumed by GT and GB at time t, respectively; $P_t^{\mathrm{e,EB}}$, $P_t^{\mathrm{e,EC}}$, and $P_t^{\mathrm{h,AC}}$ are the input power of EB, EC, and AC at time t, respectively; $\eta_{\mathrm{GT,e}}$ and $\eta_{\mathrm{GT,h}}$ are the electrical efficiency and thermal efficiency of GT, respectively; $\eta_{\mathrm{GB,h}}$, $\eta_{\mathrm{EB,h}}$, $\eta_{\mathrm{EC,c}}$, $\eta_{\mathrm{AC,c}}$, and $\eta_{\mathrm{WHB,h}}$ are the corresponding energy conversion efficiency of GB, EB, EC, AC, and WHB, respectively; and H_{g} is the calorific value of the natural gas.

3.2 CSP thermoelectric conversion model

As an emerging form of power generation in recent years, the CSP station is mainly divided into tower type, trough type, disk type, and linear Fresnel type, among which the tower type has been widely used in engineering practice for its advantages of strong economy and good performance (Gorman et al., 2021). In this paper, the heat storage tank and EB are aggregated to model the internal and external energy transfer relationships of the tower-type CSP station. The typical structure is shown in Figure 2.

The heat energy collected by the heat collector in the optical field can be stored in the heat storage tank through the heat transfer

mediums, and it can also be used to generate electricity through the heat cycle. The expression of photothermal conversion of the heat collector is shown as follows:

$$P_t^{\mathrm{SF,h}} = \eta_{\mathrm{s-h}} S_{\mathrm{SF}} D_t, \tag{2}$$

where $P_t^{\mathrm{SF,h}}$ is the thermal power obtained by the heat collector at time t; $\eta_{\mathrm{s-h}}$ is the photothermal conversion efficiency; S_{SF} is the area of the heliostat field; and D_t is the direct solar radiation index (DNI) at time t.

The heat storage tank can store the converted heat energy and can also release the heat energy to meet the generation demand or directly supply the heat to the load side. The model of the heat storage tank is shown in the following formula:

$$S_t^{\mathrm{HQ}} = S_{t-1}^{\mathrm{HQ}}(1-\rho_{\mathrm{h}}) + \eta_{\mathrm{cha}}^{\mathrm{HQ}} P_t^{\mathrm{TS,c}} - \frac{P_t^{\mathrm{TS,f}}}{\eta_{\mathrm{dis}}^{\mathrm{HQ}}}, \tag{3}$$

where S_t^{HQ} and S_{t-1}^{HQ} are the thermal storage of the heat storage tank at time t and time $t-1$, respectively; ρ_{h} is the energy self-loss coefficient; $\eta_{\mathrm{cha}}^{\mathrm{HQ}}$ and $\eta_{\mathrm{dis}}^{\mathrm{HQ}}$ are the charging and releasing efficiency of the heat storage tank, respectively; and $P_t^{\mathrm{TS,c}}$ and $P_t^{\mathrm{TS,f}}$ are the charging and releasing power of the heat storage tank at time t, respectively.

To keep the CSP station in stable operation after the participation of EB, its internal heat cycle must meet the following relations:

$$\begin{cases} P_t^{\mathrm{SF,h}} + P_t^{\mathrm{TS,f}} + P_t^{\mathrm{EB,in}} = P_t^{\mathrm{SF,r}} + P_t^{\mathrm{TS,c}} + P_t^{\mathrm{TS,ef}} + P_t^{\mathrm{HL}} + P_t^{\mathrm{abn,h}}, \\ P_t^{\mathrm{EB,in}} = P_t^{\mathrm{EB,h}} - P_t^{\mathrm{EB,load}}, \end{cases} \tag{4}$$

where $P_t^{\mathrm{SF,r}}$ and $P_t^{\mathrm{TS,ef}}$ are the thermal power directly generated by the heat collector and the heat storage tank at time t, respectively; $P_t^{\mathrm{EB,in}}$ and $P_t^{\mathrm{EB,load}}$ are the thermal power provided by EB to the heat storage tank and the heat load side, respectively; and P_t^{HL} and $P_t^{\mathrm{abn,h}}$ are the thermal power provided to the heat load side and heat energy loss at time t, respectively.

The generation power of the CSP station mainly comes from the heating power of the heat collector and the heat storage tank:

$$\begin{cases} P_t^{\mathrm{CSP,e}} = P_t^{\mathrm{SF,d}} + P_t^{\mathrm{TS,df}}, \\ P_t^{\mathrm{SF,d}} = \eta_{\mathrm{d}} P_t^{\mathrm{SF,r}}, \\ P_t^{\mathrm{TS,df}} = (1-\eta_{\mathrm{f}})\eta_{\mathrm{d}} P_t^{\mathrm{TS,ef}}, \end{cases} \tag{5}$$

where $P_t^{\mathrm{SF,d}}$ and $P_t^{\mathrm{TS,df}}$ are the heat of the collector and the storage tank that provides for power generation, respectively; η_{d} and η_{f} are the thermoelectric conversion efficiency of the heat collector and released loss rate of the heat storage tank, respectively.

The heat energy provided to the load side is expressed as follows:

$$P_t^{\mathrm{HL}} = \eta_{\mathrm{h}}\left(P_t^{\mathrm{TS,f}} - P_t^{\mathrm{TS,ef}}\right), \tag{6}$$

where η_{h} is the heat transfer efficiency of the heat storage tank.

3.3 The whole process of carbon emission including P2G collaborative operation

3.3.1 Operating characteristics of P2G

In this paper, P2G can absorb the power of abandoned wind and light, which is used to generate natural gas. The energy consumption of P2G is shown in the following equation:

$$P_t^{\mathrm{P2G}} = P_t^{\mathrm{WA}} + P_t^{\mathrm{VA}}, \tag{7}$$

where P_t^{WA} and P_t^{VA} are the power of abandoned wind and light at time t, respectively.

The amount of CO_2 consumed in P2G can be formulated as follows:

$$Q_t^{\mathrm{CO_2,P2G}} = \alpha_{\mathrm{CO_2}} \eta_{\mathrm{P2G}} P_t^{\mathrm{P2G}}, \tag{8}$$

where $\alpha_{\mathrm{CO_2}}$ is the CO_2 consumption per unit of power; η_{P2G} is the conversion efficiency of P2G.

The natural gas produced by P2G can be calculated as follows:

$$Q_t^{\mathrm{P2G,CH_4}} = \frac{3.6\eta_{\mathrm{P2G}} P_t^{\mathrm{P2G}}}{H_{\mathrm{g}}}. \tag{9}$$

3.3.2 Principles of carbon capture and carbon utilization

The CCS mainly includes the absorption tower, regeneration tower, compressor, and other structural units. The absorber uses a specific solution to absorb CO_2 from the flue gas and transfers it to the regenerator, where it is heated and separated. Then, CO_2 is compressed in the compressor for transporting. Therefore, the energy consumption of carbon capture and gas treatment generated by the three links mentioned previously are the main sources of the total energy consumption in the CCS (Yan et al., 2017), whose expression is shown as follows:

$$\begin{cases} P_t^{\mathrm{CCS}} = P_t^{\mathrm{CAP}} + P_t^{\mathrm{DEAL}}, \\ P_t^{\mathrm{CAP}} = P_t^{\mathrm{CCS,r}} + P_t^{\mathrm{CCS,f}}, \\ P_t^{\mathrm{DEAL}} = \lambda_{\mathrm{DEAL}}\left(Q_t^{\mathrm{CS}} + Q_t^{\mathrm{ST}}\right), \end{cases} \tag{10}$$

where P_t^{CAP} and P_t^{DEAL} are carbon capture energy consumption and gas treatment energy consumption of the CCS, respectively; $P_t^{\mathrm{CCS,r}}$ and $P_t^{\mathrm{CCS,f}}$ are the operating energy consumption and fixed energy consumption of carbon capture, respectively; λ_{DEAL} is the unit energy consumption coefficient of flue gas treatment; and Q_t^{CS} and Q_t^{ST} are the flue gas treatment provided by carbon source units and the flue gas storage tank at time t, respectively. The operating energy consumption and fixed energy consumption of carbon capture are, respectively, satisfied.

$$\begin{cases} P_t^{\mathrm{CCS,r}} = \lambda_{\mathrm{CO_2}} E_t^{\mathrm{CO_2}}, \\ P_t^{\mathrm{CCS,f}} = 0.1\lambda_{\mathrm{CO_2}} E_t^{\mathrm{CO_2}}, \end{cases} \tag{11}$$

where $\lambda_{\mathrm{CO_2}}$ is the operating energy consumption coefficient of unit CO_2 treated by the CCS; $E_t^{\mathrm{CO_2}}$ is CO_2 that is captured.

The capacity of the flue gas storage tank is shown as follows:

$$Q_t^{\mathrm{DEAL}} = Q_{t-1}^{\mathrm{DEAL}} + Q_t^{\mathrm{IN}} - Q_t^{\mathrm{ST}}, \tag{12}$$

where Q_t^{DEAL} and Q_{t-1}^{DEAL} are the capacities of the flue gas storage tank at time t and $t-1$, respectively.

In this paper, a combined operation strategy of wind power–photovoltaic–CSP–carbon capture based on the participation of the CCS and new energy units is proposed. The output of new energy units is partly used for carbon capture, partly used for flue gas treatment, and the rest is transported to the power grid. The energy consumption process of the carbon capture is presented in Figure 3 in the following section, and the energy consumption process of the flue gas treatment is similarly omitted.

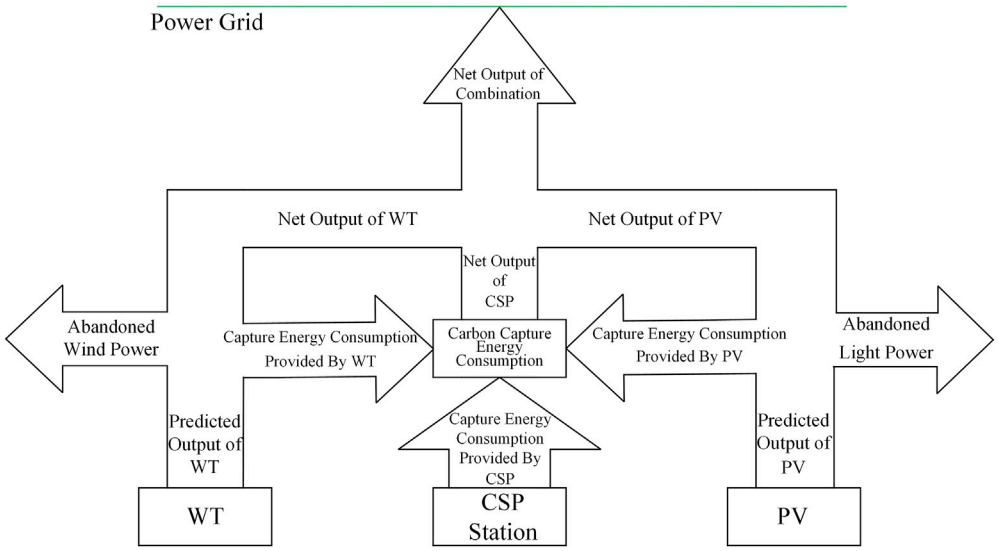

FIGURE 3
Flow chart of carbon capture energy.

The expression of joint operation is shown as follows:

$$\begin{cases} P_t^{\mathrm{CAP}} = P_t^{\mathrm{WC}} + P_t^{\mathrm{VC}} + P_t^{\mathrm{CC}}, \\ P_t^{\mathrm{DEAL}} = P_t^{\mathrm{WD}} + P_t^{\mathrm{VD}} + P_t^{\mathrm{CD}}, \\ P_t^{\mathrm{W}} = P_t^{\mathrm{WN}} + P_t^{\mathrm{WC}} + P_t^{\mathrm{WD}} + P_t^{\mathrm{WA}}, \\ P_t^{\mathrm{V}} = P_t^{\mathrm{VN}} + P_t^{\mathrm{VC}} + P_t^{\mathrm{VD}} + P_t^{\mathrm{VA}}, \\ P_t^{\mathrm{CSP,e}} = P_t^{\mathrm{CN}} + P_t^{\mathrm{CC}} + P_t^{\mathrm{CD}}, \end{cases} \tag{13}$$

where P_t^{W} and P_t^{V} are the predicted output power of WT and PV at time t, respectively; P_t^{WC}, P_t^{VC}, and P_t^{CC} are the energy consumption of carbon capture provided by WT, PV, and CSP station at time t, respectively; P_t^{WD}, P_t^{VD}, and P_t^{CD} are the energy consumption of flue gas treatment provided by WT, PV, and CSP station at time t, respectively; and P_t^{WN}, P_t^{VN}, and P_t^{CN} are the net output of power generation (on-grid power) provided by WT, PV, and CSP station at time t, respectively.

Carbon utilization refers to sending captured CO_2 into P2G to participate in the synthesis of CH_4 as its raw material. This process can decrease the carbon storage cost and increase the operating flexibility of P2G. The carbon utilization process satisfies the following relations:

$$Q_t^{\mathrm{CO_2,P2G}} = \left(1 - \eta_{\mathrm{CO_2}}\right) E_t^{\mathrm{CO_2}} - Q_t^{\mathrm{FC}}, \tag{14}$$

where $\eta_{\mathrm{CO_2}}$ is the heat loss rate of CO_2; Q_t^{FC} is the stored CO_2 at time t.

3.3.3 Carbon trading mechanism

The carbon trading mechanism regards the carbon emission as a commodity and controls it through the trading of carbon emission rights between producers and markets. If the actual carbon emission is lower than the allocated, the surplus quotas can be sold to carbon trading markets. Otherwise, the corresponding quotas need to be purchased additionally (Wang X. et al., 2022).

1) Quota models of carbon emission

Carbon emission quota is the amount of emission allowance allocated by the regulatory authorities to each carbon source within the RIES, which varies according to the type of equipment (Chen et al., 2021). In this paper, there are two main carbon sources, namely, coal-fired power plants in the power grid (superior purchasing power) and gas-fired units of the system (GT and GB). Then, the quota models of carbon emission can be expressed as follows:

$$\begin{cases} E_{\mathrm{q}}^{\mathrm{RIES}} = E_{\mathrm{q}}^{\mathrm{GRID}} + E_{\mathrm{q}}^{\mathrm{GT}} + E_{\mathrm{q}}^{\mathrm{GB}}, \\ E_{\mathrm{q}}^{\mathrm{GRID}} = \mu_{\mathrm{e}} \sum_{t=1}^{T} P_t^{\mathrm{GRID}}, \\ E_{\mathrm{q}}^{\mathrm{GT}} = \mu_{\mathrm{g}} \sum_{t=1}^{T} P_t^{\mathrm{GT}}, \\ E_{\mathrm{q}}^{\mathrm{GB}} = \mu_{\mathrm{g}} \sum_{t=1}^{T} P_t^{\mathrm{GB,h}}, \end{cases} \tag{15}$$

where $E_{\mathrm{q}}^{\mathrm{GRID}}$, $E_{\mathrm{q}}^{\mathrm{GT}}$, and $E_{\mathrm{q}}^{\mathrm{GB}}$ are carbon emission quotas of power purchase, GT, and GB, respectively; μ_{e} and μ_{g} are the baseline credits for carbon emission per unit of power consumption and per unit of gas consumption for coal-fired and gas-fired units, respectively; P_t^{GRID} is the purchased power at time t; and T is the operating cycle, which values as 24h.

2) Practical models of carbon emission

Since the CCS can absorb CO_2, the actual model of carbon emission after considering it can be expressed as follows:

$$\begin{cases} E_{\mathrm{a}}^{\mathrm{RIES}} = E_{\mathrm{a}}^{\mathrm{GRID}} + E_{\mathrm{a}}^{\mathrm{GT}} + E_{\mathrm{a}}^{\mathrm{GB}} - E_{\mathrm{a}}^{\mathrm{CO_2}}, \\ E_{\mathrm{a}}^{\mathrm{GRID}} = \delta_{\mathrm{e}} \sum_{t=1}^{T} P_t^{\mathrm{GRID}}, \\ E_{\mathrm{a}}^{\mathrm{GT}} = \delta_{\mathrm{g}} \sum_{t=1}^{T} P_t^{\mathrm{GT}}, \\ E_{\mathrm{a}}^{\mathrm{GB}} = \delta_{\mathrm{g}} \sum_{t=1}^{T} P_t^{\mathrm{GB,h}}, \\ E_a^{\mathrm{CO_2}} = \sum_{t=1}^{T} E_t^{\mathrm{CO_2}}, \end{cases} \tag{16}$$

where E_a^{GRID}, E_a^{GT}, and E_a^{GB} are the practical carbon emission of power purchase, GT, and GB, respectively; $E_a^{CO_2}$ is the total amount of CO_2 that is captured; and δ_e and δ_g are the carbon emission intensity of coal-fired units and gas-fired units, respectively.

3) Ladder-type carbon trading

After getting the quotas of carbon emission and the practical model through the process previously, the transaction volume of carbon emission rights that participate in trading markets can be formulated as follows:

$$E_r^{RIES} = E_a^{RIES} - E_q^{RIES}. \tag{17}$$

Compared with the traditional carbon trading mechanism, the ladder-type carbon trading mechanism has more strict controls over carbon emissions. The principle is dividing carbon emissions into multiple intervals through the stepped pricing method. With the increase in carbon emissions, the transaction cost within the corresponding interval will increase (Zhang et al., 2016; Fu et al., 2022; Li et al., 2022). Accordingly, the cost of ladder-type carbon trading can be expressed as follows:

$$F_{CO_2} = \begin{cases} B_{CO_2} E_r^{RIES} & E_r^{RIES} \le l, \\ B_{CO_2}\left[E_r^{RIES}\left(1+\gamma_{CO_2}\right) - l\gamma_{CO_2}\right] & l \le E_r^{RIES} \le 2l, \\ B_{CO_2}\left[E_r^{RIES}\left(1+2\gamma_{CO_2}\right) - 3l\gamma_{CO_2}\right] & 2l \le E_r^{RIES} \le 3l \\ B_{CO_2}\left[E_r^{RIES}\left(1+3\gamma_{CO_2}\right) - 6l\gamma_{CO_2}\right] & 3l \le E_r^{RIES} \le 4l, \\ B_{CO_2}\left[E_r^{RIES}\left(1+4\gamma_{CO_2}\right) - 10l\gamma_{CO_2}\right] & E_r^{RIES} \ge 4l, \end{cases} \tag{18}$$

where B_{CO_2} is the benchmark price of the carbon trading; γ_{CO_2} is the growth rate of the carbon tax price; and l is the interval length of carbon emission.

3.4 Integrated demand response of flexible loads considering compensation cost

IDR refers to the process in which users reasonably adjust energy-use modes and participate in energy interaction according to different energy prices or incentive mechanisms to optimize the load curves (Shao et al., 2021). Therefore, it is necessary to classify the loads first in the analysis of such problems. In addition to uncontrollable loads (invariable loads) in previous studies, the loads are divided into variable loads such as transferable loads, curtailable loads, and fungible loads in this paper. In addition, compared to conventional studies that only consider electrical and heat loads, this paper incorporates all types of loads involving electricity, heat, cooling, and gas into the IDR. Then, according to the characteristics of the variable loads mentioned previously, the process of IDR involved in this paper is able to divide it into the price type and the substitutable type.

3.4.1 Price-based demand response

Since different types of loads have variant sensitivities to the same price signal, this paper divides the loads involved in the price-based demand response into curtailable loads (CLs) and transferable loads (TLs) and then builds the models of them in turn.

1) Properties and modeling for CL

CL uses the price-demand elasticity matrix to describe its characteristics. In allusion to the t line and the j column element $e_{t,j}$ in the price-based elastic matrix $E(t, j)$, the elastic coefficient of the load at time t to energy price at time j is defined as follows:

$$e_{t,j} = \frac{\Delta L_{L,t}^i / L_{L,t}^i}{\Delta \kappa_j / \kappa_j^0}, \tag{19}$$

where $\Delta L_{L,t}^i$ and $L_{L,t}^i$ are the variable amount and initial amount of the load for class i participating in the price-based demand response at time t, respectively; $\Delta\kappa_j$ and κ_j^0 are the variable amounts of energy prices and initial energy prices at time j after the IDR, respectively.

Then, the CL variation of class i at time t after the IDR can be presented as follows:

$$\Delta L_{CL,t}^i = L_{CL,t}^{i0}\left[\sum_{j=1}^{T} E_{CL}^i(t,j)\frac{\kappa_j - \kappa_j^0}{\kappa_j^0}\right], \tag{20}$$

where $L_{CL,t}^{i0}$ is the amount of initial CL for class i at time t; $E_{CL}^i(t, j)$ is the price-demand elastic matrix of CL for class i; and κ_j is the corresponding load energy price of class i at time j.

2) Properties and modeling for TL

TL can realize flexible controls of working hours and power at different periods under the total load unchanged premise according to the energy prices of users' own demand response. Taking time-sharing energy prices and incentive measures as signals, users can be guided to transfer the peak loads to the normal or trough period (Azzam et al., 2023). Similarly, after expressing the characteristics of IDR in the price-demand elasticity matrix, the TL variation in class i at time t can be formulated as follows:

$$\Delta L_{TL,t}^i = L_{TL,t}^{i0}\left[\sum_{j=1}^{T} E_{TL}^i(t,j)\frac{\kappa_j - \kappa_j^0}{\kappa_j^0}\right], \tag{21}$$

where $L_{TL,t}^{i0}$ is the amount of initial TL for class i at time t; $E_{TL}^i(t, j)$ is the price-demand elastic matrix of TL for class i.

3.4.2 Substitution-type demand response

For a certain type of the heat load that can be directly supplied by heat or electricity (electricity to heat), the electrical energy can be consumed in periods of low electricity prices, while the heat energy can be directly consumed in periods of high electricity prices to meet different needs so as to realize the mutual substitution between the electrical and heat energy. The fungible load (FL) model can be expressed as follows:

$$\begin{cases} \Delta L_{FL,t}^e = \varepsilon_{e,h} \cdot \Delta L_{FL,t}^h, \\ \varepsilon_{e,h} = \dfrac{\nu_e \phi_e}{\nu_h \phi_h}, \end{cases} \tag{22}$$

where $\Delta L_{FL,t}^e$ and $\Delta L_{FL,t}^h$ are the fungible electricity load and heat load, respectively; $\varepsilon_{e,h}$ is the electric-heating substitution coefficient, which varies with the time; ν_e and ν_h are the unit calorific values of electrical energy and heat energy, respectively; and ϕ_e and ϕ_h are the energy utilization rates of electricity and heat, respectively.

Through the IDR process mentioned previously, the following conditions of load balance can be obtained as follows:

$$\begin{cases} L_{\mathrm{e}}^{\mathrm{DR}} = L_{\mathrm{e}} + \Delta L_{\mathrm{CL},t}^{\mathrm{e}} + \Delta L_{\mathrm{TL},t}^{\mathrm{e}} + \Delta L_{\mathrm{FL},t}^{\mathrm{e}}, \\ L_{\mathrm{h}}^{\mathrm{DR}} = L_{\mathrm{h}} + \Delta L_{\mathrm{CL},t}^{\mathrm{h}} + \Delta L_{\mathrm{TL},t}^{\mathrm{h}} + \Delta L_{\mathrm{FL},t}^{\mathrm{h}}, \\ L_{\mathrm{c}}^{\mathrm{DR}} = L_{\mathrm{c}} + \Delta L_{\mathrm{CL},t}^{\mathrm{c}} + \Delta L_{\mathrm{TL},t}^{\mathrm{c}}, \\ L_{\mathrm{g}}^{\mathrm{DR}} = L_{\mathrm{g}} + \Delta L_{\mathrm{CL},t}^{\mathrm{g}} + \Delta L_{\mathrm{TL},t}^{\mathrm{g}}, \end{cases} \tag{23}$$

where L_{e}, L_{h}, and L_{c} are the initial loads of electricity, heat, and cooling, respectively; L_{g} is the amount of natural gas required by the initial gas load; $L_{\mathrm{e}}^{\mathrm{DR}}$, $L_{\mathrm{h}}^{\mathrm{DR}}$, and $L_{\mathrm{c}}^{\mathrm{DR}}$ are the loads of electricity, heat, and cooling after participating in the IDR, respectively; and $L_{\mathrm{g}}^{\mathrm{DR}}$ is the amount of natural gas required by the gas load after participating in the IDR. Then, the load compensation cost can be calculated as follows:

$$\begin{cases} F_{\mathrm{cut}} = \sum_{t=1}^{T} \left(c_{\mathrm{cut}}^{\mathrm{e}} \cdot \Delta L_{\mathrm{CL},t}^{\mathrm{e}} + c_{\mathrm{cut}}^{\mathrm{h}} \cdot \Delta L_{\mathrm{CL},t}^{\mathrm{h}} + c_{\mathrm{cut}}^{\mathrm{c}} \cdot \Delta L_{\mathrm{CL},t}^{\mathrm{c}} + c_{\mathrm{cut}}^{\mathrm{g}} \cdot \Delta L_{\mathrm{CL},t}^{\mathrm{g}} \right), \\ F_{\mathrm{trans}} = \sum_{t=1}^{T} \left(c_{\mathrm{trans}}^{\mathrm{e}} \cdot \Delta L_{\mathrm{TL},t}^{\mathrm{e}} + c_{\mathrm{trans}}^{\mathrm{h}} \cdot \Delta L_{\mathrm{TL},t}^{\mathrm{h}} + c_{\mathrm{trans}}^{\mathrm{c}} \cdot \Delta L_{\mathrm{TL},t}^{\mathrm{c}} + c_{\mathrm{trans}}^{\mathrm{g}} \cdot \Delta L_{\mathrm{TL},t}^{\mathrm{g}} \right), \\ F_{\mathrm{sub}} = \sum_{t=1}^{T} \left(c_{\mathrm{sub}}^{\mathrm{e}} \cdot \Delta L_{\mathrm{FL},t}^{\mathrm{e}} + c_{\mathrm{sub}}^{\mathrm{h}} \cdot \Delta L_{\mathrm{FL},t}^{\mathrm{h}} \right), \end{cases} \tag{24}$$

where F_{cut}, F_{trans}, and F_{sub} are the compensation costs that can be reduced, transferred, and replaced, respectively; $c_{\mathrm{cut}}^{\mathrm{e}}$, $c_{\mathrm{cut}}^{\mathrm{h}}$, $c_{\mathrm{cut}}^{\mathrm{c}}$, and $c_{\mathrm{cut}}^{\mathrm{g}}$ are the compensation prices of electrical, heat, cool, and gas loads that can be reduced per unit of power, respectively; $c_{\mathrm{trans}}^{\mathrm{e}}$, $c_{\mathrm{trans}}^{\mathrm{h}}$, $c_{\mathrm{trans}}^{\mathrm{c}}$, and $c_{\mathrm{trans}}^{\mathrm{g}}$ are the compensation prices of electrical, heat, cool, and gas loads that can be transferred per unit of power, respectively; and $c_{\mathrm{sub}}^{\mathrm{e}}$ and $c_{\mathrm{sub}}^{\mathrm{h}}$ are the compensation prices of electrical and heat load that can be replaced per unit of power, respectively.

4 Double-layer optimization model of the RIES

Based on the RIES with the participation of CSP stations as shown in Figure 1, this paper establishes a double-layer optimization model that considers the whole process of carbon emission and the IDR to demonstrate the innovations. The upper layer randomly generates the planned capacities of the devices and transmits them to the lower layer. The lower layer constrains the output of the devices and transmits the results back to the upper layer. Finally, the upper layer revises the capacity configuration of each device again. The iterative process between the upper layer and the lower layer leads to the most optimal configuration and the lowest annual operating cost of the RIES.

4.1 Models of upper programming

The upper model aims at minimizing the annual planning cost and the annual net pollutant emission of the RIES, and the decision variables are the installed capacities of different devices. The mathematical formulas are shown as follows:

$$\begin{cases} \min F_{\mathrm{pc}} = F_{\mathrm{inv}} + F_{\mathrm{rc}} \\ \min E_{\mathrm{env}} = 365 \sum_{s \in \{sum,win,tra\}} \theta_s \left(E_{\mathrm{r}}^{\mathrm{SO_2}} + E_{\mathrm{r}}^{\mathrm{NO_x}} + E_{\mathrm{r}}^{\mathrm{RIES}} \right) \end{cases} \tag{25}$$

where F_{pc} and E_{env} are the annual planning cost and the annual net emission of various pollutants during the operating life of the RIES, respectively; F_{inv} and F_{rc} are the annual investment cost and the annual operating cost, respectively; and $E_{\mathrm{r}}^{\mathrm{SO_2}}$ and $E_{\mathrm{r}}^{\mathrm{NO_x}}$ are the net emissions of SO_2 and NO_x, respectively.

The annual operating cost F_{rc} is introduced separately as the objective function of the lower model, while other variables can be expressed as follows:

$$\begin{cases} F_{\mathrm{inv}} = \sum_{k} c_k S_{\max}^{k} \\ E_{\mathrm{r}}^{\mathrm{SO_2}} = \xi_{\mathrm{e}}^{\mathrm{S}} \sum_{t=1}^{T} P_t^{\mathrm{GRID}} \\ E_{\mathrm{r}}^{\mathrm{NO_x}} = \xi_{\mathrm{e}}^{\mathrm{N}} \sum_{t=1}^{T} P_t^{\mathrm{GRID}} \end{cases} \tag{26}$$

where k indicates different types of the devices; c_k is the installed investment cost of per unit capacity for device k; $S_{\max}^{k}$ is the installed capacity of device k; and $\xi_{\mathrm{e}}^{\mathrm{S}}$ and $\xi_{\mathrm{e}}^{\mathrm{N}}$ are the SO_2 and the NO_x emission intensity of coal-fired units in the power grid, respectively.

4.2 Models of lower operating

The lower layer intends to minimize the annual operating cost of the RIES, and the decision variable is the output of each device. The mathematical model is expressed in the following equation:

$$\begin{cases} \min F_{\mathrm{rc}} = 365 \sum_{m=1}^{N} \frac{m}{(1+\mathrm{r})^m} \cdot \sum_{s \in \{sum,win,tra\}} \theta_s \\ \left(F_{\mathrm{e}} + F_{\mathrm{gas}} + F_{\mathrm{oc}} + F_{\mathrm{CO_2}} + F_{\mathrm{dr}} + F_{\mathrm{fc}} \right), \\ F_{\mathrm{e}} = \sum_{t=1}^{T} C_t^{\mathrm{GRID}} P_t^{\mathrm{GRID}}, \\ F_{\mathrm{gas}} = \sum_{t=1}^{T} C_t^{\mathrm{GAS}} Q_t^{\mathrm{GAS}}, \\ F_{\mathrm{oc}} = c_{\mathrm{DP}}^{k} \sum_{t=1}^{T} P_t^{k}, \\ F_{\mathrm{dr}} = F_{\mathrm{cut}} + F_{\mathrm{trans}} + F_{\mathrm{sub}}, \\ F_{\mathrm{fc}} = \sum_{t=1}^{T} k_{\mathrm{fc}} Q_t^{\mathrm{FC}}. \end{cases} \tag{27}$$

This paper adopts the ladder-type carbon trading method, and the corresponding cost $F_{\mathrm{CO_2}}$ is shown in Eq. 18.

Here, N is the planning year; r is the discounted rate; and θ_s is the proportion of season s in the year, and three typical seasons involving summer (sum), winter (win), and transitional season (tra) are considered in this paper; F_{e}, F_{gas}, F_{oc}, F_{dr}, and F_{fc} are the costs of electrical purchase, gas purchase, operation or maintenance for each device, IDR compensation, and carbon storage in the RIES, respectively; C_t^{GRID} and C_t^{GAS} are the unit price of electrical purchase and gas purchase at time t, respectively; Q_t^{GAS} is the flow of gas purchase at time t; c_{DP}^{k} is the unit maintenance cost of device k; P_t^{k} is the output of device k at time t; and k_{fc} is the unit carbon storage price.

4.3 Constraint conditions

4.3.1 Constraints of the CSP station

$$\begin{cases} 0 \le \mu_t^{\mathrm{TS,c}} + \mu_t^{\mathrm{TS,f}} \le 1, \\ \mu_t^{\mathrm{TS,c}} \cdot 0.1 S_{\max}^{\mathrm{HQ}} \le P_t^{\mathrm{TS,c}} \le \mu_t^{\mathrm{TS,c}} \cdot S_{\max}^{\mathrm{HQ}}, \\ \mu_t^{\mathrm{TS,f}} \cdot 0.1 S_{\max}^{\mathrm{HQ}} \le P_t^{\mathrm{TS,f}} \le \mu_t^{\mathrm{TS,f}} \cdot S_{\max}^{\mathrm{HQ}}, \\ P_t^{\mathrm{TS,c}} \cdot P_t^{\mathrm{TS,f}} = 0, \\ 0.1 S_{\max}^{\mathrm{HQ}} \le S_t^{\mathrm{HQ}} \le S_{\max}^{\mathrm{HQ}}, \\ S_0^{\mathrm{HQ}} = S_{24}^{\mathrm{HQ}}, \\ 0 \le P_t^{\mathrm{CSP,e}} \le P_{\max}^{\mathrm{CSP,e}}, \\ \left| P_t^{\mathrm{CSP,e}} - P_{t-1}^{\mathrm{CSP,e}} \right| \le \Delta P^{\mathrm{CSP,e}}, \end{cases} \tag{28}$$

where $\mu_t^{\mathrm{TS,c}}$ and $\mu_t^{\mathrm{TS,f}}$ are variables of 0 − 1, which represent the charging and releasing state of the heat storage tank at time t, respectively; $S_{\max}^{\mathrm{HQ}}$ is the capacity of the heat storage tank; S_0^{HQ} and S_{24}^{HQ} are the starting and ending values of heat storage during the day, respectively; and $P_{\max}^{\mathrm{CSP,e}}$ and $\Delta P^{\mathrm{CSP,e}}$ are the upper power limit and the climbing rate of the CSP station, respectively.

4.3.2 Constraints of the CCS

$$\begin{cases} E_{\min}^{\mathrm{CO_2}} \le E_t^{\mathrm{CO_2}} \le E_{\max}^{\mathrm{CO_2}}, \\ Q_{\min}^{\mathrm{DEAL}} \le Q_t^{\mathrm{DEAL}} \le Q_{\max}^{\mathrm{DEAL}}, \\ 0 \le Q_t^{\mathrm{CS}} \le Q_{\max}^{\mathrm{CS}}, \\ 0 \le Q_t^{\mathrm{ST}} \le Q_{\max}^{\mathrm{ST}}, \\ 0 \le Q_t^{\mathrm{IN}} \le Q_{\max}^{\mathrm{IN}}, \end{cases} \tag{29}$$

where $E_{\max}^{\mathrm{CO_2}}$ and $E_{\min}^{\mathrm{CO_2}}$ are the upper and lower limits of CO_2 captured by the CCS, respectively; $Q_{\max}^{\mathrm{DEAL}}$ and $Q_{\min}^{\mathrm{DEAL}}$ are the upper and lower limits of the storage in the flue gas storage tank, respectively; $Q_{\max}^{\mathrm{CS}}$ and $Q_{\max}^{\mathrm{ST}}$ are the upper limits of the flue gas treatment provided by the carbon source unit and flue gas storage tank, respectively; and $Q_{\max}^{\mathrm{IN}}$ is the upper limit of the flue gas that flows into the flue gas storage tank.

4.3.3 Constraints of P2G

$$0 \le P_t^{\mathrm{P2G}} \le P_{\max}^{\mathrm{P2G}}, \tag{30}$$

where $P_{\max}^{\mathrm{P2G}}$ is the maximum energy consumption of P2G.

4.3.4 Constraints of new energy units and purchasing energy

$$\begin{cases} 0 \le P_t^{\mathrm{WN}} \le P_t^{\mathrm{W}}, \\ 0 \le P_t^{\mathrm{VN}} \le P_t^{\mathrm{V}}, \\ 0 \le P_t^{\mathrm{CN}} \le P_t^{\mathrm{CSP,e}}, \\ 0 \le P_t^{\mathrm{GRID}} \le P_{\max}^{\mathrm{GRID}}, \\ 0 \le Q_t^{\mathrm{GAS}} \le Q_{\max}^{\mathrm{GAS}}, \end{cases} \tag{31}$$

where $P_{\max}^{\mathrm{GRID}}$ and $Q_{\max}^{\mathrm{GAS}}$ are the maximum purchased power and gas, respectively.

4.3.5 Constraints of electrical energy storage devices

$$\begin{cases} 0 \le \mu_t^{\mathrm{cha}} + \mu_t^{\mathrm{dis}} \le 1, \\ \mu_t^{\mathrm{cha}} \cdot 0.1 S_{\max}^{\mathrm{e}} \le P_t^{\mathrm{cha}} \le \mu_t^{\mathrm{cha}} \cdot S_{\max}^{\mathrm{e}}, \\ \mu_t^{\mathrm{dis}} \cdot 0.1 S_{\max}^{\mathrm{e}} \le P_t^{\mathrm{dis}} \le \mu_t^{\mathrm{dis}} \cdot S_{\max}^{\mathrm{e}}, \\ P_t^{\mathrm{cha}} \cdot P_t^{\mathrm{dis}} = 0, \\ S_t^{\mathrm{e}} = S_{t-1}^{\mathrm{e}} + \left(\eta_{\mathrm{e}}^{\mathrm{cha}} P_t^{\mathrm{cha}} - \dfrac{P_t^{\mathrm{dis}}}{\eta_{\mathrm{e}}^{\mathrm{dis}}} \right) \Delta t, \\ 0.1 S_{\max}^{\mathrm{e}} \le S_t^{\mathrm{e}} \le S_{\max}^{\mathrm{e}}, \\ S_0^{\mathrm{e}} = S_{24}^{\mathrm{e}}, \end{cases} \tag{32}$$

where μ_t^{cha} and μ_t^{dis} are variables of 0 − 1, which represent the charging and releasing state of the storage battery at time t, respectively; $S_{\max}^{\mathrm{e}}$ is the capacity of the storage battery; P_t^{cha} and P_t^{dis} refer to the charging and releasing power of the storage battery, respectively; S_t^{e} and S_{t-1}^{e} are the charge capacities of the storage battery at time t and time $t-1$, respectively; $\eta_{\mathrm{e}}^{\mathrm{cha}}$ and $\eta_{\mathrm{e}}^{\mathrm{dis}}$ are the charging and releasing efficiency of the storage battery, respectively; Δt is the unit operating period, which values as 1; and S_0^{e} and S_{24}^{e} are the starting and ending values of the storage battery during the day, respectively.

4.3.6 Constraints of other devices

$$\begin{cases} 0 \le P_t^k \le S_{\max}^k, \\ \left| P_t^k - P_{t-1}^k \right| \le \Delta P^k, \end{cases} \tag{33}$$

where $S_{\max}^k$ and ΔP^k are the capacity and climbing rate of device k, respectively.

4.3.7 Constraints of integrated demand response

1) Curtailable loads:

$$L_{\mathrm{CL,min}}^i \le \Delta L_{\mathrm{CL},t}^i \le L_{\mathrm{CL,max}}^i, \tag{34}$$

where $L_{\mathrm{CL,max}}^i$ and $L_{\mathrm{CL,min}}^i$ are the upper and lower limits of the actual reduction for CL i at time t, respectively.

2) Transferable loads:

$$\begin{cases} \sum_{t=1}^{T} \Delta L_{\mathrm{TL},t}^i = 0, \\ L_{\mathrm{TL,min}}^i \le \Delta L_{\mathrm{TL},t}^i \le L_{\mathrm{TL,max}}^i, \end{cases} \tag{35}$$

where $L_{\mathrm{TL,max}}^i$ and $L_{\mathrm{TL,min}}^i$ are the upper and lower limits of the actual transfer for TL i at time t, respectively.

3) Fungible loads:

$$\mathbf{0} \le \Delta \boldsymbol{L}_{\mathrm{FL},t}^{i} \le \boldsymbol{L}_{\mathrm{FL,max}}^{i}, \tag{36}$$

where $L_{\mathrm{FL,max}}^{i}$ is the maximum substitution power of FL i at time t.

4.3.8 Balance of the loads

1) Load balancing before participating in IDR:

$$\begin{cases} \boldsymbol{P}_t^{\mathrm{GRID}} + \boldsymbol{P}_t^{\mathrm{WN}} + \boldsymbol{P}_t^{\mathrm{VN}} + \boldsymbol{P}_t^{\mathrm{CN}} + \boldsymbol{P}_t^{\mathrm{GT,e}} + \boldsymbol{P}_t^{\mathrm{cha}} - \boldsymbol{P}_t^{\mathrm{e,EB}} - \boldsymbol{P}_t^{\mathrm{e,EC}} - \boldsymbol{P}_t^{\mathrm{dis}} = \boldsymbol{L}_{\mathrm{e}}, \\ \boldsymbol{P}_t^{\mathrm{EB,load}} + \boldsymbol{P}_t^{\mathrm{GB,h}} + \boldsymbol{P}_t^{\mathrm{WHB,h}} + \boldsymbol{P}_t^{\mathrm{HL}} - \boldsymbol{P}_t^{\mathrm{h,AC}} = \boldsymbol{L}_{\mathrm{h}}, \\ \boldsymbol{P}_t^{\mathrm{EC,c}} + \boldsymbol{P}_t^{\mathrm{AC,c}} = \boldsymbol{L}_{\mathrm{c}}, \\ \boldsymbol{Q}_t^{\mathrm{GAS}} + \boldsymbol{Q}_t^{\mathrm{P2G,CH_4}} - \boldsymbol{Q}_t^{\mathrm{GT}} - \boldsymbol{Q}_t^{\mathrm{GB}} = \boldsymbol{L}_{\mathrm{g}}. \end{cases} \tag{37}$$

2) Load balancing after participating in IDR:

$$\begin{cases} \boldsymbol{P}_t^{\mathrm{GRID}} + \boldsymbol{P}_t^{\mathrm{WN}} + \boldsymbol{P}_t^{\mathrm{VN}} + \boldsymbol{P}_t^{\mathrm{CN}} + \boldsymbol{P}_t^{\mathrm{GT,e}} + \boldsymbol{P}_t^{\mathrm{cha}} - \boldsymbol{P}_t^{\mathrm{e,EB}} - \boldsymbol{P}_t^{\mathrm{e,EC}} - \boldsymbol{P}_t^{\mathrm{dis}} = \boldsymbol{L}_{\mathrm{e}}^{\mathrm{DR}}, \\ \boldsymbol{P}_t^{\mathrm{EB,load}} + \boldsymbol{P}_t^{\mathrm{GB,h}} + \boldsymbol{P}_t^{\mathrm{WHB,h}} + \boldsymbol{P}_t^{\mathrm{HL}} - \boldsymbol{P}_t^{\mathrm{h,AC}} = \boldsymbol{L}_{\mathrm{h}}^{\mathrm{DR}}, \\ \boldsymbol{P}_t^{\mathrm{EC,c}} + \boldsymbol{P}_t^{\mathrm{AC,c}} = \boldsymbol{L}_{\mathrm{c}}^{\mathrm{DR}}, \\ \boldsymbol{Q}_t^{\mathrm{GAS}} + \boldsymbol{Q}_t^{\mathrm{P2G,CH_4}} - \boldsymbol{Q}_t^{\mathrm{GT}} - \boldsymbol{Q}_t^{\mathrm{GB}} = \boldsymbol{L}_{\mathrm{g}}^{\mathrm{DR}}. \end{cases} \tag{38}$$

4.4 Model solving

For the double-layer optimization model constructed previously, the improved NSGA-II is employed for the upper layer. As for the lower layer, nonlinear problems are transformed into linear problems according to the MILP method, and then, the Cplex solver is called for the corresponding calculation.

4.4.1 Multi-objective problems of the upper layer solved by the improved NSGA-II

This paper uses the NSGA-II for capacity configuration with different research objects and proposes an improved NSGA-II to compare with the conventional NSGA-II. The NSGA-II treats each sub-objective in a high-dimensional multi-objective optimization problem equally without introducing weights, which can avoid the influence of local optimal solutions on capacity configuration. The conventional NSGA-II is mainly composed of selection, crossover, mutation, and non-dominated sorting, among which the mutation process is usually realized by simulated binary mutation operators (SBMO) that leads to low population diversity and search efficiency. Therefore, this paper perfected the mutation process of the conventional algorithm by using adaptive mixed mutation operators. The main principle is to mix the simulated binary mutation operator and the normal distributed mutation operator (NDMO) in an adaptive way to determine the proportion of the two operators in different periods within the algorithm. The model is shown as follows:

$$\begin{cases} \boldsymbol{z}_{1,j} = \dfrac{\boldsymbol{k}_{\mathrm{Gens}} - \boldsymbol{k}_{\mathrm{Gen}}}{\mathbf{2} \cdot \boldsymbol{k}_{\mathrm{Gens}}} \left[(\mathbf{1} + \boldsymbol{\beta}) \boldsymbol{p}_{\mathbf{1},j} + (\mathbf{1} - \boldsymbol{\beta}) \boldsymbol{p}_{\mathbf{2},j} \right] + \dfrac{\boldsymbol{k}_{\mathrm{Gen}}}{\mathbf{2} \cdot \boldsymbol{k}_{\mathrm{Gens}}} \\ \left[(\mathbf{1} + |\boldsymbol{N}(\mathbf{0},\mathbf{1})|) \boldsymbol{p}_{\mathbf{1},j} + (\mathbf{1} - |\boldsymbol{N}(\mathbf{0},\mathbf{1})|) \boldsymbol{p}_{\mathbf{2},j} \right], \boldsymbol{\lambda} \le \mathbf{0.5}, \\ \boldsymbol{z}_{1,j} = \dfrac{\boldsymbol{k}_{\mathrm{Gens}} - \boldsymbol{k}_{\mathrm{Gen}}}{\mathbf{2} \cdot \boldsymbol{k}_{\mathrm{Gens}}} \left[(\mathbf{1} + \boldsymbol{\beta}) \boldsymbol{p}_{\mathbf{1},j} + (\mathbf{1} - \boldsymbol{\beta}) \boldsymbol{p}_{\mathbf{2},j} \right] + \dfrac{\boldsymbol{k}_{\mathrm{Gen}}}{\mathbf{2} \cdot \boldsymbol{k}_{\mathrm{Gens}}} \\ \left[(\mathbf{1} - |\boldsymbol{N}(\mathbf{0},\mathbf{1})|) \boldsymbol{p}_{\mathbf{1},j} + (\mathbf{1} - |\boldsymbol{N}(\mathbf{0},\mathbf{1})|) \boldsymbol{p}_{\mathbf{2},j} \right], \boldsymbol{\lambda} > \mathbf{0.5}, \\ \boldsymbol{z}_{2,j} = \dfrac{\boldsymbol{k}_{\mathrm{Gens}} - \boldsymbol{k}_{\mathrm{Gen}}}{\mathbf{2} \cdot \boldsymbol{k}_{\mathrm{Gens}}} \left[(\mathbf{1} - \boldsymbol{\beta}) \boldsymbol{p}_{\mathbf{1},j} + (\mathbf{1} + \boldsymbol{\beta}) \boldsymbol{p}_{\mathbf{2},j} \right] + \dfrac{\boldsymbol{k}_{\mathrm{Gen}}}{\mathbf{2} \cdot \boldsymbol{k}_{\mathrm{Gens}}} \\ \left[(\mathbf{1} + |\boldsymbol{N}(\mathbf{0},\mathbf{1})|) \boldsymbol{p}_{\mathbf{1},j} + (\mathbf{1} - |\boldsymbol{N}(\mathbf{0},\mathbf{1})|) \boldsymbol{p}_{\mathbf{2},j} \right], \boldsymbol{\lambda} \le \mathbf{0.5}, \\ \boldsymbol{z}_{2,j} = \dfrac{\boldsymbol{k}_{\mathrm{Gens}} - \boldsymbol{k}_{\mathrm{Gen}}}{\mathbf{2} \cdot \boldsymbol{k}_{\mathrm{Gens}}} \left[(\mathbf{1} - \boldsymbol{\beta}) \boldsymbol{p}_{\mathbf{1},j} + (\mathbf{1} + \boldsymbol{\beta}) \boldsymbol{p}_{\mathbf{2},j} \right] + \dfrac{\boldsymbol{k}_{\mathrm{Gen}}}{\mathbf{2} \cdot \boldsymbol{k}_{\mathrm{Gens}}} \\ \left[(\mathbf{1} - |\boldsymbol{N}(\mathbf{0},\mathbf{1})|) \boldsymbol{p}_{\mathbf{1},j} + (\mathbf{1} - |\boldsymbol{N}(\mathbf{0},\mathbf{1})|) \boldsymbol{p}_{\mathbf{2},j} \right], \boldsymbol{\lambda} > \mathbf{0.5}, \end{cases} \tag{39}$$

where $z_{1,j}$ and $z_{2,j}$ are the percentages of SBMO and NDMO, respectively; k_{Gen} and k_{Gens} are the number of the current population iterations and the maximum population iterations, respectively; β and $|N(0,1)|$ are random variables of simulated binary and normal distribution, respectively; $p_{1,j}$ and $p_{2,j}$ are the mutation probabilities of SBMO and NDMO, respectively; and λ is the period of mutation.

As can be known from the formula mentioned previously, in the early stages of the algorithm, the proportion of SBMO should be higher to expand the search limit. In addition, in the later stages of the algorithm, the proportion of NDMO should be higher to promote search accuracy. By matching the search range and the search accuracy, the accuracy of the calculations can be significantly improved.

4.4.2 Transformation and solution of the lower nonlinear model

There are some nonlinear terms in the lower layer that needed to be transformed. For instance, the nonlinear terms in the ladder-type carbon trading model are solved by introducing segmenting points and auxiliary variables. As for nonlinear terms within the constraints, the Big-M method is used to deal with them, and then, the original nonlinear constraints are equitably transformed into mixed integer linear constraints by introducing several 0–1 variables. After the aforementioned process, the nonlinear problems of the lower layer are transformed into linear problems, which can be solved by the Cplex solver. The specific MILP process is shown as follows:

1) Big-M method for nonlinear constraint problems

The method is introduced by taking two subproblems of the storage battery cannot charge or release at the same moment and the charging or releasing power constraint as examples. The conversion methods of other nonlinear constraints are similar and will not be described here.

The general mathematical expression that the storage battery cannot charge or release at the same moment can be written as follows:

$$\mathbf{0} \le \boldsymbol{P}_t^{\mathrm{cha}} \perp \boldsymbol{P}_t^{\mathrm{dis}} \ge \mathbf{0}, \tag{40}$$

where "$0 \le a \perp b \ge 0$"means $a \ge 0, b \ge 0$ and $ab = 0$.

By using the Big-M method and introducing $0-1$ variables, the aforementioned equation can be equivalently transformed into

$$\begin{cases} \mathbf{0} \le \boldsymbol{P}_t^{\mathrm{cha}} \le \mathbf{M} \cdot \boldsymbol{\mu}_t, \\ \mathbf{0} \le \boldsymbol{P}_t^{\mathrm{dis}} \le \mathbf{M} \cdot (\mathbf{1} - \boldsymbol{\mu}_t), \end{cases} \tag{41}$$

where μ_t is the binary variable of $0-1$; M is a large constant.

The general expression of charging or releasing power constraint can be presented as follows:

$$\begin{cases} \mathbf{0} \le \boldsymbol{P}_t^{\mathrm{cha}} \le \boldsymbol{P}_{\max} \boldsymbol{\mu}_t^{\mathrm{cha}}, \\ \mathbf{0} \le \boldsymbol{P}_t^{\mathrm{dis}} \le \boldsymbol{P}_{\max} \boldsymbol{\mu}_t^{\mathrm{dis}}, \\ \boldsymbol{\mu}_t^{\mathrm{cha}} + \boldsymbol{\mu}_t^{\mathrm{dis}} \le \mathbf{1}, \\ \boldsymbol{\mu}_t^{\mathrm{cha}} \in \{\mathbf{0}, \mathbf{1}\}, \boldsymbol{\mu}_t^{\mathrm{dis}} \in \{\mathbf{0}, \mathbf{1}\}, \end{cases} \tag{42}$$

where $P_{\max}$ is the maximum charging and releasing power of the storage battery.

According to the Big-M method, the aforementioned equation can be equivalently transformed into

$$\begin{cases} \mathbf{0} \le \boldsymbol{P}_t^{\mathrm{cha}} \le \boldsymbol{P}_{\max}, \\ \mathbf{0} \le \boldsymbol{P}_t^{\mathrm{cha}} \le \boldsymbol{\mu}_t^{\mathrm{cha}} \mathbf{M}, \\ \mathbf{0} \le \boldsymbol{P}_t^{\mathrm{dis}} \le \boldsymbol{P}_{\max}, \\ \mathbf{0} \le \boldsymbol{P}_t^{\mathrm{dis}} \le \boldsymbol{\mu}_t^{\mathrm{dis}} \mathbf{M}, \\ \boldsymbol{\mu}_t^{\mathrm{cha}} + \boldsymbol{\mu}_t^{\mathrm{dis}} \le \mathbf{1}, \\ \boldsymbol{\mu}_t^{\mathrm{cha}} \in \{\mathbf{0}, \mathbf{1}\}, \boldsymbol{\mu}_t^{\mathrm{dis}} \in \{\mathbf{0}, \mathbf{1}\}. \end{cases} \tag{43}$$

2) Linearization of the ladder-type carbon trading

The model of ladder-type carbon trading is detailed in Eq. 18 previously, and the concrete implementation of its linearization is shown as follows.

The aforementioned formula is a piecewise function of five sections, so six piecewise points $w_1, w_2, \cdots, w_6$, six continuous auxiliary variables $u_1, u_2, \cdots, u_6$, and five binary auxiliary variables $v_1, v_2, \cdots, v_5$ are added to satisfy the following expression:

$$\begin{cases} \boldsymbol{u}_1 + \boldsymbol{u}_2 + \cdots + \boldsymbol{u}_6 = \mathbf{1}, \\ \boldsymbol{v}_1 + \boldsymbol{v}_2 + \cdots + \boldsymbol{v}_5 = \mathbf{1}, \\ \boldsymbol{u}_1 \ge \mathbf{0}, \boldsymbol{u}_2 \ge \mathbf{0}, \cdots, \boldsymbol{u}_6 \ge \mathbf{0}, \\ \boldsymbol{u}_1 \le \boldsymbol{v}_1, \boldsymbol{u}_2 \le \boldsymbol{v}_1 + \boldsymbol{v}_2, \boldsymbol{u}_3 \le \boldsymbol{v}_2 + \boldsymbol{v}_3, \\ \boldsymbol{u}_4 \le \boldsymbol{v}_3 + \boldsymbol{v}_4, \boldsymbol{u}_5 \le \boldsymbol{v}_4 + \boldsymbol{v}_5, \boldsymbol{u}_6 \le \boldsymbol{v}_5. \end{cases} \tag{44}$$

Then, the aforementioned equations can be transformed into the following linear expression:

$$\begin{cases} \boldsymbol{E}_{\mathrm{r}}^{\mathrm{RIES}} = \sum_{n=1}^{6} \boldsymbol{u}_n \boldsymbol{w}_n, \\ \boldsymbol{F}_{\mathrm{CO_2}} = \sum_{n=1}^{6} \boldsymbol{u}_n \boldsymbol{F}_{\mathrm{CO_2}}(\boldsymbol{w}_n). \end{cases} \tag{45}$$

Taking all the previous factors into consideration, the problems of MILP that are covered in this paper can be finally converted as follows:

$$\begin{cases} \min \boldsymbol{cx} \\ \mathrm{s.t.}\ \boldsymbol{Ax} \begin{Bmatrix} \ge \\ = \\ \le \end{Bmatrix} \boldsymbol{b}, \\ \boldsymbol{x}_{\min} \le \boldsymbol{x}_p \le \boldsymbol{x}_{\max}\ \boldsymbol{p} \in \mathbf{I}, \\ \boldsymbol{x}_q \in \{\mathbf{0}, \mathbf{1}\}\ \boldsymbol{q} \in \mathbf{J}, \end{cases} \tag{46}$$

where cx is the objective function, which stands for the annual operating cost of the RIES; A and b are the coefficient matrix and its corresponding value of subfunctions, respectively; x_p is the continuous variable, which represents the upper and lower limits of constraint conditions; and x_q is the integer variable, which values as 0 or 1.

4.4.3 Solving procedure

Combined with the double-layer model, the solving procedure in this paper can be described as follows:

1) We input the efficiency and the unit cost of each device, as well as the related load data, forecast output power of WT and PV, time-of-use electrical price and gas price, etc.
2) We initialize the improved NSGA-II. The basic parameters of the algorithm in the upper programming model should be reasonably set. In this paper, the population number is 50, and the maximum number of iterations is 500. Then initial values are assigned to the decision variables and the number of iterations to generate a random initial population and start the iteration process.
3) Based on the two optimization objectives of each population, the fitness (objective function value) can be calculated, respectively, and the corresponding capacity configuration of the device is substituted into the lower operating model as the constraint condition of running for each device.
4) The MILP method transforms the nonlinear model into a linear one in the lower layer, and the Cplex solver is called to calculate for it. Then, the lower layer returns the calculation results of the whole carbon emission process and the output power of the devices under IDR to the upper layer as the constraints.
5) According to the constraints returned by the lower model, the upper model completes the non-dominated sorting process and calculates the crowding degree of the objective functions.
6) The adaptive mixed mutation operators are used to complete the mutation process of the NSGA-II and combine it with the crossover process to merge the populations. Then, the non-dominated sorting process and the calculation of the crowding degree are performed again to decrease the error.
7) The elite retention strategy is introduced to generate new populations and update their positions through the tournament selection mechanism after the competitive process is completed.
8) We determine whether the termination condition is just satisfied. If the current number of iterations does not reach the maximum one, we skip back to step (3) to continue iterating to continuously improve the accuracy of the calculation. Otherwise, the configuration capacity and the planned operation scheme of each device can be output.

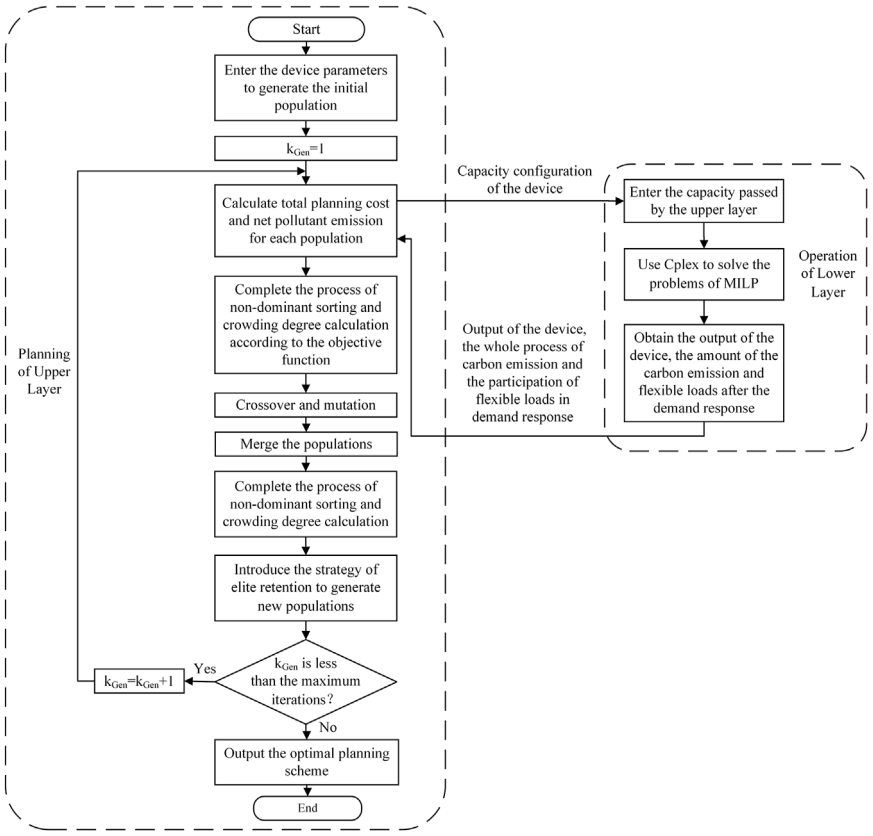

FIGURE 4
Flow chart of solving the double-layer optimization model based on the improved NSGA-II and MILP method.

The specific solving process is presented in Figure 4.

5 Example analysis

5.1 Comparative analysis under different cases

For further study impacts of the whole carbon emission process and the IDR on the operation and capacity configuration in the system, this paper makes some improvements on the example shown in the work of Wei et al. (2022) and Zeng et al. (2023), and the following four cases are built for comparative analysis:

Case I: The whole process of carbon emission and the IDR involving flexible loads are not considered.

Case II: The whole process of carbon emission is not considered, and the IDR involving flexible loads is considered.

Case III: The whole process of carbon emission is considered, and the IDR involving flexible loads is not considered.

Case IV: The whole process of carbon emission and the IDR involving flexible loads are both considered.

According to the four cases constructed previously, the outcome is enumerated in Table 1.

As shown in Table 1, compared with case I, the costs of carbon trading and annual operating in case III are reduced by 81.61% and 2.84%, respectively. This is because case III considers the whole process of carbon emission and sends the captured CO_2 into P2G for carbon utilization, which effectively reduces the net emission of CO_2. Moreover, introducing the ladder-type carbon trading mechanism makes the initial carbon quotas offset part of the carbon trading cost, thus reducing the annual operating cost. In addition, compared with case I, the cost of purchasing electricity and gas in case II is reduced by 73.43% and 16.47%, respectively. This is because the process of IDR can significantly cut down the peak-time flexible loads and scale up the valley-time flexible loads, especially the change in the electrical load, which allows the energy purchasing method to be more economical and selective. Compared with case III, the cost of carbon storage in case IV is lower. This is because the electrical load is decreased during peak periods after considering the IDR, which leads to the output power reduction of new energy units. In addition, the reduced part is converted to abandoned wind and light, which increases the amount of CO_2 consumed by P2G. Compared with case II, the compensatory cost of IDR in case IV is slightly lower. This is because the peak-to-valley differences of the electrical load are reduced by increasing the on-grid power of new energy units under the combined operation demand, which decreases the compensatory cost of IDR. In addition, the annual operating cost, electricity and gas purchasing cost, device operation and maintenance cost, and carbon trading cost in case IV are all smaller than those in case III, because considering the IDR in the whole process of carbon emission can transfer parts of flexible loads in high-price periods to low-price periods and lower their energy consumption. Moreover, the response process of the mutual substitution involving electricity,

TABLE 1 Cost results of comparative cases within the year (unit: ten thousand Yuan/year).

Case	Annual operating cost	Electrical purchasing	Gas purchasing	Device operation and maintenance cost	Carbon trading cost	Carbon storage cost	IDR compensatory
		Cost	Cost				Cost
I	1371.31	310.57	685.34	247.80	127.60	0	0
II	1359.05	82.51	572.44	256.37	141.63	0	306.10
III	1332.35	267.21	679.84	253.59	23.46	108.25	0
IV	1326.79	107.94	587.56	248.74	23.20	87.26	272.09

TABLE 2 Relevant parameters of test functions and the calculation results.

Test function	Dimension	Search range	Global optimal value	Calculation result	Conventional NSGA-II	Improved NSGA-II
Sphere	30	[−30,30]	0	SD	990.3178	0.7183
				AF	3196.4603	26.5767
				OV	1663.2302	25.4100
				WV	5203.9448	27.9232
Rastrigrin	30	[−1.28,1.28]	0	SD	0.0140	0.0006
				AF	0.0533	0.0013
				OV	0.0334	0.0002
				WV	0.0820	0.0026

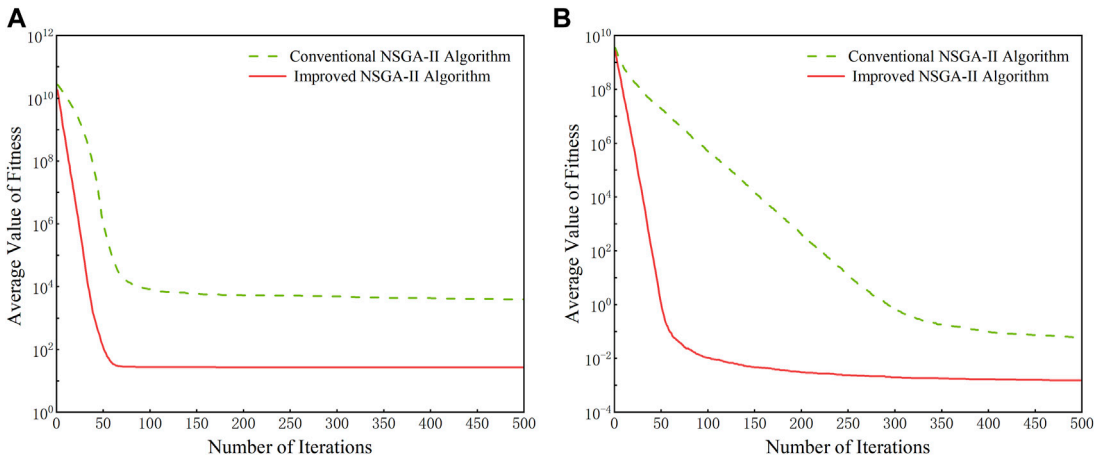

FIGURE 5
Average convergence curve of the test. **(A)** Results of the function Sphere, and **(B)** results of the function Rastrigrin.

heat, and other energy sources also significantly reduces the energy purchasing cost, thus making the operating modes more reasonable, and the economy and the environmental protection tend to be more coordinated in the system.

In addition, compared to case IV, cases I, II, and III have the lowest cost for their respective parts, but the other costs are at a higher level and the overall performance is poor. Case IV has generally lower costs for each subcomponent and has the best overall performance with annual operating cost improvement rates of 3.25%, 2.37%, and 0.42%.

Meanwhile, in an effort to validate the availability and the superiority of the algorithm that is proposed in this paper, quantitative analysis is added on the basis of qualitative analysis to compare the improved NSGA-II with the conventional one. Assuming that the number of populations is 50, the maximum number of iterations is 500, and running each standard test function

TABLE 3 Configuration results of different algorithms.

Capacity	Conventional NSGA-II	Improved NSGA-II
WT/kW	4,998	3857
PV/kW	2,416	1,586
CSP/kW	1805	1,282
EB/kW	624	515
EC/kW	301	426
GT/kW	1,650	1,449
GB/kW	562	601
AC/kW	298	283
P2G/kW	473	354
WHB/kW	957	938
SB/kW	800	445
Annual planning cost/(¥)	35,890,772	31,853,419
Annual net pollutant emission/(kg)	3,417,055	2,943,648

TABLE 4 Main parameters of various types of the devices.

Variable	Value	Variable	Value	Variable	Value /(¥$(kW)^{-1}$)	Variable	Value /(¥$(\mathbf{kW})^{-1}$)
$\eta_{GT,e}$	0.50	η_{P2G}	0.60	c_{WT}	1000	c_{DP}^{WT}	0.10
$\eta_{GT,h}$	0.45	η_e^{cha}	0.95	c_{PV}	1000	c_{DP}^{PV}	0.10
$\eta_{GB,h}$	0.95	η_e^{dis}	0.90	c_{CSP}	1500	c_{DP}^{CSP}	0.38
$\eta_{EB,h}$	0.80	λ_{DEAL}	0.513	c_{EB}	3500	c_{DP}^{EB}	0.10
$\eta_{EC,c}$	0.80	λ_{CO_2}	0.269	c_{EC}	3000	c_{DP}^{EC}	0.02
$\eta_{AC,c}$	0.80	$\mu_e/(kg\cdot(kW\cdot h)^{-1})$	0.76	c_{GT}	2000	c_{DP}^{GT}	0.13
$\eta_{WHB,h}$	0.60	$\mu_g/(kg\cdot(kW\cdot h)^{-1})$	0.52	c_{GB}	2500	c_{DP}^{GB}	0.008
ρ_h	0.03	$\delta_e/(kg\cdot(kW\cdot h)^{-1})$	15.96	c_{AC}	1500	c_{DP}^{AC}	0.10
η_d	0.45	$\delta_g/(kg\cdot(kW\cdot h)^{-1})$	15.45	c_{P2G}	5000	c_{DP}^{P2G}	0.075
η_f	0.03	$\xi_e^S/(kg\cdot(kW\cdot h)^{-1})$	0.0648	c_{WHB}	1000	c_{DP}^{WHB}	0.20
η_h	0.60	$\xi_e^N/(kg\cdot(kW\cdot h)^{-1})$	0.0288	c_{SB}	800	c_{DP}^{SB}	0.20

30 times, the relevant parameters of test functions (Tao et al., 2019) and the final results including the standard deviation (SD), average fitness (AF), optimal value (OV), worst value (WV), and convergence curve can be obtained as shown in Table 2 and Figure 5.

As is shown in Table 2, both the conventional algorithm and improved NSGA-II can complete the search process, but the improved NSGA-II exhibits higher search accuracy and more divergent data, which indicates the better population diversity. In addition, as shown in Figure 5, the improved NSGA-II is superior to the conventional one in terms of convergence speed, convergence accuracy, global search ability, and optimized stability.

Table 3 shows the configuration of each device obtained by the two algorithms in case IV. As shown in Table 3, capacity configuration results under the improved NSGA-II are generally lower than those under the conventional one, especially for new energy units and storage batteries. This shows that the improved NSGA-II is able to reduce the annual investment cost effectively and then further decrease the annual planning cost of the system, which can diminish approximately 4.03 million Yuan. In addition, the net emission of pollutants is also cut down so that environmental protection can be improved. Main parameters of various types of the devices are listed in Table 4 below.

5.2 Analysis of optimized comparison

This paper takes a typical day in winter to analyze the operating results of the entire RIES. The operating period is 24 h, and the unit operating period is 1 h. The output forecast of renewable energy on a

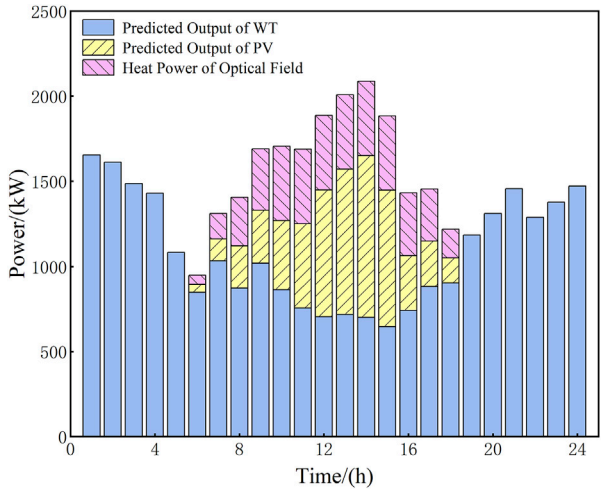

FIGURE 6
Output forecast of renewable energy on a typical winter day in the RIES.

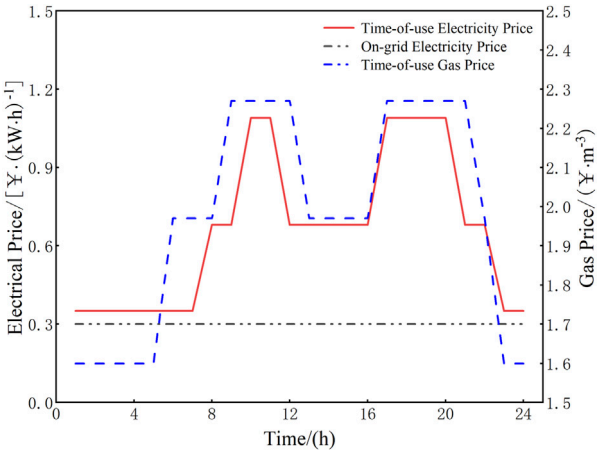

FIGURE 7
Time-of-use price curves.

typical winter day is shown in Figure 6. In addition, the corresponding time-of-use price curves are shown in Figure 7.

The situation of carbon emission in different cases is shown in Figure 8, and the flexible load curves such as electricity, heat, cooling, and gas under the IDR as well as their detailed composition in case IV are presented in Figure 9.

As shown in Figure 8, compared with case I and case II, net carbon emissions in case III and case IV are significantly diminished after considering the whole process of carbon emission. Compared with case III, case IV has lower carbon emission and higher carbon capture, which can reduce carbon trading costs to enhance environmental benefits. This is because the IDR of peak cutting and valley filling can reduce some of the purchased power and make the output of new energy units and GTs increase slightly; as a result, the energy consumption of the CCS also increases.

As presented in Figure 9, compared with case III, the CLs, TLs, and FLs of each period in case IV are dynamically changed after considering the IDR, and the maximum peak-to-valley differences of each flexible load are reduced by 36.32%, 35.75%, 26.31%, and 11.42%, thus smoothing the load curves and realizing the process of peak cutting and valley filling. For instance, according to the electrical load in Figure 9A, the variation of CL is reflected in peak periods; the variation of TL is larger in peak and valley periods and smaller in normal periods; and the variation of FL is positive in valley periods and negative in peak and normal periods, which can better reflect the peak and valley characteristics of electricity prices. In addition, the peak-to-valley differences of the flexible electrical load curve in Figure 9A are effectively reduced to make the cost of power purchase continuously decrease. In addition, it is easily known from Figure 9A that the CL of electricity is reflected in peak periods (10:00–11:00 and 17:00–20:00) when the electrical load and price are high, and the reduced load would be converted into incentive subsidies to users. The TL of electricity is shifted from the high-electricity-price periods (10:00–11:00 and 17:00–20:00) to the low-electricity-price periods (23:00–08:00 and 12:00–16:00), which realizes the process of transferring electrical load from peak periods to the valley called peak cutting and valley filling to promote the economy of using the electricity. The FL of electricity converts part of the electrical load into heat load in high electricity price periods to alleviate the mismatch and imbalance between the electrical load demand and the supply capacity. In addition, during the periods of low electricity prices, part of the heat load is transformed into the electrical load for central heating.

The analysis method of the flexible heat load shown in Figure 9B is similar to that of the electrical load. As for the flexible cool and gas loads shown in Figures 9C, D, the system smoothes their load curves by cutting or transferring to realize the process of stabilizing the load fluctuation, which makes the output of the corresponding device more reasonable and perfect.

The aforementioned analysis shows that the IDR under case IV can achieve peak cutting and valley filling to improve economic benefits. Meanwhile, the peak-to-valley differences of each load are reduced by 430.41, 70.60, 33.22 kW, and 29.08 m^3 compared with case III, which makes the whole system more flexible in terms of energy purchase so that the environmental benefits are significantly increased.

5.3 Analysis of operating results

Figure 10 shows the optimized operation scheme of storage devices involving the storage battery and heat storage tank of the CSP station. Since the energy storage devices can be used as a part of the flexible load, they have abilities to participate in the whole peak-cutting and valley-filling process. For the storage battery, during the valley period of electrical consumption from 23: 00 to 07: 00, the electrical load and price are both lower, so the storage battery charges at this time to cope with the subsequent peak load. During the peak periods of 10: 00–11: 00 and 17: 00–20: 00, the electrical load and price are both higher, so the storage battery discharges to relieve the pressure in the grid. For the CSP heat storage tank, the main

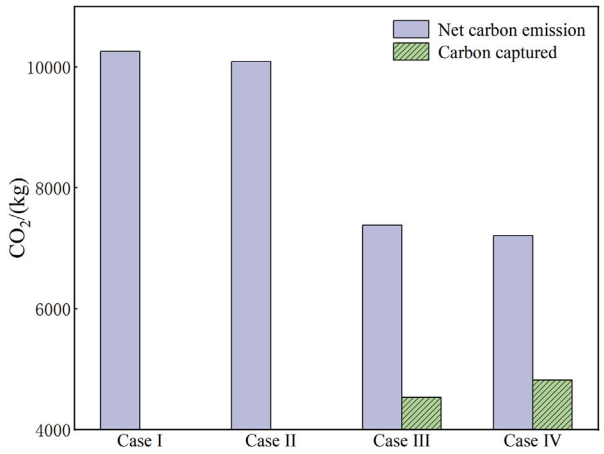

FIGURE 8
Net emission and capture volume of CO_2.

thermal source is the heat-conducting medium of the heat absorber in the optical field, so it will be affected by the operation mode of the CSP station in most periods. For example, from 09: 00 to 12: 00, the heat storage tank can provide thermal energy to the load side. In addition, during the period of 13: 00–16: 00, the light is abundant so that the heat storage tank collects heat from the optical field to meet the demand of thermal use in the evening (17: 00–20: 00). During the period of 23: 00–08: 00, the partial output of the electric boiler will flow into the CSP heat storage tank to realize the heat storage backup process.

The input of the two energy storage equipment makes the operation of the system more reasonable, and the maximum variation range of power storage and heat storage can reach 770 and 911 kW, respectively, which enables the flexibility of energy storage increase significantly to reduce the cost of energy purchase.

Figure 11 shows the optimized operation results of the four energy sources on the typical winter day, which are analyzed as follows:

1) Balance of electricity

As shown in Figure 11A, during the period of 23: 00–05: 00, the electrical demand is mainly satisfied through WT and GT to reduce the costs of electricity generation and device operation. Since the electrical

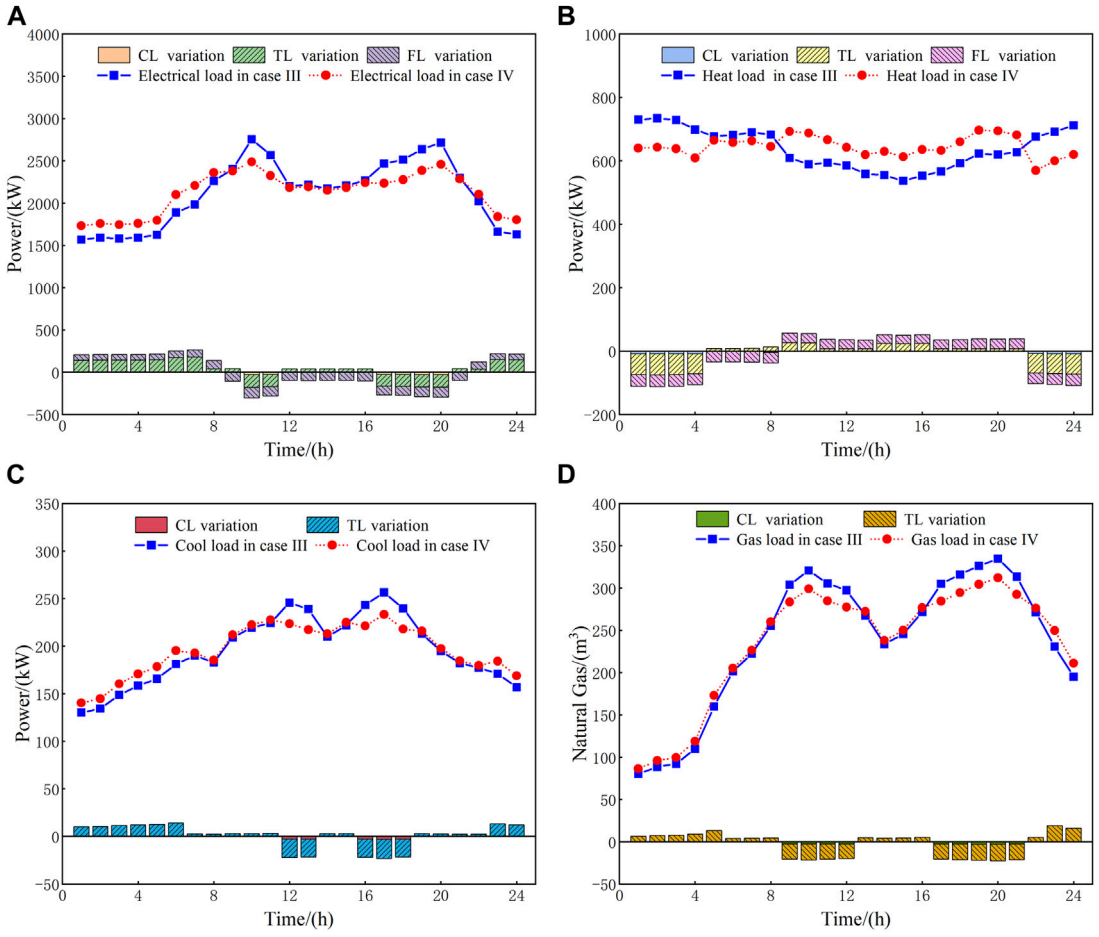

FIGURE 9
Detailed composition of flexible loads. **(A)** Electrical load, **(B)** heat load, **(C)** cool load, and **(D)** gas load.

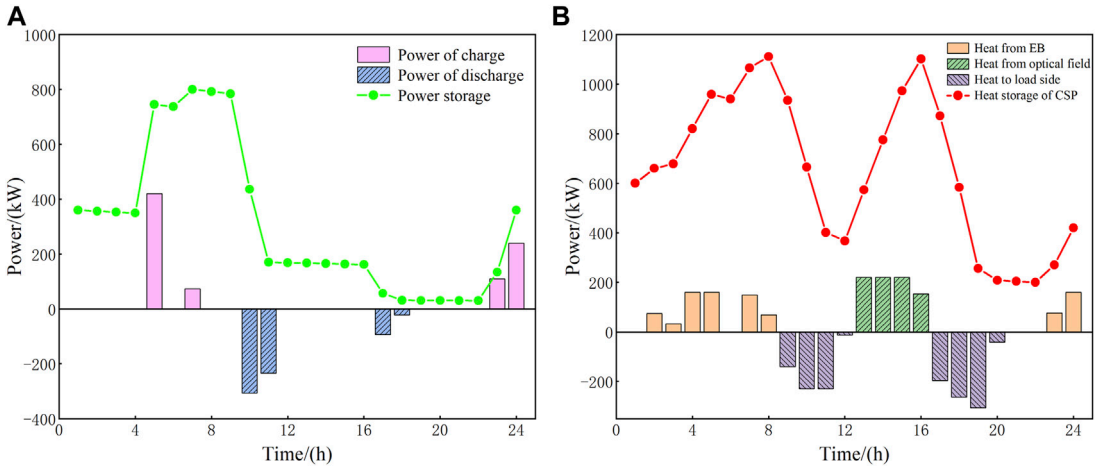

FIGURE 10
Charge/discharge power and the capacity of storage devices. **(A)** Storage battery and **(B)** CSP heat storage tank.

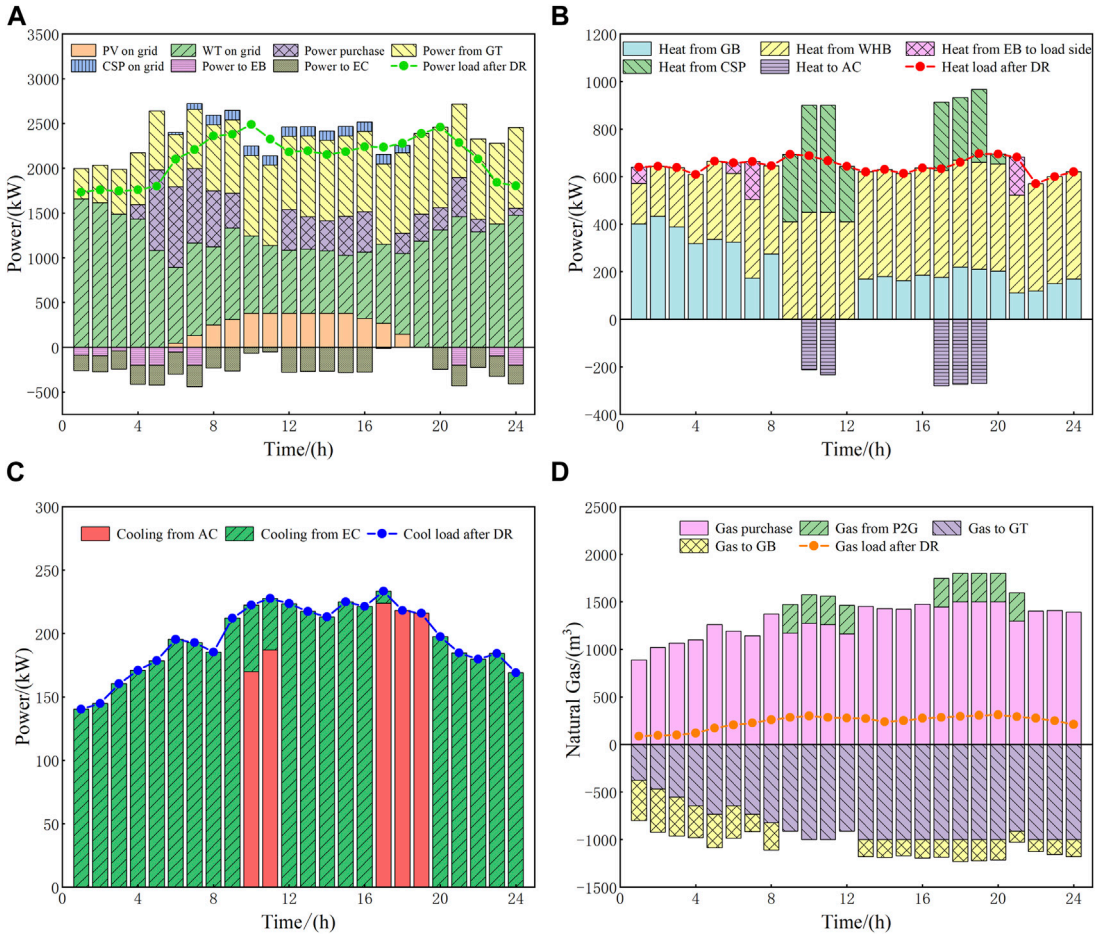

FIGURE 11
Optimal balance scheduling results on a typical winter day. **(A)** Electrical load, **(B)** heat load, **(C)** cool load, and **(D)** gas load.

price in this period is at the trough value, the flexible heat load will be converted into electrical load through the IDR, and the system will purchase a small amount of electricity for the storage battery. During the periods of 06: 00–09: 00 and 12: 00–16: 00, the electricity is afforded by WT, PV, CSP station, and GT in priority, and the insufficient part will be supplemented through electrical purchase. During the periods of 10: 00–11: 00 and 17: 00–22: 00, the electrical demands of users are relatively larger. At this time, except for the output of new energy units and GTs, the electrical shortage can be provided by storage battery and electrical purchase, in turn, to maintain the balance. In addition, the participation of flexible electrical load in IDR during this period can further reduce and transfer the peak electricity consumption, thus significantly decreasing the power impact of electrical devices on the grid and their required configuration capacities.

2) Balance of heat

As shown in Figure 11B, during the period of 22: 00–08: 00, the heat is mainly afforded by GB and WHB while the demand is larger than at any other time, so the total amount and the peak value of heat energy can be reduced by cutting and transferring part of the flexible heat load. In addition, due to the low electricity price at this time, a small amount of the heat that is output by EB will be transported to the load side as well as the residual output of EB will flow into the heat storage tank of the CSP station to meet the lower capacity limit. During the period of 09: 00–21: 00, the heat is mainly provided by WHB, and part of the flexible electrical load will be converted into heat load through the IDR. During the period from 09: 00 to 12: 00, as the light gradually increases, the heat storage tank of the CSP station releases the heat to the load side, which reduces the output of GB to 0. During the period from 13: 00 to 16: 00, WHB takes most of the heat load, and the heat storage tank of the CSP station uses this period to charge as the reserve for the next period. During the period from 17: 00 to 21: 00, the gas prices are high so that the output of GB is decreased, and at the same time, the output of electrical generation in the CSP station is continuously reduced; as a result, the heat storage tank of the CSP station releases the heat to the load side. If the demand cannot be satisfied, EB will provide part of the required heat.

3) Balance of cooling

As shown in Figure 11C, the output of EC completes the supply of cool load in the valley and normal time of electrical price, such as the periods of 21: 00–09: 00 and 12: 00–16: 00. During the periods of high electricity price such as 10: 00–11: 00 and 17: 00–19: 00, the output of EC is less than before and AC bears all the cool load, which is helpful for peak cutting and valley filling. Since there is little demand for cool energy in winter, the cool mode of the system is relatively flexible. As a result, the flexible cooling load only needs to be partially reduced and transferred at the peak.

4) Balance of gas

As shown in Figure 11D, the gas load and the consumption of gas-fired units are satisfied through gas purchase during the periods of 22: 00–08: 00 and 13: 00–16: 00. During the period from 22: 00 to 05: 00, although the gas price is at the trough value, the consumption of gas is generally small, and as a result, the gas purchase is still relatively small. During the period from 06: 00 to 08: 00, the gas purchase is growing and GT becomes the main source of gas consumption and continuously increases its output to satisfy the demands of electricity and heat. During the period from 13: 00 to 16: 00, the consumption of the gas-fired units is maintained within a certain range due to the influence of the climbing rate. At this time, the gas load fluctuates slightly but the amplitude is small; therefore, the corresponding gas purchase is basically at a stable level. During the periods of 09: 00–12: 00 and 17: 00–21: 00, constraints on carbon capture and flue gas treatment make regulating abilities of the system decline, which leads to the abandonment of wind and light. At this time, P2G makes efforts to absorb the abandoned power of wind and light, which can synthesize natural gas to alleviate the imbalance between gas purchase and gas demands. Moreover, due to the high gas price in this period, the flexible gas load will be reduced and transferred accordingly.

6 Conclusion

In this paper, an operating model of RIES that considers the whole process of carbon emission and IDR is constructed. Meanwhile, a double-layer optimal configuration method based on the improved NSGA-II and MILP is proposed with the participation of the CSP station. The following conclusions can be drawn by setting up four cases:

1) The proposed double-layer optimal configuration model can reasonably optimize the capacities and the output of the devices to obtain the optimal operation scheme. Meanwhile, the participation of the CSP station can improve the coordinated optimization abilities of the RIES.
2) Compared to not considering carbon emissions, introducing the whole process of carbon emission can significantly reduce the net carbon emission, in which the combined operation strategy of wind power–photovoltaic–CSP–carbon capture can coordinate the output of each device and suppress the fluctuation of renewable energy, the process of carbon utilization decreases the storage cost and promotes P2G to absorb the abandoned power of wind and light, and the ladder-type carbon trading mechanism can strictly control the cost of carbon emission to enhance the economy and environmental protection.
3) Compared to not considering IDR, classifying flexible loads including electricity, heat, cooling, and gas into curtailable, transferable, or fungible loads for participating in the IDR can effectively smooth the load curves, reduce the peak-to-valley differences, and realize multi-energy complementarities. Meanwhile, the compensatory mechanism of the IDR can rationally adjust the energy consumption strategies to optimize the energy structure and improve energy efficiency.
4) Compared with the conventional NSGA-II, the improved NSGA-II can obtain the optimal non-dominated solution sets in the upper layer, and its capacity configuration and operation scheme have lower annual planning cost and net pollutant discharge. Meanwhile, the optimized accuracy of the improved NSGA-II is higher, and the convergent speed and ability reach the optimal level.

At present, this paper mainly studies the day-ahead configuration and operation of the single-region RIES. In the

follow-up work, the whole process of carbon emission and IDR will be further extended to the energy network with multi-RIES interconnection by considering the effects of source-load uncertainty on capacity configuration and the step-by-step refinement of time scales to realize the decoupling, coordinated optimization, and stable operation of different energies.

Data availability statement

The original contributions presented in the study are included in the article/Supplementary Material; further inquiries can be directed to the corresponding author.

Author contributions

XZ: methodology, algorithm finding, and experimental platform provision. JW: programming, simulation, and writing original draft preparation. YZ: algorithm refinement, editing, supervision, and review. HL: raw data provision, algorithm testing, and article refinement. All authors contributed to the article and approved the submitted version.

Funding

This work was supported by the National Natural Science Foundation of China (No. 52167014); Small and Medium-sized Enterprise Innovation Fund of Gansu Province (No. 22CX3JA002); and Natural Science Foundation Project of Gansu Province (No. 21JR7RA211).

Conflict of interest

The authors declare that the research was conducted in the absence of any commercial or financial relationships that could be construed as a potential conflict of interest.

Publisher's note

All claims expressed in this article are solely those of the authors and do not necessarily represent those of their affiliated organizations, or those of the publisher, the editors, and the reviewers. Any product that may be evaluated in this article, or claim that may be made by its manufacturer, is not guaranteed or endorsed by the publisher.

References

Azzam, S. M., Elshabrawy, T., and Ashour, M. (2023). A bi-level framework for supply and demand side energy management in an islanded microgrid. *IEEE Trans. Ind. Inf.* 191, 220–231. doi:10.1109/tii.2022.3144154

Chen, B., Wu, W., Guo, Q., and Sun, H. (2022). An efficient optimal energy flow model for integrated energy systems based on energy circuit modeling in the frequency domain. *Appl. Energy* 326, 119923. doi:10.1016/j.apenergy.2022.119923

Chen, W., Ma, Y., and Bai, C. (2021). The impact of carbon emission quota allocation regulations on the investment of low-carbon technology in electric power industry under peak-valley price policy. IEEE Trans. Eng. Manage. *early access*, 1–18. doi:10.1109/tem.2021.3121002

Dong, W., Lu, Z., He, L., Geng, L., Guo, X., and Zhang, J. (2022). Low-carbon optimal planning of an integrated energy station considering combined power-to-gas and gas-fired units equipped with carbon capture systems. *Int. J. Electr. Power & Energy Syst.* 138, 107966. doi:10.1016/j.ijepes.2022.107966

Fan, H., Yu, Z., Xia, S., and Li, X. (2021). Review on coordinated planning of source-network-load-storage for integrated energy systems. *Front. Energy Res.* 9, 641158. doi:10.3389/fenrg.2021.641158

Fu, X., Zeng, G., Zhu, X., Zhao, J., Huang, B., and Liu, J. (2022). Optimal scheduling strategy of grid-connected microgrid with ladder-type carbon trading based on Stackelberg game. *Front. Energy Res.* 10, 961341. doi:10.3389/fenrg.2022.961341

Gorman, B. T., Lanzarini-Lopes, M., Johnson, N. G., Miller, J. E., and Stechel, E. B. (2021). Techno-economic analysis of a concentrating solar power plant using redox-active metal oxides as heat transfer fluid and storage media. *Front. Energy Res.* 9, 734288. doi:10.3389/fenrg.2021.734288

Jiang, P., Dong, J., and Huang, H. (2020). Optimal integrated demand response scheduling in regional integrated energy system with concentrating solar power. *Appl. Therm. Eng.* 166, 114754. doi:10.1016/j.applthermaleng.2019.114754

Li, Y., Bu, F., Gao, J., and Li, G. (2022). Optimal dispatch of low-carbon integrated energy system considering nuclear heating and carbon trading. *J. Clean. Prod.* 378, 134540. doi:10.1016/j.jclepro.2022.134540

Shao, C., Ding, Y., Siano, P., and Lin, Z. (2019). A framework for incorporating demand response of smart buildings into the integrated heat and electricity energy system. *IEEE Trans. Ind. Electron.* 662, 1465–1475. doi:10.1109/tie.2017.2784393

Shao, C., Ding, Y., Siano, P., and Song, Y. (2021). Optimal scheduling of the integrated electricity and natural gas systems considering the integrated demand response of energy hubs. *IEEE Syst. J.* 153, 4545–4553. doi:10.1109/jsyst.2020.3020063

Tao, J., Xu, W., and Li, Y. (2019). Optimal operation of integrated energy system combined cooling heating and power based on multi-objective algorithm. *Sci. Tech. Engrg.* 19(33), 200–205. doi:10.3969/j.issn.1671-1815.2019.33.029

Wang, B., Sun, H., and Song, X. (2022). Optimal dispatching modeling of regional power-heat-gas interconnection based on multi-type load adjustability. *Front. Energy Res.* 10, 931890. doi:10.3389/fenrg.2022.931890

Wang, L., Hou, C., Ye, B., Wang, X., Yin, C., and Cong, H. (2021). Optimal operation analysis of integrated community energy system considering the uncertainty of demand response. *IEEE Trans. Power Syst.* 364, 3681–3691. doi:10.1109/tpwrs.2021.3051720

Wang, X., Xin, A., Chen, X., Fang, L., Jia, Q., Ma, L., et al. (2022). Optimal dispatching of ladder-type carbon trading in integrated energy system with advanced adiabatic compressed air energy storage. *Front. Energy Res.* 10, 933786. doi:10.3389/fenrg.2022.933786

Wei, Z., Ma, X., Guo, Y., Wei, P., Lu, B., and Zhang, H. (2022). Optimized operation of integrated energy system considering demand response under carbon trading mechanism. *Electr. Power Constr.* 431, 1–9. doi:10.12204/j.issn.1000-7229.2022.01.001

Yan, M., Li, Y., Chen, G., Zhang, L., Mao, Y., and Ma, C. (2017). A novel flue gas pre-treatment system of post-combustion CO_2 capture in coal-fired power plant. *Chem. Eng. Res. Des.* 128, 331–341. doi:10.1016/j.cherd.2017.10.005

Yan, N., Ma, G., Li, X., and Guerrero, J. M. M. (2023). Low-carbon economic dispatch method for integrated energy system considering seasonal carbon flow dynamic balance. *IEEE Trans. Sustain. Energy* 141, 576–586. doi:10.1109/tste.2022.3220797

Yang, H., Li, M., Jiang, Z., and Zhang, P. (2020). Multi-time scale optimal scheduling of regional integrated energy systems considering integrated demand response. *IEEE Access* 8, 5080–5090. doi:10.1109/access.2019.2963463

Zeng, X., Zhang, J., and Wang, X. (2023). Optimal configuration of regional integrated energy system after taking into account multiple uncertainties and the participation of concentrating solar power stations. *High. Volt. Eng.* 491, 353–363. doi:10.13336/j.1003-6520.hve.20211326

Zhang, D., Yun, Y., Wang, X., He, J., and Dong, H. (2021). Economic dispatch of integrated electricity-heat-gas energy system considering generalized energy storage and concentrating solar power plant. *Autom. Electr. Power Syst.* 4519, 33–42. doi:10.7500/AEPS20210220002

Zhang, D., Zhu, H., Zhang, H., Goh, H. H., Liu, H., and Wu, T. (2022). Multi-objective optimization for smart integrated energy system considering demand responses and dynamic prices. *IEEE Trans. Smart Grid* 132, 1100–1112. doi:10.1109/tsg.2021.3128547

Zhang, G., Xie, P., Huang, S., Chen, Z., Du, M., Tang, N., et al. (2021). Modeling and optimization of integrated energy system for renewable power penetration considering carbon and pollutant reduction systems. *Front. Energy Res.* 9, 767277. doi:10.3389/fenrg.2021.767277

Zhang, N., Hu, Z., Dai, D., Dang, S., Yao, M., and Zhou, Y. (2016). Unit commitment model in smart grid environment considering carbon emissions trading. *IEEE Trans. Smart Grid* 71, 420–427. doi:10.1109/tsg.2015.2401337

Zhao, S., Fang, Y., and Wei, Z. (2019). Stochastic optimal dispatch of integrating concentrating solar power plants with wind farms. *Int. J. Electr. Power & Energy Syst.* 109, 575–583. doi:10.1016/j.ijepes.2019.01.043

frontiers | Frontiers in Energy Research

TYPE Methods
PUBLISHED 13 October 2023
DOI 10.3389/fenrg.2023.1252624

OPEN ACCESS

EDITED BY
Yongxin Xiong,
Aalborg University, Denmark

REVIEWED BY
Xu Xu,
Xi'an Jiaotong-Liverpool University, China
Zhiqiang Jiang,
Huazhong University of Science and Technology, China

*CORRESPONDENCE
Jia Lu,
442895549@qq.com

RECEIVED 04 July 2023
ACCEPTED 18 September 2023
PUBLISHED 13 October 2023

CITATION
Lu J, Liu Y, Cao H, Xu Y, Ma H, Zhang Z, Wang T and Yang Y (2023), Mid-term scheduling and trading decisions for cascade hydropower stations considering multiple variable uncertainties.
Front. Energy Res. 11:1252624.
doi: 10.3389/fenrg.2023.1252624

Mid-term scheduling and trading decisions for cascade hydropower stations considering multiple variable uncertainties

Jia Lu*, Yaxin Liu, Hui Cao, Yang Xu, Haoyu Ma, Zheng Zhang, Tao Wang and Yuqi Yang

Hubei Key Laboratory of Intelligent Yangtze and Hydroelectric Science, China Yangtze Power Co. Ltd., Yichang Hubei, China

Cascade hydropower producers face two stages of risk when participating in medium and long-term market transactions: transaction risk during the bidding stage; and the operational risk during the scheduling and operation stage due to the uncertainty of runoff and market-clearing prices. Therefore, how to measure the above risks and make corresponding decisions has become an urgent problem for producers.This paper combines the real market structure and rules of a certain hydropower dominated market in Southwest China, and establishes a mid-term operation and trading decision-making method based on the Joint Information Gap Decision Theory (IGDT) and Prospect Theory. To address the main uncertainty variables that producers face in participating in transactions, this paper obtains the maximum fluctuation range of variables that satisfy the expected revenue in a robust model based on IGDT. Then, using Prospect Theory, a bidding strategy model that takes into account the psychological factors of producers is constructed within this range.To solve the nonlinear programming problem and address the accuracy issues caused by curve fitting during the solution process, a nonlinear programming combined with an improved stepwise optimization hybrid algorithm is employed.Using actual data from a hydropower grid in southwest China participating in the market as an example. The results indicate that the method provides the fluctuation range of runoff and market prices under different expected return targets, and can formulate reasonable bidding decisions and operation plans based on producers different risk preferences within this range.

KEYWORDS

power market, information gap decision theory, prospect theory, robust optimization, cascade hydropower stations, risk decision

1 Introduction

As the new round of power market reform gradually enters deep water area, China's provinces and cities have established well-regulated and well-structured medium- and long-term power markets (Cheng et al., 2018; Liu et al., 2019; Yao et al., 2020).Because medium- and long-term transactions have relatively low risks and stable returns, they have become a "ballast stone" for market participants to avoid risks (Li et al., 2022). At the same time, they also plays a role in anchoring the spot market prices. For cascade hydropower producers, the medium and long-term market can effectively mitigate operational risks caused by

hydrological uncertainty, especially for long-term operation and transaction plans with large errors. Hydropower producers can adjust long-term plans and make trading strategies through mid-term optimization scheduling based on more accurate forecasting results. However, when participating in monthly medium- and long-term markets, there will inevitably be errors in the predicted values of runoff and prices which may lead to insufficient generation output, failure to fulfill contracts, or high bidding prices that result in failed clearing. Therefore, how to formulate corresponding operation plans and bidding strategies has become an urgent practical demand for cascade hydropower producers.

In the market, the traditional dispatching method has been significantly impacted as well (Li et al., 2012). Unlike other power generation, when participating in the market, hydropower producers needs to consider not only the transaction risks caused by market structure, rules, and bidding strategies, but also the operation risks caused by uneven and uncertain distribution of runoff. In addition, when participating in the market every month, producers usually take two approaches to pursue higher profits: increasing power generation and bidding higher prices. However, there are inevitable errors in their predicted runoff and prices, which may lead to insufficient generation output that cannot be fulfilled or high bidding prices that result in failed clearing. Therefore, when participating in mid-to-long-term trading, producers face a two-stage risk that needs to be considered: 1) transactional risk in the mid-to-long-term market bidding stage; and 2) operational risk in the mid-term dispatch stage due to the uncertainty of market-clearing electricity prices and the randomness of daily runoff. How to jointly consider the above risks and make reasonable decisions in the corresponding stages has become the main practical and theoretical challenge currently faced by hydropower producers in China.

At present, there has been some research on the above issues. In response to the risk decision-making issue during the bidding stage, a methodology to design an optimal bidding strategy for a generator according to his or her degree of risk aversion is established (Rodriguez and Anders, 2004).Based on the coordinated interaction between units output and market clearing prices, the benefit/risk/emission comprehensive generation optimization model with objectives of maximal profit and minimal bidding risk and emissions is established (Peng et al., 2012).The uncertainty model of market price is considered based on the concept of weighted average squared error using a variance–covariance matrix. IGDT is used to develop the bidding strategy of a generation company (Za et al., 2013). Introducing evolutionary game theory into the bidding strategy of thermal power units, a thermal power peak shaving bidding model based on the bidding mechanism of the auxiliary service market of Northeast China Power Grid was established (Lu et al., 2021).A robust optimization approach is proposed to obtain the optimal bidding strategy of retailer, which should be submitted to pool market (Nojavan et al., 2015a).A hybrid approach based on IGDT and modified particle swarm optimization (MPSO) is used to develop the optimal bidding strategy (Nojavan et al., 2015b).Proposes a bilevel stochastic optimization model to obtain the optimal bidding strategy for a strategic wind power producer in the short-term market (Dai and Qiao, 2015).

However, from the perspective of usage scenarios, current research still has some shortcomings, mainly manifested in the following three aspects: 1) Most research focuses on thermal and wind power, which is not applicable to risk decision-making problems for cascaded hydropower stations with close water-electricity connections. 2) When using scenario analysis to handle uncertainty, a sufficient number of scenarios are usually required to make the description more accurate and comprehensive, which can lead to low solution efficiency and overly conservative results. 3) Current research mostly considers decision-making risks in the bidding stage or performance risks in the operational stage separately, while in practical use, these two types of risks need to be coupled together. 4) Most studies use solvers to improve computational efficiency, but this approach requires fitting some curves, resulting in a decrease in computational accuracy.

In order to solve the above problems, this paper introduces the power market structure and rules of a certain hydropower dominated market in Southwest China. The trading varieties in this market are divided into three time categories: annual, monthly, and daily. The annual trading is bilateral, and the monthly trading is carried out in the order of bilateral, matchmaking, and listing. Considering the risks in the bidding stage and the dispatching operation stage, a method for cascade hydropower producers is proposed by combining the IGDT and prospect theory. Firstly, considering the risk in the medium-term operation stage, the IGDT is used in conjunction with a robust optimization model to solve for the maximum deviation range of runoff and clearing prices from the predicted values when satisfying the producer's predetermined revenue. Then, considering the trading decision risks in market bidding stage based on the fluctuation range of uncertain variables, the prospect theory is used to analyze and study the bidding strategy of producer's in the market from the perspective of limited rationality and establish a corresponding bidding decision model. Considering the precision problem caused by curve fitting due to the use of optimization solvers for solving nonlinear programming problems, this paper chooses to use a nonlinear programming and improved stepwise optimization hybrid algorithm to solve the problem. Finally, a cascade hydropower station is used as an example to verify that the method provided in this paper provides the fluctuation range of runoff and clearing prices under different expected revenue targets, and develops reasonable bidding decision-making and operation plans based on different risk tolerance levels within this range.

2 Introduction to prospect theory

Prospect theory (Tversky, 1979; Amos Tversky and Kahneman, 2016) is a method that takes into account the subjective feelings of decision-makers, where they exhibit risk aversion when facing gains and risk-seeking behavior when facing losses, and are more sensitive to losses than gains. In practice, decision-makers face a highly complex and dynamic electricity market, and the many uncertainties and risks associated with it make it difficult for decision-makers to meet the assumption of a "perfectly rational person". This means that their information is limited, and their predictions of the market are always subject to some level of error. In addition, limited insight into the essence of the problem makes it difficult for decision-makers to maintain consistent risk preferences, highlighting the characteristic of changing risk preferences. Therefore, in contrast to assuming decision-makers are perfectly

rational using the mean-variance or value-at-risk/conditional value-at-risk methods, prospect theory assumes that decision-makers are boundedly rational, meaning their information is limited and risk preferences can change with different objective factors, and typically uses prospect value as a basis for decision-making. Prospect value is determined by both the value function and decision weights, and the calculation formula is as follows:

$$V = \sum_{k=1}^{K} \omega(pro_k) v(x_k) \tag{1}$$

Where V represents prospect value; k represents a certain event and K represents all possible events; (pro_k) is the probability weight function; $v(x_k)$ is the value function; pro_k is the probability of event k occurring; and x_k is the index value of event k. In prospect theory, the decision-making process of a decision-maker is influenced by two subjective factors: their subjective value perception of the benefits obtained from the decision and their subjective perception of the probability of achieving those benefits.

The value function is a subjective representation of value formed by the decision-maker, and commonly used forms of the value function include the following:

$$v(x_k) = \begin{cases} x^a & x \geq 0 \\ -\lambda(-x_k)^b & x < 0 \end{cases} \tag{2}$$

Where the parameters a and b represent the concavity and convexity of the power functions for gains and losses, respectively, reflecting the decision-maker's sensitivity to gains and losses. Generally, a and b are greater than 1. The parameter λ reflects the decision-maker's aversion to losses, and is generally greater than 1.

The probability weight function represents the decision-maker's subjective judgment of the probability p of an event occurring, and commonly used forms of the probability weight function include the following:

$$\omega(pro_k)^+ = \frac{{pro_k}^\theta}{\left[{pro_k}^\theta + (1 - pro_k)^\theta\right]^{1/\theta}} \tag{3}$$

$$\omega(pro_k)^- = \frac{{pro_k}^\delta}{\left[{pro_k}^\delta + (1 - pro_k)^\delta\right]^{1/\delta}} \tag{4}$$

Where $(pro_k)^+$ and $(pro_k)^-$ represent the probability weight functions when the decision-maker perceives gains and losses, respectively. θ is the coefficient of the attitude towards risk for gains, and σ is the coefficient of the attitude towards risk for losses.

3 The risk decision model based on the joint information gap decision theory and prospect theory

When market participants evaluate a decision as a gain or a loss, they usually consider the change in wealth rather than the total wealth. The carrier of subjective value is the change in wealth, not the final state of wealth. Therefore, when evaluating market risks for a cascaded hydropower producer, expected gains must be set in advance. Next, different bidding decisions and operating plans are evaluated based on the electricity sales revenue. Finally, the optimal decision is chosen based on the decision-maker's attitude towards risk.

3.1 Medium and long term market income model of cascade hydropower producers

The market share of each power producer studied in this paper is relatively small, and their bidding method has no impact on the transaction results, indicating that they can be considered price takers. Transactions in the market are settled according to pay-as-bid (PAB), which is a payment based on the offer (Federico and Rahman, 2001; Kahn et al., 2001). When participating in market, corresponding application decisions and operation plans will be formulated based on the predicted runoff and the clearing price. As the decision-makers of cascade hydropower stations are limited rational price takers who cannot obtain unbiased estimates of uncertain variables. Therefore, the bidding based on the predicted clearing price may lead to excessively high bids due to prediction error, which will eventually lead to bidding failure. In this case, the settlement is based on the on grid price. At the same time, due to the strong volatility of natural runoff, there are often errors in the prediction results, resulting in the transaction contracts in the medium-term dispatching operation stage can not be completed or overfulfilled, so it is necessary to consider the assessment of the default part. Therefore, the revenue for a hydropower producer is shown as follows:

$$B_{1,i} = e_{1,i} \times p_1 \tag{5}$$

$$B_{2,i} = e_{2,i} \times p_2,\ e_{1,i} \geq 0 \tag{6}$$

$$e_{2,i} = e_i - e_{1,i},\ e_i \geq e_{1,i} \tag{7}$$

$$B_{3,i} = e_{3,i} \times p_3 \tag{8}$$

$$e_{3,i} = e_{1,i} - e_1,\ e_i < e_{1,i} \tag{9}$$

Where $B_{1,i}$ and $e_{1,i}$ represent the medium- and long-term market revenue and settlement electricity quantity, respectively, for station i; p_1 is the settlement electricity price for the mid-to-long-term market. $B_{2,i}$ and $e_{2,i}$ represent the excess power generation revenue and excess electricity quantity, respectively, for station i when the bid is successful; p_2 is the settlement electricity price for excess electricity quantity. $B_{3,i}$ and $e_{3,i}$ represent the default loss and default power quantity, respectively, e_i is the power generation of station i; p_3 is the default electricity price used for assessment.

3.2 Medium term optimal operation model of cascade hydropower producers

3.2.1 Objective function of optimal scheduling in operation stage

Considering that the generation cost of cascaded hydropower stations mainly consists of fixed costs and does not affect model optimization, this paper will ignore it. With a monthly scheduling cycle and 1 day as a time period, the optimization goal for a producer in the market is to maximize total revenue, as shown in the following formula.

$$\max B_0 = \max B^+\beta + B^-(1-\beta) \tag{10}$$

$$B^+ = \sum_{i=1}^{N}(B_{1,i} + B_{2,i}) \tag{11}$$

$$B^- = \sum_{i=1}^{N}(B_{1,i} - B_{3,i}) \tag{12}$$

Where, B_0 refers to the total revenue of the producer; N is the number of cascaded hydropower stations. B^+ and B^- correspond to the total revenue of the producer when overcompleted and in contract breach, respectively. β is a binary variable where β = 1 represents overgeneration and β = 0 represents an uncompleted contract.

According to formulas (5) to (10), the generation revenue of a producer mainly depends on the total electricity generation of the current month. This is calculated as follows:

$$e_i = \sum_{j=1}^{T}\eta_i \times Q_{i,j} \times H_{i,j} \times \Delta t_j \tag{13}$$

$$H_{i,j} = \frac{Z_{i,j-1} + Z_{i,j}}{2} - Z^d_{i,j} - H^d_{i,j} \tag{14}$$

Where: e_i is the total power generation of station i for the period j; T is the total number of time periods; $Q_{i,j}$, $H_{i,j}$, $Z_{i,j}$, $Z^{\mathrm{d}}{}_{i,j}$, and $H^{\mathrm{d}}{}_{i,j}$ represent the average power generation, average discharge, water head, decision-making reservoir water level, downstream tail water level, and head loss of station i on the jth day, respectively; η_i is the output coefficient of station i; and Δt_j is the time step length.

3.2.2 Objective function

To avoid repetition, this article follows the conventional hydro constraints of the hydropower station as shown in reference (Lu et al., 2021). This paper only demonstrates the relevant market-based power constraints, which are shown below:

$$e_{1,i} + e_{2,i} - e_{3,i} = e_i \tag{15}$$

$$e_{2,i} \times e_{3,i} = 0 \tag{16}$$

$$e_i - \beta M \le e_{1,i} \le (1-\beta)M + e_i \tag{17}$$

Where M is a sufficiently large constant.

3.3 Robust optimization modeling and solution based on IGDT

3.3.1 Objective function

To mitigate the impacts of uncertain runoff and prices during the bidding and operation stages of cascaded hydropower producers, this paper adopts the IGDT (Wright, 2004) robust model for modeling. The model calculates the maximum deviation range between the predicted values of runoff and clearing prices for the mid-term operation stage to achieve expected revenue. To avoid repetition with Section 3.2, only unique content is presented below:

$$\bar{\alpha} = \max_{\alpha, e_{i,t}} \; i = 1, 2, ..., N \tag{18}$$

$$s.t.\ B^* \ge B_c = (1-\sigma)B_0 \tag{19}$$

$$\begin{aligned} B^* = \Big\{ & \min_{e_i, p_1, p_2, p_3} B^+\beta + B^-(1-\beta) \\ & e_i = \sum_{j=1}^{T}\eta_i \times Q_{i,j} \times H_{i,j} \times \Delta t_j, \\ & s.t.\ (1-\alpha) \times \bar{q}_{i,j} \le q_{i,j} \le (1+\alpha) \times \bar{q}_{i,j}, \\ & (1-\alpha) \times \bar{p}_1 \le p_1 \le (1+\alpha)\bar{p}, \\ & (1-\alpha) \times \bar{p}_2 \le p_2, \\ & p_3 \le (1+\alpha) \times \bar{p}_3 \Big\} \end{aligned} \tag{20}$$

Where $\bar{\alpha}$ represents the maximum fluctuation range of runoff and prices compared to the predicted values. In order to better describe the basic idea of IGDT and its applicability in solving the problem at hand, it is assumed that the predicted errors for both prices and runoff are the same. B^* represents the optimal selling revenue of the producers in the robust model, while B_c represents the expected selling revenue. σ represents the risk tolerance level, which is the degree of deviation between the expected revenue target B_c and the actual revenue B_0. $\bar{p}_i$ represents the predicted values of various prices, while $\bar{q}_{i,j}$ represents the predicted values of runoff. α represents the fluctuation range of runoff and prices compared to the predicted values.

3.3.2 Model solving method

According to the established model, the goal of the lower layer of the model is to calculate the market revenue of the producers based on the maximum revenue model when the uncertain variable fluctuates within [1-α,1+α]. The goal of the upper layer of the model is to solve for the maximum deviation range of the uncertain variable α and obtain the corresponding power bidding strategy $e_{1,i}$ when the market revenue meets the model's predetermined target. This paper analyzes the market participation goals of the producers and performs an equivalent transformation on the two-layer model constructed according to literature (Moradi-Dalvand et al., 2015). The transformation steps and solving process are outlined in literature (Li et al., 2021). In order to use the Lingo or Gurobi solver to solve the problem of maximum monthly power generation, literature (Li et al., 2021) performed corresponding fitting on the relationship curves between the storage capacity-water level and the runoff rate-downstream water level of the cascade reservoir. However, since these curves are not smooth and regular, the curve fitting inevitably led to calculation results that deviate from the actual operating conditions.

In order to solve the calculation error problem caused by fitting, this article adopts a nonlinear programming and improved stepwise optimization hybrid algorithm for solution. Firstly, the initial scheduling process of a cascade hydropower station, which satisfies the constraints related to water level, flow rate, and reservoir capacity, is obtained using nonlinear optimization. And then, building upon the initial scheduling process, a stepwise optimization algorithm is employed, which converts the multi-stage optimization problem into several two-stage optimization subproblems. In each successive two-stage optimization subproblem, a combination set is formed by drawing random values for the variable values of each power station within their respective ranges. The combination that yields the optimal objective function value is then used to replace the original variable values. And last, this process is repeated sequentially for all subproblems,

completing one iteration. The process is iterated iteratively until the termination condition is met, resulting in the maximum power generation of the cascade hydropower producer for the current month under operational constraints.

The objective function of the two-stage optimization subproblem is defined as:

$$\begin{aligned}\max E' = \sum_{i=1}^{N}\sum_{t=1}^{T}\Big[&P_{i,t}\times\Delta t_t - \gamma_{i,1}\max\left(0, Q_{i,j}^{\min} - Q_{i,j}\right)\\ &-\gamma_{i,2}\left(0, Q_{i,j} - Q_{i,j}^{\min}\right) - \gamma_{i,3}\left(0, \left|\left|Q_{i,j} - Q_{i,j}^{\min}\right| - \Delta Q_{i,j}\right|\right)\\ &-\gamma_{i,4}\left(0, P_{i,j}^{\min} - P_{i,j}\right)\Big]\end{aligned} \tag{21}$$

Where $E^{'}$ is the objective function value of the subproblem. $\gamma_{i,1}$, $\gamma_{i,2}$,$\gamma_{i,3}$ and $\gamma_{i,4}$ are the penalty coefficients for station i violating the minimum discharge constraint, maximum discharge constraint, discharge ramp constraint, and minimum power output constraint, respectively.

When generating the water level combination set, if there is no reserved storage capacity constraint for the cascade hydropower stations, the water level combination is generated by randomly selecting n mutually exclusive random numbers within each power station's water level range. The Cartesian product is then used to generate the cascade hydropower station's water level combination set. If there is a reserved storage capacity constraint for the cascade hydropower stations, the water level combination set is composed of combinations that satisfy the storage capacity constraint.

$$\begin{cases} S_{i,j}^{\min} \le S_{i,j} \le S_{i,j}^{\max} \\ \sum_{i\in\Omega} S_{i,j} \le A_j^{\max} - A_j \\ Z_{i,j} = f_i\left(S_{i,j}\right) \end{cases} \tag{22}$$

The specific implementation method is as follows:

①Sort the power stations in Ω_j from upstream to downstream in ascending order and represent them as $i_1, i_2, ..., i_K$, where $K = |\Omega_j|$ is the number of power stations in the set.

②For each power station i_1, randomly select n^K numbers within the following reservoir storage range:

$$S_{i_1,j}^{\min} \le S_{i_1,j} \le \min\left[S_{i_1,j}^{\max}, A_j^{\max} - A_j - \sum_{k\in\{i_2,...,i_K\}} S_{k,j}^{\min}\right] \tag{23}$$

③For each reservoir storage level $S_{i_1,j}^{*}$ of power station i_1, randomly select one number within the following reservoir storage range of power station i_2 and associate it with $S_{i_1,j}^{*}$

$$S_{i_2,j}^{\min} \le S_{i_2,j} \le \min\left[S_{i_2,j}^{\max}, A_j^{\max} - A_j - S_{i_1,j}^{*} \sum_{k\in\{i_3,...,i_K\}} S_{k,j}^{\min}\right] \tag{24}$$

④Similarly, until the Kth power station is reached, there will be n^K combinations of reservoir storage levels. Based on the relationship between reservoir storage and water level, the combinations of reservoir storage levels are converted to combinations of water levels.

⑤For the N-K power stations without reservoir capacity constraints, randomly select n different water level combinations from their respective water level ranges and use the Cartesian product with the water level combination set in step ④ to generate the water level combination set for the cascaded hydropower stations.

The problem-solving process is shown in Figure 1.

3.4 Decision making model of mid long term market bidding based on prospect theory

3.4.1 Modeling

The Prospect theory suggests that a decision-maker's decision depends on the difference between the outcome and the expected value, rather than the outcome itself, based on different reference points. Based on this fundamental idea, $B_c = (1\text{-}\sigma)^* B_0$ in 3.3 is used as the expected revenue during the bidding phase. Therefore, the psychological perception revenue deviation ΔB between the revenue of selling electricity from cascade hydropower producers and B_c is:

$$\Delta B = B(x_k) - B_c \tag{25}$$

$$B(x_k) = \begin{cases} \sum_{i=1}^{N} B_{1,i}, & e_{1,i} > 0 \\ \sum_{i=1}^{N} e_i \times p_4, & e_{1,i} = 0 \end{cases} \tag{26}$$

where $B\ (x_k)$ is the revenue function of producers for proposal k during the bidding phase, considering both successful and failed bidding scenarios; p_4 is the on-grid electricity price of power station i, which is set to a uniform value for convenience of calculation in this paper.

The value function reflects the subjective value perception of the decision-maker of the producers towards the revenue deviation ΔB. When the electricity sales revenue exceeds its expected revenue, that is, $\Delta B>0$, according to the characteristics of the value function, the decision-maker is psychologically "gain-oriented" and tends to avoid risks. Conversely, they have risk-seeking characteristics. Therefore, combined with formulas 25 and 26, the value function is modified as follows:

$$v(x_k)_s = \begin{cases} \left(\sum_{i=1}^{N} B_{1,i} - B_c\right)^a, \Delta B \ge 0, e_{1,i} > 0 \\ -\lambda\left(B_c - \sum_{i=1}^{N} B_{1,i}\right)^b, \Delta B \le 0, e_{1,i} > 0 \end{cases} \tag{27}$$

$$v(x_k)_s = \begin{cases} \left(\sum_{i=1}^{N} e_i \times p_4 - B_c\right)^a, \Delta B \ge 0, e_{1,i} = 0 \\ -\lambda\left(B_c - \sum_{i=1}^{N} e_i \times p_4\right)^b, \Delta B \le 0, e_{1,i} = 0 \end{cases} \tag{28}$$

where $v\ (x_k)_s$ is the value function when scheme k is successfully declared, and $v\ (x_k)_d$ is the value function when scheme k is unsuccessfully declared.

As the market adopts the PAB settlement method in this paper, the higher the bidding prices of decision-makers for the producers, the greater the revenue obtained when the bid is successfully submitted. However, at the same time, the higher the bidding prices, the greater the risk of bid failure faced by them. Therefore, when bidding, decision-makers need to fully

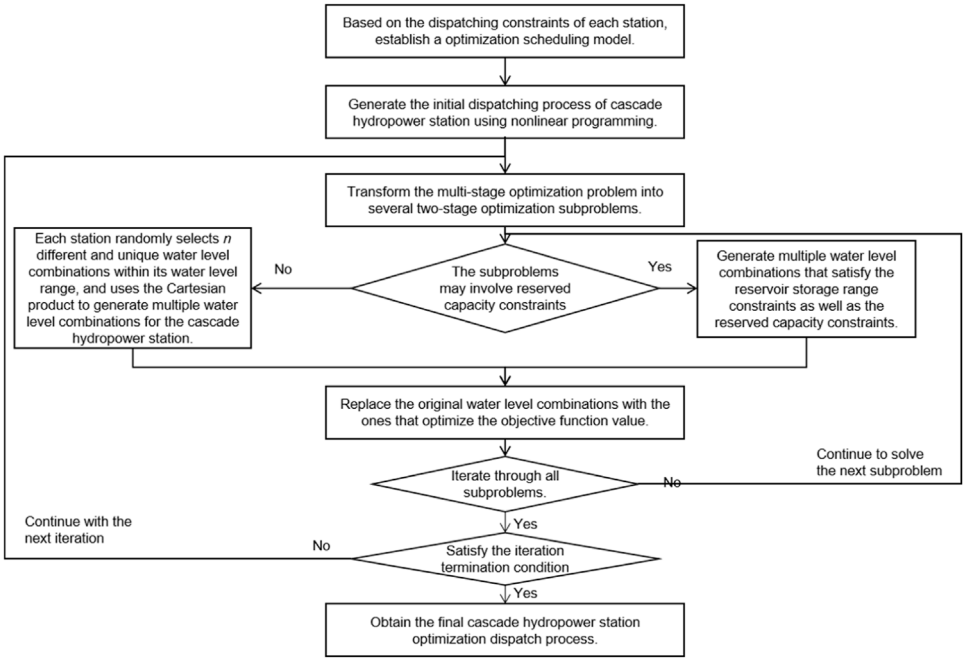

FIGURE 1
Flow chart of the model solution.

consider the risk of their decision-making programs and modify formulas 3 and 4 based on the successful bidding probability, as shown below:

$$\omega(p_{rok})_s = \frac{[F(p_{\max}) - F(p_k)]^{\theta}}{\{[F(p_{\max}) - F(p_k)]^{\theta} + [1 - F(p_{\max}) + F(p_k)]^{\theta}\}^{1/\theta}} \tag{29}$$

$$\omega(p_{rok})_d = \frac{[F(p_k) - F(p_{\min})]^{\sigma}}{\{[F(p_k) - F(p_{\min})]^{\sigma} + [1 - F(p_k) + F(p_{\min})]^{\sigma}\}^{1/\sigma}} \tag{30}$$

where $\omega(p_{rok})_s$ is the probability weight for scheme k when it is successfully cleared, and $\omega(p_{rok})_d$ is the probability weight for scheme k when it is unsuccessfully cleared; $p_{\max}$ and $p_{\min}$ are the maximum and minimum predicted clearing prices, respectively; p_k is the bidding price for the kth scheme; $F(p_{\max})$, $F(p_{\min})$ and $F(p)$ represent the probabilities corresponding to $p_{\max}$, $p_{\min}$ and p_k under a certain distribution, respectively; $F(p_{\max})$- $F(p_k)$ and $F(p_k)$- $F(p_{\min})$ represent the probabilities of successful and failed bidding, respectively.

Based on the analysis of the value function and probability weight function for producers during successful and failed bidding as described above, the bidding decision-making model is as follows:

$$\max V_k = v(x_k)_s \omega(p_{rok})_s + v(x_k)_d \omega(p_{rok})_d \tag{31}$$

where V_k is the comprehensive prospect value under the kth proposal; $v(x_k)_s$ and $v(x_k)_d$ are the value functions for the kth scheme when the bid is successful and unsuccessful, respectively.

3.4.2 Model solving method

The calculation process of the bidding decision-making model for the producers in the market based on prospect theory during the bidding stage is shown in Supplementary Appendix Figure A1. According to the objective function in Section 3.4.1, the optimization process is as follows:

①Using the expected revenue B_c obtained in Section 3.3 and the range of market clearing prices and daily discharge changes from [1-α,1+α] that satisfy the expected revenue as the reference point and the range of bidding prices for the prospect theory model.

②Select a representative daily flow process and use the maximum power output model to calculate the power output of the cascade hydropower station. Then, starting from $p_k = p_{\min}$, increase the bidding price by a fixed step, and calculate the revenue of the cascade hydropower station under various bidding decisions according to formulas (25) to (26).

③Calculate the value function $v(x_k)_s$ and $v(x_k)_d$ for each scheme when the bid is successful and unsuccessful based on the predetermined revenue B_c and formulas (27) and (28). Then, using formulas (29) and (30), calculate the probability weights $\omega(p_{rok})_s$ and $\omega(p_{rok})_d$ for each proposal when the bid is successful and unsuccessful. Finally, obtain the prospect value V_k for each scheme.

④Calculate the prospect value V_k for all scheme, and find the scheme with the maximum V_k. This scheme is the optimal bidding strategy for the producers.

4 Example analysis

The research background and examples of this paper are shown in reference (Li et al., 2021). Based on actual operation data, the historical

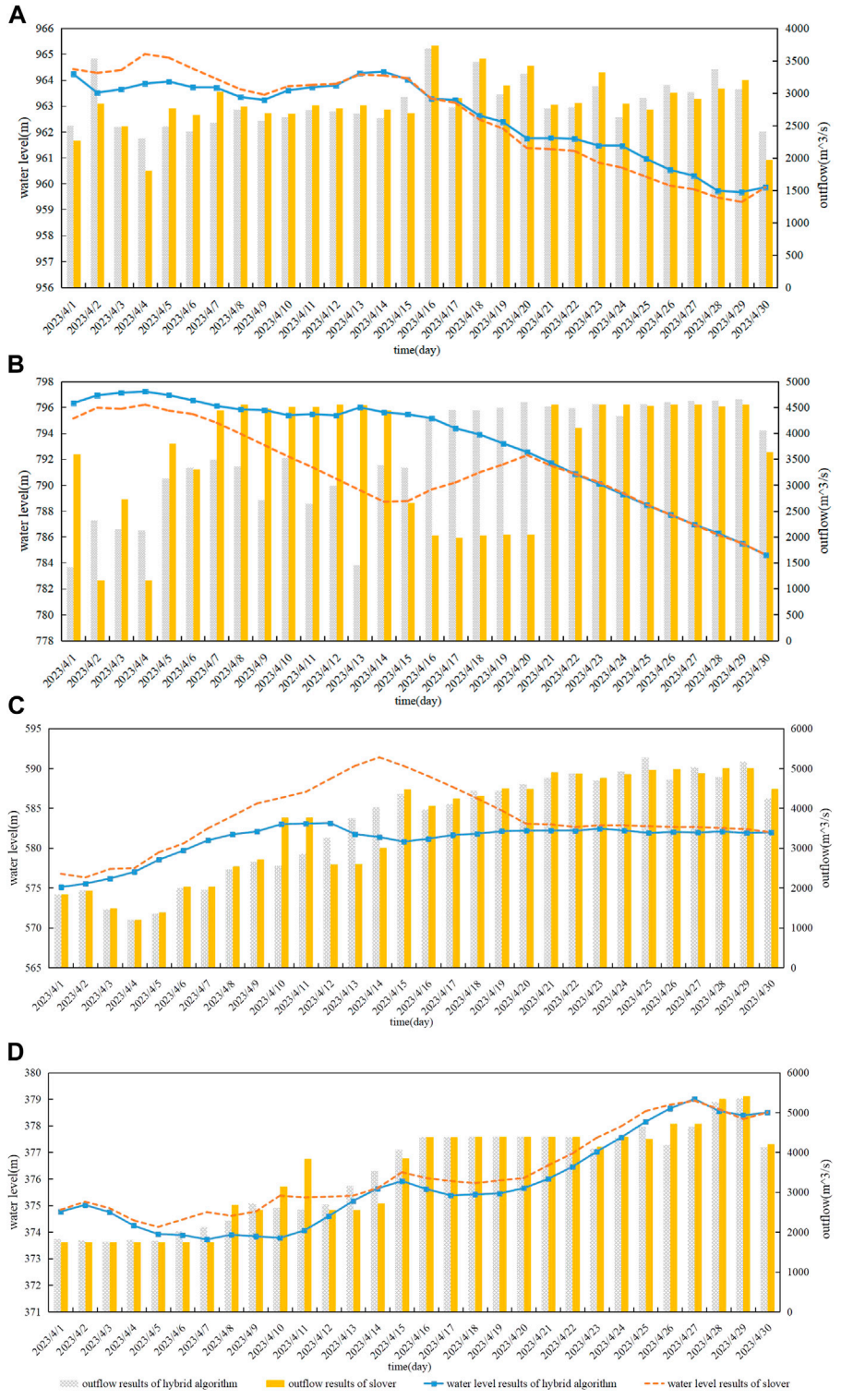

FIGURE 2
Display of calculation results of two algorithms. **(A)** Operating Process of Station A, **(B)** Operating Process of Station B, **(C)** Operating Process of Station C, **(D)** Operating Process of Station D.

average is used as the predicted value. The predicted market clearing price is 0.2553 yuan/kWh, the excess completion price is 0.19358 yuan/kWh, and the default assessment price is 0.2734 yuan/kWh. The on-grid price of 0.2 yuan/kWh is a constant. The basic information of each power station and the predicted storage level are shown in Appendices A1-A2. For the uncertainty of runoff, this paper only considers the leading hydropower station A. The interval runoff of downstream stations with weak regulation performance is calculated using the

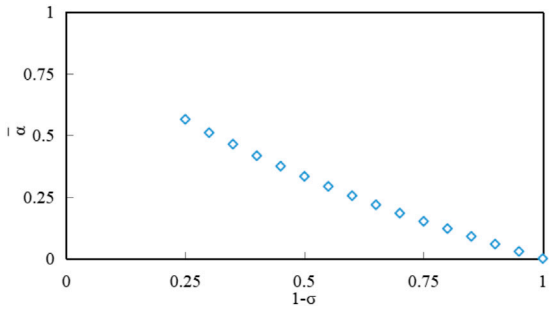

FIGURE 3
Variation curve of the robust region with the risk tolerance factor 1-σ.

multi-year average runoff value. The reason is that the generation of cascade hydropower stations in the dry season is mainly affected by the generation flow of upstream leading station which is not at the same level as that of the interval runoff.

4.1 Accuracy verification of solving algorithm

When the inflow forecast deviation α = At 0.151, the calculation results of the two algorithms are shown in Figure 2. The results of the hybrid algorithm are 14.417 billion kW hours, and the results of the solver are 14.325 billion kW hours.From the operation process of the cascade hydropower stations, the hybrid solution algorithm has a smoother process, and there are significant fluctuations in the output of the b and c stations in the solver's calculation results. Overall, the results of the hybrid algorithm are better than those of the solver.To verify the improvement in solving accuracy of the nonlinear programming and improved stepwise optimization hybrid algorithm used in this article.The generation results of the two algorithms are rechecked based on the method of controlling the water level process, and then the operating water level process is rechecked based on the method of controlling the outflow flow. If the difference between the recheck results and the original calculation results is smaller, it indicates that the corresponding algorithm has higher solution accuracy.According to the method of controlling water level, the review result of the hybrid algorithm is 14.42 billion kW hours, and the review result of the solver is 13.52 billion kW hours. From the results of the generation review, the calculation accuracy of the hybrid algorithm is higher. Due to the linear function of the water balance equation of the reservoir, it is only necessary to convert the water level into water volume in advance to perform linear calculations in the solution. Therefore, there is no deviation in the results of both algorithms when rechecking the water level process using the method of controlling the outflow. Overall, the hybrid algorithm has higher solving accuracy.

4.2 Risk analysis of cascade hydropower stations in operation stage

Based on the research in reference (Li et al., 2021)' the predicted clearing price and runoff are substituted into the maximum revenue model to solve the problem of maximizing the revenue of producers participating in markets. The revenue B_0 at this time is 3349.02 million yuan. The model established in this paper assumes that the actual runoff and clearing price in the future will fluctuate around the predicted values, with a fluctuation range of α. According to the different expected revenue targets or risk tolerance σ of producers, the curve of robust model objective $\bar{\alpha}(B_c)$ varying with risk tolerance or preference degree σ can be obtained, as shown in Figure 3. The calculation results are shown in Supplementary Appendix Table A3. The robust region refers to the maximum fluctuation range of price and runoff that satisfies the robust solution when the minimum expected revenue is met.

As can be seen from the model proposed in this paper, with the increase of the risk tolerance of producers, the maximum fluctuation range of uncertain variables also increases. That is, when the expected revenue is lower, the greater the fluctuation range of runoff and market price, the better the robustness of the power distribution strategy obtained, which is more resistant to larger runoff fluctuations. It is worth noting that no feasible solution can be obtained when σ< 0.25. Analysis of the reasons shows that the end water level of station C is 581.98 m, which is higher than the initial water level of 575.27 m. However, σ< 0.25 represents that the actual forecast inflow is significantly lower than the predicted value. In the current situation of low inflow, it is impossible to meet the initial and final water level requirements of station C.

After obtaining the maximum fluctuation range of clearing price and runoff, in order to facilitate producers formulating corresponding medium-term operation plans based on predetermined revenue, this paper draws the medium-term water level operation and output range of cascade hydropower stations when the robust region is [1-α,1+α].The specific results are shown in Figure 4. Figures 4A–D depict the operating water level range of stations A, B, and C when the runoff and market clearing price fluctuate by α = 0.151 around the predicted value. That is, when operating within this water level range, as long as the predicted error of electricity price and runoff does not exceed 15.1%, the marketized revenue of stations will not be lower than the expected revenue. Therefore, decision-makers can formulate corresponding operation and output plans within this range according to their own risk preferences, optimize medium-term dispatch plans, and avoid risks.

4.3 Risk analysis of cascade hydropower station bidding decision in bidding stage

Using the calculation results from the previous section, when 1-σ = 0.75, the expected revenue of the station is B_c = 2511.86 million yuan. The maximum fluctuation range of the actual values of runoff and clearing price relative to the predicted values is α = 0.151.That is, when the actual daily runoff and clearing price fluctuate by no more than 15.1% around the predicted values, the station's revenue can be guaranteed to be at least B_c = 2511.86 million yuan in the worst case. Based on Kahneman and Tversky's experimental measurements, the risk preference coefficient a is set to 0.88, the risk aversion coefficient b is set to 0.88, the risk attitude coefficients θ and θ are set to 0.61 and 0.67, respectively, and the sensitivity coefficient λ is set to 1.25. Different scenarios are then analyzed and solved.

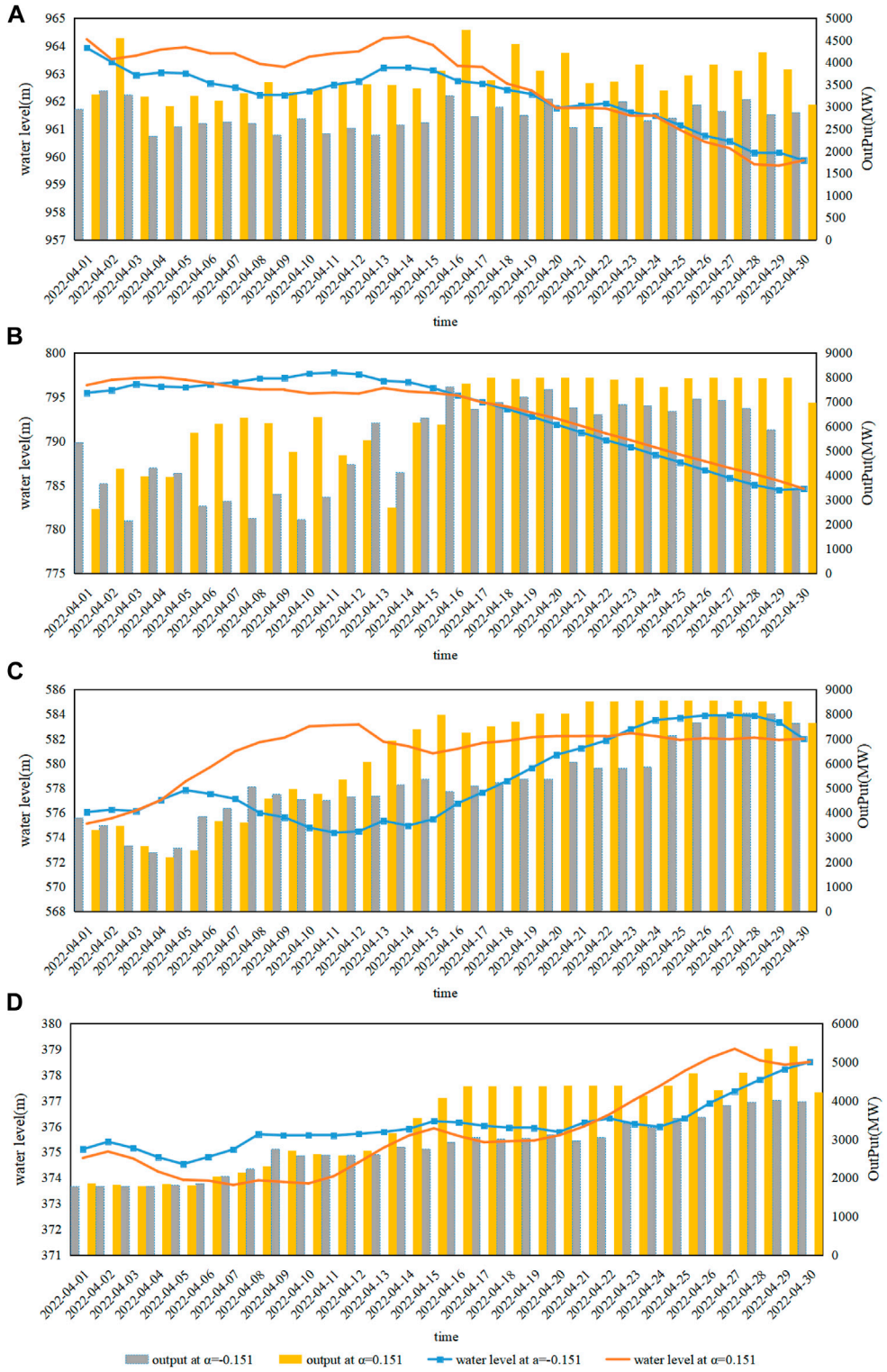

FIGURE 4
Operation range of cascade hydropower stations meeting the predetermined revenue. **(A)** Operating Process of Station **(A)** **(B)** Operating Process of Station **(B)** **(C)** Operating Process of Station **(C)** **(D)** Operating Process of Station **(D)**.

4.3.1 Model solving method

With a fixed expected revenue of B_c = 2511.86 million yuan and a clearing price ranging from 0.2168 to 0.2939, due to the limited data and potential fitting errors, it is assumed that the market clearing price follows a normal distribution of N (0.2553,0.016). The daily runoff is set to (1-α)*$q_{i,t}$, and the generation output of the station is 11.59 billion kW hours. The bidding price is fixed at a step size of 0.005 yuan/kWh, and the prospect value of different bidding

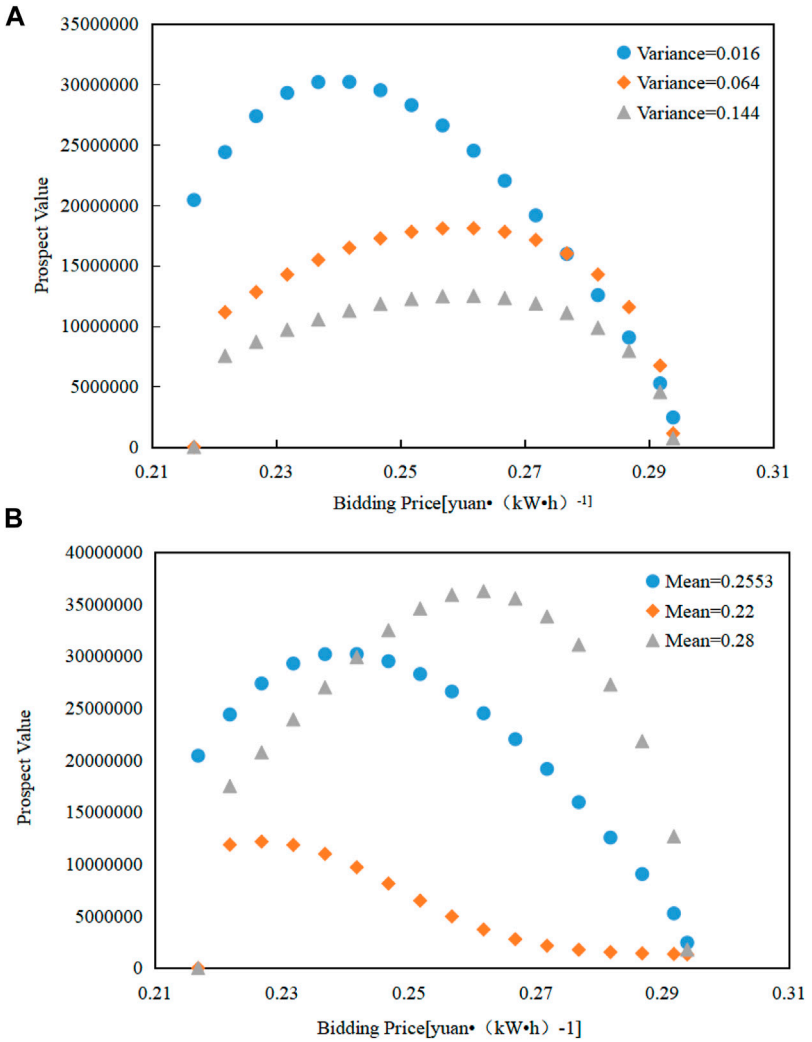

FIGURE 5
Optimal bidding price under different parameters with fixed expected return. **(A)** Influence of variance on optimal decision. **(B)** Influence of mean value on optimal decision.

strategies is calculated. Then, by varying the mean and variance of the market clearing price, the prospect value is calculated and plotted as shown in Figure 3.

From Figure 5A, it can be seen that the variance represents the degree of fluctuation in predicted market clearing price. The smaller the variance, the smaller the price fluctuation, leading to a more concentrated price distribution and a higher probability of falling within the given $[1-\alpha,1+\alpha]$ interval. Conversely, the larger the variance, the greater the price fluctuation, leading to a more dispersed price distribution and a lower probability of falling within the given interval.When the variance is 0.016, the price distribution is mostly concentrated within the interval specified by the IGDT robust model. To avoid losses from quoting too high and not being able to successfully cleared, the optimal bidding price for the decision-makers is 0.2368 yuan/kWh. When the variance is 0.064 and 0.144, the proportion of price distribution within the interval specified by the IGDT robust model is relatively small and dispersed. At this time, the optimal bidding prices for the decision-makers are 0.2568 yuan/kWh and 0.2618 yuan/kWh, slightly higher than the prices when the variance is 0.016.

As can be seen from Figure 5B, the mean has a greater impact on the bidding strategy than the variance.The mean represents the central location of the predicted market clearing price and affects the probability of a successful cleared. Within the price interval specified by the IGDT robust model, if the mean is closer to the lower bound, the optimal bidding price to ensure a successful cleared will also decrease. For example, when the mean is 0.22 yuan/kWh, the optimal bidding price for the decision-makers is 0.2168 yuan/kWh, and the prospect is negative, representing that this bidding strategy cannot meet the expected revenue of the decision-making, and its psychology is “loss”. When the mean is larger, the optimal bidding price also increases. For example, when the mean is 0.2553 yuan/kWh and 0.28 yuan/kWh, the optimal bidding price is 0.2368 yuan/kWh and 0.2568 yuan/kWh, respectively, and the model results are consistent with the facts.

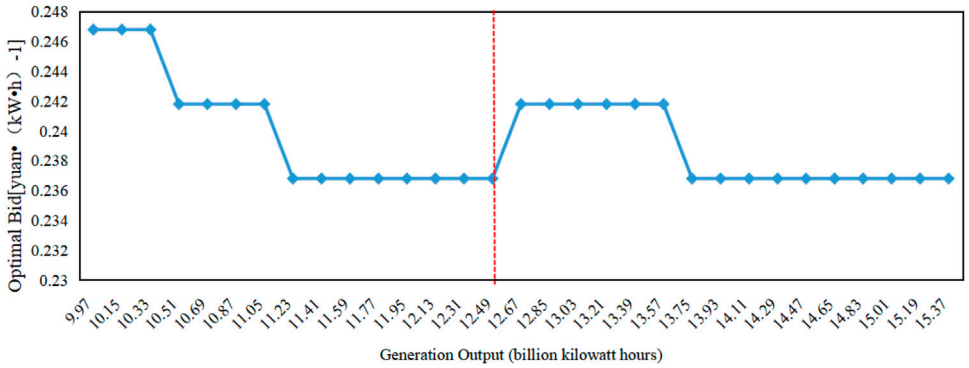

FIGURE 6
Influence of expected return on generation in IGDT robust model.

4.3.2 Impact of bidding volume change on bidding strategy

When the daily runoff varies within $[(1-\alpha)^*q_{i,t}, (1+\alpha)^*q_{i,t}]$, the generation output of the cascade hydropower station changes within [9.96878, 15.36877] billion kW hours, while other parameters remain unchanged. The optimal bidding price for the decision-maker is calculated under different generation outputs, as shown in Figure 6.

As shown in Figure 4, the expected revenue of the station is B_c = 2511.86 million RMB. According to the transaction settlement rules, when the power generation company fails to bid, the settlement price shall be 0.2 yuan/kWh.The producers needs to ensure at least 12.5 billion kW hours of electricity to meet its own expected revenue, even if the bidding fails.Therefore, when the generation output is less than 12.5 billion kW hours, that is, the sales revenue is less than the expected revenue, the decision-maker is "loss-averse" in terms of psychology. When facing a "loss-averse" situation, decision-maker often have a strong risk appetite and will choose higher-risk prices for bidding. As the generation output increases, the revenue increase from only relying on the on-grid tariff settlement, that is, the "loss" from failed bidding decreases, and the risk appetite of decision-maker weakens, so they will choose relatively lower-risk prices for clear. When the generation output is in the range of 12.5–12.6 billion kW hours, the optimal bidding price will increase slightly, that is, as the decision-maker transitions from "loss" to "gain" in terms of psychology, the comprehensive prospect value of slightly increasing the bidding price is greater than that only relying on the on-grid tariff settlement. When the generation output is greater than 12.5 billion kW hours, that is, the sales revenue is greater than the expected revenue, the decision-maker is "gain-seeking" in terms of psychology, and has a strong risk aversion tendency. They will choose lower-risk prices for bidding. However, after the generation output increases to a certain degree, the optimal bidding price of decision-maker remains unchanged. The model in this paper reflects the characteristic of decision-maker being loss-averse and gain-seeking in terms of risk appetite when facing different psychological expectations, which makes the decision results more in line with the psychological desires of decision-maker.

5 Conclusion

Based on IGDT and prospect theory, this paper proposes a mid-term optimization scheduling and trading decision-making method for cascade hydropower producers in the power market that jointly considers the bidding stages and the dispatching and operation risks. The optimization scheduling model for the dispatching stage is conceptually clear, operationally simple, and the results are intuitive, enabling the calculation of the maximum deviation range of daily runoff and market clearing prices from the predicted values when satisfying the decision-maker's predetermined revenue. From the perspective of limited rationality, the model considers the decision-maker's risk appetite for different revenue reference points in bidding stages, which is more in line with the facts, and obtains the optimal bidding strategy within a given range of clearing price changes. In order to solve the calculation error problem caused by fitting, this article adopts a nonlinear programming and improved stepwise optimization hybrid algorithm for solution. The research indicates that:

①When analyzing the risks of cascade hydropower producers in the power market environment, it is not sufficient to solely rely on the total revenue of each scenario. Instead, evaluations need to be conducted based on their psychological reference points. Therefore, the degree of risk preference held by operators is a key factor in determining both bidding and operating strategies. Furthermore, an operator's risk appetite can vary depending on their changing psychological expectations.

②This method provides robust models that can withstand fluctuations in daily runoff and market clearing prices for mid-term scheduling and operation plans that meet different expected revenue targets for producers. Then, using prospect theory, the optimal bidding strategy in the long-term and medium-term markets within a given range of expected revenue and electricity price changes is obtained. Risk-averse and risk-seeking entities can evaluate different plans and adopt corresponding strategies to ensure expected revenue targets.

③The IGDT method requires little information about uncertain factors and does not require obtaining the probability distribution of uncertain parameters, making it

suitable for dealing with risk decision-making problems with severe uncertainty. The robustness of the model is reflected in the maximum deviation range of the uncertain variables from the predicted values when ensuring that the expected target is not worse than a certain minimum preset result. Prospect theory takes into account the decision-maker's psychology, making electricity price bidding decisions more in line with the actual decision-maker's behavioral patterns.

Data availability statement

The original contributions presented in the study are included in the article/Supplementary Material, further inquiries can be directed to the corresponding author.

Author contributions

All authors listed have made a substantial, direct, and intellectual contribution to the work and approved it for publication.

Funding

This study is supported by the National Key Research and Development Program of China (No. 2019YFC0409000).

Acknowledgments

The authors are very grateful to the anonymous reviewers and editors for their constructive comments.

Conflict of interest

Authors JL, YL, HC, YX, HM, ZZ, TW, and YY were employed by China Yangtze Power Co. Ltd.

Publisher's note

Supplementary material

The Supplementary Material for this article can be found online at: https://www.frontiersin.org/articles/10.3389/fenrg.2023.1252624/full#supplementary-material

References

Cheng, C., Chen, F., Li, G., Ristić, B., Mirchi, A., Qiyu, T., et al. (2018). Reform and renewables in China: the architecture of yunnan's hydropower dominated electricity market. *Renew. Sustain. Energy Rev.* 94, 682–693. doi:10.1016/j.rser.2018.06.033

Dai, T., and Qiao, W. (2015). Optimal bidding strategy of a strategic wind power producer in the short-term market. *IEEE Trans. Sustain. energy* 6 (3), 707–719. doi:10.1109/TSTE.2015.2406322

Federico, G., and Rahman, D. M. (2001). Bidding in an electricity pay-as-bid auction. *J. Regul. Econ.* 24 (2), 175–211. doi:10.2139/ssrn.271700

Kahn, A. E., Porter, C., Robert, R. H., and Tabors, R. D. (2001). Uniform pricing or pay-as-bid pricing. *Electr. J.* 14 (6), 70–79. doi:10.1016/S1040-6190(01)00216-0

Li, G., Lu, J., Yang, R., and Chuntian, C. (2021). IGDT-based medium-term optimal cascade hydropower operation in multimarket with hydrologic and economic uncertainties. *J. Water Resour. Plan. Manag.* 147 (10), 1–11. doi:10.1061/(asce)wr.1943-5452.0001444

Li, S., Liao, S., Li, G., Cheng, C., and Li, X. (2012). Integrated power generation scheduling compilation method for large-scale small hydropower station group. *Proc. Csee* 32 (13), 29–35. doi:10.13334/j.0258-8013.pcsee.2012.13.003

Li, T., Gao, C., Chen, T., and Zhang, T. (2022). Medium and long-term electricity market trading strategy considering renewable portfolio standard in the transitional period of electricity market reform in Jiangsu, China. *Energy Econ.* 57, 107–112. doi:10.3760/cma.j.cn112144-20211009-00457

Liu, S., Yang, Q., Cai, H., Yan, M., Zhang, M., Wu, D., et al. (2019). Marketreform of yunnan electricity in southwestern China: practice,challenges and implications. *Renew. Sustain. Energy Rev.* 113, 109265. doi:10.1016/j.rser.2019.109265

Lu, J., Li, G., Cheng, C., and Liu, B. (2021). A long-term Intelligent operation and management model of cascade hydropower stations based on chance constrained programming under multi-market coupling. *Environ. Res. Lett.* 16 (5), 055034. doi:10.1088/1748-9326/abef90

Moradi-Dalvand, M., Mohammadi-IvatlooAmjady, B., Zareipour, H., and Mazhab-Jafari, A. (2015). Self-scheduling of a wind producer based on information gap decision theory. *Energy* 81, 588–600. doi:10.1016/j.energy.2015.01.00

Nojavan, S., Mohammadi-Ivatloo, B., and Zare, K. (2015a). Retracted: robust optimization based price-taker retailer bidding strategy under pool market price uncertainty. *Int. J. Electr. Power & Energy Syst.* 73, 955–963. doi:10.1016/j.ijepes.2015.06.025

Nojavan, S., Zare, K., and Ashpazi, M. A. (2015b). A hybrid approach based on IGDT–MPSO method for optimal bidding strategy of price-taker generation station in day-ahead electricity market. *Int. J. Electr. Power & Energy Syst.* 69, 335–343. doi:10.1016/j.ijepes.2015.01.006

Peng, C., Sun, H., Guo, J., and Liu, G. (2012). Multi-objective optimal strategy for generating and bidding in the power market. *Energy Convers. Manag.* 57, 13–22. doi:10.1016/j.enconman.2011.12.006

Rodriguez, C. P., and Anders, G. J. (2004). Bidding strategy design for different types of electric power market participants. *Power Syst. IEEE Trans.*19 (2), 964–971. doi:10.1109/TPWRS.2004.826763

Tversky, A., and Kahneman, D. (1992). Advances in prospect theory. *J Risk Uncertain.* 5 (4), 297–323. doi:10.1007/bf00122574

Tversky, K. A. (1979). Prospect theory: an analysis of decision under risk. *Econometrica* 47 (2), 263–291. doi:10.2307/1914185

Wright, L. F. (2004). Information gap decision theory: decisions under severe uncertainty. *J. R. Stat. Soc.* 167 (1), 185–186. doi:10.1111/j.1467-985x.2004.298_4.x

Yao, Y., Gao, C., Tian, H., and Zhang, H. (2020). Review of mid-to long-term trading mechanism for renewable electricity consumption in Ningxia, China. *Renew. Sustain. Energy Rev.* 134, 110325. doi:10.1016/j.rser.2020.110325

Zare, N. K., and Zare, K. (2013). Risk-based optimal bidding strategy of generation company in day-ahead electricity market using information gap decision theory. *Int. J. Electr. Power & Energy Syst.* 48, 83–92. doi:10.1016/j.ijepes.2012.11.028

frontiers | Frontiers in Energy Research

TYPE Policy and Practice Reviews
PUBLISHED 20 October 2023
DOI 10.3389/fenrg.2023.1271934

OPEN ACCESS

EDITED BY
Bin Zhou,
Hunan University, China

REVIEWED BY
Xiong Cheng,
China Three Gorges University, China
Shijun Chen,
Sichuan University, China

*CORRESPONDENCE
Jianjian Shen,
shenjj@dlut.edu.cn

RECEIVED 03 August 2023
ACCEPTED 29 September 2023
PUBLISHED 20 October 2023

CITATION
Han X, Shen J and Cheng C (2023), Market bidding method for the inter-provincial delivery of cascaded hydroelectric plants in day-ahead markets considering settlement rules. *Front. Energy Res.* 11:1271934. doi: 10.3389/fenrg.2023.1271934

Market bidding method for the inter-provincial delivery of cascaded hydroelectric plants in day-ahead markets considering settlement rules

Xu Han, Jianjian Shen* and Chuntian Cheng

Institute of Hydropower and Hydroinformatics, Dalian University of Technology, Dalian, China

Chinese electricity market reform poses huge challenges to hydropower operations and electricity trading. This study proposes a scheduling method coupling priority electricity and day-ahead trading for large hydropower plants. The study focuses on complex factors such as tariff uncertainty, different types of electricity settlement rules, and inter-provincial electricity transmission links. Spot market tariff scenarios are determined through the Latin hypercube and the K-means methods. A performance formulation of priority electricity deviation considering settlement assessment rules is established. A transmission description for different sub-plants and a triangular linear interpolation method based on binary independent branching mode are proposed to solve inter-regional transmission connections and hydraulic coupling in cascaded hydropower plants, respectively. Finally, the Big M method is employed to equivalently transform the complex non-linear problem into a mixed-integer linear programming (MILP) model. The method is verified with the day-ahead operation of four large hydropower plants downstream of the Jinsha River in China as a case study. Settlement assessment rules, inter-regional power transmission, and price uncertainty are analyzed in three different cases. Three conclusions are obtained: 1) the priority electricity performance rate and the price are positively correlated, which is useful to guide hydropower plants to actively participate in the market. 2) Introducing the prediction error of electricity price in the model can help avoid market decision risk and improve the expected return by approximately 1.2%. 3) Considering the settlement penalty rule is helpful for power generation enterprises to improve power allocation and thus seek higher revenue compared to traditional methods without considering it.

KEYWORDS

electricity market, mixed-integer linear programming, electricity decomposition, day-ahead market, settlement rules

1 Introduction

In March 2015, China issued "Several Opinions on Further Deepening the Reform of the Electricity System," kicking off the reform of China's electricity (Chen et al., 2022; Cheng et al., 2023). The aim is to restore the commodity attributes of electric energy, establish a fully competitive, open, and orderly Chinese electricity market, and enable the market to play a decisive role in power resource allocation. There are significant

advantages for hydropower to participate in the electricity market. Hydropower exhibits high regulation capacity (Pérez-Díaz et al., 2010; Gómez-Navarro and Ribó-Pérez, 2018; Shen et al., 2022) with low operating costs (Cheng et al., 2018; Rodríguez-Sarasty et al., 2021). At the same time, hydropower faces unprecedented challenges. In long-term operation, hydropower generation is strongly dependent on the water stored in the reservoir and inflow uncertainty in the future. In short-term generation scheduling, the electricity price in the day-ahead (Golmohamadi et al., 2021; Lago et al., 2021; Tschora et al., 2022) market is another important factor that is influenced by the load and nodal blockage in each receiving province. Currently, hydropower simultaneously faces long-term trading and short-term spot markets (Cai et al., 2020; Jia et al., 2022). The former involves both priority electricity and market trading, and the latter has to meet complex hydraulic connections and constraints, as well as market limitations (Guo et al., 2021). Such a complex situation inevitably poses severe challenges to hydropower scheduling, the decomposition of priority electricity, and the participation in the electricity market. Specifically, large hydropower plants with inter-provincial power transmission tasks must consider the multiple different markets, which further lead to additional complexities in market bidding and operations.

In the central dispatch mode, hydropower plants usually consider the results of medium- and long-term priority electricity decomposition, runoff forecast information, unit operating restrictions, transmission channel blockage, and other conditions to make day-ahead generation schedules (Avesani et al., 2022; Jiang et al., 2023; Zhang et al., 2023). However, in the electricity market environment with priority electricity and market trading, hydropower plants need to deal with three major day-ahead production tasks: 1) decomposing power curves of priority electricity for multiple power grids; 2) making day-ahead markets for declaration; and 3) determining day-ahead generation schedules for each hydropower unit.

As is known, the spot market price is affected by complex supply and demand relationships, bringing significant uncertainty to short-term trading decisions (Tang and Zhang, 2020; Guo et al., 2021; Wu et al., 2022). There have been many studies about hydropower operations and bidding in the electricity market. We summarize four main categories.

The first is market design and mechanism optimization (Fang et al., 2017; Shen et al., 2018; Stančin et al., 2020; Xinhong et al., 2020). These studies focused on the design and mechanism of hydropower marketing in order to facilitate effective supply and demand matching and optimize price discovery and transaction efficiency, for example, a trading decision-making method that uses the electricity market to promote established clean energy accommodation. Making full use of load difference, peak-to-valley difference, and time difference, a joint optimization model of clean energy purchasing–selling–transmission is established to promote clean energy accommodation. The second is cross-regional and inter-national hydropower trading (Lu et al., 2021). For instance, Lu et al. (2021) analyzed the types and channels of trans-provincial and trans-regional power transactions and then analyzed the mechanism of resource optimization allocation of trans-provincial and trans-regional power transactions. The third is cross-energy scheduling and trading (Merkert et al., 2015; Xiao et al., 2015; Wang and Huang, 2018). These studies focused on the collaborative scheduling and trading of hydropower with other energy sources (such as wind, solar, and storage) to optimize the overall utilization of renewable energy and the stability of the power system. This requires consideration of complementarities between different energy sources, coordinated dispatch, and market trading. For example, Wang and Huang (2018) studied the interactions among interconnected autonomous microgrids and developed a joint energy trading and scheduling strategy. The last aspect is uncertainty and risk management (Yuan et al., 2016; Carvajal et al., 2017; Kebede et al., 2022; Xu et al., 2022). These studies focused on investigating how to effectively deal with uncertainties and risks in hydropower dispatch (Kebede et al., 2022), such as water source changes, market price fluctuations, and external environmental changes. This may involve aspects such as uncertainty modeling, risk assessment, and risk management strategies. In particular, Carvajal et al. (2017) presented a method to assess the sensitivity of hydropower generation to uncertain water resource availability driven by future climate change.

Few of the aforementioned studies considered power defaults and hydropower flexibility in market trading, and even fewer studies involved both the complex actual operation constraints of hydropower units and power decomposition requirements for multiple power grids. In this paper, we propose a scheduling method coupling priority electricity and day-ahead trading for large hydropower plants, considering complex factors such as electricity price uncertainty, different types of power settlement rules, and inter-provincial power transmission connections. In this method, the spot market electricity price scenarios are determined using Latin hypercube sampling (Zhang et al., 2020; Bulut et al., 2021; Karolczuk and Kurek, 2022) and K-means clustering. A performance formulation of priority electricity deviation considering settlement assessment rules is established. A transmission description for different sub-plants and a triangular linear interpolation method based on binary independent branching mode are proposed to solve inter-regional transmission connections and hydraulic coupling in cascaded hydropower plants, respectively. Finally, the Big M method (Ding et al., 2014; Zhang et al., 2021) is employed to equivalently transform the complex non-linear problem into a mixed-integer linear programming (MILP) model (Krien et al., 2020; Zhao et al., 2021; Cao et al., 2022).

The remainder of the paper is organized as follows: the objective function and constraints are described in Section 2. Section 3 describes the tariff uncertainty approach and the associated linearization strategy. Section 4 shows the results of the demonstration calculation. Finally, Section 5 providesthe conclusion.

2 Mathematical models

2.1 Objective function

Taking into account the basic benefits of the medium- and long-term decomposition of planned electricity to day, the

negative deviation penalty of the actual decomposition of day-ahead, and the day-ahead market time-of-use tariff settlement benefits, the model objective function is divided into the following three components:

$$\max F = f_1 - f_2 + f_3, \tag{1}$$

$$f_1 = \sum_{i=1}^{I} \sum_{k \in K_i} \sum_{t=1}^{T} R_{i,k}^{p} \cdot E_{i,k,t}^{p}. \tag{2}$$

Negative deviation penalty rule for planned electricity. Negative deviation power is penalized by planned electricity price.

$$f_2 = \sum_{i=1}^{I} \sum_{k \in K_i} \sum_{t=1}^{T} (1+\alpha) \cdot R_{i,k}^{p} \cdot \max\left(E_{i,k,t}^{p} - p_{i,k,t}^{r} \cdot \Delta t, 0\right), \tag{3}$$

$$f_3 = \sum_{i=1}^{I} \sum_{k \in K_i} \sum_{t=1}^{T} R_{i,k,t}^{m} \cdot \max\left(p_{i,k,t}^{r} \cdot \Delta t - E_{i,k,t}^{p}, 0\right). \tag{4}$$

Here, f_1 is the contract electricity revenue; f_2 is the planned electricity negative deviation penalty; f_3 is the day-ahead market revenue; α is the penalty coefficient of planned electricity; $R_{i,k}^{p}$ is the planned electricity of power station i in province k; $R_{i,k,t}^{m}$ is the market price of power station i in province k at time t; $E_{i,k,t}^{p}$ is the planned electricity of power station i in province k at time t; and $p_{i,k,t}^{r}$ is the output of power station i in province k at time t;

2.2 Constraints

2.2.1 Hydroelectric power plant-related constraints

(1) Water balance constraint

$$v_{i,t} = v_{i,t-1} + \left(QIN_{i,t} + \sum_{i' \in DUP_i} u_{i',t} - u_{i,t} \right), \tag{5}$$

where $v_{i,t}$ is the reservoir capacity of power station i at time t, in billions; $QIN_{i,t}$ is the interval inflow of power station i at time t; DUP_i is the set of upstream power stations with hydraulic connection of power station i; and $u_{i,t}$ is the outflow of power station i at time t.

(2) Water level–reservoir capacity relationship and upper and lower limits of the water level

$$v_{i,t} = fzv_i(z_{i,t}), \tag{6}$$

$$Z\min_{i,t} \le z_{i,t} \le Z\max_{i,t}, \tag{7}$$

where fzv_i is the relationship between the water level and reservoir capacity of power station i and $Z\min_{i,t}$ and $Z\max_{i,t}$ are the upper and lower limits of the water level of power station i at time t, respectively.

(3) Flow balance and upper and lower limit constraints

$$u_{i,t} = q_{i,t} + s_{i,t}, \tag{8}$$

$$U\min_{i} \le u_{i,t} \le U\max_{i}, \tag{9}$$

$$Q\min_{i} \le q_{i,t} \le Q\max_{i}, \tag{10}$$

where $u_{i,t}$ is the outgoing flow of power station i at time t; $q_{i,t}$ is the generation flow of power station i at time t; $s_{i,t}$ is the disposal flow of power station i at time t; $U\min_i$ and $U\max_i$ are the minimum and maximum outgoing flows of power station i, respectively; and $Q\min_i$ and $Q\max_i$ are the minimum and maximum generation flows of power station i, respectively.

(4) The relationship between the flow rate and the tailwater level

$$zd_{i,t} = fzdu_i(u_{i,t}), \tag{11}$$

where $zd_{i,t}$ is the tailwater level of power station i at time t and $fzdu_i$ is the tailwater level–discharge flow relationship of power station i.

2.2.2 Unit-related constraints

(1) Power generation characteristic curve relationship of the unit

$$pe_{i,e,t} = fphq_{i,e}(qe_{i,e,t}, he_{i,e,t}), \tag{12}$$

where $fphq_{i,e}$ is the output characteristic relationship of unit e power station i; $pe_{i,e,t}$ is the output of unit e power station i at time t; $qe_{i,e,t}$ is the generation flow of unit e power station i at time t; and $he_{i,e,t}$ is the head of unit e power station i at time t.

(2) Unit stable output operation area

$$oc_{i,e,t} \cdot \underline{P}_{i,e} \le pe_{i,e,t} \le oc_{i,e,t} \cdot \bar{P}_{i,e}, \tag{13}$$

where $oc_{i,e,t}$ is the start–stop status of unit e power station i at time t, with 0 for off and 1 for on; $\bar{P}_{i,e}$ is the upper limit of stable operation output of unit e power station i; and $\underline{P}_{i,e}$ is the lower limit of stable operation output of unit e power station i.

(3) Stable flow constraint of the unit

$$oc_{i,e,t} \cdot \underline{Q}_{i,e} \le qe_{i,e,t} \le oc_{i,e,t} \cdot \bar{Q}_{i,e}, \tag{14}$$

where $\bar{Q}_{i,e}$ is the upper limit of the quoted flow rate for the stable operation of unit e power station i and $\underline{Q}_{i,e}$ is the lower limit of the quoted flow rate for the stable operation of unit e power station i.

(4) Head calculation constraint

$$he_{i,e,t} = \frac{(z_{i,t} + z_{i,t-1})}{2} - zd_{i,t} - hl_{i,e,t}, \tag{15}$$

where $hl_{i,e,t}$ is head loss of unit e power station i at time t.

(5) Start/stop-related constraints

Although hydro units can be adjusted quickly, frequent start-ups and shutdowns still have a negative impact on the unit's service life and operating costs. To avoid frequent start-ups and shutdowns of hydro units, online and offline hourly constraints are introduced.

$$\begin{cases} o_{i,e,t} + \sum_{\eta=t+1}^{t+\alpha_{i,e}-1} c_{i,e,\eta} \le 1, \\ c_{i,e,t} + \sum_{\eta=t+1}^{t+\alpha_{i,e}-1} o_{i,e,\eta} \le 1, \\ o_{i,e,t} - c_{i,e,t} = oc_{i,e,t} - oc_{i,e,t-1}, \\ o_{i,e,t} + c_{i,e,t} \le 1, \end{cases} \tag{16}$$

where $o_{i,e,t}$ indicates whether unit e power station i performs start-up action at time t, where 0 represents no and 1 represents yes; $c_{i,e,t}$ indicates whether unit e power station i performs shutdown action at time t, where 0 represents no and 1 represents yes.

(6) Correlation between power station and unit output

$$p_{i,t} = \sum_{e \in e_i} pe_{i,e,t}. \tag{17}$$

(7) Correlation between power station and unit generation flow

$$q_{i,t} = \sum_{e \in e_i} qe_{i,e,t}. \tag{18}$$

Here, $pe_{i,e,t}$ is the output of unit e power station i at time t and $qe_{i,e,t}$ is the generation flow of unit e power station i at time t.

2.2.3 Market power decomposition constraints

$$\sum_{k \in K_i} p^r_{i,k,t} = p_{i,t}, \tag{19}$$

$$\begin{aligned} (PR_{i,k} + RC) \cdot \sum_{k^* \in K_i} \sum_{t=1}^{T} \max\left(p^r_{i,k^*,t} - E^p_{i,k^*,t}, 0\right), \\ \geq \max\left(p^r_{i,k,t} - E^p_{i,k,t}, 0\right) \geq, \\ (PR_{i,k} - RC) \cdot \sum_{k^* \in K_i} \sum_{t=1}^{T} \max\left(p^r_{i,k^*,t} - E^p_{i,k^*,t}, 0\right), \end{aligned} \tag{20}$$

where $PR_{i,k}$ is the proportional requirement of power delivery of power station i in province k and RC is the floatable proportional limit of marketed power (set at 0.2 in this paper)

3 Model processing strategy

3.1 Uncertainty description method of the price

Since electricity prices are affected by multiple complex factors such as grid blockage (Golmohamadi et al., 2021), market transactions (Tschora et al., 2022), and weather conditions (Lago et al., 2021), coupled with limitations in spot electricity price forecasting technology, there are bound to be certain deviations between the predicted and actual values of spot market electricity prices. Therefore, the uncertainty of the next day's spot market electricity price should be fully considered when formulating short-term dispatching plans. In general, the forecast error distribution law of the electricity price is a finite skewed distribution at both ends, but generally the corresponding normal and skewed distributions do not differ much. Therefore, this model describes the electricity price uncertainty as follows (Figure 1):

(1) Assume that the forecast error $\{R^d_1, R^d_2, ..., R^d_T\}$ of the spot tariff for each time period follows a normal distribution with a mean of $\mu = 0$ and a mean squared deviation of $0.2 \cdot \bar{R}^d_t$, where $\bar{R}^d_t$ is the forecast tariff for time period t.

(2) The Latin hypercube sampling (LHS) method is used to generate multiple tariff simulation scenarios. The core technique of this method is to first stratify the probability distribution of the samples and then randomly select samples from each stratum in turn. The cumulative probability distribution function $F(R^d_t)$ is calculated for each time period based on the mean and mean squared deviation assumed in (1), and $F(R^d_t)$ is divided into N non-overlapping subintervals, each with a spacing of $1/N$. An integer i is randomly selected from the set $\{1, 2...N\}$, representing the interval where the cumulative probability distribution lies. Subsequently, a random number in a range of $[0, 1]$ is generated, which is denoted as r corresponding to the interval i. The cumulative probability function for P^*_t is $P^*_t = (1/N)r + (i-1)/N$. Finally, the inverse function of the cumulative probability distribution function $F^{-1}(R^d_t)$ is substituted by P^*_t to obtain the corresponding tariff data sampling value.

(3) In order to fully reflect the stochastic variation characteristics of the spot market clearing price, the LHS method in (2) is used to generate many electricity price scenarios. If all scenarios are considered in the model, it will significantly affect the computational efficiency, but if very few scenarios are considered, the computational accuracy will be lower. Therefore, in order to balance solution accuracy and efficiency, the K-means clustering algorithm based on the initial clustering centers and contour coefficients is used (Cheng et al., 2023) to reduce the number of scenarios as much as possible while maintaining the important features of the tariff scenarios.

3.2 Power station–substation difference regional outbound relationship processing

The Jinxia terraced power station contains various differential cases of outgoing transmission of sub-plants: (1) the power stations in the left and right banks represented by the Wudongde power station have the same outgoing and retained provinces. (2) The left and right bank outgoing provinces represented by Baihetan are different, but the retained provinces are the same. (3) In the case of Xiluodu, the power plants in both the left and right banks are different in terms of outgoing and retained provinces.

First, the aforementioned three cases require refined modeling of the outgoing power and the output of the corresponding substations, given K = 1, 2, 3, 4, 5, 6, and 7 corresponding to the provinces Guangdong, Guangxi, Jiangsu, Zhejiang, Shanghai, Sichuan, and Yunnan.

Case (1): No further refinement modeling is required because the sub-plant feeder areas are the same. Case (2): The following additional refinement modeling constraints are required.

➢ The output of the left bank unit is greater than or equal to the outgoing output to Jiangsu.

$$\sum_{e \in E_{BHT\_L}} pe_{i,e,t} \geq p^r_{2,3,t}. \tag{21}$$

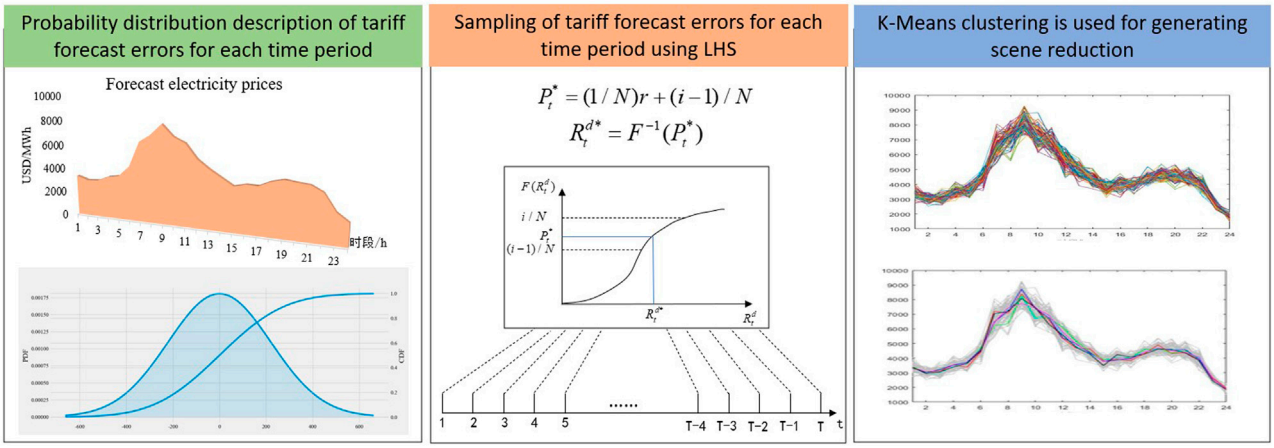

FIGURE 1
Uncertainty description method of the price.

➢ The output of the right bank unit is greater than or equal to the outgoing output to Zhejiang.

$$\sum_{e \in E_{BHT\_R}} pe_{2,e,t} \geq pc_{2,4,t}. \tag{22}$$

Case (3): The following additional refinement modeling constraints are required.

➢ The output of the left bank unit is equal to outgoing output for Zhejiang and the retained output for Sichuan.

$$\sum_{e \in E_{XLD\_L}} pe_{3,e,t} = pc_{3,4,t} + pc_{3,6,t}. \tag{23}$$

➢ The output of the right bank unit is equal to the outgoing output for Guangxi and the retained output for Yunnan.

$$\sum_{e \in E_{XLD\_R}} pe_{3,e,t} = pc_{3,2,t} + pc_{3,7,t}. \tag{24}$$

3.3 Target linearization processing

Since Eq. 3 contains the max function, resulting in a non-linearly constrained objective, it needs to be linearized to transform the mixed-integer non-linear programming (MINLP) model into a MILP model. Then, a sophisticated and efficient optimization solver is used to solve the MILP model in order to obtain the optimal solution efficiently.

Variables 0–1, auxiliary variables b_i (i represents whether there is a positive deviation in the power plant plan power), o_i, and x_i, and infinity value constant M are introduced, where $\max(E^p_{i,k,t} - p^r_{i,k,t}, 0)$ in Eq. 3 and $\max(p^r_{i,k,t} - E^p_{i,k,t}, 0)$ in Eq. 5 are transformed into the following mathematical expression:

$$\max\left(E^p_{i,k,t} - p^r_{i,k,t}, 0\right) = x_{i,k,t} + \left(1 - b_{i,k,t}\right) \cdot p^r_{i,k,t}, \tag{25}$$

$$\max\left(p^r_{i,k,t} - E^p_{i,k,t}, 0\right) = b_{i,k,t} \cdot p^r_{i,k,t} - o_{i,k,t}. \tag{26}$$

3.4 Description of the flow curve under the tailwater level considering the top support of the return water

The backwater is a complex hydraulic connection between coupled reservoirs (Figure 2). Under normal conditions, there exists a stable relationship curve between the tailwater level and outflow. However, when the upstream and downstream dam sites of the reservoirs are closer, a high downstream reservoir level produces backwater. Furthermore, the stabilized water level–flow relationship curve will be disrupted, which is known as the backwater effect (Zhao et al., 2019). The requirements for short-term scheduling refinement of hydropower are becoming more stringent due to the gradual increase in the capacity of wind power and photovoltaic power. Addressing the influence of downstream backwater in the model and realizing an efficient solution is one of the key points and difficulties in current reservoir scheduling.

The example shows that if the optimal scheduling model is not constructed by taking into account the complex hydraulic coupling relationship between power stations, there will be deviations between the calculation results and the actual operation process, which does not meet the requirements of accuracy and practicality of hydropower scheduling. Therefore, this paper constructs the relationship between the upstream reservoir level, tailwater level, and downstream flow based on the triangular linear interpolation method in binary independent branching mode, as described in Cheng et al. (2022).

4 Example analysis

4.1 Calculation parameters

This paper takes Wudongde, Baihetan, Xiluodu, and Xiangjiaba (hereinafter referred to as Wu–Bai–Xi–Xiangba),

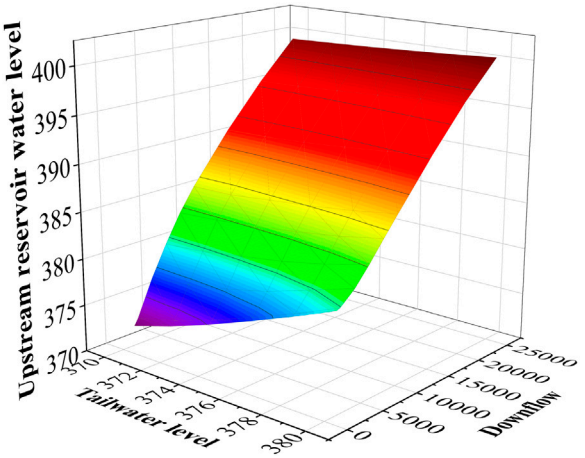

FIGURE 2
Description of backwater.

TABLE 1 Effect of punishment rules on the compliance rate.

Punishment rule	Planned electricity price	Mean market price	Compliance rate (%)
According to the planned electricity price	0.30	0.258	100
	0.25	0.258	96.23
	0.20	0.258	33.84
According to the market price	0.30	0.258	74.50
	0.25	0.258	74.50
	0.20	0.258	74.50

the four mega power stations that have been put into operation in the lower Jinsha River gradient, as the research objects. The installed capacities are 10,200 MW, 16,000 MW, 12,600 MW, and 6,000 MW, respectively. Seven provinces (cities), namely, Guangdong, Guangxi, Jiangsu, Zhejiang, Shanghai, Sichuan, and Yunnan, are included in the grid at the receiving end of the gradient.

4.2 Analysis of penalty rules

As we can see from the aforementioned table (Table 1), according to the planned electricity price penalty (Figure 3), the planned electricity compliance rate decreases with the planned electricity price. According to the market price penalty (Figure 4), the planned electricity compliance rate does not change with the planned price. When the planned price is close to or much larger than the mean market price, the compliance rate of the punishment rule according to the planned electricity price is much larger than that according to the market price. In this case, the planned electricity price is higher than the market price during most periods. The punishment rule according to the planned electricity price can cause generators to suffer large revenue losses. According to the punishment rule based on the market price, power plants can seek higher revenue by defaulting on planned electricity during the period of low market price and participating in the day-ahead market during the high market price. Considering the policy specificity of planned power, grid companies use planned tariffs for compliance deviation penalties in order to ensure the compliance rate of planned power.

From another perspective, if the planned power price is appropriately reduced, the willingness of hydropower plants to contract planned power will be weakened at the same time, so this paper tries to explore the correlation between planned power pricing and market performance, as shown in Figure 5.

4.3 Scheduling result analysis

The model proposed in this paper can obtain the short-term dispatching scheme of cascade hydropower stations under the corresponding electricity price scenario. Figure 6 respectively, shows the changes in water level and output of each power station during the scheduling period, and their water levels and output meet the operation constraints and are within a reasonable range.

10.3389/fenrg.2023.1271934

FIGURE 3
Penalized negative deviations with planned electricity prices.

10.3389/fenrg.2023.1271934

FIGURE 4
Penalized negative deviations with market electricity prices.

It can be seen that the variation in the upstream water level is greater than that in the downstream water level, and the downstream power station can maintain stable high-head power generation as far as possible through the adjustment of upstream discharge flow so as to increase the overall power generation and benefits.

10.3389/fenrg.2023.1271934

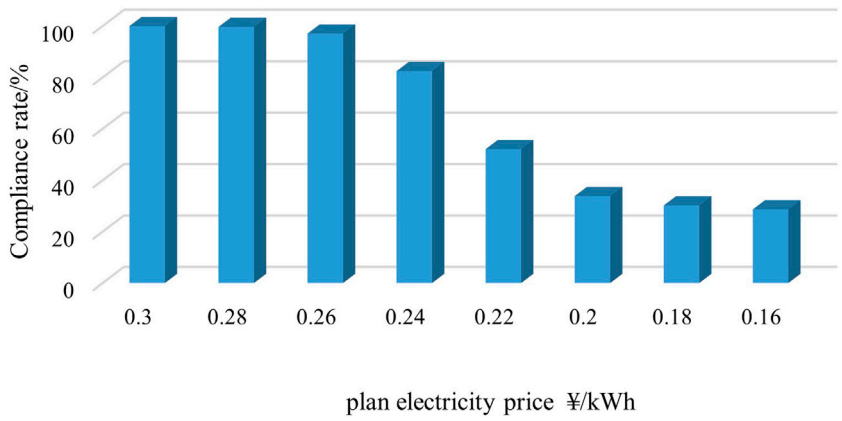

FIGURE 5
Relationship between the compliance rate and planned electricity price.

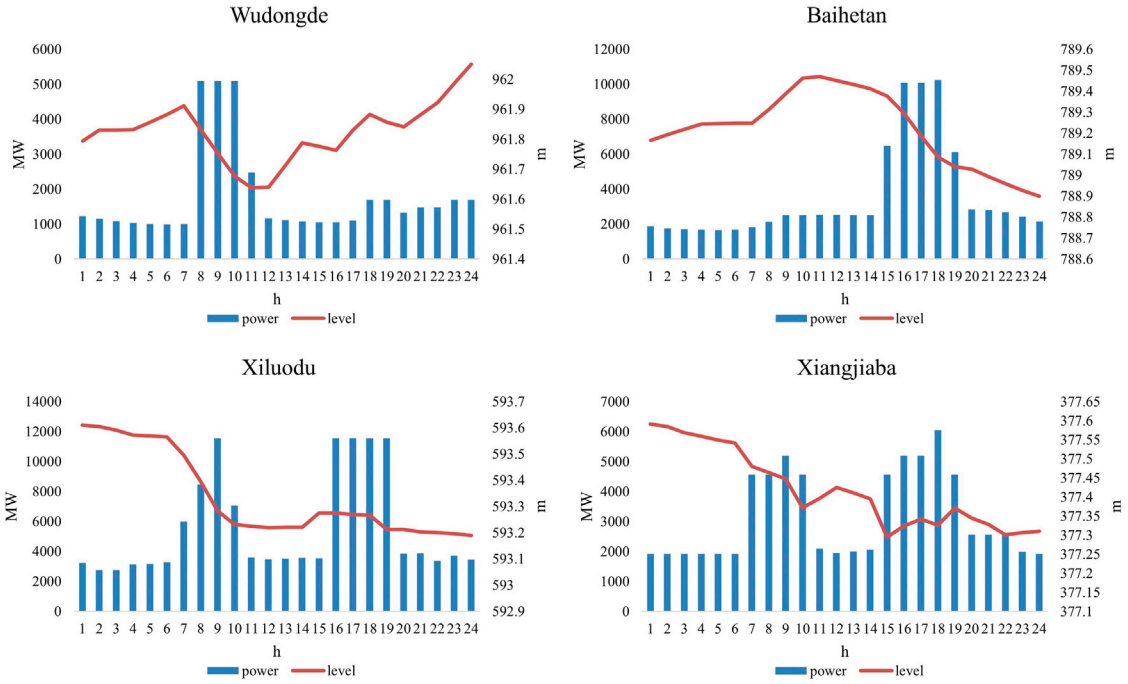

FIGURE 6
Power generation and level.

Further analysis of the overall output of cascade power stations shows that the electricity price is higher in the peak period and lower in the trough period. Under the guidance of the market price before the day, cascade hydropower stations give play to the spatial–temporal coupling characteristics and maximize the total revenue of the cascade hydropower station during the operation period through the spatial cooperation between its upstream and downstream and the coordination between different periods. It is consistent with the experience of hydropower optimal dispatching and the profit-seeking rule in the market environment and verifies the rationality of the dispatching results.

4.4 Analysis of the stable unit operation

As shown in Figure 7, power stations such as Baihetan and Xiluodu with different regions of the left and right bank sending provinces (refer Section 3.2 Power station–substation difference regional outbound relationship processing) can be

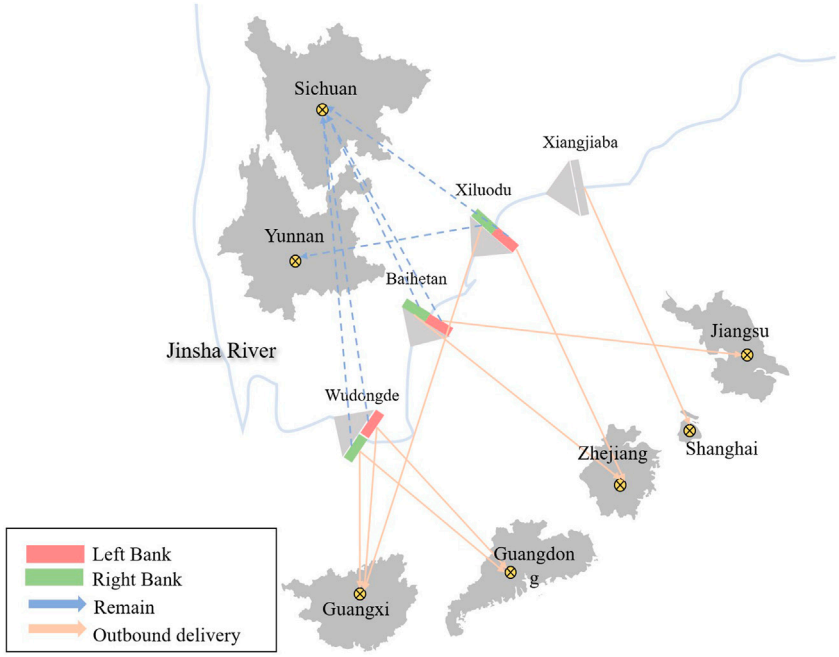

FIGURE 7
Hydroelectric power plant power outflow map.

TABLE 2 Unit stabilization parameters.

Hydropower station	Unit	Minimum power-on time/h	Minimum power-off time/h	Capacity up limit for stable operation	Capacity down limit for stable operation
Wudongde	#1~#12	4	4	170	850
Baihetan	#1~#16	4	4	200	1000
Xiluodu	#1~#18	4	4	154	770
Xiangjiaba	#1~#8	4	4	160	800

considered in the process of unit load distribution of the complex provinces of the sub-bank sending demand, at the peak of the two provinces, to increase the power allocation in a timely manner while taking into account the safe and stable operation of the unit (Table 2; Figure 8), to ensure the practicality of the power plan.

4.5 Analysis of market price uncertainty

Using the methodology described in Section 4, five typical electricity price scenarios were generated based on the uncertainty of the forecast electricity price error (Figure 9). Two regional grids, the National Grid (NG) and the Southern Grid (SG), are included in the electricity price scenario. In this section, the planned electricity price is set to 0.3¥.

The aforementioned table shows the mean and maximum prices in different regions for different scenarios (Table 3). Overall, the average price in the SG region is higher than that in the NG region. Within the same region, the mean price for different scenarios does not vary much, but the maximum price difference accounts for approximately 4% of the mean price. Maximum tariffs are very important for market-based electricity allocation.

In order to facilitate the comparison between multiple scenarios of tariff uncertainty and single tariff scenarios, this subsection adopts "Plan Electricity Negative Deviation Penalty Rule II" and conducts a comparative analysis according to the principles of the plan tariff penalty.

The main difference between a single scenario and multiple scenarios (Figure 10) is observed in the seventh, 11th, and 16th time periods. The seventh and 11th time periods show a significant decrease in market decision power in the 11th time period with the single scenario. There was a significant increase in market decision power in the seventh time period compared with the single scenario, which is mainly due to the fact that

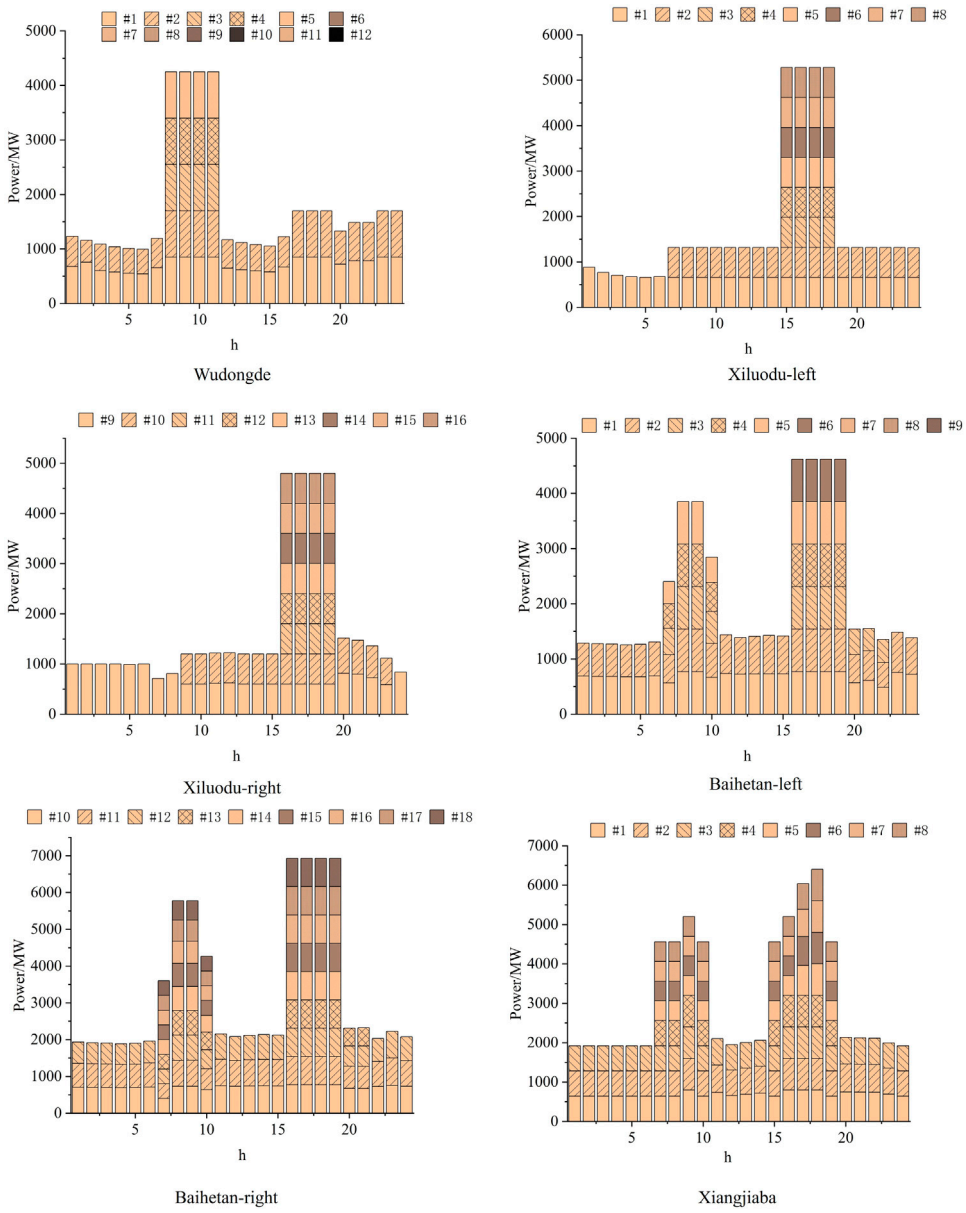

FIGURE 8
Unit output distribution.

only one scenario of price scenario 1 is considered in the single-scenario mode. The price in the seventh time period is lower than the tariff in the 11th time period in tariff scenario 1, while the other scenarios are the opposite. Therefore, in order to take into account the possibility of multiple tariffs and improve the expected revenue of the power plant, the power output in the seventh period is increased and the power output in the 11th and 16th periods is reduced in the multi-scenario decision to avoid the revenue risk. Using the decision results from scenario 1 to find the possible expected revenue for all price scenarios, there is a 3% reduction in revenue compared to the present expected return maximization model. It shows that expectation modeling is very important for risk aversion.

5 Conclusion

Currently, in the stage of market reform where planned electricity and marketed electricity coexist, hydropower taking on the task of delivering power to multiple-recipient provinces plays a decisive role. In the current market background, how to take into account the planned electricity and the cross-provincial market revenue is an important problem that cascade hydropower plants face. In this paper, taking the Jinsha River cascade hydropower plants as a relying project, we propose a day-ahead planned electricity compliance strategy and market electricity decision-making methods considering complex settlement rules and many end-user provinces. Finally, the

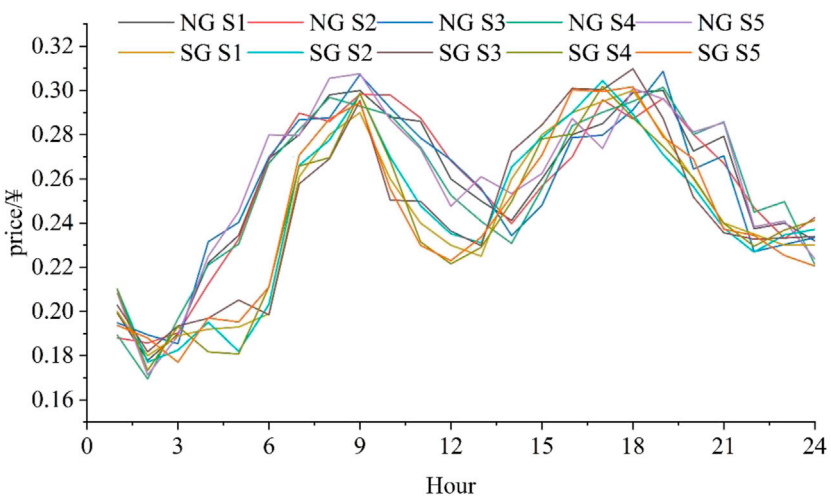

FIGURE 9
Multi-scenario electricity prices.

TABLE 3 Multi-scenario electricity prices.

Area	SG	SG	SG	SG	SG	NG	NG	NG	NG	NG
Scenario	1	2	3	4	5	1	2	3	4	5
Mean price/¥	0.258	0.257	0.256	0.256	0.259	0.243	0.244	0.246	0.242	0.244
Maximum price/¥	0.300	0.298	0.309	0.301	0.308	0.300	0.304	0.310	0.302	0.302

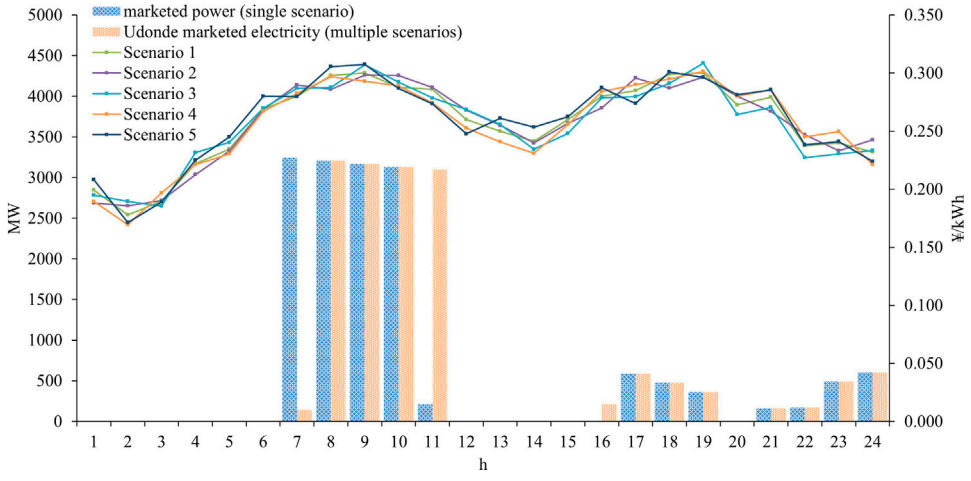

FIGURE 10
Comparison between single scenario and multiple scenarios.

expected revenue maximization model, considering the price uncertainty, is developed. The following conclusions were obtained:

(1) Hydropower plants have a much larger planned power compliance rate for the planned electricity compliance penalty rule based on the planned electricity price than based on the market price.

(2) The model proposed in this paper hedges the market decision risk by taking into account the tariff forecast error.
(3) While taking into account the demand for power delivery from complex provinces, the model can obtain an operation plan that meets the safe and stable operation of the units.

Author contributions

XH: software and writing–original draft. JS: writing–review and editing. CC: writing–review and editing.

Funding

The author(s) declare that financial support was received for the research, authorship, and/or publication of this article. The National Natural Science Foundation of China (Nos 52079014 and 52039002) and the Fundamental Research Funds supported this research for the Central Universities (Nos DUT22QN224 and DUT22JC21).

Acknowledgments

The authors are very grateful to the reviewers and editors for their constructive comments.

Conflict of interest

The authors declare that the research was conducted in the absence of any commercial or financial relationships that could be construed as a potential conflict of interest.

Publisher's note

References

Avesani, D., Zanfei, A., Di Marco, N., Galletti, A., Ravazzolo, F., Righetti, M., et al. (2022). Short-term hydropower optimization driven by innovative time-adapting econometric model. *Appl. Energy* 310, 118510. doi:10.1016/j.apenergy.2021.118510

Bulut, E., Albak, E. 0., Sevilgen, G., and Öztürk, F. (2021). A new approach for battery thermal management system design based on Grey Relational Analysis and Latin Hypercube Sampling. *Case Stud. Therm. Eng.* 28, 101452. doi:10.1016/j.csite.2021.101452

Cai, Z., Zhang, C., Hu, X., Zhang, G., and Lu, Y. (2020). "Design of Hydropower Dominated Provincial Electricity Spot Markets in China," in 2020 4th International Conference on Power and Energy Engineering (ICPEE), Xiamen, China, 19-21 November 2020 (IEEE), 206–212.

Cao, Y., Zhang, Z., Cheng, F., and Su, S. (2022). Trajectory Optimization for High-Speed Trains via a Mixed Integer Linear Programming Approach. *IEEE Trans. Intelligent Transp. Syst.* 23, 17666–17676. doi:10.1109/tits.2022.3155628

Carvajal, P. E., Anandarajah, G., Mulugetta, Y., and Dessens, O. (2017). Assessing uncertainty of climate change impacts on long-term hydropower generation using the CMIP5 ensemble—the case of Ecuador. *Clim. Change* 144, 611–624. doi:10.1007/s10584-017-2055-4

Chen, H., Cui, J., Song, F., and Jiang, Z. (2022). Evaluating the impacts of reforming and integrating China's electricity sector. *Energy Econ.* 108, 105912. doi:10.1016/j.eneco.2022.105912

Cheng, C., Chen, F., Li, G., Ristić, B., Mirchi, A., Qiyu, T., et al. (2018). Reform and renewables in China: the architecture of Yunnan's hydropower dominated electricity market. *Renew. Sustain. Energy Rev.* 94, 682–693. doi:10.1016/j.rser.2018.06.033

Cheng, Q., Luo, P., Liu, P., Li, X., Ming, B., Huang, K., et al. (2022). Stochastic short-term scheduling of a wind-solar-hydro complementary system considering both the day-ahead market bidding and bilateral contracts decomposition. *Int. J. Electr. Power & Energy Syst.* 138, 107904. doi:10.1016/j.ijepes.2021.107904

Cheng, Y., Chung, M., and Tsang, K. (2023). Electricity Market Reforms for Energy Transition: lessons from China. *Energies* 16, 905. doi:10.3390/en16020905

Ding, T., Bo, R., Gu, W., and Sun, H. (2014). Big-M Based MIQP Method for Economic Dispatch With Disjoint Prohibited Zones. *IEEE Trans. Power Syst.* 29, 976–977. doi:10.1109/tpwrs.2013.2287993

Fang, W., Huang, Q., Huang, S., Yang, J., Meng, E., and Li, Y. (2017). Optimal sizing of utility-scale photovoltaic power generation complementarily operating with hydropower: A case study of the world's largest hydro-photovoltaic plant. *Energy Convers. Manag.* 136, 161–172. doi:10.1016/j.enconman.2017.01.012

Golmohamadi, H., Guldstrand Larsen, K., Gjøl Jensen, P., and Riaz Hasrat, I. (2021). Optimization of power-to-heat flexibility for residential buildings in response to day-ahead electricity price. *Energy Build.* 232, 110665. doi:10.1016/j.enbuild.2020.110665

Gómez-Navarro, T., and Ribó-Pérez, D. (2018). Assessing the obstacles to the participation of renewable energy sources in the electricity market of Colombia. *Renew. Sustain. Energy Rev.* 90, 131–141. doi:10.1016/j.rser.2018.03.015

Guo, H., Ma, Z., Zhang, H., Zhou, Q., Wang, D., Lv, Q., et al. (2021). "The Coordination Mechanism between Medium- and Long-term Market and Spot Market in China," in 2021 3rd International Conference on Electrical Engineering and Control Technologies (CEECT), Macau, Macao, 16-18 December 2021 (IEEE), 14–18.

Jia, Z., Shen, J., Cheng, C., Zhang, Y., and Lyu, Q. (2022). Optimum day-ahead clearing for high proportion hydropower market considering complex hydraulic connection. *Int. J. Electr. Power & Energy Syst.* 141, 108211. doi:10.1016/j.ijepes.2022.108211

Jiang, W., Liu, Y., Fang, G., and Ding, Z. (2023). Research on short-term optimal scheduling of hydro-wind-solar multi-energy power system based on deep reinforcement learning. *J. Clean. Prod.* 385, 135704. doi:10.1016/j.jclepro.2022.135704

Karolczuk, A., and Kurek, M. (2022). Fatigue life uncertainty prediction using the Monte Carlo and Latin hypercube sampling techniques under uniaxial and multiaxial cyclic loading. *Int. J. Fatigue* 160, 106867. doi:10.1016/j.ijfatigue.2022.106867

Kebede, A. A., Kalogiannis, T., Van Mierlo, J., and Berecibar, M. (2022). A comprehensive review of stationary energy storage devices for large scale renewable energy sources grid integration. *Renew. Sustain. Energy Rev.* 159, 112213. doi:10.1016/j.rser.2022.112213

Krien, U., Schönfeldt, P., Launer, J., Hilpert, S., Kaldemeyer, C., and Pleßmann, G. (2020). oemof.solph—A model generator for linear and mixed-integer linear optimisation of energy systems. *Softw. Impacts* 6, 100028. doi:10.1016/j.simpa.2020.100028

Lago, J., Marcjasz, G., De Schutter, B., and Weron, R. (2021). Forecasting day-ahead electricity prices: A review of state-of-the-art algorithms, best practices and an open-access benchmark. *Appl. Energy* 293, 116983. doi:10.1016/j.apenergy.2021.116983

Lu, Y., Meng, F., Hao, C., Yang, J., Song, L., and Tian, Z. (2021). Mechanism and benefit analysis of resource optimal allocation of China's trans-provincial and trans-regional power trading. *IOP Conf. Ser. Earth Environ. Sci.* 827, 012017. doi:10.1088/1755-1315/827/1/012017

Merkert, L., Harjunkoski, I., Isaksson, A., Säynevirta, S., Saarela, A., and Sand, G. (2015). Scheduling and energy – Industrial challenges and opportunities. *Comput. Chem. Eng.* 72, 183–198. doi:10.1016/j.compchemeng.2014.05.024

Pérez-Díaz, J. I., Wilhelmi, J. R., and Arévalo, L. A. (2010). Optimal short-term operation schedule of a hydropower plant in a competitive electricity market. *Energy Convers. Manag.* 51, 2955–2966. doi:10.1016/j.enconman.2010.06.038

Rodríguez-Sarasty, J. A., Debia, S., and Pineau, P. (2021). Deep decarbonization in Northeastern North America: the value of electricity market integration and hydropower. *Energy Policy* 152, 112210. doi:10.1016/j.enpol.2021.112210

Shen, J., Cheng, C., Jia, Z., Zhang, Y., Lv, Q., Cai, H., et al. (2022). Impacts, challenges and suggestions of the electricity market for hydro-dominated power systems in China. *Renew. Energy* 187, 743–759. doi:10.1016/j.renene.2022.01.089

Shen, J., Cheng, C., Zhang, X., and Zhou, B. (2018). Coordinated operations of multiple-reservoir cascaded hydropower plants with cooperation benefit allocation. *Energy* 153, 509–518. doi:10.1016/j.energy.2018.04.056

Stančin, H., Mikulčić, H., Wang, X., and Duić, N. (2020). A review on alternative fuels in future energy system. *Renew. Sustain. Energy Rev.* 128, 109927. doi:10.1016/j.rser.2020.109927

Tang, C., and Zhang, F. (2020). Study on the connection and settlement of forward electricity market and spot electricity market. IOP conference series. *Earth Environ. Sci.* 508, 12061. doi:10.1088/1755-1315/508/1/012061

Tschora, L., Pierre, E., Plantevit, M., and Robardet, C. (2022). Electricity price forecasting on the day-ahead market using machine learning. *Appl. Energy* 313, 118752. doi:10.1016/j.apenergy.2022.118752

Wang, H., and Huang, J. (2018). Incentivizing Energy Trading for Interconnected Microgrids. *IEEE Trans. Smart Grid* 9, 2647–2657. doi:10.1109/tsg.2016.2614988

Wu, Y., Su, C., Liu, S., Guo, H., Sun, Y., Jiang, Y., et al. (2022). Optimal Decomposition for the Monthly Contracted Electricity of Cascade Hydropower Plants Considering the Bidding Space in the Day-Ahead Spot Market. *Water* 14, 2347. doi:10.3390/w14152347

Xiao, Y., Niyato, D., Han, Z., and DaSilva, L. A. (2015). Dynamic Energy Trading for Energy Harvesting Communication Networks: A Stochastic Energy Trading Game. *IEEE J. Sel. Areas Commun.* 33, 2718–2734. doi:10.1109/jsac.2015.2481204

Xinhong, S., Yefei, Z., Panjiajia, Z., Gaoqin, W., and Jianhu, L. (2020). Trans-regional power trading optimization for promoting clean energy accommodation. *IOP Conf. Ser. Earth Environ. Sci.* 431, 012053. doi:10.1088/1755-1315/431/1/012053

Xu, B., Sun, Y., Huang, X., Zhong, P. A., Zhu, F., Zhang, J., et al. (2022). Scenario-Based Multiobjective Robust Optimization and Decision-Making Framework for Optimal Operation of a Cascade Hydropower System Under Multiple Uncertainties. *Water Resour. Res.* 58, 30965. doi:10.1029/2021wr030965

Yuan, L., Zhou, J., Li, C., Xie, M., and Mo, L. (2016). Benefit and Risk Balance Optimization for Stochastic Hydropower Scheduling. *Water Resour. Manag.* 30, 3347–3361. doi:10.1007/s11269-016-1354-2

Zhang, F., Cheng, L., Wu, M., Xu, X., Wang, P., and Liu, Z. (2020). Performance analysis of two-stage thermoelectric generator model based on Latin hypercube sampling. *Energy Convers. Manag.* 221, 113159. doi:10.1016/j.enconman.2020.113159

Zhang, L., Zhang, Q., Fan, H., Wu, H., and Xu, C. (2021). Big-M based MILP method for SCUC considering allowable wind power output interval and its adjustable conservativeness. *Glob. Energy Interconnect.* 4, 193–203. doi:10.1016/j.gloei.2021.05.001

Zhang, R., Zhang, S., Wen, X., and Jing, Z. (2023). Refined Scheduling Based on Dynamic Capacity Model for Short-term Hydropower Generation. *Water Resour. Manag.* 37, 21–35. doi:10.1007/s11269-022-03352-5

Zhao, Z., Liu, J., and Cheng, C. (2019). A MILP model for day-ahead peak operation of cascade hydropower stations considering. *backwater ournal Hydraulic Eng.* 50, 925–935.

Zhao, Z., Liu, S., Zhou, M., and Abusorrah, A. (2021). Dual-Objective Mixed Integer Linear Program and Memetic Algorithm for an Industrial Group Scheduling Problem. *IEEE/CAA J. Automatica Sinica* 8, 1199–1209. doi:10.1109/jas.2020.1003539

frontiers | Frontiers in Energy Research

TYPE Original Research
PUBLISHED 14 November 2023
DOI 10.3389/fenrg.2023.1292204

OPEN ACCESS

EDITED BY
IMR Fattah,
University of Technology Sydney,
Australia

REVIEWED BY
Baoli Lu,
University of Portsmouth,
United Kingdom
Kenneth E. Okedu,
Melbourne Institute of Technology,
Australia
Virginia Radulescu,
University of Craiova, Romania
Srinvasa Rao Gampa,
Seshadri Rao Gudlavalleru Engineering
College, India

*CORRESPONDENCE
Bin Zhong,
asd75357@outlook.com

RECEIVED 11 September 2023
ACCEPTED 17 October 2023
PUBLISHED 14 November 2023

CITATION
Zhong B (2023), Deep learning integration optimization of electric energy load forecasting and market price based on the ANN–LSTM–transformer method.
Front. Energy Res. 11:1292204.
doi: 10.3389/fenrg.2023.1292204

Deep learning integration optimization of electric energy load forecasting and market price based on the ANN–LSTM–transformer method

Bin Zhong*

State Grid Shanghai Electric Power Company, Shanghai, China

Introduction: Power load forecasting and market price analysis have become crucial in the context of complex power energy systems and volatile market prices. Deep learning technology has gained significant attention in time series forecasting, and this article aims to enhance the accuracy and reliability of power load and market price predictions by integrating and optimizing deep learning models.

Methods: We propose a deep learning framework that combines artificial neural networks (ANNs), long short-term memory (LSTM), and transformer models to address key challenges in electricity load forecasting and market price prediction. We leverage ANNs for their versatility and use LSTM networks for sequence modeling to generate initial predictions. Additionally, we introduce transformer technology and utilize its self-attention mechanism to capture long-distance dependencies within the data, further enhancing the model's performance.

Results: In our experiments, we validate the proposed framework using multiple public datasets. We compare our method with traditional forecasting approaches and a single-model approach. The results demonstrate that our approach outperforms other methods in predicting power load and market prices. This increased accuracy and reliability in forecasting can be of significant value to decision-makers in the energy sector.

Discussion: The integration of deep learning models, including ANN, LSTM, and transformer, offers a powerful solution for addressing the challenges in power load and market price prediction. The ability to capture long-distance dependencies using the transformer's self-attention mechanism improves forecasting accuracy. This research contributes to the field of energy and finance by providing a more reliable framework for decision-makers to make informed choices in a complex and dynamic environment.

KEYWORDS

electricity, new energy forecasting technology, deep learning, hybrid energy system, multi-source data, market price

1 Introduction

In today's world, the supply and demand relationship of electric energy and market price fluctuations have increasingly become key issues in the field of global energy. As one of the infrastructures of modern society, electricity directly affects the country's development, industrial production, and people's lives. However, the continuous increase in energy consumption leads to the increased complexity of the power system. How to ensure the stability of power supply and the rationality of market prices has become an urgent challenge that needs to be solved (Mujeeb et al., 2019). Electric power loadforecasting and market price analysis have become critical in the field of energy and finance. Electric power load forecasting can help power system operators rationally plan energy supply and effectively allocate resources, thereby improving the efficiency and reliability of the power system, while market price fluctuations directly affects the investment decisions and returns of energy market participants. Accurately predicting price changes in the electricity market can help investors gain greater returns in the market.

The main objective of this study is to conduct electricity load forecasting and market price analysis to solve key issues in the energy and financial sectors. Electricity load forecasting is an important task related to balancing power supply and demand, while market price analysis is of strategic importance to energy market participants, including suppliers and investors. We selected these two as study subjects because they play an integral role in modern society.

The importance of power load forecasting is self-evident. As the complexity of power systems continues to increase, energy suppliers and power network managers need to accurately predict power loads in order to rationally allocate resources and adjust power generation plans. This is a regression problem because our goal is to predict continuous electrical load values in order to better meet demand, reduce waste, and improve energy efficiency. Therefore, our research methods and metrics are matched to the regression problem to ensure that we can provide accurate electricity load forecasts.

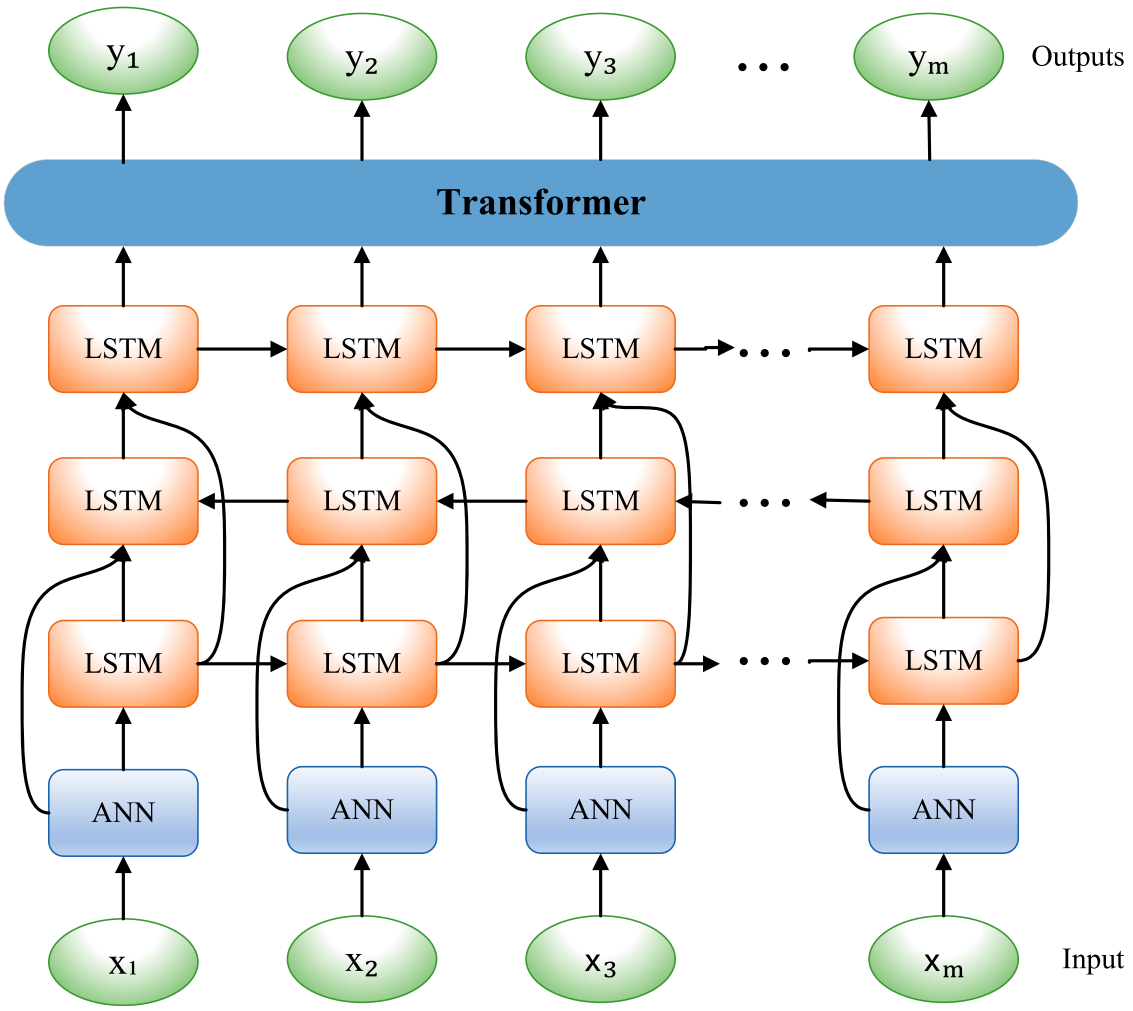

FIGURE 1
Overall flow chart of the model.

Market price analysis is equally important. With the continuous development of new energy technologies, the energy market has become more complex and price fluctuations have become more frequent. Investors need to understand market price trends and fluctuations in order to develop smart investment strategies. This is also a regression problem since our goal is to predict continuous market price fluctuations to help decision-makers make more informed financial decisions. Our research methods and metrics are aligned with this goal to ensure reliability in market price forecasts.

Deep learning technology has great potential in solving these problems. We selected to integrate artificial neural networks (ANNs), long short-term memory (LSTM) networks, and transformer models because their respective advantages can complement each other to improve prediction accuracy (Dabbaghjamanesh et al., 2020). ANN is versatile, LSTM is good at sequence modeling, and the transformer introduces a self-attention mechanism that can capture long-distance dependencies. This integrated approach is expected to provide more accurate and reliable solutions for power load forecasting and market price analysis.

As the complexity of power systems continues to increase, and market prices fluctuate, researchers and practitioners seek more accurate, stable, and efficient forecasting methods. Previous solutions usually relied on traditional time series analysis methods, such as autoregressive integrated moving average (ARIMA) and generalized autoregressive conditional heteroskedasticity (GARCH) models (Yousaf et al., 2021). These methods can model power loads and market prices to a certain extent but encounter difficulty in dealing with nonlinear, non-stationary, and multi-source data. Furthermore, these methods often require manual engineering of features and fail to fully exploit the information of the original data (Alipour et al., 2020). The development of deep learning technology has aroused widespread interest, and significant progress has been made in the field of time series forecasting. Deep learning models, such as ANN, LSTM and transformer, have been widely used in power load forecasting and market price analysis (Rafi et al.,

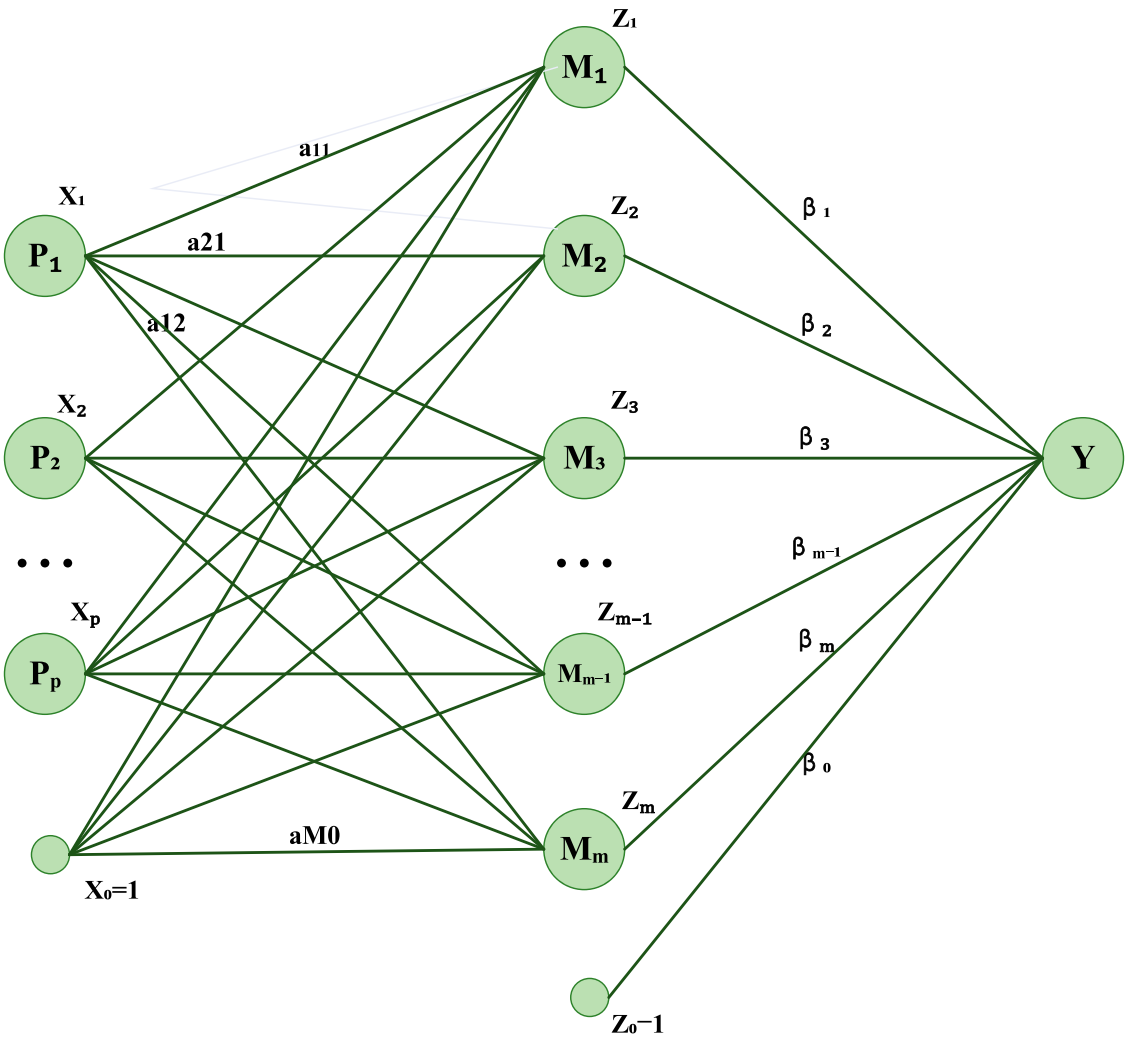

FIGURE 2
Flow chart of the ANN model.

2021). They can extract automatic features, handle nonlinear relationships, and handle the fusion of multi-source data, thereby improving prediction accuracy. However, despite the excellent performance of these deep learning models in improving prediction performance, there are still some challenges. For example, model training requires large amounts of data and requires careful tuning of hyperparameters (Tan et al., 2020). Furthermore, they may be sensitive to noise, thus requiring more powerful regularization and generalization techniques to improve stability. These problems prompt us to study more efficient and stable integrated optimization methods, combining ANN, LSTM, and transformer to make full use of their advantages and solve the limitations of traditional methods and single models.

Therefore, this research aims to integrate and optimize deep learning technologies, such as ANN, LSTM, and transformer, to improve the accuracy of power load and market price prediction. Specifically, we propose a comprehensive framework based on the ANN–LSTM--transformer method, which combines their respective advantages to effectively capture the spatiotemporal changes in power load and market price. In experiments, we validate our method using multiple public datasets and compare its performance with other traditional methods (Deng et al., 2019). Our comprehensive approach is expected to provide more accurate and stable prediction results in the field of power energy, thereby supporting decision-makers to make more informed decisions and promoting the sustainable development of the energy industry.

In addition to ANN, LSTM, and transformer, there are other commonly used models in the fields of power load forecasting and deep learning, including but not limited to the following five models:

Autoregressive integral moving average: ARIMA is a time series analysis model that combines the concepts of autoregressive (AR) and moving average (MA), as well as differential operation (I), and is suitable for stationary or differential stationary time series data (Benvenuto et al., 2020). This model has been used for many years and is one of the classic time series forecasting methods. In power energy forecasting, the ARIMA model can be used to model long-term trends and seasonal patterns of power load data to perform load forecasting (Fan et al., 2021). In terms of market price analysis, the ARIMA model can be used to predict the changing trend of electricity market prices.

Convolutional neural network: The convolutional neural network (CNN) is a deep learning model mainly used for image recognition and processing. It captures local patterns and features in images using convolutional layers, then reduces the dimensionality of data through pooling layers, and finally classifies or predicts through fully connected layers (Bhatt et al., 2021). CNN initially achieved great success in the field of computer vision, such as winning the ImageNet competition (Li et al., 2020). Subsequently, people began to apply CNN to other fields, including time series data processing. In power energy forecasting, one-dimensional CNN can be used to capture local patterns in power load data, such as changing trends in certain specific time periods.

Gated recurrent unit: The gated recurrent unit (GRU) is a variant of the recurrent neural network (RNN), designed to solve the long-term dependency problem of RNN (Cheon et al., 2020). It contains update gates and reset gates, which allow the network to selectively update and forget information to better capture key features in the sequence (Daniels et al., 2020). It is an improvement over traditional RNN, attempting to solve the vanishing and exploding gradient problems, and has fewer parameters than LSTM, so it is easier to

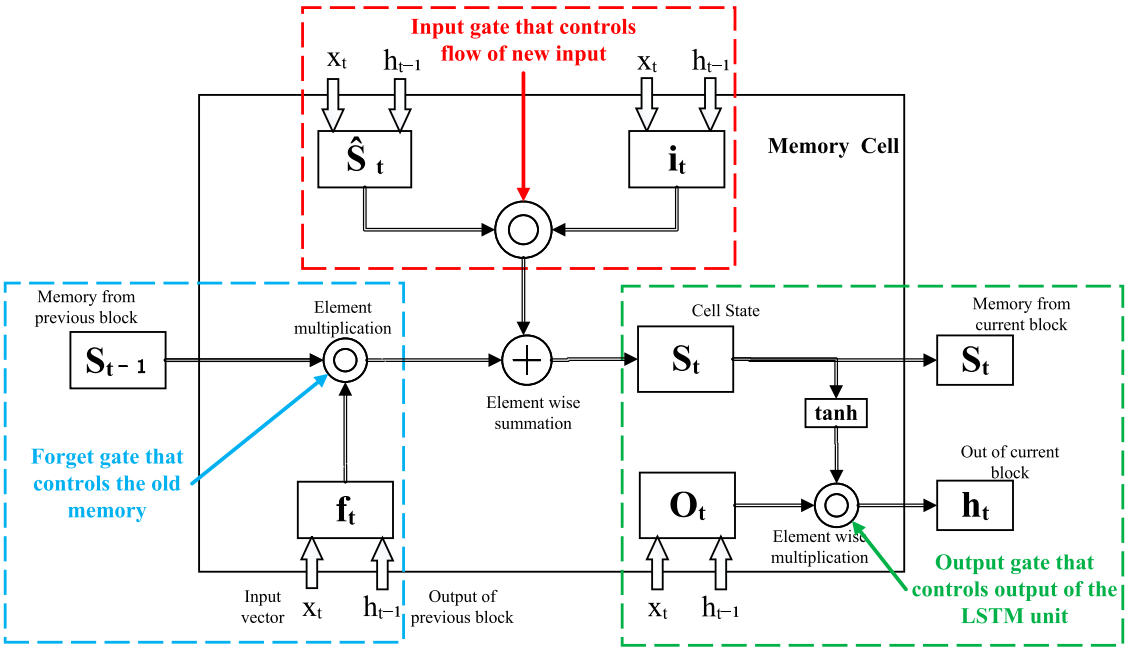

FIGURE 3
Flow chart of the LSTM model.

train in some cases. In power energy forecasting, GRU can be used to model the time dependence in power load data to perform load forecasting.

Recurrent neural network: RNN is a neural network specially used to process sequence data. It was first introduced in the 1980s; however, its application has been restricted to a certain extent due to its limitations in dealing with long-term dependency problems such as vanishing gradient and exploding problems (Xiao and Zhoum, 2020). However, with the emergence of variants such as the LSTM network and GRU, the development of RNN has been greatly promoted (Dhruv and Naskar, 2020). These variants successfully solve the long-term dependency problem by introducing a gating mechanism, thereby enabling RNN to better capture patterns and information in sequence data. RNN is often used to capture the temporal patterns and sequence dependencies of power load data.

Temporal convolutional network: The temporal convolutional network (TCN) is a deep learning model specially designed for processing sequence data. It is based on convolution operations, but it is designed to pay more attention to the time dependence in sequence data. By expanding the convolution operation and introducing residual connections to effectively capture long-term dependencies (Arumugham et al., 2023), it captures sequence patterns at different scales by stacking one-dimensional convolutional layers while focusing on the importance of different time steps through an attention mechanism. TCN aims to overcome the long-term dependency problem in traditional RNNs and provide better performance (Fan et al., 2023). In power energy forecasting, TCN can be used to simultaneously capture power load patterns at different time scales, thereby improving forecasting accuracy.

However, although CNN models perform well in the field of image processing, they may fail to adequately capture temporal dependencies, especially for long-term dependencies, when processing sequential data. The GRU model is improved over traditional RNNs, but it may still be limited in processing more complex sequence patterns. Although RNN is a natural choice for sequence data, it is difficult to capture longer time dependencies due to its short-term memory issues. Although the TCN model overcomes some limitations of traditional RNNs, it may still require a large number of computing resources when processing extremely long sequences. The ARIMA model may not perform well when dealing with nonlinear and non-stationary data, and it may be difficult to accurately predict some complex market price change patterns.

In view of the shortcomings of the aforementioned model, this paper proposes a deep learning framework, ANN–LSTM–transformer, for use in power energy forecasting and market price analysis problems, capable of feature extraction and modeling of data at different levels. ANN is used to capture overall patterns, LSTM is used to handle time series dependencies, and transformer can handle both long-term and global dependencies. By combining multiple deep learning techniques, it can effectively capture long-term dependencies, seasonal patterns, and complex trends in power load and market price data, thus showing unique advantages in the fields of power energy forecasting and market price analysis.

The main contributions of this study are as follows:

- This study pioneers the integration of ANN, LSTM, and transformer models into a unified framework, yielding a multi-faceted prediction approach. By concurrently capturing overarching patterns, time-based dependencies, and spatiotemporal correlations in power load and market price data, this integration enhances feature representation and modeling capabilities, thus bolstering forecasting accuracy.
- The LSTM and transformer models in the framework of this paper focus on capturing long-term dependencies and spatiotemporal associations in sequence data, respectively. The transformer's self-attention mechanism enables the model to more effectively handle the relationship between patterns and features at different time scales, thereby improving the performance of power load forecasting and market price analysis. This capability for integrated spatiotemporal modeling is rare in traditional models.

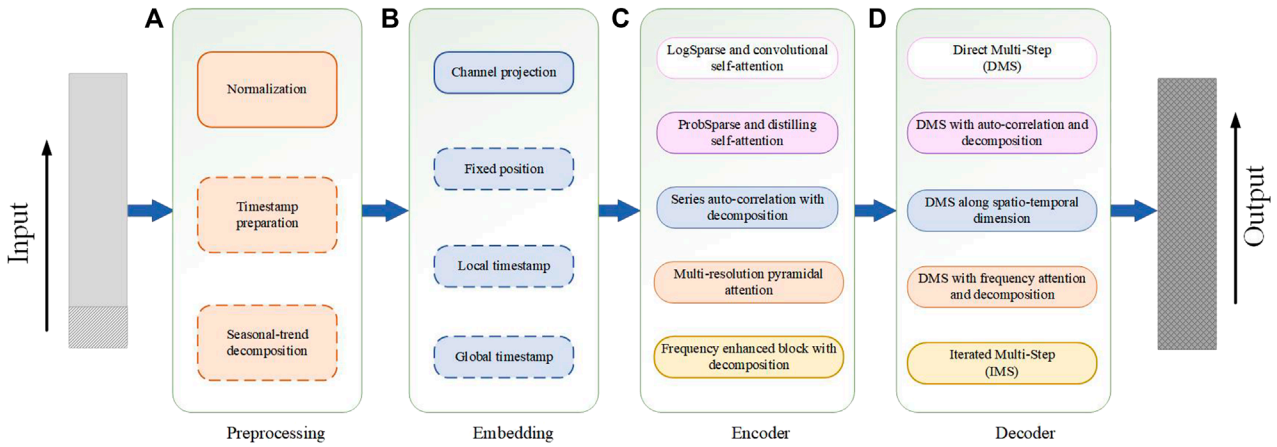

FIGURE 4
Flow chart of the transformer model.

- The ANN–LSTM–transformer framework can capture complex trends and multiple patterns in power load and market price data. This framework is not only suitable for processing a single trend but also can better cope with different seasonal, cyclical, and nonlinear patterns, making the forecast results more accurate and comprehensive.

2 Methodology

2.1 Overview of our network

Our proposed ANN–LSTM–transformer-based model aims to solve the problems of electricity load forecasting and market price analysis. First, we chose to use ANN as part of our model due to its broad versatility and ability to handle various types of data. ANN can effectively capture nonlinear relationships in input data, which is crucial for complex time series data such as electricity load and market prices. Second, we adopted the LSTM model because it performs well when processing sequence data. The long short-term memory unit of LSTM can capture short-term and long-term dependencies in data, which is very helpful for time series modeling of electricity load and market prices. Most importantly, we introduced the transformer model. The transformer model has achieved significant success in the fields of natural language processing and time series, and its self-attention mechanism can effectively capture long-distance dependencies in sequence data. In the experiment, we first collected historical power load and market price data as well as related influencing factors, such as seasonality and holidays, and performed data cleaning, preprocessing, and outlier processing to ensure the accuracy and quality of the data. These processed data were fed into the feature extraction and modeling stages of the model. At this stage, ANN was used to capture the overall pattern, LSTM was used to handle time series dependencies, and transformer was used to focus on long-distance dependencies and spatiotemporal relationships. By integrating these models, the capabilities of feature representation and modeling were enhanced. Finally, by optimizing the model, the prediction of future power load and market price was realized. The model adaptively captures the importance of different features, thereby improving the accuracy of electricity load forecasting and market price analysis. Through verification in practical applications, it can provide more precise support for energy management and decision-making, thereby promoting the efficient utilization of power resources.

The operation process of the RCNN–GAN model is shown in Figure 1.

Algorithm 1 represents the operation process of the ANN–LSTM–transformer model.

Input: Training data: $\mathcal{D} = \{(X_i, y_i)\}_{i=1}^{N}$, Epochs: E, Learning rate: α
Output: Trained ANN-LSTM-Transformer model
Initialize ANN weights: θ_{ann};
Initialize LSTM weights: θ_{lstm};
Initialize Transformer weights: $\theta_{transformer}$;
for $e \leftarrow 1$ **to** E **do**
  for $(X, y) \in \mathcal{D}$ **do**
    /* Feedforward ANN */
    $h_{ann} = \text{ANN}(X, \theta_{ann})$;
    /* Apply LSTM */
    $h_{lstm} = \text{LSTM}(h_{ann}, \theta_{lstm})$;
    /* Apply Transformer */
    $h_{transformer} = \text{Transformer}(h_{lstm}, \theta_{transformer})$;
    /* Final prediction */
    $\hat{y} = \text{OutputLayer}(h_{transformer})$;
    /* Calculate loss */
    $L = \text{Loss}(\hat{y}, y)$;
    /* Backpropagation */
    $\nabla_{\theta_{ann}}, \nabla_{\theta_{lstm}}, \nabla_{\theta_{transformer}} = \text{Backpropagate}(L)$;
    /* Update weights */
    $\theta_{ann} \leftarrow \theta_{ann} - \alpha \cdot \nabla_{\theta_{ann}}$;
    $\theta_{lstm} \leftarrow \theta_{lstm} - \alpha \cdot \nabla_{\theta_{lstm}}$;
    $\theta_{transformer} \leftarrow \theta_{transformer} - \alpha \cdot \nabla_{\theta_{transformer}}$;
  end
end

Algorithm 1. Training ANN–LSTM–transformer.

2.2 ANN model

ANN is a network structure composed of neuron layers, which is used to simulate the information processing method of the human brain (Hoang et al., 2021). Each neuron receives input from the neurons of the previous layer, weights it through weights and activation functions, and finally generates an output (Otchere et al., 2021). The role of ANN in power load forecasting and market analysis was to extract features and patterns from multi-dimensional time series data and gradually extract high-level abstract features through multiple hidden layers for prediction and analysis (Khan et al., 2020). In the overall model, ANN played the role of a feature extractor in the overall framework, which gradually extracted abstract features of time series data through layer-by-layer forward propagation. These characteristics can include seasonal changes, cyclical patterns, and other complex nonlinear relationships.

The operation process of the ANN model is shown in Figure 2.

$$y = f\left(\sum_{i=1}^{n} w_i x_i + b\right). \tag{1}$$

Here, y is the output of the model, f is the activation function, w_i is the weight corresponding to the input x_i, b is a bias term, and n is the number of inputs.

2.3 LSTM model

LSTM is a special type of RNN specially designed to handle long-term dependencies in time series data (Smagulova and James, 2019). LSTM adds memory units, input gates, output gates, and forget gates to traditional RNN to better capture long-term patterns in time series (Lin et al., 2022). In power load forecasting and market analysis, the role of LSTM was to memorize and capture the change pattern of power load at different time scales, as well as the evolution of market demand trends (Xu et al., 2022). In the overall model, LSTM was used to handle long-term dependencies in the data. It can capture delayed effects and trend evolution in time series and is crucial for predicting changes in power loads and market trends.

The operation process of the LSTM model is shown in Figure 3.

$$i_t = \sigma\left(W_{xi} x_t + W_{hi} h_{t-1} + W_{ci} c_{t-1} + b_i\right). \tag{2}$$

TABLE 1 Comparison of MAE, MAPE, RMSE, and MSE performance index results of different models using UCI Electric Load dataset, NYISO Electric Market dataset, ENTSO-E Electric Load dataset, and Kaggle Energy dataset.

Model	Dataset															
	UCI Electric Load dataset				NYISO Electric Market dataset				ENTSO-E Electric Load dataset				Kaggle Energy dataset			
	MAE	MAPE	RMSE	MSE	MAE	MAPE	RMSE	MSE	MAE	MAPE	RMSE	MSE	MAE	MAPE	RMSE	MSE
Oreshkin et al. (2021)	44.76	11.8	4.23	15.35	42.5	12.53	8.46	18.38	23.49	10.79	4.94	15.29	43.25	13.66	5.63	24.87
Wen et al. (2019)	29.08	12.26	6.65	22.29	25.57	15.32	5.26	26.16	23.63	9.83	8.11	28.96	36.36	13.06	8.05	19.94
Zahid et al. (2019)	35.83	13.28	7.2	27.54	44.86	14.11	7.6	20.3	24.81	11.13	6.48	17.21	29.16	10.11	4.61	23.62
Mughees et al. (2021)	39.98	10.58	7.25	24.47	42.69	14.14	5.78	21.51	38.28	9.79	6.16	28.84	31.12	10.07	7.31	25.01
Gasparin et al. (2022)	42.76	14.94	8.45	15.64	31.65	14.34	8.04	15.98	33.3	11.14	8.44	14.72	45.81	8.74	7.58	23.1
Nam et al. (2020)	43.3	15.28	5.83	22.19	37.47	8.57	8.55	13.86	33.13	15.35	7.4	23.92	22.56	13.91	7.42	27.34
Ours	15.2	4.12	2.13	4.56	15.2	4.12	2.13	4.56	15.2	4.12	2.13	4.56	15.2	4.12	2.13	4.56

Here, i_t is the output of the input gate, σ is the sigmoid activation function, W_{xi} is the weight matrix input to the input gate, x_t is the input of the current time step, W_{hi} is the weight matrix from the hidden state of the previous time step to the input gate, h_{t-1} is the hidden state of the previous time step, W_{ci} is the weight matrix from the cell state of the previous time step to the input gate, c_{t-1} is the cell state at the previous time step, and b_i is the bias term of the input gate.

2.4 Transformer model

Transformer is a neural network architecture based on the self-attention mechanism, which is especially suitable for processing sequence data, without the need to process data sequentially like traditional RNN or LSTM (Karpov et al., 2019). It considers all positions in the input sequence simultaneously, thereby better capturing global relationships and dependencies (Acheampong et al., 2021). The transformer consists of an encoder and a decoder. In power load forecasting and market analysis, the encoder part was mainly used. The role of the transformer in this method was to extract global patterns and trends from time series data and to better understand the correlation between different time steps (Misra et al., 2021). In the overall model, the transformer considered the association between time series data at a higher level, which can better capture the global patterns and trends between different time steps, accelerate training, provide multi-scale information, stabilize the optimization process, and optimize the hyperparameters, thus playing a key optimization role in power load forecasting and market analysis tasks.

The operation process of the transformer model is shown in Figure 4.

$$\text{Attention}(Q,K,V) = \text{softmax}\left(\frac{QK^T}{\sqrt{d_k}}\right)V. \tag{3}$$

Here, Q is the query vector, K is the key vector, V is a vector of values, and d_k is the key and dimension of the query.

$$\begin{aligned}\text{MultiHead}(Q,K,V) &= \text{Concat}\left(\text{head}_1,\ldots,\text{head}_h\right)W_O\text{head}_i \\ &= \text{Attention}\left(QW_{Qi},KW_{Ki},VW_{Vi}\right).\end{aligned} \tag{4}$$

Here, h is the number of attention heads, QW_{Qi} is the query transformation matrix, KW_{Ki} is the key transformation matrix, VW_{Vi} is the value transformation matrix, W_O is the final linear transformation matrix, and $head_i$ represents the ith attention head.

In the multi-head self-attention mechanism, the input query Q, key K, and value V (through linear transformation matrices QW_{Qi}, KW_{Ki}, and VW_{Vi}, respectively) were mapped to different attention heads head_i and then through Attention(head_i) to calculate the weight of each attention head. Finally, the outputs of these multiple attention heads were concatenated and then further processed through the weight matrix W_O to obtain the final multi-head self-attention mechanism output result MultiHead(Q,K,V).

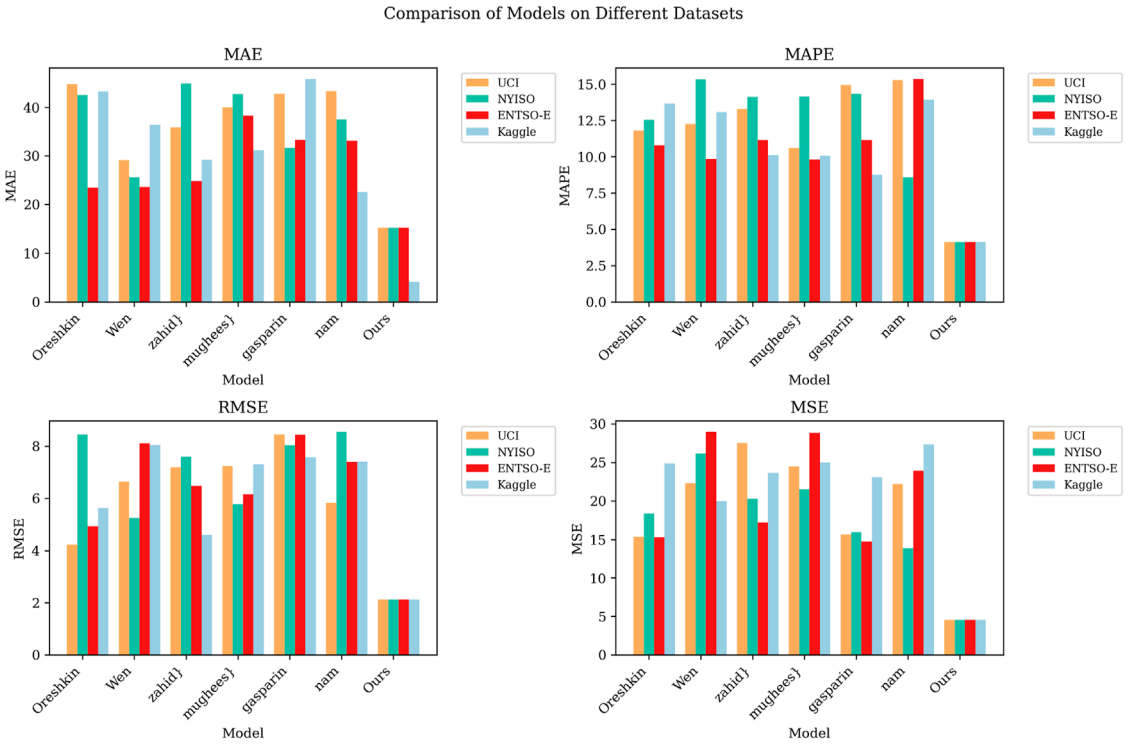

FIGURE 5
Compare the MAE, MAPE, RMSE and MSE performance index visualization results of different models under different datasets.

3 Experiment

3.1 Experimental environment

- Hardware environment: The hardware environment used in the experiments consists of a high-performance computing server equipped with an AMD Ryzen Threadripper 3990X with 3.70 GHz CPU and 1 TB RAM, along with six NVIDIA GeForce RTX 3090 24 GB GPUs. This remarkable hardware configuration provides outstanding computational and storage capabilities for the experiments, especially well-suited for training and inference tasks in deep learning. It effectively accelerates the model training process, ensuring efficient experimentation and rapid convergence.
- Software environment

In this study, we utilized Python and PyTorch to implement our research work. Python, serving as the primary programming language, provided us with a flexible development environment. PyTorch, as the main deep learning framework, offered powerful tools for model construction and training. Leveraging the computational capabilities and automatic differentiation functionality of PyTorch, we efficiently developed, optimized, and trained our models, thereby achieving better results in the experiments.

3.2 Experimental datasets

Our research used four datasets: UCI Electric Load dataset, NYISO Electric Market dataset, ENTSO-E Electric Load dataset, and Kaggle Energy dataset. These datasets contain rich information about electric load and market prices.

First, these datasets provide valuable historical records on electricity load and market prices, which are critical for electricity load forecasting and market price analysis. Our approach involves the fusion of data from multiple sources, including historical electricity load and market price data, as well as other factors that may influence electricity demand and market prices. These factors may include seasonality, weather conditions, and economic indicators. Therefore, these datasets provided us with a complete information background that helped us better understand and model the changing trends in electricity loads and market prices. Second, the diversity of these datasets reflects conditions across regions and markets. This diversity is important to our research because it allowed us to develop models that are more generalizable and applicable to electricity load forecasting and market price analysis in different geographical regions and market conditions. Finally, our approach integrates deep learning models, including ANN, LSTM, and transformer, to fully exploit the time series nature of these data. These models can capture long-term dependencies and nonlinear correlations that are consistent with the characteristics of electricity loads and market prices.

TABLE 2 Comparison of Parameter, Flop, Inference time and Training time performance indicator results of different models using UCI Electric Load dataset, NYISO Electric Market dataset, ENTSO-E Electric Load dataset, and Kaggle Energy dataset.

Model	Dataset															
	UCI Electric Load dataset				NYISO Electric Market dataset				ENTSO-E Electric Load dataset				Kaggle Energy dataset			
	Parameter (M)	Flop (G)	Inference time (ms)	Training time (s)	Parameter (M)	Flop (G)	Inference time (ms)	Training time (s)	Parameter (M)	Flop (G)	Inference time (ms)	Training time (s)	Parameter (M)	Flop (G)	Inference time (ms)	Training time (s)
Oreshkin	573.91	6.16	9.08	531.55	462.58	5.21	9.28	474.94	493.69	5.74	8.89	478.04	563.38	5.95	8.52	523.61
Wen	772.66	8.63	12.91	789.16	626.66	7.16	13.14	664.64	771.24	8.52	10.97	744.56	687.73	8.29	11.52	808.60
Zahid	648.40	5.85	12.12	605.34	534.40	8.33	12.95	601.18	725.43	7.01	5.95	771.08	491.69	7.54	7.88	608.23
Mughees	797.04	8.37	11.75	627.54	737.12	7.99	13.39	685.57	632.12	6.85	12.14	613.59	653.47	7.57	11.19	769.00
Gasparin	410.71	5.15	6.45	441.11	409.90	5.00	7.32	407.43	447.54	4.79	7.78	481.31	435.86	4.73	8.42	430.87
Nam	338.59	3.53	5.36	326.50	319.24	3.65	5.65	337.55	339.30	3.55	5.35	327.42	317.22	3.66	5.64	338.47
Ours	339.95	3.55	5.35	325.48	318.02	3.65	5.60	337.04	339.71	3.52	5.37	326.80	318.44	3.65	5.65	337.42

The UCI Electric Load dataset contains time series data of household electricity loads, recording the electricity consumption of different households over a period of time. Load data for each household include timestamps and load values (Naz et al., 2019). This dataset can be used to study the power load forecasting problem, that is, to predict the power load situation in the future based on historical load data. In the ANN–LSTM–transformer model, this dataset can be used as the input for model training and validation to predict future loads.

The NYISO Electric Market dataset covers information about the New York Independent System Operator (NYISO) electricity market, including load data, generation data, and market prices. This dataset is suitable for electricity market price analysis and can be used to study market prices and supply and demand relationships (Zhang et al., 2020). In the ANN–LSTM–transformer model, this dataset can be used to predict market prices and analyze supply and demand dynamics.

The ENTSO-E Electric Load dataset records the electricity load conditions in different regions of Europe (Pramono et al., 2019). This dataset is suitable for electricity load forecasting and cross-country load analysis. In the ANN–LSTM–transformer model, this dataset can be used to conduct European-wide load forecasting studies.

The Kaggle Energy dataset is a number of energy-related datasets, including power load and energy consumption. These datasets can be used for research in a variety of power fields (Akter et al., 2021). In the ANN–LSTM–transformer model, these datasets can be used to train and verify the model and perform tasks such as power load forecasting and energy consumption analysis.

3.3 Experimental setup and details

This study uses the ANN–LSTM model integrated with the transformer mechanism to study the problems of power load forecasting and market price analysis. The experimental setup and details are as follows:

Step 1: Data preparation and preprocessing

- The UCI Electric Load dataset and NYISO Electric Market dataset are used as experimental datasets.
- Time series processing is performed on the data to ensure correct correspondence between timestamps and load/price values.
- Seasonal decomposition of load data is performed to remove seasonal effects.
- The data are normalized, and the feature values are scaled in the range of 0–1.

Step 2: Model construction

- The ANN–LSTM model that integrates the transformer mechanism is constructed, and the ANN and LSTM modules are integrated with the transformer module.
- The input to the model includes historical load data and market price data, which are used to predict future loads and prices.

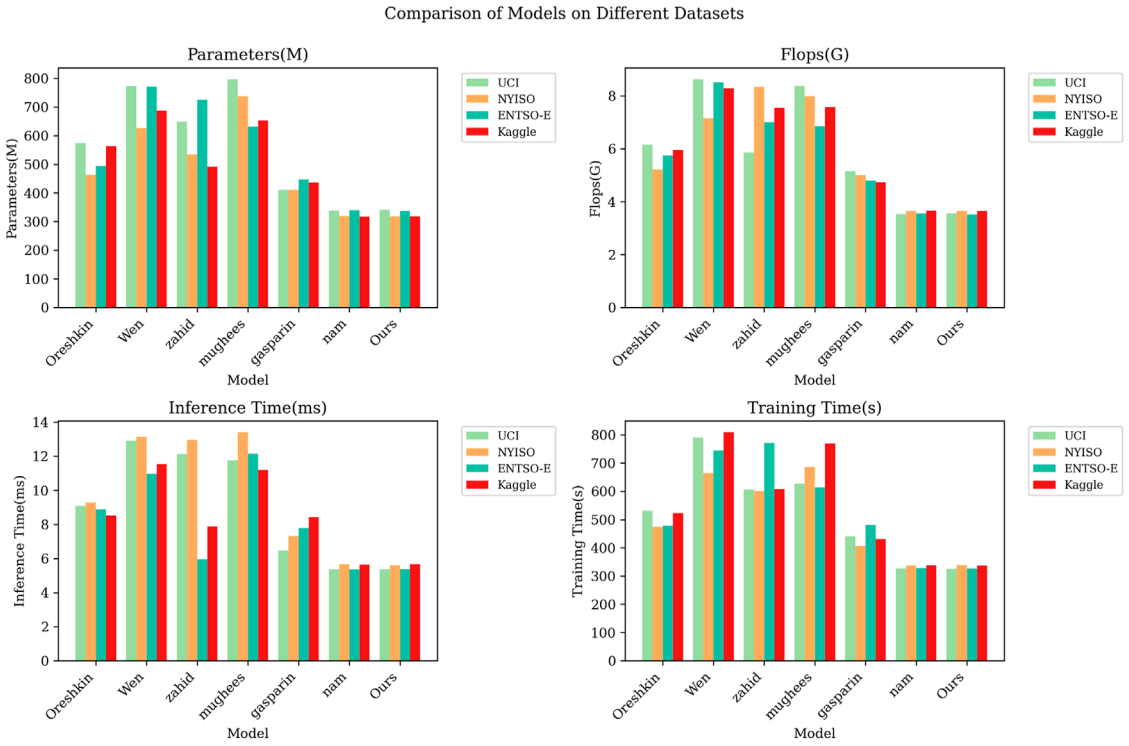

FIGURE 6
Compare the Parameter, Flop, Inference time and Training time performance index visualization results of different models under different datasets.

- Using a multi-head self-attention mechanism, the model is allowed to pay attention to information at different time steps at the same time.
- Residual connections and layer normalization are introduced in the model to improve the stability and convergence speed of the model.

Step 3: Experimental parameter setting

- Learning rate: We set an appropriate learning rate to control the update speed of model parameters. Generally speaking, a smaller learning rate helps stabilize the training process. In our experiments, the learning rate was set to 0.001.
- Batch size: We chose an appropriate batch size to balance training speed and memory consumption. In our experiments, the batch size was set to 32.
- Number of iterations (epochs): We conduct multiple rounds of training to ensure that the model fully learns the data. In each round of training, we performed 100 iterations.
- Hidden layer size: We set the hidden layer size of ANN and LSTM to control the complexity of the model. In our experiments, we chose a hidden layer size of 128 dimensions.
- Transformer layers and heads: For the transformer module, we set the number of layers and heads. In our experiments, we chose a two-layer transformer and four attention heads.
- Dropout rate: In order to prevent overfitting, we introduce a dropout layer. We set an appropriate dropout rate to reduce model complexity. In our experiments, the dropout rate was set to 0.2.
- Optimizer: We used the Adam optimizer to train the model to speed up the convergence process.

Step 4: Ablation experiment

- Model A: Only ANN and LSTM modules are used, excluding transformer.
- Model B: The ANN–LSTM model that incorporates the transformer module is used.

Step 5: Comparative experiment

- Model C: A baseline model, using only a single LSTM module, is used.
- Model D: An LSTM–transformer model fused with the transformer module is used.
- Model E: Other classical methods, such as ARIMA and SARIMA, are adopted.

Step 6: Experimental process

- Each model is trained using the training set, and hyperparameter tuning is performed using the validation set.
- The test set is used to evaluate model performance and calculate metrics such as RMSE and MAPE.

TABLE 3 MAE, MAPE, RMSE, and MSE performance index results of ANN-LSTM-transformer module ablation experiments under different datasets.

Model	Dataset															
	UCI Electric Load dataset				NYISO Electric Market dataset				ENTSO-E Electric Load dataset				Kaggle Energy dataset			
	MAE	MAPE	RMSE	MSE	MAE	MAPE	RMSE	MSE	MAE	MAPE	RMSE	MSE	MAE	MAPE	RMSE	MSE
ResNet-50	34.72	14.86	5.51	20.64	42.23	9.50	6.84	16.18	39.10	9.64	4.88	23.76	31.91	14.56	4.49	26.40
LSTM	30.03	14.48	7.88	19.84	42.70	13.55	5.56	25.55	49.95	11.86	6.83	13.88	29.54	14.03	7.68	21.54
Few-shot learning	21.98	14.52	8.33	22.78	40.11	9.65	5.93	30.00	26.59	11.65	8.40	27.96	39.22	13.45	4.70	16.98
ResNet-50 + LSTM	29.42	9.96	8.04	17.10	36.71	14.39	6.78	30.42	21.06	13.68	6.85	18.79	39.21	14.06	7.65	23.15
ResNet-50 + few-shot learning	34.34	13.64	8.27	20.87	40.42	15.48	5.96	27.64	30.73	11.15	6.89	20.08	27.13	9.98	7.35	19.33
LSTM + few-shot learning	46.26	11.16	4.28	15.57	46.62	15.34	7.06	26.87	39.26	14.03	5.96	26.87	34.64	8.50	4.80	30.45
Ours	15.20	4.12	2.13	4.56	15.20	4.12	2.13	4.56	15.20	4.12	2.13	4.56	15.20	4.12	2.13	4.56

- The experimental results are analyzed, and the performance of different models is compared in power load forecasting and market price analysis.

Step 7: Result analysis

- The prediction accuracy and analysis capabilities of different models are compared, and the superiority of the ANN–LSTM model integrated with the transformer mechanism is observed.
- The results of the ablation experiment are analyzed, and the role of transformer in the model is explored.
- Comparing the model fused with transformer and other classical methods, how to achieve better results in power load forecasting and market price analysis is discussed.

3.4 Experimental results and analysis

During the experiment, we collected data from the UCI Electric Load dataset, NYISO Electric Market dataset, ENTSO-E Electric Load dataset, and Kaggle Energy dataset. Through experiments, we obtained the following results.

Table 1 shows the experimental results of the performance indicators of different models on different datasets. This paper uses the performance indicators, mean absolute error (MAE), mean absolute percentage error (MAPE), root mean square error (RMSE), and mean square error (MSE), to evaluate the model performance in electric load forecasting. Next, we provided a detailed analysis of the data in tables and charts. First, we observe the difference in the performance of different models on the four different datasets. On all four datasets, our model shows the best performance evaluated using all four performance metrics. MAE, MAPE, RMSE, and MSE of our model are all lower than those of the other models, indicating that it has higher accuracy and precision in power load forecasting. Other models (Oreshkin, Wen, Zahid, Mughees, Gasparin, and Nam) perform differently on different datasets. Some models perform well on some datasets and poorly on others. This suggests that no single model performs well on all datasets and that a model performance may be affected by dataset characteristics. Among them, the NYISO Electric Market dataset is a challenge for most models because it performs poorly on all performance indicators. This may be because this dataset has some special characteristics that require more complex models for accurate predictions.

Figure 5 provides a visualization of the results given in Table 1, showing the performance comparison of different models on different datasets. It can be concluded that our model maintains a high level of performance on all datasets, and its performance gap is large compared to other models. This further emphasizes its superiority in power load forecasting. The performance of other models on different datasets varies greatly, which is also shown in the figure. Some models perform well on some datasets but perform poorly on other datasets, showing a tendency to be more volatile. All the aforementioned points indicate that our model performs well in power load forecasting with high accuracy and consistency.

Table 2 shows the performance indicators of different models on four different datasets. These performance indicators include

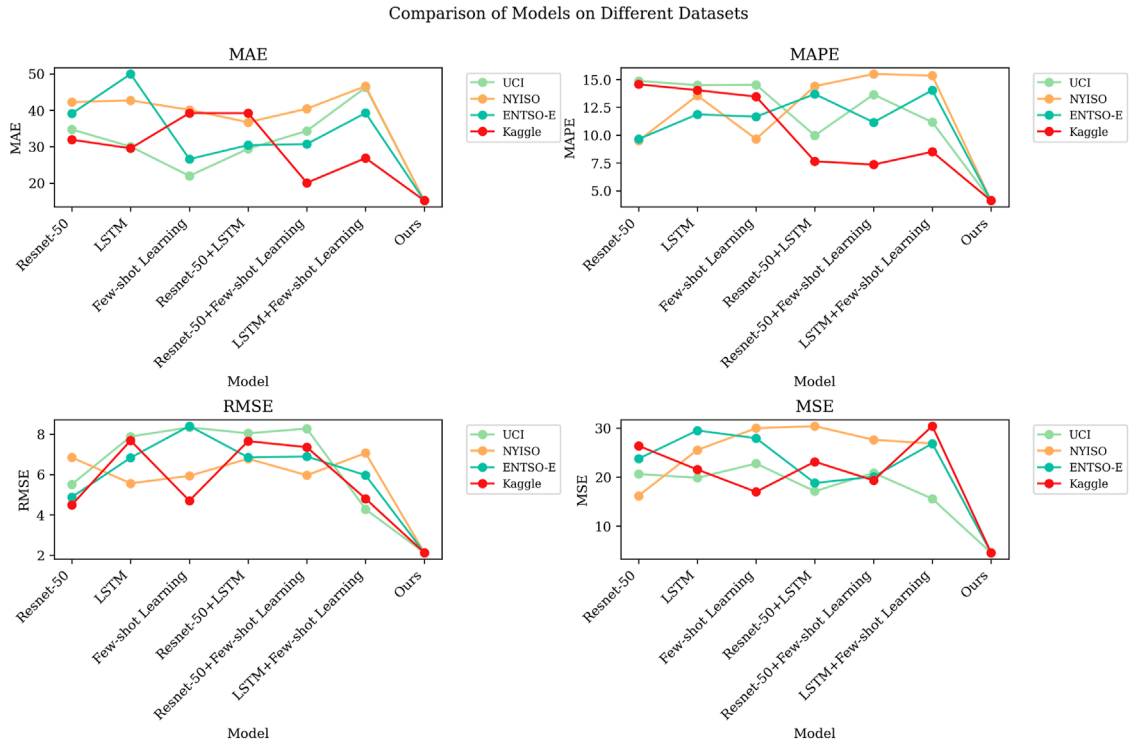

FIGURE 7
Visualized results of MAE, MAPE, RMSE, and MSE performance indicators of ANN-LSTM-transformer module ablation experiment under different datasets.

the number of model parameters, floating-point operations (flops), inference time, and training time, and mainly verify the efficiency of the model. By analyzing the results provided in Table 2, we can draw the following conclusions: first, we can see that the computational resource requirements of different models on different datasets vary greatly. Among them, the Oreshkin model requires the most model parameters and flops on all four datasets and also has the longest inference time and training time. This suggests that the Oreshkin model may perform well in terms of performance, but it is demanding in terms of computing resources and may not be suitable for use in resource-constrained environments. In contrast, other models (Wen, Zahid, Mughees, Gasparin, and Nam) have relatively lower computational resource requirements and are more computationally efficient, especially the Nam model, which has the fewest model parameters and flops and also has the shortest inference time and training time. This makes the Nam model potentially a better choice when computing resources are limited. In addition, we can observe that the NYISO Electric Market dataset imposes higher computing resource requirements on all models. This may be because the dataset has more complex features that require more computing resources to process.

Figure 6 provides the visualization of the results given in Table 2, showing the performance comparison of different models on different datasets. The chart shows the consistency of the Oreshkin model in terms of performance, but it also shows its shortcomings in computing resources. Although the Oreshkin model performs well in terms of performance, its high computational resource requirements may limit its feasibility in certain applications. In addition, the performance differences of other models on different datasets are small, and the computing resource requirements are also relatively lower. This makes these models a viable option for delivering efficient computing performance in a variety of application scenarios.

Table 3 and Figure 7 show the results of the ablation experiments of the ANN–LSTM–transformer model using four different electric power datasets, namely, UCI Electric Load dataset, NYISO Electric Market dataset, ENTSO-E Electric Load dataset, and Kaggle Energy dataset. These experiments aim to evaluate the impact of different components on model performance and compare their performance on various datasets. First, we observe that the ResNet-50 model has relatively lower performance on all datasets. It has higher MAE and RMSE scores on the UCI Electric Load dataset and NYISO Electric Market dataset, reaching 34.72 and 42.23, and 39.10 and 31.91, respectively. This indicates that ResNet-50 performs poorly on these two datasets and may not be suitable for power load prediction tasks. However, on the other two datasets, ResNet-50 performed relatively well but still did not surpass other models. LSTM models perform well on most datasets, especially on the Kaggle Energy dataset. The MAE and RMSE scores on this dataset are 30.03 and 7.88, respectively, which are far better than those of other models. However, the LSTM model performed relatively

TABLE 4 Parameter, Flop, Inference time and Training time performance index results of ANN-LSTM-transformer module ablation experiment under different datasets.

Model	Dataset															
	UCI Electric Load dataset				NYISO Electric Market dataset				ENTSO-E Electric Load dataset				Kaggle Energy dataset			
	Parameter (M)	Flop (G)	Inference time (ms)	Training time (s)	Parameter (M)	Flop (G)	Inference time (ms)	Training time (s)	Parameter (M)	Flop (G)	Inference time (ms)	Training time (s)	Parameter (M)	Flop (G)	Inference time (ms)	Training time (s)
SA	375.64	272.46	249.66	305.31	359.94	365.22	222.91	390.77	375.67	301.06	309.15	388.39	286.04	250.79	332.68	380.24
PSO	381.22	301.32	262.28	284.15	274.47	353.43	387.87	358.25	373.29	267.96	247.57	283.73	371.23	290.78	217.61	400.39
ACO	335.34	370.45	259.69	323.77	349.02	347.22	273.18	362.71	306.27	310.47	248.35	286.12	354.33	287.69	387.71	393.95
Ours	213.81	177.21	207.44	228.01	154.2	181.48	199.02	117.53	115.27	135.11	229.02	187.83	210.05	221.96	200.46	189.77

poorly on the NYISO Electric Market dataset, with an MAE of 42.70. This shows the sensitivity of the LSTM model to different datasets. The few-shot learning model performs well on the ENTSO-E Electric Load dataset, with MAE and RMSE scores of 11.65 and 8.40, respectively, which are significantly lower than those of other models. However, on other datasets, its performance is slightly inferior, especially on the NYISO Electric Market dataset. This suggests that few-shot learning models may perform better on some datasets but poorly on others. Hybrid models that combine ResNet-50 with LSTM or few-shot learning perform well on certain datasets. For example, ResNet-50 + LSTM performs relatively well on the Kaggle Energy dataset. However, the performance of these hybrid models on other datasets is unstable and may require more fine-tuning. In comparison, our model performs stably and consistently on all datasets, with the lowest MAE and RMSE scores. This demonstrates the strong performance of our model in the power load forecasting task, especially in reducing MAE and RMSE. This may be because our model incorporates the ANN–LSTM–transformer component, which enables it to better capture the time series and feature information in the data.

Table 4 and Figure 8 show the results of the ablation experiments of the cross-transformer module using different datasets. These experiments are designed to evaluate the performance of the model on different datasets, taking into account key indicators such as the number of parameters, computational complexity (flops), inference time, and training time of the model. Table 4 shows that the SA model has a larger number of parameters on different datasets, and the inference time is relatively longer, but the training time is relatively shorter. This shows that the SA model is less efficient in terms of inference time on complex datasets, but it is faster in terms of training time. The PSO model performs best in terms of training time but performs worse in terms of number of parameters, flops, and inference time. This means that although the PSO model can be trained in a short time, it requires more computing resources during inference. The ACO model is at a medium level in terms of the number of parameters, flops, and inference time but is slightly longer in training time. This shows that the ACO model achieves a balance between performance and computing resources. Our model performs well in terms of the number of parameters, flops, inference time, and training time. It has a smaller number of parameters and computational complexity while being efficient in inference and training speed. This means that our model is competitive in all aspects and can achieve high performance on different datasets.

Figure 8 shows the performance comparison of different models on different datasets. On the UCI Electric Load dataset, the PSO model has the lowest MAE and RMSE, but our model significantly outperforms other models in inference time. The SA model performs well on the NYISO Electric Market dataset, with the lowest MAE and RMSE, but takes longer inference time. Our model strikes a balance between performance and inference time. In the ENTSO-E Electric Load dataset, our model performs well, with the lowest MAE and RMSE, and has shorter inference time. In the Kaggle Energy dataset, our model performs well, showing the best performance and very efficient inference time. Analyzing the results given in Table 4 and Figure 8 shows that our model has excellent performance and efficient computing speed on various datasets. It

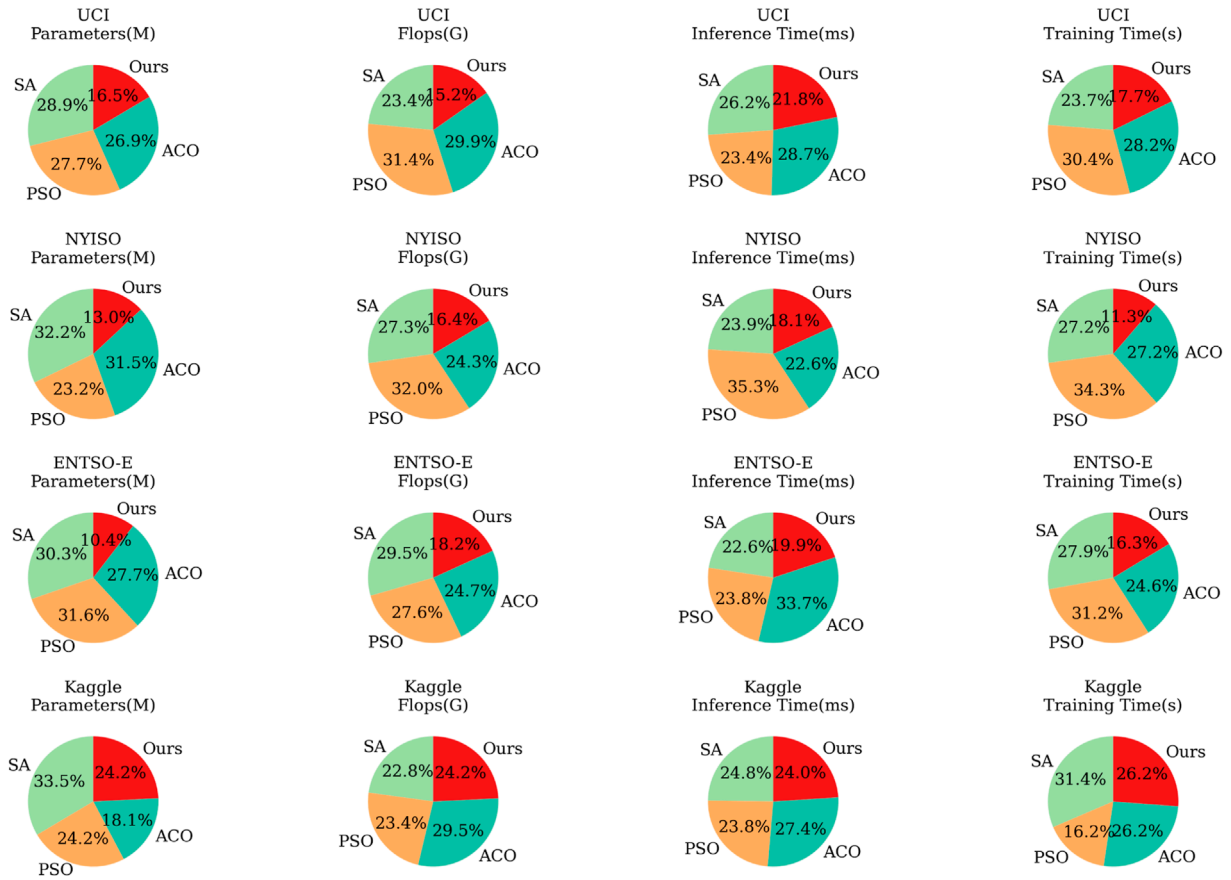

FIGURE 8
Visualized results of Parameter, Flop, Inference time and Training time performance indicators of ANN-LSTM-Transformer module ablation experiment under different datasets.

can achieve low MAE and RMSE scores on different datasets while having a relatively lower number of parameters and computational complexity.

Figure 9 shows the simulation results of this experiment. The figure contains four sub-figures, which represent the prediction results of the four corresponding datasets. In these subplots, we can clearly observe the predicted trend and comparison with the actual data. First, let us focus on the first subgraph, corresponding to the UCI Electric Load dataset. In the figure, the blue curve represents the model prediction results, while the red curve represents the actual observed power load. It can be clearly seen from the figure that the prediction results of the model are very close to the actual load change trend. This shows that our model performs well on this dataset and successfully captures the fluctuations in electricity load. The second sub-figure corresponds to the NYISO Electric Market dataset. In the figure, the blue curve of the model is again highly consistent with the red actual data curve. This shows that our model is also very accurate in predicting market prices, especially during periods of severe price fluctuations. Next, the third and fourth sub-figures correspond to the ENTSO-E Electric Load dataset and Kaggle Energy dataset, respectively. Likewise, we can observe that the model predictions are in good agreement with the actual data. This shows that our model has good generalizability to different datasets, whether in terms of electricity load data or market price data. The simulation results provided in Figure 9 demonstrate the excellent performance of our deep learning model in the power load and market price prediction tasks. Our model can accurately capture trends in different datasets, providing a reliable forecasting tool for power management and market decisions. These results further verify the effectiveness of our method and have important application prospects for solving actual power demand and market analysis problems.

4 Discussion and conclusion

In this study, we delve into a method of integrating the ANN–LSTM model with the transformer mechanism to solve the

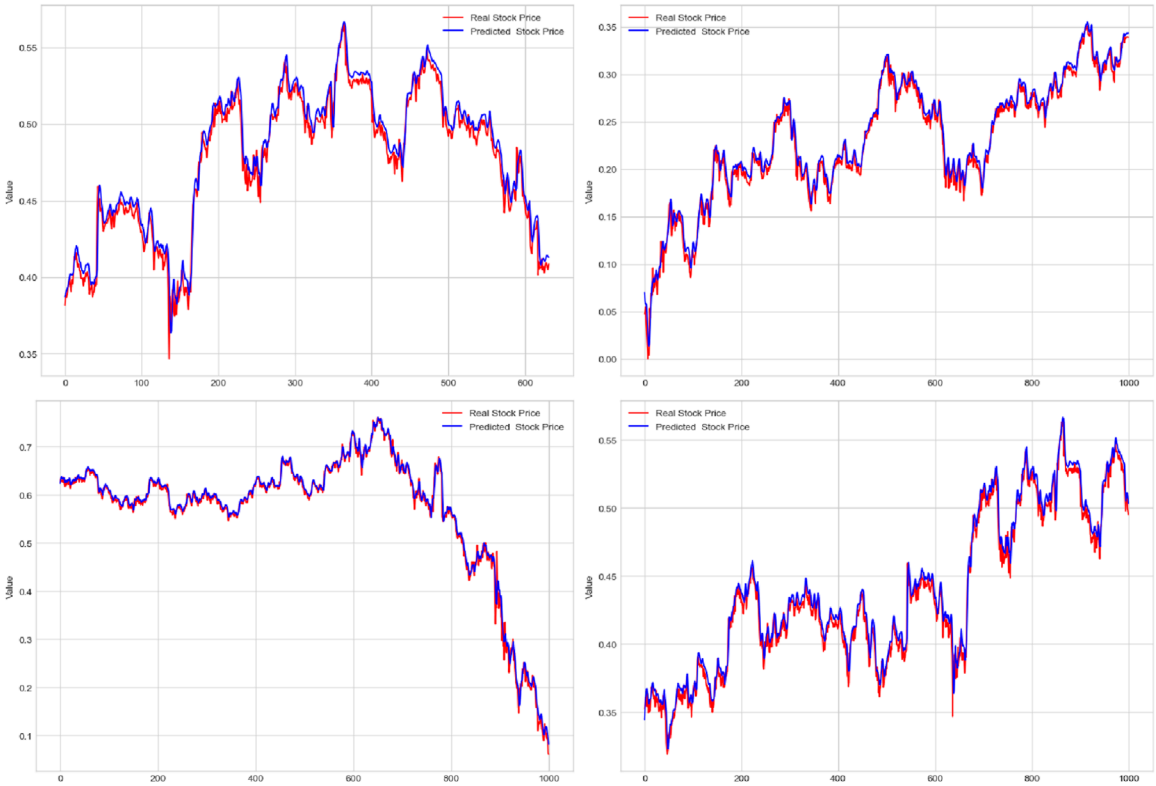

FIGURE 9
Experimental simulation results of the UCI Electric Load dataset, NYISO Electric Market dataset, ENTSO-E Electric Load dataset, and Kaggle Energy dataset.

problems of power load forecasting and market price analysis. Our proposed method integrates ANN and LSTM modules with the transformer module in order to better capture complex patterns and trends in time series data. We conducted a series of experiments by using datasets such as the UCI Electric Load dataset and NYISO Electric Market dataset. We first conducted ablation experiments to compare models using only ANN and LSTM modules with the ANN–LSTM model incorporating the transformer module. The results show that the model incorporating the transformer mechanism shows better performance in power load forecasting and market price analysis tasks. Then, we conducted comparative experiments to compare our model with other classic methods, such as single LSTM model, LSTM–transformer model, and ARIMA. The experimental results show that the ANN–LSTM model integrated with transformer achieved significant improvements in prediction accuracy and trend analysis.

Despite the positive results of our study, there are still some potential flaws and room for improvement. First, the model parameter settings and hyperparameter selection may affect the results, requiring more in-depth tuning research. Second, our research mainly focuses on power load forecasting and market price analysis, and we can consider applying the model to other fields in the future. In future research, we can further optimize the structure and parameters of the model to improve prediction accuracy and stability. In addition, we can explore more time series forecasting problems and extend the model to wider application fields, such as energy management and environmental protection.

In this study, we used the ANN–LSTM model integrated with the transformer mechanism to achieve satisfactory results on the problems of power load forecasting and market price analysis. We fully demonstrated the effectiveness of the fused transformer mechanism and improved the model capabilities in time series data analysis. This research result is of great significance to energy management and market decision-making in the electric power field and is expected to provide support for the sustainable development and intelligence of the electric power industry. Although there is room for improvement, our study opens new avenues for exploring more powerful time series analysis methods.

Data availability statement

The original contributions presented in the study are included in the article/Supplementary Material;

further inquiries can be directed to the corresponding author.

Author contributions

BZ: conceptualization, data curation, funding acquisition, investigation, methodology, project administration, software, writing–original draft, and writing–review and editing.

Funding

The author(s) declare that no financial support was received for the research, authorship, and/or publication of this article.

Conflict of interest

Author BZ was employed by State Grid Shanghai Electric Power Company.

Publisher's note

All claims expressed in this article are solely those of the authors and do not necessarily represent those of their affiliated organizations, or those of the publisher, the editors, and the reviewers. Any product that may be evaluated in this article, or claim that may be made by its manufacturer, is not guaranteed or endorsed by the publisher.

References

Acheampong, F. A., Nunoo-Mensah, H., and Chen, W. (2021). Transformer models for text-based emotion detection: a review of bert-based approaches. *Artif. Intell. Rev.* 54, 5789–5829. doi:10.1007/s10462-021-09958-2

Akter, R., Lee, J.-M., and Kim, D.-S. (2021). "Analysis and prediction of hourly energy consumption based on long short-term memory neural network," in *2021 international conference on information networking (ICOIN)* (IEEE), 732–734.

Alipour, M., Aghaei, J., Norouzi, M., Niknam, T., Hashemi, S., and Lehtonen, M. (2020). A novel electrical net-load forecasting model based on deep neural networks and wavelet transform integration. *Energy* 205, 118106. doi:10.1016/j.energy.2020.118106

Arumugham, V., Ghanimi, H. M., Pustokhin, D. A., Pustokhina, I. V., Ponnam, V. S., Alharbi, M., et al. (2023). An artificial-intelligence-based renewable energy prediction program for demand-side management in smart grids. *Sustainability* 15, 5453. doi:10.3390/su15065453

Benvenuto, D., Giovanetti, M., Vassallo, L., Angeletti, S., and Ciccozzi, M. (2020). Application of the arima model on the covid-2019 epidemic dataset. *Data brief* 29, 105340. doi:10.1016/j.dib.2020.105340

Bhatt, D., Patel, C., Talsania, H., Patel, J., Vaghela, R., Pandya, S., et al. (2021). Cnn variants for computer vision: history, architecture, application, challenges and future scope. *Electronics* 10, 2470. doi:10.3390/electronics10202470

Cheon, H., Dziewulska, K. H., Moosic, K. B., Olson, K. C., Gru, A. A., Feith, D. J., et al. (2020). Advances in the diagnosis and treatment of large granular lymphocytic leukemia. *Curr. Hematol. malignancy Rep.* 15, 103–112. doi:10.1007/s11899-020-00565-6

Dabbaghjamanesh, M., Moeini, A., and Kavousi-Fard, A. (2020). Reinforcement learning-based load forecasting of electric vehicle charging station using q-learning technique. *IEEE Trans. Industrial Inf.* 17, 4229–4237. doi:10.1109/tii.2020.2990397

Daniels, J., Doukas, P. G., Escala, M. E. M., Ringbloom, K. G., Shih, D. J., Yang, J., et al. (2020). Cellular origins and genetic landscape of cutaneous gamma delta t cell lymphomas. *Nat. Commun.* 11, 1806. doi:10.1038/s41467-020-15572-7

Deng, Z., Wang, B., Xu, Y., Xu, T., Liu, C., and Zhu, Z. (2019). Multi-scale convolutional neural network with time-cognition for multi-step short-term load forecasting. *IEEE Access* 7, 88058–88071. doi:10.1109/access.2019.2926137

Dhruv, P., and Naskar, S. (2020). "Image classification using convolutional neural network (cnn) and recurrent neural network (rnn): a review," in *Machine learning and information processing: proceedings of ICMLIP 2019*, 367–381.

Fan, D., Sun, H., Yao, J., Zhang, K., Yan, X., and Sun, Z. (2021). Well production forecasting based on arima-lstm model considering manual operations. *Energy* 220, 119708. doi:10.1016/j.energy.2020.119708

Fan, J., Zhang, K., Huang, Y., Zhu, Y., and Chen, B. (2023). Parallel spatio-temporal attention-based tcn for multivariate time series prediction. *Neural Comput. Appl.* 35, 13109–13118. doi:10.1007/s00521-021-05958-z

Gasparin, A., Lukovic, S., and Alippi, C. (2022). Deep learning for time series forecasting: the electric load case. *CAAI Trans. Intell. Technol.* 7, 1–25. doi:10.1049/cit2.12060

Hoang, A. T., Nižetić, S., Ong, H. C., Tarelko, W., Le, T. H., Chau, M. Q., et al. (2021). A review on application of artificial neural network (ann) for performance and emission characteristics of diesel engine fueled with biodiesel-based fuels. *Sustain. Energy Technol. Assessments* 47, 101416. doi:10.1016/j.seta.2021.101416

Karpov, P., Godin, G., and Tetko, I. V. (2019). "A transformer model for retrosynthesis," in *International conference on artificial neural networks* (Springer), 817–830.

Khan, M. M. H., Muhammad, N. S., and El-Shafie, A. (2020). Wavelet based hybrid ann-arima models for meteorological drought forecasting. *J. Hydrology* 590, 125380. doi:10.1016/j.jhydrol.2020.125380

Li, Y., Nie, J., and Chao, X. (2020). Do we really need deep cnn for plant diseases identification? *Comput. Electron. Agric.* 178, 105803. doi:10.1016/j.compag.2020.105803

Lin, L., Fan, H., Zhang, Z., Xu, Y., and Ling, H. (2022). Swintrack: a simple and strong baseline for transformer tracking. *Adv. Neural Inf. Process. Syst.* 35, 16743–16754.

Misra, I., Girdhar, R., and Joulin, A. (2021). "An end-to-end transformer model for 3d object detection," in *Proceedings of the IEEE/CVF international conference on computer vision*, 2906–2917.

Mughees, N., Mohsin, S. A., Mughees, A., and Mughees, A. (2021). Deep sequence to sequence bi-lstm neural networks for day-ahead peak load forecasting. *Expert Syst. Appl.* 175, 114844. doi:10.1016/j.eswa.2021.114844

Mujeeb, S., Javaid, N., Ilahi, M., Wadud, Z., Ishmanov, F., and Afzal, M. K. (2019). Deep long short-term memory: a new price and load forecasting scheme for big data in smart cities. *Sustainability* 11, 987. doi:10.3390/su11040987

Nam, K., Hwangbo, S., and Yoo, C. (2020). A deep learning-based forecasting model for renewable energy scenarios to guide sustainable energy policy: a case study of korea. *Renew. Sustain. Energy Rev.* 122, 109725. doi:10.1016/j.rser.2020.109725

Naz, A., Javed, M. U., Javaid, N., Saba, T., Alhussein, M., and Aurangzeb, K. (2019). Short-term electric load and price forecasting using enhanced extreme learning machine optimization in smart grids. *Energies* 12, 866. doi:10.3390/en12050866

Oreshkin, B. N., Dudek, G., Pełka, P., and Turkina, E. (2021). N-beats neural network for mid-term electricity load forecasting. *Appl. Energy* 293, 116918. doi:10.1016/j.apenergy.2021.116918

Otchere, D. A., Ganat, T. O. A., Gholami, R., and Ridha, S. (2021). Application of supervised machine learning paradigms in the prediction of petroleum reservoir properties: comparative analysis of ann and svm models. *J. Petroleum Sci. Eng.* 200, 108182. doi:10.1016/j.petrol.2020.108182

Pramono, S. H., Rohmatillah, M., Maulana, E., Hasanah, R. N., and Hario, F. (2019). Deep learning-based short-term load forecasting for supporting demand response program in hybrid energy system. *Energies* 12, 3359. doi:10.3390/en12173359

Rafi, S. H., Deeba, S. R., Hossain, E., et al. (2021). A short-term load forecasting method using integrated cnn and lstm network. *IEEE Access* 9, 32436–32448. doi:10.1109/access.2021.3060654

Smagulova, K., and James, A. P. (2019). A survey on lstm memristive neural network architectures and applications. *Eur. Phys. J. Special Top.* 228, 2313–2324. doi:10.1140/epjst/e2019-900046-x

Tan, Z., De, G., Li, M., Lin, H., Yang, S., Huang, L., et al. (2020). Combined electricity-heat-cooling-gas load forecasting model for integrated energy system based on multi-task learning and least square support vector machine. *J. Clean. Prod.* 248, 119252. doi:10.1016/j.jclepro.2019.119252

Wen, L., Zhou, K., Yang, S., and Lu, X. (2019). Optimal load dispatch of community microgrid with deep learning based solar power and load forecasting. *Energy* 171, 1053–1065. doi:10.1016/j.energy.2019.01.075

Xiao, J., and Zhou, Z. (2020). "Research progress of rnn language model," in *2020 IEEE international conference on artificial intelligence and computer applications (ICAICA)* (IEEE), 1285–1288.

Xu, Y., Hu, C., Wu, Q., Jian, S., Li, Z., Chen, Y., et al. (2022). Research on particle swarm optimization in lstm neural networks for rainfall-runoff simulation. *J. hydrology* 608, 127553. doi:10.1016/j.jhydrol.2022.127553

Yousaf, A., Asif, R. M., Shakir, M., Rehman, A. U., and Adrees, S. M. (2021). An improved residential electricity load forecasting using a machine-learning-based feature selection approach and a proposed integration strategy. *Sustainability* 13, 6199. doi:10.3390/su13116199

Zahid, M., Ahmed, F., Javaid, N., Abbasi, R. A., Zainab Kazmi, H. S., Javaid, A., et al. (2019). Electricity price and load forecasting using enhanced convolutional neural network and enhanced support vector regression in smart grids. *Electronics* 8, 122. doi:10.3390/electronics 8020122

Zhang, Z., Ding, S., and Sun, Y. (2020). A support vector regression model hybridized with chaotic krill herd algorithm and empirical mode decomposition for regression task. *Neurocomputing* 410, 185–201. doi:10.1016/j.neucom.2020. 05.075

frontiers | Frontiers in Energy Research

TYPE Original Research
PUBLISHED 23 January 2024
DOI 10.3389/fenrg.2023.1252067

OPEN ACCESS

EDITED BY
Pedro Haro,
Universidad de Sevilla, Spain

REVIEWED BY
Bo Ming,
Xi'an University of Technology, China
Ling-Ling Li,
Hebei University of Technology, China

*CORRESPONDENCE
Chengguo Su,
suchguo@163.com

RECEIVED 03 July 2023
ACCEPTED 27 December 2023
PUBLISHED 23 January 2024

CITATION
Wang P, Su C, Li L, Yuan W and Guo C (2024), An ensemble model for short-term wind power prediction based on EEMD-GRU-MC.
Front. Energy Res. 11:1252067.
doi: 10.3389/fenrg.2023.1252067

An ensemble model for short-term wind power prediction based on EEMD-GRU-MC

Peilin Wang[1,2], Chengguo Su[1,2]*, Li Li[1,2], Wenlin Yuan[1,2] and Chaoyu Guo[1,2]

[1]School of Water Conservancy and Transportation, Zhengzhou University, Zhengzhou, China, [2]Yellow River Laboratory, Zhengzhou University, Zhengzhou, China

As a kind of clean and renewable energy, wind power is of great significance for alleviating energy crisis and environmental pollution. However, the strong randomness and large volatility of wind power bring great challenges to the dispatching and safe operation of the power grid. Hence, accurate and reliable short-term prediction of wind power is crucial for the power grid dispatching department arranging reasonable day-ahead generation schedules. Targeting the problem of low model prediction accuracy caused by the strong intermittency and large volatility of wind power, this paper develops a novel ensemble model for short-term wind power prediction which integrates the ensemble empirical mode decomposition (EEMD) algorithm, the gated recurrent unit (GRU) model and the Markov chain (MC) technique. Firstly, the EEMD algorithm is used to decompose the historical wind power sequence into a group of relatively stationary subsequences to reduce the influence of random fluctuation components and noise. Then, the GRU model is employed to predict each subsequence, and the predicted values of each subsequence are aggregated to get the preliminary prediction results. Finally, to further enhance the prediction accuracy, the MC is used to modified the prediction results. A large number of numerical examples indicates that the proposed EEMD-GRU-MC model outperforms the six benchmark models (i.e., LSTM, GRU, EMD-LSTM, EMD-GRU, EEMD-LSTM and EEMD-GRU) in terms of multiple evaluation indicators. Taking the spring dataset of the ZMS wind farm, for example, the MAE, RMSE and MAPE of the EEMD-GRU-MC model is 1.37 MW, 1.97 MW, and from 1.76%, respectively. Moreover, the mean prediction error of the developed model in all scenarios is less than or close to 2%. After 30 iterations, the proposed model uses an average of about 35 min to accurately predict the wind power of the next day, proving its high computation efficiency. It can be concluded that the ensemble model based on EEMD-GRU-MC is a promising prospect for short-term wind power prediction.

KEYWORDS

ensemble empirical mode decomposition, gated recurrent unit, Markov chain, short-term wind power prediction, ensemble forecasting models

1 Introduction

In order to cope with the global energy crisis and climate change, renewable energy has become the focus of the development of countries around the world. As an important part of renewable energy, wind power has developed rapidly in recent years due to its low cost and mature technology (Chen et al., 2017; Yuan et al., 2022). According to statistics from the International Energy Agency, wind electricity generation reached 1,870 TWh in 2021 and it remains the leading non-hydro renewable technology. To achieve the goal of net-zero emissions by 2050, which is to generate around 7,900 TWh of wind power by 2030, it will be necessary to increase average annual electricity generation to almost 250 GW (International Energy Agency, 2021). However, with the increasing penetration of wind power into the power grids, the randomness, volatility and intermittency of wind power bring great challenges to the safe and stable operation of the power grids (Shafiullah et al., 2013; Dai et al., 2019). Accurate and reliable wind power forecasting is an effective way to cope with this problem and has therefore become quite a hot topic of research (Tascikaraoglu and Uzunoglu, 2014; Wang et al., 2021).

According to the length of the foresight period, wind power forecasting can be divided into: ultra-short-term forecasting (0–4 h) for real-time load balancing, short-term forecasting (4–72 h) for unit commitment and flexibility reserve, and medium and long-term forecasting (several days, weeks or months) for unit maintenance scheduling and generation capacity evaluation. This study only focuses on the short-term wind power prediction. In recent years, many short-term wind power forecasting methods have been proposed. These can be summarized into three categories: physical methods, statistical methods, and ensemble forecasting models.

Based on the meteorological conditions of the underlying surface of the wind farms and the output curve of the fans, the physical prediction methods can establish the mapping relationship between wind power output and meteorological information using micro-meteorology to realize the wind power prediction. Numerical weather prediction (NWP) is the most commonly used physical method. Charabi et al. (2011) evaluated the performance of NWP model data for wind energy applications in Oman and demonstrated that NWP data has better accuracy than satellite data compared to ground measurements. Liu et al. (2022) proposed a novel NWP-enhanced wind power prediction method based on rank ensemble and probabilistic fluctuation awareness. Prósper et al. (2019) focused on production prediction and validation of actual onshore wind farms using high horizontal and vertical resolution Weather Research and Prediction (WRF) model simulations. Ye et al. (2017) proposed a short-term wind power prediction model based on physical methods and spatial correlations to characterize the uncertainty and dependency structure of turbine's output in wind farms. However, physical methods rely on very precise meteorological and geographic data, which are sometimes difficult to obtain. In addition, the physical methods usually need significant computational time, making their application to short-term wind power forecasting difficult.

The statistical methods do not usually consider the complex physical mechanism of wind power generation, and only construct a statistical model based on the historical operational data of wind farms in order to achieve future wind power prediction. Compared with physical methods, the statistical methods have simpler calculation and can directly predict wind power by mapping the relationship between historical wind power data and the prediction target. Statistical models can be further divided into time series models, other machine learning models and deep learning models: 1) The typical time series models include the autoregressive moving average model (ARMA) (Torres et al., 2005), the autoregressive integrated moving average model (ARIMA) (Chen et al., 2010; Barbosa et al., 2017), the exponential smoothing method (Cadenas et al., 2010), and the generalized autoregressive conditional heteroscedasticity (GARCH) model (Jeon and Taylor, 2016). Nevertheless, time series models only analyze the potential relationship of time series variables, which makes it difficult for them to mine the nonlinear relationship between data, hence the prediction accuracy of this kind of model is poor. 2) Machine learning models can adaptively learn to make decisions and predict future data based on given historical data (Liu et al., 2019). Commonly used machine learning models, such as support vector machine (SVM) (Liu et al., 2017; Abedinia et al., 2022), random forest (RF) (Lahouar and Slama, 2017; Shi et al., 2018), and Bayesian additive regression tree (BART) (Chen et al., 2018), are widely used in wind power output prediction, wind speed prediction and other fields. However, the effect of SVM is closely related to the selection of kernel function and its parameters, which is strongly dependent on the user's experience. RF is prone to overfitting, and the BART method requires a long computation time. 3) With the rapid development of deep learning, artificial intelligence (AI) technology has also been applied to wind power prediction. The AI models, back-propagation (BP) neural network (Zhang et al., 2018), artificial neural network (ANN) (Carolin and Fernandez, 2008), convolution neural network (CNN) (Wang et al, 2017a; Afrasiabi et al., 2019) and recursive neural network (RNN) (Li et al., 2019) have been the focus of previous research on prediction models. These models have higher prediction accuracy than other machine learning models but have the same problem with difficulty in model training. Hence improved RNN and CNN models, such as long short-term memory (LSTM) (Zhang et al., 2019a; Zhang et al, 2019b; Wu et al., 2019), GRU (Ding et al., 2019; Chen et al., 2022), and temporal convolutional network (TCN) (Gan et al., 2021; He et al., 2022) have been widely used in wind power prediction. In recent years, the generative adversarial network (GAN) has attracted a lot of attention (Yuan et al., 2021; Zhou et al., 2021; Xia et al., 2022). Its generative model maps noise variables to multi-layer perceptron networks to make the generated data as close as possible to the distribution of training samples. In general, the AI models can better mine the hidden feature information of the wind power series, improve the overall prediction accuracy, and have strong learning ability and robustness.

Due to the high randomness and volatility of wind power, the prediction abilities of a single model often do not meet actual needs. In recent years, ensemble forecasting models which combine the advantages of multiple single models have become a popular direction for wind power prediction research. Current research on ensemble forecasting models can be summarized in four categories. 1) Ensemble forecasting models based on multi-model weighting. In these models, multiple single models, such as SVM and RNN (Yu et al., 2018), extreme learning machine (ELM), Elman neural network (ENN) and LSTM (Abedinia and Bagheri, 2022),

least square SVM (LSSVM) and radial basis function neural network (RBFNN) (Shi et al., 2013), outlier robust ELM (ORELM), ENN, and bidirectional LSTM (BiLSTM) (Chen and Liu, 2020), are used to predict wind power series, and the prediction results are weighted to improve the prediction accuracy. 2) Ensemble forecasting models based on data preprocessing. To cope with the non-stationary wind power sequence, these methods use signal decomposition and denoising algorithms to decompose the original wind power data into multiple stationary subsequences, and use the prediction model to predict each subsequence separately. Commonly used mode decomposition algorithms include empirical mode decomposition (EMD) (Amjady and Abedinia, 2017; Abedinia et al., 2020), variational mode decomposition (VMD) (Yin et al., 2019; Duan et al., 2021), singular value decomposition (Wang et al., 2020), ensemble empirical mode decomposition (EEMD) (Wang et al, 2017b), wavelet transform (WT) (Zucatelli et al., 2021; Khazaei et al., 2022), and complete ensemble empirical mode decomposition with adaptive noise (CEEMDAN) (Lu et al., 2020) Ensemble forecasting models based on optimization techniques. In order to improve the prediction accuracy, the parameters of the forecasting model are optimized by using optimization techniques. These models include the Multilayer Perceptron (MLP) neural network optimized by Non-dominated Sorting Genetic Algorithm II (NSGA-II) (Khazaei et al., 2022), SVM optimized by cuckoo search algorithm (SVM-CSA) (Li et al., 2021), ENN optimized by multi-objective grey wolf optimization (ENN-MOGWO) (Wang et al., 2019a), ELM optimized by Particle Swarm Optimization (ELM-PSO) (Tian et al., 2019), Echo State Network optimized by MOGWO (ESN-MOGWO) (Wang et al., 2019b) Ensemble forecasting models based on error correction. In order to further reduce the prediction error, error correction technology has been widely used in wind power prediction, usually by predicting the error extracted from the initial prediction result as a secondary prediction. The Markov chain (MC) model (Zhang et al., 2014; Zhang et al., 2021), the GARCH (Jiang and Huang, 2017), the temporally local moving window technique (Yan et al., 2015), and machine learning methods (Liang et al., 2016) are commonly used to deal with the error component.

Although many advances have been made in wind power forecasting methods, wind power forecasting remains challenging due to the high instability of wind power output. Moreover, few prediction methods combine data decomposition, model prediction, and error correction techniques to further improve the prediction accuracy. Based on the above analysis, this research is driven by the following concepts: The EEMD method is an improved and robust decomposition technique, and can effectively discover the potential characteristics of wind power output; The GRU model shows good performance in extracting temporal correlation hidden features from time series, hence is making a figure in short-term power prediction of new energy sources; The MC approach is a very popular error correction technique because it is easy to understand and implement. Hence in this paper, following the concept of "data decomposition - model prediction - error correction", a novel ensemble forecasting model for short-term wind power sequences based on EEMD-GRU-MC is developed. The proposed model consists of three important steps: Firstly, the EEMD method is employed to decompose the original wind power output sequence into a set of relatively stationary subsequences and denoise the data sequence. Secondly, the GRU model is used to individually forecast each subsequence, and the predicted value of each subsequence is superimposed to obtain the predicted result of the original data. Finally, to further enhance the prediction accuracy, the MC is applied to correct the preliminary prediction results. Extensive numerical experiments are conducted to test the performance of the proposed forecasting model when applied to different wind farms and in different seasons. This testing indicates that the proposed hybrid model outperforms the benchmark models in terms of multiple evaluation indicators. Moreover, the mean prediction error of the developed model in all scenarios is less than or close to 2%, proving that it is a promising prospect for short-term wind power prediction.

The rest of this paper is structured as follows: Section 2 introduces the proposed ensemble forecasting method for short-term wind power sequences. Case studies are presented and discussed in Section 3. Finally, conclusions are drawn in Section 4.

2 Methodology

2.1 Data decomposition based on EEMD

EMD is a signal preprocessing analysis method proposed by Wu and Huang (2009), which is widely used in non-stationary and nonlinear signal processing. It progressively breaks down fluctuations or trends in different frequencies in the signal, and finally obtains a set of intrinsic mode functions (IMFs), where each decomposed IMF represents the characteristic signals of different frequencies in the original signal. However, mode mixing may occur in EMD signal processing, which prevents the IMFs from being separated effectively. The EEMD method introduces Gaussian white noise into the original signal and realizes the automatic distribution of the signal for the appropriate timescale after several averaging calculations, which effectively solves the mode mixing problem. Wind power output is easily affected by wind direction, wind speed and other factors, and presents large random fluctuations, which result in a large number of outliers in the wind power sequence. Therefore, the EEMD algorithm is applied to decompose and denoise the wind power sequence, extract the main trend component in the sequence, and eliminate the random fluctuation component. The decomposition of the wind power sequence by EEMD can be summarized as the following steps:

Step 1: The white noise signal $s_{k,t}$ is added to the original wind power sequence P_t, and the new power sequence $P_{k,t}$ is obtained using Eq. 1:

$$P_{k,t} = P_t + s_{k,t}, k = 1, \ldots, K \tag{1}$$

Step 2: The new sequence $P_{k,t}$ (see Eq. 2) is decomposed into a series of IMFs using the EMD algorithm (Naik et al., 2018):

$$P_{k,t} = \sum_{m=1}^{M} C_{k,t}^{m} + r_{k,t}^{M} \tag{2}$$

Step 3: Steps (1) and (2) are repeated K times, and white noise with different amplitude is added each time.

Step 4: Since the mean value of the white noise spectrum is 0, the mean value of all IMFs calculated for K iterations is the final IMF obtained by the EEMD method (see Eq. 3):

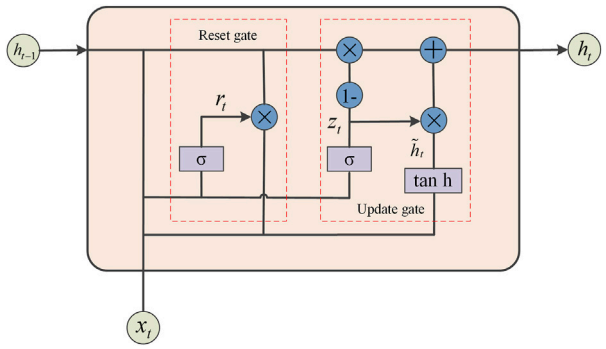

FIGURE 1
Structure of the GRU neuron.

$$C_t^m = \sum_{k=1}^{K} C_{k,t}^m / k \tag{3}$$

Step 5: The original wind power sequence can be reconstructed as Eq. 4:

$$P_t = \sum_{m=1}^{M} C_t^m + r_t^M \tag{4}$$

The amplitude of r_t^M is so small that it can be ignored in wind power prediction.

2.2 Model prediction based on GRU neural network

LSTM is an enhanced type of RNN, which effectively solves the problem of the vanishing collateral gradient of traditional RNNs. GRU is an improved version of LSTM, simplifying the number of gating units and improving the computational efficiency of the model while ensuring the output accuracy. The GRU neuron is the basic unit of the GRU neural network (GRUNN) model and its structure is shown in Figure 1. The GRU neuron includes reset gate r_t and update gate z_t. The update gate receives the current state x_t and the previously hidden state h_{t-1}. After receiving the input and the matrix operation, the sigmoid function σ determines whether the neuron is activated. The reset gate receives x_t and h_{t-1}, and the result determines how much past information needs to be forgotten. The current memory h_t is a summary of the input and output of the previous hidden layer. $\tilde{h}_t$ and h_{t-1} determine the final output h_t by dynamic control of the update gate and transmit h_t to the next GRU neuron. The mathematical model of GRU is shown as Eqs (5–8).

$$z_t = \sigma(W_z \cdot [h_{t-1}, x_t]) \tag{5}$$

$$r_t = \sigma(W_z \cdot [h_{t-1}, x_t]) \tag{6}$$

$$\tilde{h}_t = tanh(W_h \cdot [r_t \odot h_{t-1}, x_t]) \tag{7}$$

$$h_t = (1 - z_t) \odot h_{t-1} + \tilde{h}_t \odot z_t \tag{8}$$

Based on the GRU neuron, the time series prediction of GRUNN is shown in Figure 2.

2.3 Detailed description of error correlation based on MC

2.3.1 Basic theory of Markov chain

The Markov process is a typical stochastic process proposed by the famous mathematician Markov, which is applicable to both time series and interval sequences. The main content of the Markov process research is the state of a given stochastic process and its transition law. The MC refers to the Markov process with discrete time and state, and it can predict the changing trend of each state according to the initial probability of each state and the transition probability between each state. Hence the preliminary prediction results are corrected by MC to make up for the prediction error caused by the elimination of some components in the data decomposition process and the corrected wind power output is therefore closer to the actual value.

Assuming that $\{X_t, t = 1, 2, \ldots, T\}$ is a random sequence where t represents any time period, if for any state $i_0, i_1, \ldots, i_{t-1}$ state i and j satisfy Eq. 9, then $\{X_t, t = 1, 2, \ldots, T\}$ is a MC. i and j represent the possible states of the system at present and in future time, respectively:

$$p\{X_{t+1} = j | X_t = i, X_{t-1} = i_{t-1}, \ldots, X_1 = i_0\} = p\{X_{t+1} = j | X_t = i\} \tag{9}$$

Supposing there are n states in state space I and, since each state can turn to itself, each state has n turns. So, the one-step transition probability from state i to state j can be expressed as Eq. 10:

$$p_{ij}^{(1)} = M_{ij}^{(1)} / M_j \tag{10}$$

The matrix composed of the one-step transition probability set of all states is called the one-step transition probability matrix, and is expressed as Eq. 11:

$$P^{(1)} = \begin{bmatrix} p_{11}^{(1)} & p_{12}^{(1)} & \cdots & p_{1n}^{(1)} \\ p_{21}^{(1)} & p_{22}^{(1)} & \cdots & p_{2n}^{(1)} \\ \vdots & \vdots & \cdots & \vdots \\ p_{n1}^{(1)} & p_{n2}^{(1)} & \cdots & p_{nn}^{(1)} \end{bmatrix} \tag{11}$$

Accordingly, the matrix composed of the k-step transition probabilities of all states is called the k-step transition probability matrix of the system. According to the homogeneity of MC, the k-step state transition probability matrix is expressed as Eq. 12:

$$P^{(k)} = \begin{bmatrix} p_{11}^{(k)} & p_{12}^{(k)} & \cdots & p_{1n}^{(k)} \\ p_{21}^{(k)} & p_{22}^{(k)} & \cdots & p_{2n}^{(k)} \\ \vdots & \vdots & \cdots & \vdots \\ p_{n1}^{(k)} & p_{n2}^{(k)} & \cdots & p_{nn}^{(k)} \end{bmatrix} = \left(P^{(1)}\right)^k \tag{12}$$

In the process of MC error correction, the classification of states is very important. In this paper, the mean-standard deviation classification method, which is simple in theory and widely used, is employed to divide the state space according to the mean and standard deviation of the samples. Let the sample sequence be $\{X_n, n = 1, 2, \ldots, N\}$, the sample mean is $\bar{x}$, and the standard deviation is δ. According to the central limit theorem in mathematical statistics, the sample sequence can be divided into five intervals: $H_1(min\{X_n, \forall n\}, \bar{x} - \delta]$, $H_2(\bar{x} - \delta, \bar{x} - 0.5\delta]$,

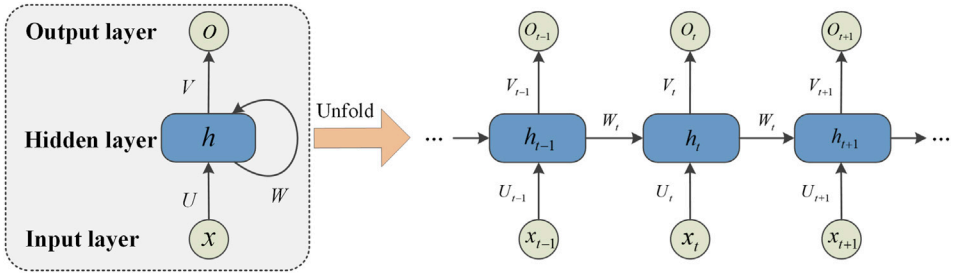

FIGURE 2
Schematic diagram of GRUNN prediction.

$H_3(\bar{x}-0.5\delta, \bar{x}+0.5\delta]$, $H_4(\bar{x}+0.5\delta, \bar{x}+\delta]$, $H_5(\bar{x}+\delta, max\{X_n, \forall n\})$.

2.3.2 Basic theory of Markov chain

Based on the above analysis, the correction process for wind power prediction error is as follows:

Step 1: Calculate the historical wind power error sequence using Eq. 13:

$$e_s = p_s^h - p_s^{pf}, \forall s = 1, 2, \ldots, S \tag{13}$$

where p_s^h denotes the actual historical wind power output value of sample point s; p_s^{pf} denotes the predicted value of sample point s obtained by the EEMD-GRU model; S is the total number of sample points.

Step 2: Calculate the mean and standard deviation of the error sequence and divide the error sequence into five intervals H_1, H_2, H_3, H_4 and H_5 using the mean-standard deviation classification method.

Step 3: The number of sample points belonging to different intervals is counted, and then the one-step and k-step transition probability matrices of each error state are calculated by using Eqs. 11 and (2), respectively.

Step 4: The states of the error sequence 5 days before the forecast days are taken as the initial states. In the transition matrix $P^{(5)}$, the row vectors corresponding to each initial state $P_i^{(5)} = (P_{i1}^{(5)}, P_{i2}^{(5)}, \cdots, P_{i5}^{(5)}), i = 1, \ldots, 5$ are taken to form a new probability matrix (see Eq. 14):

$$R = \begin{bmatrix} p_{i1}^{(5)} & p_{i2}^{(5)} & \cdots & p_{i5}^{(5)} \\ p_{i1}^{(5)} & p_{i2}^{(5)} & \cdots & p_{i5}^{(5)} \\ \vdots & \vdots & \cdots & \vdots \\ p_{i1}^{(5)} & p_{i2}^{(5)} & \cdots & p_{i5}^{(5)} \end{bmatrix} \tag{14}$$

Step 5: The state corresponding to $max\left\{P_j = \sum_{i=1}^{5} p_{ij}^5, j \in [1,5]\right\}$, i.e., the state to which the error is most likely to be transferred in the future, is taken as the state of the modified error. Thus the modified error $\widetilde{e_k} = e_s + 0.5(H_{el} + H_{eu})$, where H_{el} and H_{eu} are the lower and upper bound of the state interval of the error to be modified.

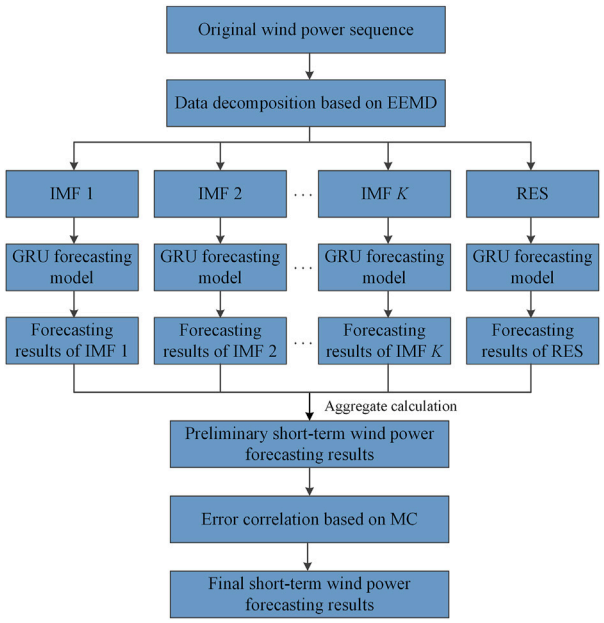

FIGURE 3
Flowchart of the proposed forecasting model.

Step 6: Correct the predicted wind power sequence on the forecast days using Eq. 15:

$$p_k^f = \widetilde{e_k} + p_k^{pf} \tag{15}$$

2.4 Overall model prediction process

The overall flowchart of the proposed EEMD-GRU-MC model is depicted in Figure 3, and the main steps are as follows:

Step 1: Use the EEMD method to decompose the historical power data into K IMF components (subsequences) and one RES component.

Step 2: Divide each subsequence into a training set and a test set, and then use the GRU model to predict each component. The prediction results of each subsequence are aggregated as the preliminary prediction results of the EEMD-GRU model.

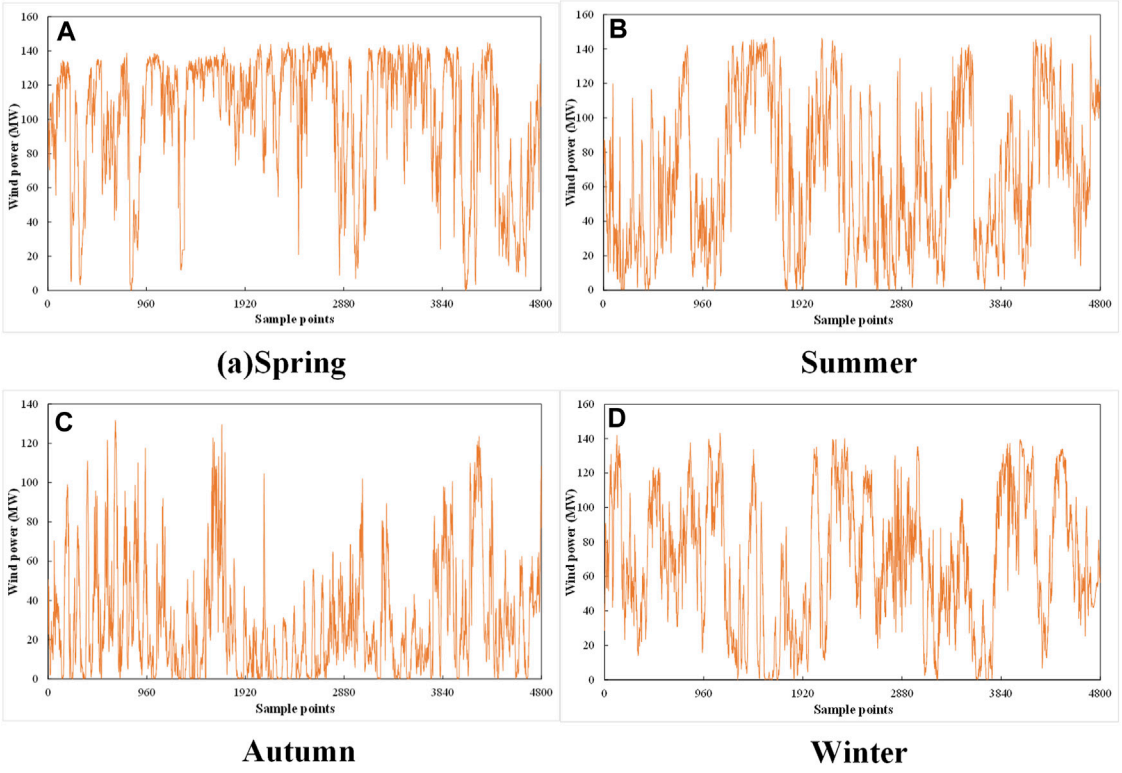

FIGURE 4
Wind power dataset for the ZMS wind farm.

Step 3: Calculate the prediction error between the historical wind power and the predicted power, then use the MC to correct the preliminary prediction results to get the final predicted wind power sequence.

3 Case studies

3.1 Data description

To verify the effectiveness and practicability of the EEMD-GRU-MC model, it was applied to the short-term wind power prediction of two wind farms, ZMS and YMC, which are located in Yunnan Province, China. For each wind farm, four datasets were collected to test the forecasting performance of the proposed model in different seasons. The datasets were collected from 1 February 2021 to 22 March 2021, from 1 June 2021 to 20 July 2021, from 1 September 2021 to 20 October 2021 and from 1 December 2021 to 19 January 2022, representing the wind power data in spring, summer, autumn and winter, respectively. Each dataset was recorded for a time period of 15 min. As shown in Figures 4, 5, there is a total of 50 days, representing 4800 sample points, included in each dataset. The first 3840 sample points are used for the training set, the middle 864 are used for the validation set to avoid modeling over fitting, and the last 96 are used for the test set. This study focuses on short-term wind power prediction 24 h in advance to assist day-ahead dispatching of power grids (Alham et al., 2016; Hu et al., 2019; Liu et al., 2021). Therefore, 96 sample points are selected as the test set in this study. The ratio of training set, verification set and test set is usually 6:2:2. In order to improve the prediction accuracy of the model, a longer training set and verification set were selected in this study, which made the data volume of the whole data set reach 4800. Table 1 lists the statistical information for the datasets, including the maximum, minimum, mean, median and standard deviation. It can be observed that the power variation of each wind farm in all seasons is close to the installed capacity, showing strong volatility and non-stationarity. The power output of all wind farms is larger in spring and winter, but smaller in summer.

The root mean square error (RMSE), mean absolute error (MAE) and mean absolute percentage error (MAPE) are used as indexes to evaluate the predictive performance of the forecasting models (see Eqs 16–18). The smaller the RMSE, MAE and MAPE, the better the predictive performance of the models:

$$RMSE = \sqrt{\sum_{l=1}^{L}\left(p_l^a - p_l^f\right)^2/L} \tag{16}$$

$$MAE = \left(\sum_{l=1}^{L}\left|p_l^a - p_l^f\right|\right)/L \tag{17}$$

$$MAPE = \left(\sum_{l=1}^{L}\left|p_l^a - p_l^f\right|/p_l^a\right)/L \tag{18}$$

Where L is the number of sample points in the test set, which is 96 in this paper; p_l^a is the actual wind power value of sample point l; p_l^f is the predicted value.

The EEMD decomposition of the wind power sequence and MC error correction of the preliminary prediction results were realized

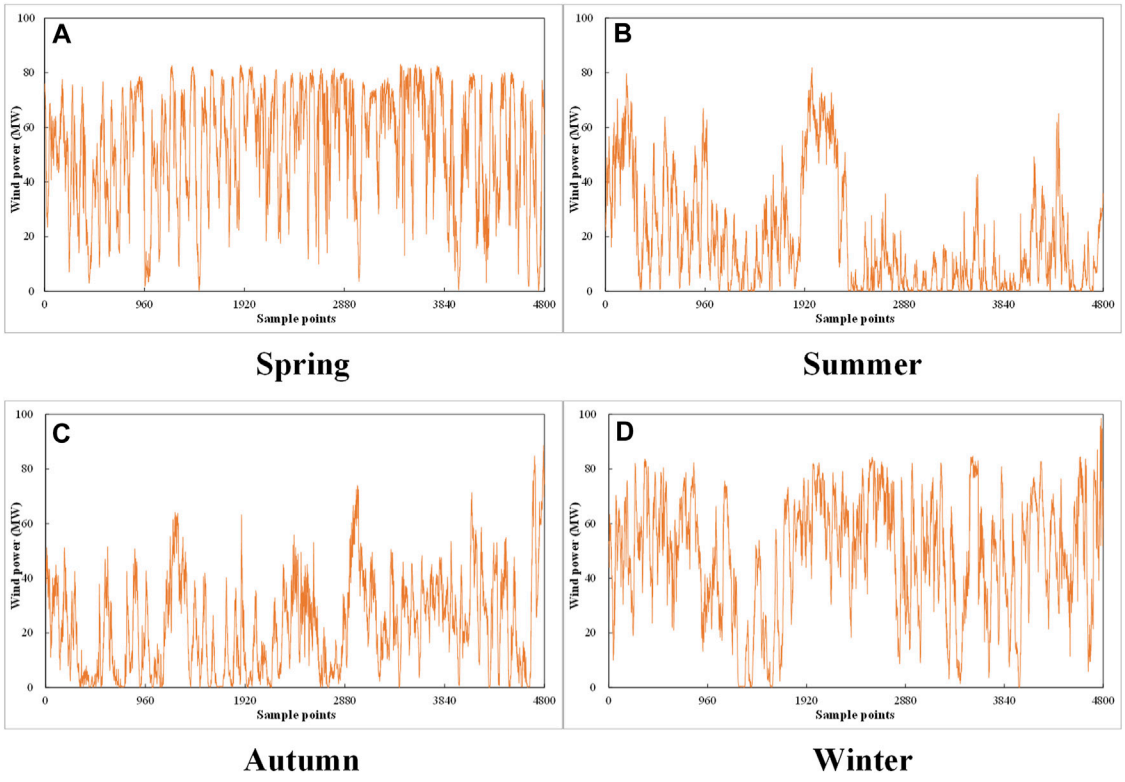

FIGURE 5
Wind power dataset for the YMS wind farm.

TABLE 1 Statistical information of the datasets used in this study.

Wind farm	Dataset	Maximum	Minimum	Range	Mean	Median	Std.
ZMS	Spring	145.2	0	145.2	101.4	114.4	37.2
	Summer	147.6	0	147.6	66.8	61.9	41.9
	Autumn	131.8	0	131.8	29.4	21.4	27.9
	Winter	143.3	0	143.3	68.5	67.3	38.7
YMS	Spring	83.0	0.1	82.9	53.7	58.5	20.9
	Summer	81.8	0	81.8	18.9	11.5	19.7
	Autumn	88.6	0	88.6	22.6	20.8	17.4
	Winter	98.5	0	98.5	48.5	51.7	21.6

by Matlab 2020a, and the training and prediction of the GRU model were realized by Python programming language. All numerical experiments were conducted on a Dell workstation equipped with an Intel Xeon Gold processor, with 20 cores and 40 threads, 2.1G main frequency and 64G memory.

3.2 Case 1: short-term wind power prediction for the ZMS wind farm

Aiming to solve the problem of poor model robustness caused by the randomicity and intermittent nature of wind power, the EEMD algorithm was introduced to decompose wind power data into a set of subsequences. Due to space limitations, Supplementary Figure S1 only displays the EEMD decomposition results of the spring dataset. It can be seen that EEMD decomposes the wind power sequence into seven IMF subsequences and one residual subsequence with different frequency characteristics, which facilitates the analysis of the hidden information in the data and overcomes the shortcomings of the original wind power sequence with its high volatility and non-stationarity.

In order to verify the superiority, reliability and stability of the proposed model, six other forecasting models based on LSTM, GRU, EMD-LSTM, EMD-GRU, EEMD-LSTM and EEMD-GRU were

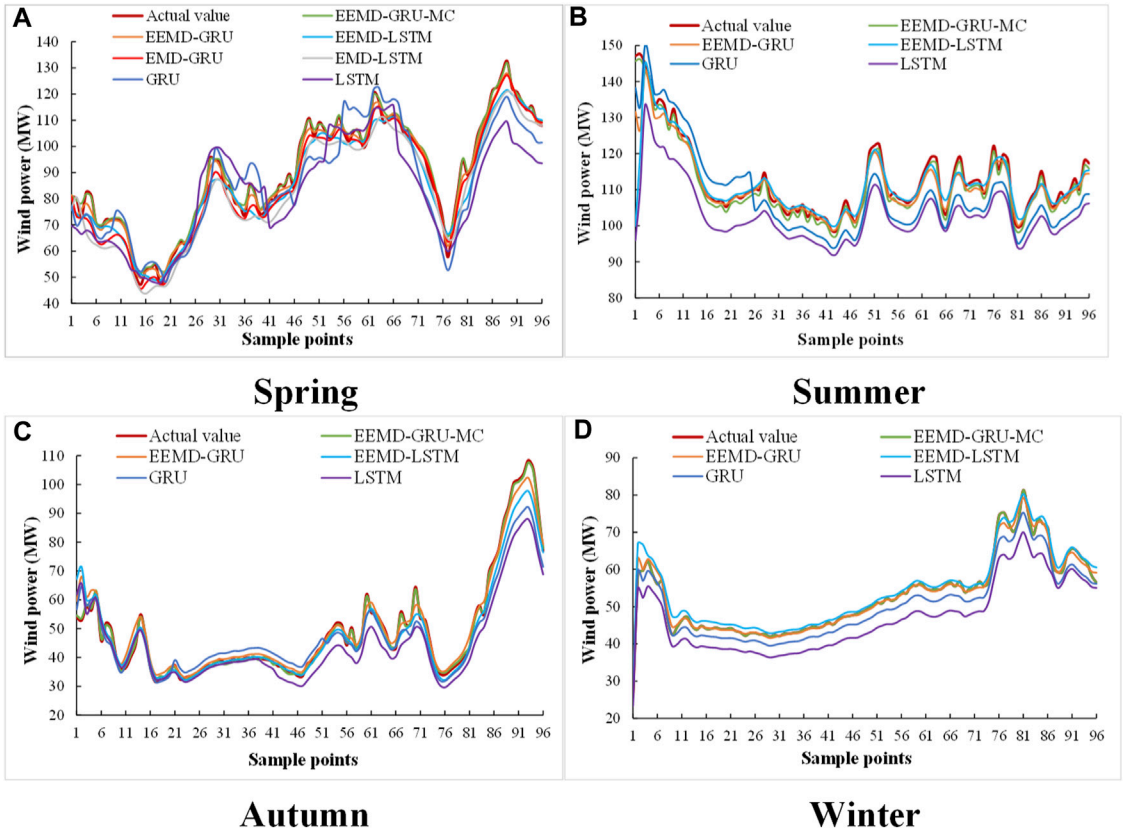

FIGURE 6
Short-term wind power forecasting results for the ZMS wind farm.

constructed as comparison models. It should be mentioned that the LSTM and GRU methods are adopted by (Duan et al., 2021; Chen et al., 2022), respectively. The prediction results of the seven models in different seasons are shown in Figure 6, and regression analysis of the prediction results for the ZMS wind farm using different models is presented in Figure 7. For further quantitative comparison, the evaluation indicators of various prediction models, including MAE, RMSE and MAPE are listed in Table 2. The detailed analyses are summarized as follows: (1) The predicted wind power curves of all models are generally consistent with the trend of the actual power curve. However, it is clear that the predicted wind power curve obtained by the proposed EEMD-GRU-MC model is very close to the actual power curve, and has the smallest RMSE, MAE and MAPE among the seven models for all seasons. In addition, the correlation between the observed data and the predicted data generated by the proposed model is greater than that of comparison models. Therefore, the proposed model connecting EEMD and MC to the GRU model has the ability to capture the dynamic characteristics of wind power output data series. (2) The LSTM has the largest prediction error and the prediction effect of EEMD-LSTM is also inferior to that of EEMD-GRU for different seasons, which proves that GRU has more advantages in predicting short-term wind power time series data compared to LSTM. (3) EEMD-LSTM and EEMD-GRU models are superior to LSTM and GRU respectively in various performance evaluation indexes. Taking the summer dataset with the strongest stochastic wind power volatility as an example, the MAE, RSME and MAPE of the EEMD-GRU model are 1.90 MW, 3.36 MW and 1.58%, which decreased by 69.3%, 48.7% and 71.2% compared with the GRU model. Similar results also appear in the comparison of the EEMD-LSTM and LSTM model, whose MAE, RMSE and MAPE decreased by 77.9%, 47.3% and 79.2%, respectively. This proves that EEMD can separate the noise information from the complex wind power data and facilitate the prediction model to extract the hidden information in the data. (4) Compared with EMD-LSTM and EMD-GRU, EEMD-LSTM and EEMD-GRU have better predictive performance, showing EEMD technique is more helpful for improving the prediction accuracy than EMD technique. (5) The prediction accuracy of the EEMD-GRU model can be further improved after MC error correlation. Taking the spring dataset, for example, after MC correction, the MAE, RMSE and MAPE of the EEMD-GRU model decreased from 1.87 MW to 1.37 MW, from 2.37 MW to 1.97 MW, and from 2.18% to 1.76%, respectively.

3.3 Case 2: Short-term wind power prediction of the YMS wind farm

In order to verify its robustness, the proposed model was applied to the short-term power prediction of the YMS wind farm, whose

10.3389/fenrg.2023.1252067

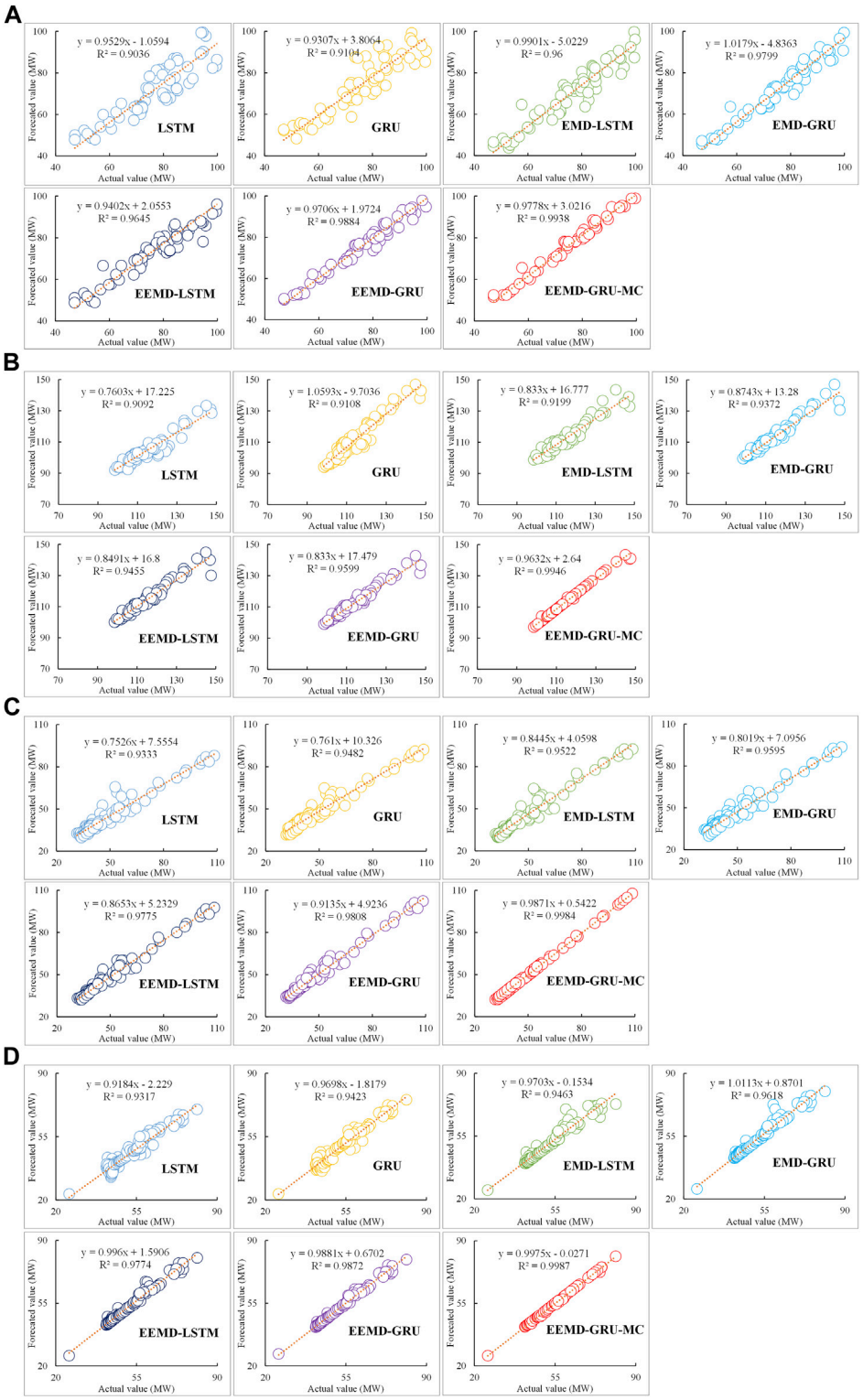

FIGURE 7
(A) Spring Regression analysis of prediction results for the ZMS wind farm using different models. **(B)** Summer Regression analysis of prediction results for the ZMS wind farm using different models. **(C)** Autumn Regression analysis of prediction results for the ZMS wind farm using different models. **(D)** Winter Regression analysis of prediction results for the ZMS wind farm using different models.

TABLE 2 Statistical indexes of short-term power prediction for the ZMS wind farm using different models.

Dataset	Model	MAE(MW)	RMSE(MW)	MAPE (%)
Spring	LSTM	9.82	11.50	10.74
	GRU	7.49	8.61	8.32
	EMD-LSTM	6.13	7.26	7.27
	EMD-GRU	3.61	4.45	4.38
	EEMD-LSTM	4.03	5.15	4.59
	EEMD-GRU	1.87	2.37	2.18
	EEMD-GRU-MC	1.37	1.97	1.76
Summer	LSTM	9.62	11.11	8.35
	GRU	6.19	6.55	5.49
	EMD-LSTM	3.58	7.97	2.90
	EMD-GRU	2.27	6.03	1.84
	EEMD-LSTM	2.13	5.86	1.74
	EEMD-GRU	1.90	3.36	1.58
	EEMD-GRU-MC	1.43	1.41	1.28
Autumn	LSTM	5.45	7.41	9.69
	GRU	4.07	5.52	7.43
	EMD-LSTM	4.37	5.72	8.15
	EMD-GRU	3.95	5.67	7.00
	EEMD-LSTM	2.68	4.32	4.67
	EEMD-GRU	2.24	3.22	4.49
	EEMD-GRU-MC	0.76	0.84	1.69
Winter	LSTM	6.08	6.33	11.53
	GRU	2.64	2.90	4.94
	EMD-LSTM	2.48	3.01	4.62
	EMD-GRU	1.60	2.52	3.00
	EEMD-LSTM	1.50	2.07	2.85
	EEMD-GRU	0.75	1.15	1.33
	EEMD-GRU-MC	0.03	0.07	0.68

output characteristics are quite different from those of ZMS. The experiments were also conducted using six comparison models as mentioned in Section 3.1. The forecasting results from these models and regression analysis are shown in Figures 8, 9, while the evaluation indicators of the forecasting results are illustrated in Table 3. It can be found that the LSTM and GRU based models without data preprocessing fail to obtain satisfactory forecasting results. Especially in spring and summer, the MAPE values of both models exceed 10%. The proposed EEMD-GRU-MC model achieves the smallest MAE, RMSE and MAPE among the models for the four seasons, and the forecasted wind power curves closely match the trend of the actual power curves. Except for in spring, the MAPE values of the predicted results of the developed model are all within 2%. Although the developed model's prediction accuracy dropped slightly in the spring dataset where the wind power fluctuation is more severe, the proposed model performs best in the wind power prediction for the YMS wind farm. It can be concluded that the developed ensemble forecasting model has more outstanding potential and is better able to capture valuable information in complex and non-stationary wind power data.

3.3 Analysis of computational efficiency of the proposed model

Computational complexity is an important index to evaluate the efficiency of a wind power forecasting method, which describes how

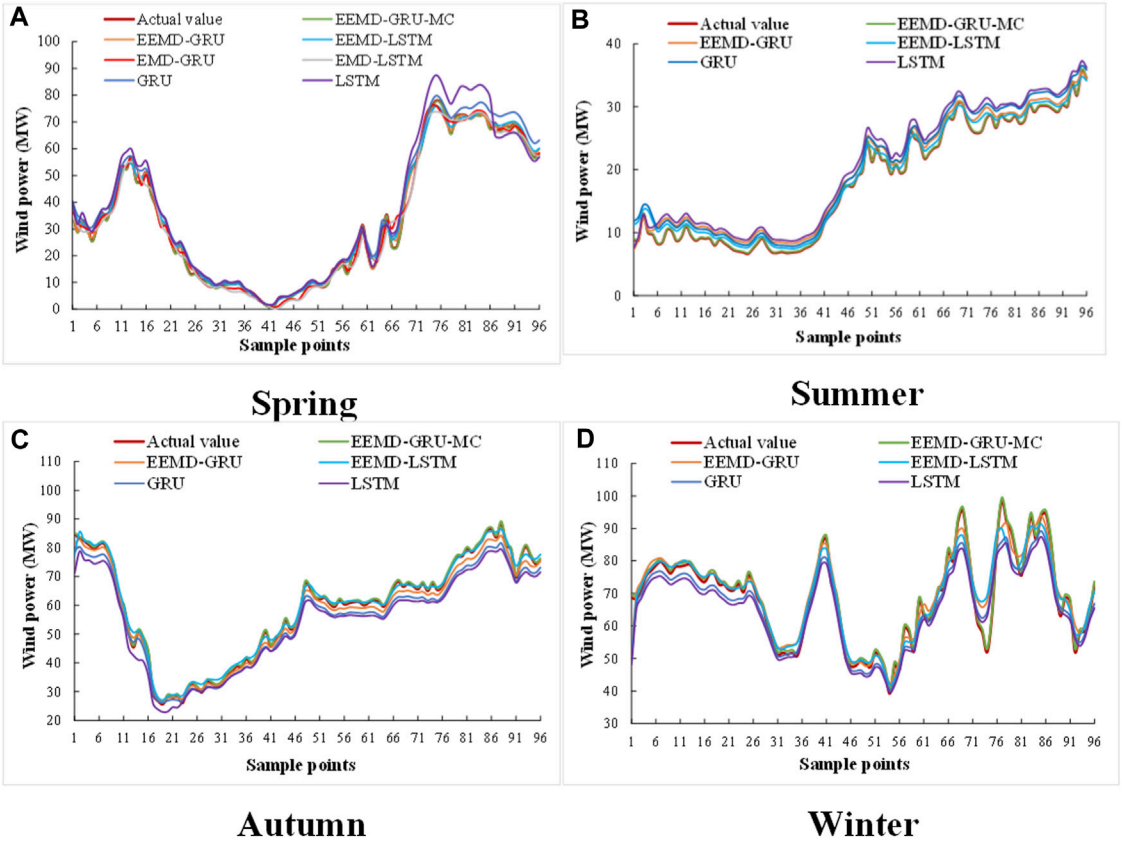

FIGURE 8
Short-term wind power forecasting results for the YMS wind farm.

the execution time of a method changes with the increase of the input size. The computational complexity of EEMD-GRU-MC model mainly depends on the respective complexity of EEMD, GRU and MC. EEMD is an adaptive signal processing method for nonlinear and non-stationary data. The time complexity of EEMD is actually equivalent to the time complexity of Fourier transform. This means that although EEMD is considered computationally intensive, it is actually a computationally efficient method. A GRU is a recurrent neural network used to process sequential data. The computational complexity of a GRU depends on several factors, including sequence length, number of network layers, and number of hidden units per layer. In general, the computational complexity of a GRU is proportional to these factors. An MC is a statistical model that describes random changes in the state of a system. The computational complexity of MC depends on the number of states. If the number of states is fixed, then the computational complexity of MC can be considered constant. In general, computational complexity is related to the parameters of the model and the amount of data.

In order to ensure that the proposed prediction model is realizable in practical applications, the prediction efficiency of the proposed model is analyzed, which is shown in Table 4. This model is designed to predict the day-ahead wind power output, rather than real-time prediction. After 30 iterations, the model uses an average of about 35 min to accurately predict the wind power of the next day. Considering that the accuracy of the model prediction is very high, the prediction time is completely acceptable and can meet the timeliness requirement of the short-term wind power prediction.

Few prediction methods combine data decomposition, model prediction, and error correction techniques to further improve the prediction accuracy. The EEMD-GRU-MC model proposed in this paper provides a novel method for wind power prediction. By integrating EEMD algorithm, GRU model and MC technology, this model effectively deals with the strong intermittency and large volatility of wind power, thus improving the accuracy of model prediction. This novel method provides a new perspective and idea for the theoretical research of wind power prediction. For the research community, the EEMD-GRU-MC model has enriched the theoretical research of wind power prediction, and provided a new reference and inspiration for the subsequent research. For practitioners, especially power grid dispatching departments, the research results of this paper can help them make more accurate and reliable short-term wind power forecasts, so as to arrange more reasonable day-ahead generation plans. Moreover, the wind farms' historical operation data and the source code of the proposed EEMD-GRU-MC model will be made available on request.

10.3389/fenrg.2023.1252067

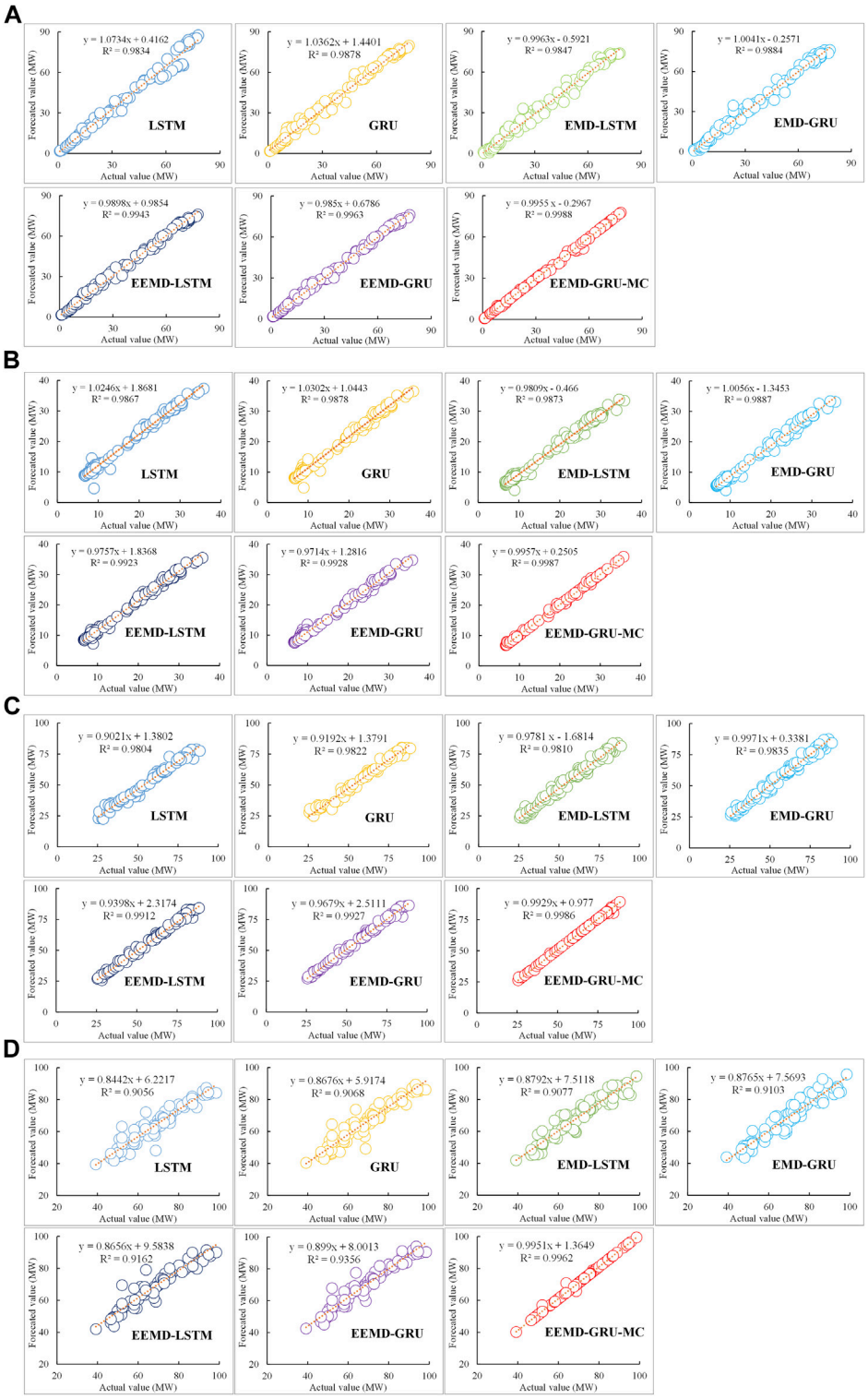

FIGURE 9
(A) Spring Regression analysis of prediction results for the YMS wind farm using different models. **(B)** Summer Regression analysis of prediction results for the YMS wind farm using different models. **(C)** Autumn Regression analysis of prediction results for the YMS wind farm using different models. **(D)** Winter Regression analysis of prediction results for the YMS wind farm using different models.

TABLE 3 Statistical indexes of short-term power prediction for YMS wind farm using different models.

Dataset	Model	MAE(MW)	RMSE(MW)	MAPE (%)
Spring	LSTM	3.59	4.87	11.58
	GRU	2.55	3.22	10.07
	EMD-LSTM	2.38	3.14	12.87
	EMD-GRU	1.95	2.68	10.61
	EEMD-LSTM	1.49	1.96	6.94
	EEMD-GRU	1.14	1.52	5.86
	EEMD-GRU-MC	0.32	0.39	2.55
Summer	LSTM	2.36	2.47	16.89
	GRU	1.71	1.90	12.05
	EMD-LSTM	1.34	1.60	9.90
	EMD-GRU	1.00	1.33	6.57
	EEMD-LSTM	1.41	1.57	11.55
	EEMD-GRU	0.92	1.12	7.29
	EEMD-GRU-MC	0.15	0.32	1.12
Autumn	LSTM	4.57	5.10	7.63
	GRU	3.20	3.61	5.16
	EMD-LSTM	3.31	3.86	6.14
	EMD-GRU	1.81	2.31	3.40
	EEMD-LSTM	1.68	2.03	2.78
	EEMD-GRU	1.26	1.70	2.47
	EEMD-GRU-MC	0.61	0.77	1.15
Winter	LSTM	4.52	5.57	6.35
	GRU	3.52	4.69	4.99
	EMD-LSTM	3.63	5.28	5.29
	EMD-GRU	2.85	5.06	4.11
	EEMD-LSTM	2.77	4.36	4.15
	EEMD-GRU	2.61	3.95	4.00
	EEMD-GRU-MC	0.98	1.15	1.44

TABLE 4 Prediction time for different wind farms in different seasons.

Wind farm	Dataset	Time (s)		
		Decomposition	Total prediction	Average
ZMS	Spring	10.135	2,135	2,140
	Summer	10.158	2,124	
	Autumn	10.206	2,138	
	Winter	10.319	2,162	
YMS	Spring	10.159	2,141	2,154
	Summer	10.171	2,136	
	Autumn	10.238	2,150	
	Winter	10.338	2,170	

4 Conclusion

Accurate and reliable short-term prediction of wind power is of important reference value for the power grid dispatching department to arrange reasonable day-ahead generation plans. This study innovatively combines a data decomposition technique, an AI-based prediction model and an error correction technique, and proposes a short-term wind power prediction method based on EMD-GRU-MC. Two case studies, including two wind farms and eight datasets, are used to verify the performance of the proposed forecasting model when applied to different wind farms and in different seasons. The conclusions can be summarized as follows:

(1) Compared with LSTM, GRU, EMD-LSTM, EMD-GRU, EEMD-LSTM and EEMD-GRU models, the proposed EEMD-GRU-MC model achieves the smallest MAE, RMSE and MAPE for all datasets, and the forecasted wind power curves very closely match the trend of the actual power curves. Taking the spring dataset of the ZMS wind farm for example, the MAE, RMSE and MAPE of the EEMD-GRU-MC model is 1.37 MW, 1.97 MW, and from 1.76%, respectively. Moreover, except for the YMS wind farm in spring, the mean forecasting error of the proposed model is always within 2%. This demonstrates that the proposed model has excellent forecasting performance and generalization ability, and can be used as an effective tool for short-term wind power prediction.
(2) After 30 iterations, the proposed model uses an average of about 35 min to accurately predict the wind power of the next day, proving its high computation efficiency.
(3) GRU has more advantages in predicting short-term wind power sequences than LSTM. EEMD-LSTM and EEMD-GRU models are also achieve better prediction performance than LSTM and GRU respectively in various scenarios, indicating that the EEMD algorithm can overcome the shortcomings of the original wind power sequence with its high volatility and non-stationarity and facilitate the prediction model to extract the hidden information in the data. Taking the summer dataset of the ZMS wind farm as an example, the MAE, RSME and MAPE of the EEMD-GRU model are 1.90 MW, 3.36 MW and 1.58%, which decreased by 69.3%, 48.7% and 71.2%, respectively, compared with the GRU model.
(4) For the spring dataset of the ZMS wind farm, the MAE, RMSE and MAPE of the EEMD-GRU model decreased by 26.73%, 16.88% and 19.27%, respectively, after MC correction. Similar results also appear in other datasets. This proves the effectiveness and applicability of the MC error correlation technique in short-term wind power forecasting.

The proposed EEMD-GRU-MC model is a deterministic wind power forecasting model, and does not take into account the complex meteorological factors. Moreover, the process of dissecting and projecting all of the data is not online forecasting, resulting in its temporary can not be applied to real-time forecasting. In future studies, the uncertainty of wind power prediction error will be considered and meteorological factors will be embedded to build a multi-feature interval prediction model, so as to obtain more comprehensive wind power prediction results. Moreover, the number of decomposed IMFs of EEMD and CEEMDAN, along with the standard EMD and its upgraded algorithms, is uncertain for different data characteristics. The developed model and the commercial solver Matlab 2020a can be integrated into the wind farm short-term power prediction support systems. In this case, the system program can automatically identify each IMF decomposed by the EEMD method, and then give it to the GRU model one by one for training and prediction. The support system would cope with the problem that the number of decomposed IMFs is uncertain for different data characteristics and realize online wind power forecasting. Hence, how to integrate the hybrid prediction model based on EEMD-GRU-MC into the decision support system for the short-term power prediction of wind farms to realize online and real-time prediction is our next research direction.

Data availability statement

The original contributions presented in the study are included in the article/Supplementary Material, further inquiries can be directed to the corresponding author.

Author contributions

PW: Software, Writing–Original Draft, Conceptualization. CS: Methodology, Writing–Review and Editing, Funding acquisition, Supervision. LL: Validation, Writing–Review and Editing. WY: Investigation, Validation. CG: Data Curation, Formal analysis. All authors contributed to manuscript revision, read, and approved the submitted version.

Funding

The research presented in this paper was supported by the National Natural Science Foundation of China (No. 52109041), China Postdoctoral Science Foundation (No. 2021M690139) and First-class Project Special Funding of Yellow River Laboratory (No. YRL22LT08).

Conflict of interest

The authors declare that the research was conducted in the absence of any commercial or financial relationships that could be construed as a potential conflict of interest.

Publisher's note

Supplementary material

The Supplementary Material for this article can be found online at: https://www.frontiersin.org/articles/10.3389/fenrg.2023.1252067/full#supplementary-material

References

Abedinia, O., and Bagheri, M. (2022). Execution of synthetic Bayesian model average for solar energy forecasting. *IET Renew. Power Gener.* 16 (6), 1134–1147. doi:10.1049/rpg2.12389

Abedinia, O., Ghasemi-Marzbali, A., Shafiei, M., Sobhani, B., Gharehpetian, G., and Bagheri, M. (2022). "A multi-level model for hybrid short term wind forecasting based on SVM, wavelet transform and feature selection," in Proceedings of the 2022 IEEE International Conference on Environment and Electrical Engineering and 2022 IEEE Industrial and Commercial Power Systems Europe (EEEIC/I&CPS Europe), Prague, Czech Republic, July 2022 (IEEE), 1–6. doi:10.1109/EEEIC/ICPSEUROPE54979.2022.9854519

Abedinia, O., Lotfi, M., Bagheri, M., Sobhani, B., Shafie-khah, M., and Catalao, J. P. S. (2020). Improved EMD-based complex prediction model for wind power forecasting. *IEEE Trans. Sustain. Energy* 11 (4), 2790–2802. doi:10.1109/TSTE.2020.2976038

Afrasiabi, M., Mohammadi, M., Rastegar, M., and Kargarian, A. (2019). Probabilistic deep neural network price forecasting based on residential load and wind speed predictions. *IET Renew. POWER Gen.* 13 (11), 1840–1848. doi:10.1049/iet-rpg.2018.6257

Alham, M., Elshahed, M., Ibrahim, D. K., and Zahab, E. (2016). A dynamic economic emission dispatch considering wind power uncertainty incorporating energy storage system and demand side management. *Renew. energy* 96, 800–811. doi:10.1016/j.renene.2016.05.012

Amjady, N., and Abedinia, O. (2017). Short term wind power prediction based on improved Kriging interpolation, empirical mode decomposition, and closed-loop forecasting engine. *Sustainability* 9 (11), 2104. doi:10.3390/su9112104

Barbosa, A. D., de Mattos Affonso, C., Limão, O. R., Moya, R. J., Leite, J., and Reston, F. J. (2017). Different models for forecasting wind power generation: case study. *ENERGIES* 10 (12), 1976. doi:10.3390/en10121976

Cadenas, E., Jaramillo, O. A., and Rivera, W. (2010). Analysis and forecasting of wind velocity in chetumal, quintana roo, using the single exponential smoothing method. *Renew. ENERGY* 35 (5), 925–930. doi:10.1016/j.renene.2009.10.037

Carolin, M. M., and Fernandez, E. (2008). Analysis of wind power generation and prediction using ANN: a case study. *Renew. ENERGY* 33 (5), 986–992. doi:10.1016/j.renene.2007.06.013

Charabi, Y., Al-Yahyai, S., and Gastli, A. (2011). Evaluation of NWP performance for wind energy resource assessment in Oman. *Renew. Sust. ENERG Rev.* 15 (3), 1545–1555. doi:10.1016/j.rser.2010.11.055

Chen, C., and Liu, H. (2020). Medium-term wind power forecasting based on multi-resolution multi-learner ensemble and adaptive model selection. *ENERG Convers. MANAGE* 206, 112492. doi:10.1016/j.enconman.2020.112492

Chen, P., Pedersen, T., Birgitte, B. J., and Chen, Z. (2010). ARIMA-based time series model of stochastic wind power generation. *IEEE T POWER Syst.* 25 (2), 667–676. doi:10.1109/TPWRS.2009.2033277

Chen, T., Lehr, J. M., Lavrova, O., and Martinez-Ramon, M. (2018). Distribution feeder-level day-ahead peak load forecasting methods and comparative study. *IET Gener. Transm. Dis.* 12 (13), 3270–3278. doi:10.1049/iet-gtd.2017.1745

Chen, X., Mcelroy, M. B., and Kang, C. (2017). Integrated energy systems for higher wind penetration in China: formulation, Implementa-tion and Impacts. *IEEE T POWER Syst.* 33 (2), 1–1319. doi:10.1109/TPWRS.2017.2736943

Chen, Y., Hu, X., and Zhang, L. (2022). A review of ultra-short-term forecasting of wind power based on data decomposition-forecasting technology combination model. *ENERGY Rep.* 8, 14200–14219. doi:10.1016/j.egyr.2022.10.342

Dai, W., Yang, Z., Yu, J., Zhao, K., Wen, S., Lin, W., et al. (2019). Security region of renewable energy integration: characterization and flexibility. *ENERGY* 187, 115975. doi:10.1016/j.energy.2019.115975

Ding, M., Zhou, H., Xie, H., Wu, M., Nakanishi, Y., and Yokoyama, R. (2019). A gated recurrent unit neural networks based wind speed error correction model for short-term wind power forecasting. *NEUROCOMPUTING* 365, 54–61. doi:10.1016/j.neucom.2019.07.058

Duan, J., Wang, P., Ma, W., Tian, X., Fang, S., Cheng, Y., et al. (2021). Short-term wind power forecasting using the hybrid model of improved variational mode decomposition and Correntropy Long Short -term memory neural network. *ENERGY* 214, 118980. doi:10.1016/j.energy.2020.118980

Gan, Z., Li, C., Zhou, J., and Tang, G. (2021). Temporal convolutional networks interval prediction model for wind speed forecasting. *Electr. Pow. Syst. Res.* 191, 106865. doi:10.1016/j.epsr.2020.106865

He, K., Su, Z., Tian, X., Yu, H., and Luo, M. (2022). RUL prediction of wind turbine gearbox bearings based on self-calibration temporal convolutional network. *IEEE T Instrum. Meas.* 71, 1–12. doi:10.1109/TIM.2022.3143881

Hu, F., Hughes, K. J., Ingham, D. B., Ma, L., and Pourkashanian, M. (2019). Dynamic economic and emission dispatch model considering wind power under Energy Market Reform: a case study. *Int. J. Electr. power & energy Syst.* 110, 184–196. doi:10.1016/j.ijepes.2019.03.004

International Energy Agency (2021). Wind generation increased by a record amount in 2021, but even faster growth is needed to get on the Net Zero Scenario trajectory. Available at: https://www.iea.org/reports/wind-electricity.

Jeon, J., and Taylor, J. W. (2016). Short-term density forecasting of wave energy using ARMA- GARCH models and kernel density estimation. *Int. J. Forecast* 32 (3), 991–1004. doi:10.1016/j.ijforecast.2015.11.003

Jiang, Y., and Huang, G. (2017). Short-term wind speed prediction: hybrid of ensemble empirical mode decomposition, feature selection and error correction. *ENERGY Convers. MANAG.* 144, 340–350. doi:10.1016/j.enconman.2017.04.064

Khazaei, S., Ehsan, M., Soleymani, S., and Mohammadnezhad-Shourkaei, H. (2022). A high-accuracy hybrid method for short-term wind power forecasting. *ENERGY* 238, 122020. doi:10.1016/j.energy.2021.122020

Lahouar, A., and Slama, J. B. H. (2017). Hour-ahead wind power forecast based on random forests. *Renew. ENERGY* 109, 529–541. doi:10.1016/j.renene.2017.03.064

Li, F., Ren, G., and Lee, J. (2019). Multi-step wind speed prediction based on turbulence intensity and hybrid deep neural networks. *ENERG Convers. MANAGE* 186, 306–322. doi:10.1016/j.enconman.2019.02.045

Li, L., Cen, Z., Tseng, M., Shen, Q., and Ali, M. H. (2021). Improving short-term wind power prediction using hybrid improved cuckoo search arithmetic - support vector regression machine. *J. Clean. Prod.* 279, 123739. doi:10.1016/j.jclepro.2020.123739

Liang, Z., Liang, J., Wang, C., Dong, X., and Miao, X. (2016). Short-term wind power combined forecasting based on error forecast correction. *ENERGY Convers. MANAG.* 119, 215–226. doi:10.1016/j.enconman.2016.04.036

Liu, C., Zhang, X., Mei, S., Zhen, Z., Jia, M., Li, Z., et al. (2022). Numerical weather prediction enhanced wind power forecasting: rank ensemble and probabilistic fluctuation awareness. *Appl. ENERG* 313, 118769. doi:10.1016/j.apenergy.2022.118769

Liu, H., Chen, C., Lv, X., Wu, X., and Liu, M. (2019). Deterministic wind energy forecasting: a review of intelligent predictors and auxiliary methods. *ENERGY Convers. MANAG.* 195, 328–345. doi:10.1016/j.enconman.2019.05.020

Liu, Y., Sun, Y., Infield, D., Zhao, Y., Han, S., and Yan, J. (2017). A hybrid forecasting method for wind power ramp based on orthogonal test and support vector machine (OT-SVM). *IEEE T SUSTAIN ENERG* 8 (2), 451–457. doi:10.1109/TSTE.2016.2604852

Liu, Z., Li, L., Liu, Y., Liu, J., Li, H., and Shen, Q. (2021). Dynamic economic emission dispatch considering renewable energy generation: a novel multi-objective optimization approach. *Energy (Oxford)* 235, 121407. doi:10.1016/j.energy.2021.121407

Lu, H., Ma, X., Huang, K., and Azimi, M. (2020). Prediction of offshore wind farm power using a novel two-stage model combining kernel-based nonlinear extension of the Arps decline model with a multi-objective grey wolf optimizer. *Renew. SUSTAIN ENERGY Rev.* 127, 109856. doi:10.1016/j.rser.2020.109856

Naik, J., Satapathy, P., and Dash, P. K. (2018). Short-term wind speed and wind power prediction using hybrid empirical mode decomposition and kernel ridge regression. *Appl. SOFT Comput.* 70, 1167–1188. doi:10.1016/j.asoc.2017.12.010

Prósper, M. A., Otero-Casal, C., Fernández, F. C., and Miguez-Macho, G. (2019). Wind power forecasting for a real onshore wind farm on complex terrain using WRF high resolution simulations. *Renew. ENERG* 135, 674–686. doi:10.1016/j.renene.2018.12.047

Shafiullah, G. M., Oo, A. M. T., Ali, A. B. M. S., and Wolfs, P. (2013). Potential challenges of integrating large-scale wind energy into the power grid-A review. *Renew. Sust. ENERG Rev.* 20, 306–321. doi:10.1016/j.rser.2012.11.057

Shi, J., Ding, Z., Lee, W. J., Yang, Y., Liu, Y., and Zhang, M. (2013). Hybrid forecasting model for very-short term wind power forecasting based on grey relational analysis and wind speed distribution features. *IEEE T SMART GRID* 5 (1), 521–526. doi:10.1109/TSG.2013.2283269

Shi, K., Qiao, Y., Zhao, W., Wang, Q., Liu, M., and Lu, Z. (2018). An improved random forest model of short-term wind-power forecasting to enhance accuracy, efficiency, and robustness. *WIND ENERGY* 21 (12), 1383–1394. doi:10.1002/we.2261

Tascikaraoglu, A., and Uzunoglu, M. (2014). A review of combined approaches for prediction of short-term wind speed and power. *Renew. Sust. ENERG Rev.* 34, 243–254. doi:10.1016/j.rser.2014.03.033

Tian, Z., Ren, Y., and Wang, G. (2019). Short-term wind speed prediction based on improved PSO algorithm optimized EM-ELM. *ENERG SOURCE PART A* 41, 26–46. doi:10.1080/15567036.2018.1495782

Torres, J. L., Garcíaa, A., De Blas, M., and De Francisco, A. (2005). Forecast of hourly average wind speed with ARMA models in Navarre (Spain). *Sol. ENERGY* 79 (1), 65–77. doi:10.1016/j.solener.2004.09.013

Wang, C., Zhang, H., Fan, W., and Ma, P. (2017a). A new chaotic time series hybrid prediction method of wind power based on EEMD-SE and full-parameters continued fraction. *ENERGY* 138, 977–990. doi:10.1016/j.energy.2017.07.112

Wang, C., Zhang, H., and Ma, P. (2020). Wind power forecasting based on singular spectrum analysis and a new hybrid Laguerre neural network. *Appl. ENERGY* 259, 114139. doi:10.1016/j.apenergy.2019.114139

Wang, H., Li, G., Wang, G., Peng, J., Jiang, H., and Liu, Y. (2017b). Deep learning based ensemble approach for probabilistic wind power forecasting. *Appl. ENERG* 188, 56–70. doi:10.1016/j.apenergy.2016.11.111

Wang, J., Wang, S., and Yang, W. (2019a). A n*ovel non*-linear combination system for short-term wind speed forecast. *Renew. ENERG* 143, 1172–1192. doi:10.1016/j.renene.2019.04.154

Wang, J., Wu, C., and Niu, T. (2019b). A novel system for wind speed forecasting based on multi-objective optimization and Echo state network. *SUSTAINABILITY-BASEL* 11 (2), 526. doi:10.3390/su11020526

Wang, Y., Zou, R., Liu, F., Zhang, L., and Liu, Q. (2021). A review of wind speed and wind power forecasting with deep neural networks. *Appl. ENERG* 304, 117766. doi:10.1016/j.apenergy.2021.117766

Wu, Y., Wu, Q., and Zhu, J. (2019). Data-driven wind speed forecasting using deep feature extraction and LSTM. *IET Renew. POWER Gen.* 13 (12), 2062–2069. doi:10.1049/iet-rpg.2018.5917

Wu, Z., and Huang, N. E. (2009). Ensemble empirical mode decomposition: a noise-assisted data analysis method. *Adv. DATA Sci. ADAPT* 1, 1–41. doi:10.1142/s1793536909000047

Xia, B., Huang, Q., Wang, H., and Ying, L. (2022). Wind power prediction in view of ramping events based on classified spatiotemporal network. *Front. ENERGY Res.* 9, 754274. doi:10.3389/fenrg.2021.754274

Yan, J., Li, K., Bai, E., Deng, J., and Foley, A. M. (2015). Hybrid probabilistic wind power forecasting using temporally local Gaussian process. *IEEE T SUSTAIN ENERG* 7 (1), 87–95. doi:10.1109/TSTE.2015.2472963

Ye, L., Zhao, Y., Zeng, C., and Zhang, C. (2017). Short-term wind power prediction based on spatial model. *Renew. ENERG* 101, 1067–1074. doi:10.1016/j.renene.2016.09.069

Yin, H., Ou, Z., Huang, S., and Meng, A. (2019). A cascaded deep learning wind power prediction approach based on a two-layer of mode decomposition. *ENERGY* 189, 116316. doi:10.1016/j.energy.2019.116316

Yu, C., Li, Y., Bao, Y., Tang, H., and Zhai, G. (2018). A novel framework for wind speed prediction based on recurrent neural networks and support vector machine. *ENERG Convers. MANAGE* 178, 137–145. doi:10.1016/j.enconman.2018.10.008

Yuan, R., Wang, B., Mao, Z., and Watada, J. (2021). Multi-objective wind power scenario forecasting based on PG-GAN. *ENERGY* 226, 120379. doi:10.1016/j.energy.2021.120379

Yuan, W., Xin, W., Su, C., Cheng, C., Yan, D., and Wu, Z. (2022). Cross-regional integrated transmission of wind power and pumped-storage hydropower considering the peak shaving demands of multiple power grids. *Renew. ENERG* 190, 1112–1126. doi:10.1016/j.renene.2021.10.046

Zhang, J., Yan, J., Infield, D., Liu, Y., and Lien, F. (2019a). Short-term forecasting and uncertainty analysis of wind turbine power based on long short-term memory network and Gaussian mixture model. *Appl. ENERG* 241, 229–244. doi:10.1016/j.apenergy.2019.03.044

Zhang, Y., Chen, B., Zhao, Y., and Pan, G. (2018). Wind speed prediction of IPSO-BP neural network based on lorenz disturbance. *IEEE ACCESS* 6, 53168–53179. doi:10.1109/ACCESS.2018.2869981

Zhang, Y., Han, J., Pan, G., Xu, Y., and Wang, F. (2021). A multi-stage predicting methodology based on data decomposition and error correction for ultra-short-term wind energy prediction. *J. Clean. Prod.* 292, 125981. doi:10.1016/j.jclepro.2021.125981

Zhang, Y., Wang, J., and Wang, X. (2014). Review on probabilistic forecasting of wind power generation. *Renew. SUSTAIN ENERGY Rev.* 32, 255–270. doi:10.1016/j.rser.2014.01.033

Zhang, Z., Qin, H., Liu, Y., Wang, Y., Yao, L., Li, Q., et al. (2019b). Long Short-Term Memory Network based on Neighborhood Gates for processing complex causality in wind speed prediction. *ENERG Convers. MANAGE* 192, 37–51. doi:10.1016/j.enconman.2019.04.006

Zhou, B., Duan, H., Wu, Q., Wang, H., Or, S. W., Chan, K. W., et al. (2021). Short-term prediction of wind power and its ramp events based on semi-supervised generative adversarial network. *Int. J. ELEC POWER* 125, 106411. doi:10.1016/j.ijepes.2020.106411

Zucatelli, P. J., Nascimento, E. G. S., Santos, A. Á. B., Arce, A. M. G., and Moreira, D. M. (2021). An investigation on deep learning and wavelet transform to nowcast wind power and wind power ramp: a case study in Brazil and Uruguay. *ENERGY* 230, 120842. doi:10.1016/j.energy.2021.120842

Nomenclature

Sets and indices

K	Total number of times white noise is added
k	Index of times white noise is added
M	Total number of decomposed IMFs
m	Index of decomposed IMFs
t	Index of time periods
S	Total number of sample points
s	Index of sample points

Constants

P_t	Original wind power sequence
W_Z	Weight matrixes of the update gate
W_r	Weight matrixes of the reset gate
W_h	Weight matrixes of the intermediate state
p_s^h	Actual historical wind power output value of sample point s

Variables

$P_{k,t}$	Wind power sequence after adding white noise for the kth time
$C_{k,t}^m$	The mth IMF obtained by the EMD method for the kth time
C_t^m	The mth IMF obtained by the EEMD method
$r_{k,t}^M$	RES after EMD decomposition for the kth time
r_t^M	RES after EEMD decomposition
r_t	Reset gate
$s_{k,t}$	White noise signal added at the kth time
z_t	Update gate
x_t	hidden state and load data of GRU neuron at time t
$\tilde{h}_t$	Intermediate state
h_t	Output of GRU neuron
$M_{kij}^{(1)}$	Number of times state i turns into state j after one step
M_j	Total number of occurrences of state j
p_s^{pf}	Predicted value of sample point s obtained by the EEMD-GRU model

Functions

σ	Sigmoid function
$\odot$	Element-wise multiplication (Hadamard product)

Abbreviations

MC	Markov chain
GRU	Gated recurrent unit
EEMD	Ensemble empirical mode decomposition
NWP	Numerical weather prediction
WRF	Weather Research and Forecasting
ARMA	Autoregressive moving average model
ARIMA	Autoregressive integrated moving average model
GARCH	Generalized autoregressive conditional heteroscedasticity
SVM	Support vector machine
RF	Random forest
BART	Bayesian additive regression tree
AI	Artificial intelligence
BP	Back-propagation
CNN	Convolution neural network
RNN	Recursive neural network
LSTM	Long short-term memory
TCN	Temporal convolutional network
ELM	Extreme learning machine
ENN	Elman neural network
LSSVM	Least square SVM
RBFNN	Radial basis function neural network
ORELM	Outlier robust ELM
BiLSTM	Bidirectional LSTM
EMD	Empirical mode decomposition
VMD	Variational mode decomposition
WT	Wavelet transform
CEEMDAN	Complete ensemble empirical mode decomposition with adaptive noise
MLP	Multilayer Perceptron
NSGA- II	Non-dominated Sorting Genetic Algorithm II
MOGWO	Multi-objective grey wolf optimization
PSO	Particle Swarm Optimization
ESN	Echo State Network
IMF	Intrinsic mode function
RES	Residual
GRUNN	GRU neural network
RMSE	Root mean square error
MAE	Mean absolute error
MAPE	Mean absolute percentage error

frontiers | Frontiers in Energy Research

TYPE Methods
PUBLISHED 08 February 2024
DOI 10.3389/fenrg.2023.1273805

OPEN ACCESS

EDITED BY
Chengguo Su,
Zhengzhou University, China

REVIEWED BY
Sheng Xiang,
Changsha University of Science and Technology, China
Mojtaba Nedaei,
University of Padua, Italy

*CORRESPONDENCE
Fengjiao Xu,
xufj@tsintergy.com
Shuangquan Liu,
Liushuangquan@yn.csg.cn

RECEIVED 07 August 2023
ACCEPTED 12 December 2023
PUBLISHED 08 February 2024

CITATION
Wu Y, Xie Y, Xu F, Zhu X and Liu S (2024), A runoff-based hydroelectricity prediction method based on meteorological similar days and XGBoost model.
Front. Energy Res. 11:1273805.
doi: 10.3389/fenrg.2023.1273805

A runoff-based hydroelectricity prediction method based on meteorological similar days and XGBoost model

Yang Wu[1], Yigong Xie[1], Fengjiao Xu[2]*, Xinchun Zhu[1] and Shuangquan Liu[1]*

[1]Yunnan Power Dispatching and Control Center, Yunnan Power Grid Co, Ltd., Kunming, China, [2]Beijing Tsintergy Technology Co, Ltd., Beijing, China

This paper proposes a runoff-based hydroelectricity prediction method based on meteorological similar days and XGBoost model. Accurately predicting the hydroelectricity supply and demand is critical for conserving resources, ensuring power supply, and mitigating the impact of natural disasters. To achieve this, historical meteorological and runoff data are analyzed to select meteorological data that are similar to the current data, forming a meteorological similar day dataset. The XGBoost model is then trained and used to predict the meteorological similar day dataset and obtain hydroelectricity prediction results. To evaluate the proposed method, the hydroelectricity cluster in Yunnan, China, is used as sample data. The results show that the method exhibits high prediction accuracy and stability, providing an effective approach to hydroelectricity prediction. This study demonstrates the potential of using meteorological similar days and the XGBoost model for hydroelectricity prediction and highlights the importance of accurate hydroelectricity prediction for water resource management and electricity production.

KEYWORDS

hydroelectricity prediction, meteorological similar days, XGBoost model, runoff-based hydroelectricity, distributed

1 Introduction

In recent years, with the rapid development of distributed small hydropower, its position in the field of clean energy has become increasingly important (Li et al., 2021). However, the power transmission distance in distributed small hydropower-rich areas is far, and the channel resources of the main power grid are limited. Furthermore, large and small hydropower stations occupy the channel resources, which has an impact on the main power grid. The problem of small interference stability is prominent, and it is difficult for the power dispatching department to accurately grasp the power generation capacity of small hydropower stations, resulting in the frequent occurrence of large-scale power generation and water abandonment of small hydropower stations, which seriously affects the utilization efficiency of clean energy and the safe and stable operation of the power grid (Graciano-Uribe et al., 2021; Zhang et al., 2022). Therefore, it has become an urgent problem to carry out the distributed small hydropower generation capacity prediction and provide reference for the power dispatching department to carry out the coordinated dispatch of multiple power sources.

TABLE 1 Summary of characteristics.

Feature type	Generated feature	Effect
Hysteresis characteristics	Hydropower output lag T-2	Historical data reflect output characteristics
	Water flow lag T-2	Time lag effect of flow and output
Meteorological characteristics	Rainfall	Rainfall directly affects runoff hydropower output
	Temperature	Temperature affects rainwater evaporation
Time characteristics	Year	Reflects seasonal variation
	Month	Reflects seasonal variation
	Day	Reflects seasonal variation
Statistical characteristics	Average rate of flow	Reflects the correlation between hydropower generation and runoff
	Variance rate of flow	Reflects the correlation between hydropower generation and runoff
	Maximum rate of flow	Reflects the correlation between hydropower generation and runoff
	Minimum rate of flow	Reflects the correlation between hydropower generation and runoff

TABLE 2 Comparison of prediction accuracy.

Dry/wet season	Date	Similar-day weighted XGBoost/%	Original XGBoost/%	GM/%
Dry season	December 8	100.00	97.16	98.17
	December 9	100.00	98.15	98.53
	December 10	100.00	99.44	99.42
	December 11	100.00	96.98	99.71
	December 12	91.50	88.84	89.33
	December 13	100.00	99.54	99.41
	December 14	85.60	60.50	70.56
Average accuracy in the dry season		96.73	91.51	93.60
Wet season	July 2	96.18	93.24	92.51
	July 3	95.49	91.63	89.75
	July 4	97.50	93.84	91.23
	July 5	96.09	90.52	88.41
	July 6	97.85	93.56	90.24
	July 7	99.72	96.63	93.38
Average accuracy in the wet season		97.14	93.24	90.92

In recent years, the field of hydropower has become the focus of many experts and scholars in the new energy sustainable development industry (Kougias et al., 2019). The traditional runoff hydropower forecasting method is mainly based on the trend extrapolation method, which has fast calculation speed and is suitable for forecasting with small load fluctuations (Zhou et al., 2022). However, the modeling process of this method is relatively complex and requires high stability of the historical data trend, which has certain limitations.

Jung et al. (2021) predicted the potential of small hydropower in the future by building a neural network model using climate change scenarios and artificial simulations. The prediction results are generally optimistic, but they cannot directly guide the power dispatching department to carry out the coordinated dispatch of multiple power sources, and they need to be combined with hydropower output prediction. Demir et al. (2023) comprehensively analyzed the advantages of using the XGBoost algorithm in prediction from the aspects of samples, characteristics, index performance, and model robustness. Hanoon et al. (2023) verified the effective application of different machine learning algorithms in hydropower forecasting by modeling three different scenarios in quarterly, monthly, and daily dimensions with different machine learning methods. With the continuous development of artificial intelligence technology, application of some machine

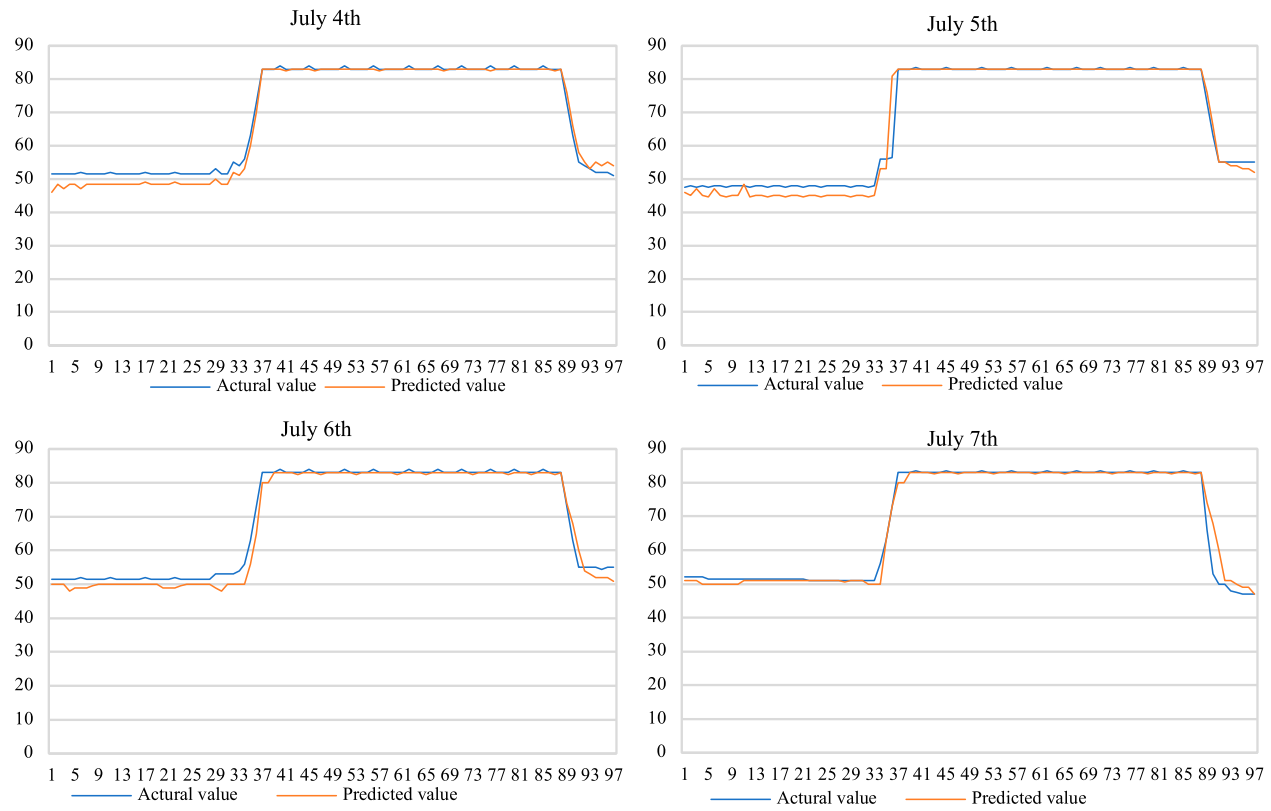

FIGURE 1
Similar-day weighted XGBoost result prediction.

learning methods, such as XGBoost algorithm, is gradually becoming feasible for runoff hydropower prediction (Zhang et al., 2021; Kumar et al., 2021). These methods use the historical data as training samples, utilize the intelligent processing and self-learning mode of the algorithm, learn the mapping relationship between the historical data and the influencing factors, and apply the algorithm to predict the future load data after strengthening learning and improving the accuracy (Bordin et al., 2020; Bernardes et al., 2022; Lai et al., 2020). The XGBoost method shows the nonlinear mapping ability and strong self-adaptation ability and is expected to become an effective means to solve the problem of distributed small hydropower generation capacity prediction. Bilgili et al. (2022) introduced a deep learning method based on long short-term memory (LSTM) to predict the power generation of a run-of-the-river hydroelectric power plant 1 day in advance. In addition, in order to compare the prediction accuracy, the adaptive neural fuzzy inference system (ANFIS) and fuzzy C-means (FCM), ANIS and subtractive clustering (SC), and ANFIS grid partitioning (GP) methods were adopted, which shows that the LSTM neural network provides higher accuracy results in short-term energy production forecasting. Dehghani et al. (2019) combined the gray wolf method with ANFIS to predict hydroelectric power.

1.1 Research highlights

Forecasting the generation capacity of distributed small hydropower is an effective means to solve the problem of frequent large-scale water abandonment due to its long transmission distance, limited channel resources, unknown generation capacity, and other factors.

The XGBoost algorithm applied to runoff hydropower prediction has the ability of nonlinear mapping and strong self-adaptation, which can effectively improve the prediction accuracy and overall accuracy.

The artificial intelligence forecasting method takes historical data as training samples, and its intelligent processing and self-learning mode can learn the mapping relationship between historical data and the influencing factors and apply it to forecast future load data, which is an effective means to solve the problem of distributed small hydropower generation capacity forecasting.

2 Hydropower forecasting method

2.1 Principle of the XGBoost algorithm

The main problems of traditional runoff hydropower forecasting methods are as follows:

Complicated modeling process: Traditional runoff-based hydropower forecasting methods often involve complex modeling processes, which require specialized knowledge and skills, increasing the difficulty and cost of prediction.

High requirements for the stability of historical data trends: The effectiveness of these methods depends heavily on the

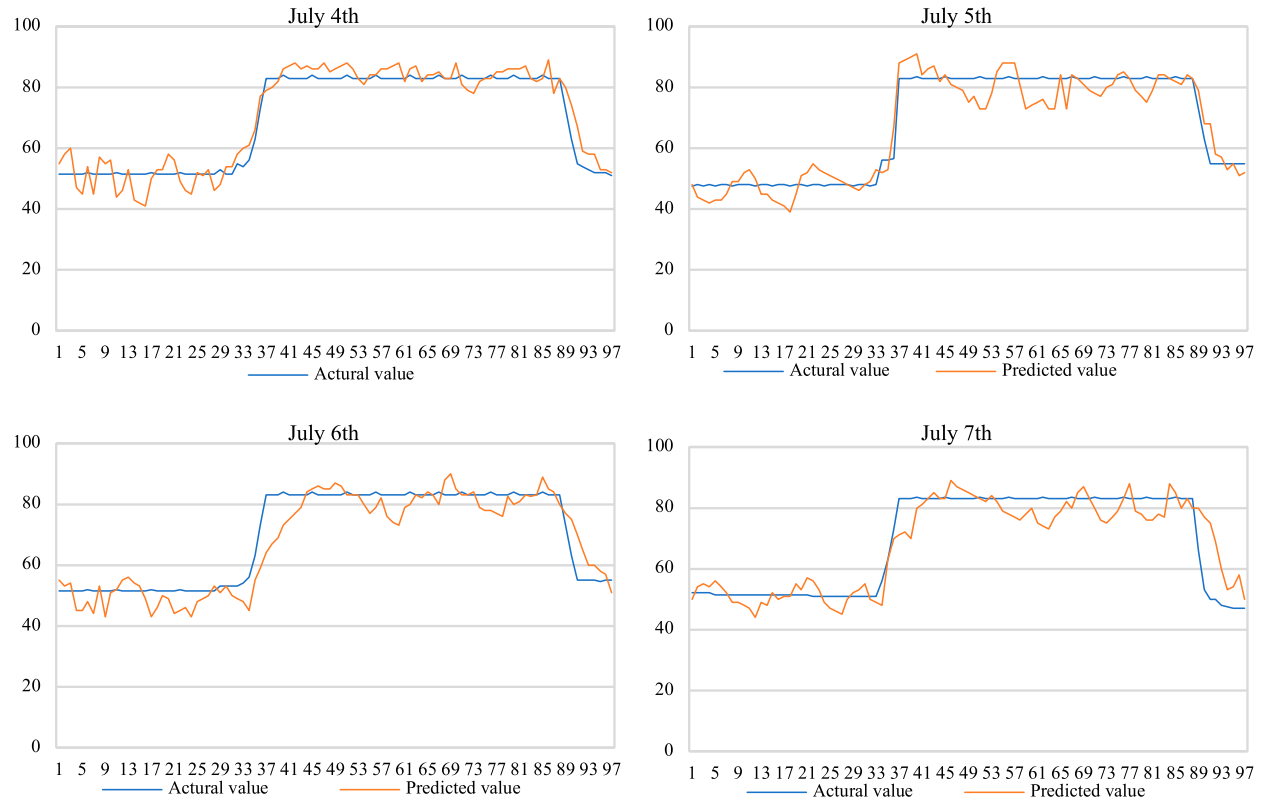

FIGURE 2
Original XGBoost result prediction.

stability of historical data. If the historical data trends change significantly, the accuracy of predictions based on these data may be affected.

Suitability for predictions with fewer load fluctuations: Due to the computational process and results of traditional methods being limited by the consistency and stability of historical data, they may be more suitable for predictions with fewer load fluctuations. For situations with greater load fluctuations, the accuracy of predictions may be reduced.

Limited adaptability to future changes in hydropower output: Traditional runoff-based hydropower forecasting methods are mainly based on extrapolating historical data, which may have limited the adaptability to future changes in hydropower output. If there are significant changes in hydropower output in the future, these methods may need to be adjusted or re-modeled.

Lack of handling of uncertainties: Traditional methods usually assume that the future hydropower output is deterministic, but in reality, the future hydropower output may be affected by many uncertain factors, such as climate change and fluctuations in the energy demand. Traditional methods lack effective handling of these uncertainties.

For the prediction of many quantities with uncertain characteristics, i.e., random variables, people often use the method of probability and statistic in engineering practice. The probability and statistic method requires finding statistical laws from a large number of data samples, and this statistical law must be easy to be processed by mathematical methods (Walpole et al., 1993). Different from probability and statistics, the gradient boosting decision tree (GBDT) is a type of machine learning algorithm (Ke et al., 2017); its good performance in the prediction and classification of problems has been widely observed by industry researchers (Charbuty et al., 2021). The algorithm is composed of multiple decision trees and uses the negative gradient value of the loss function in the current model as the approximate value of the residual in the lifting tree for the regression fit of the decision tree (Natekin et al., 2013). The general steps of the GBDT algorithm are as follows:

1) Input n training samples X and set relevant parameters. The number of iterations is N, F is the function space composed of all trees, and f_k is the single decision tree model; the initial value is $f_0 = 0$, and the expression of the GBDT algorithm is as follows:

$$\hat{y}_i = \sum_{k=1}^{K} f_k(x_i), \tag{1}$$

where x_i is the eigenvector of the i-th sample; K is the number of weak regression trees; $f_k(x_i)$ is the output value of the k-th weak regression tree; and $\hat{y}_i$ is the final predicted value of the ith sample.

2) Define the objective function of the GBDT algorithm as

$$Obj = \sum_{i=1}^{n} l(y_i, \hat{y}_i) + \sum_{k=1}^{K} \Omega(f_k), \tag{2}$$

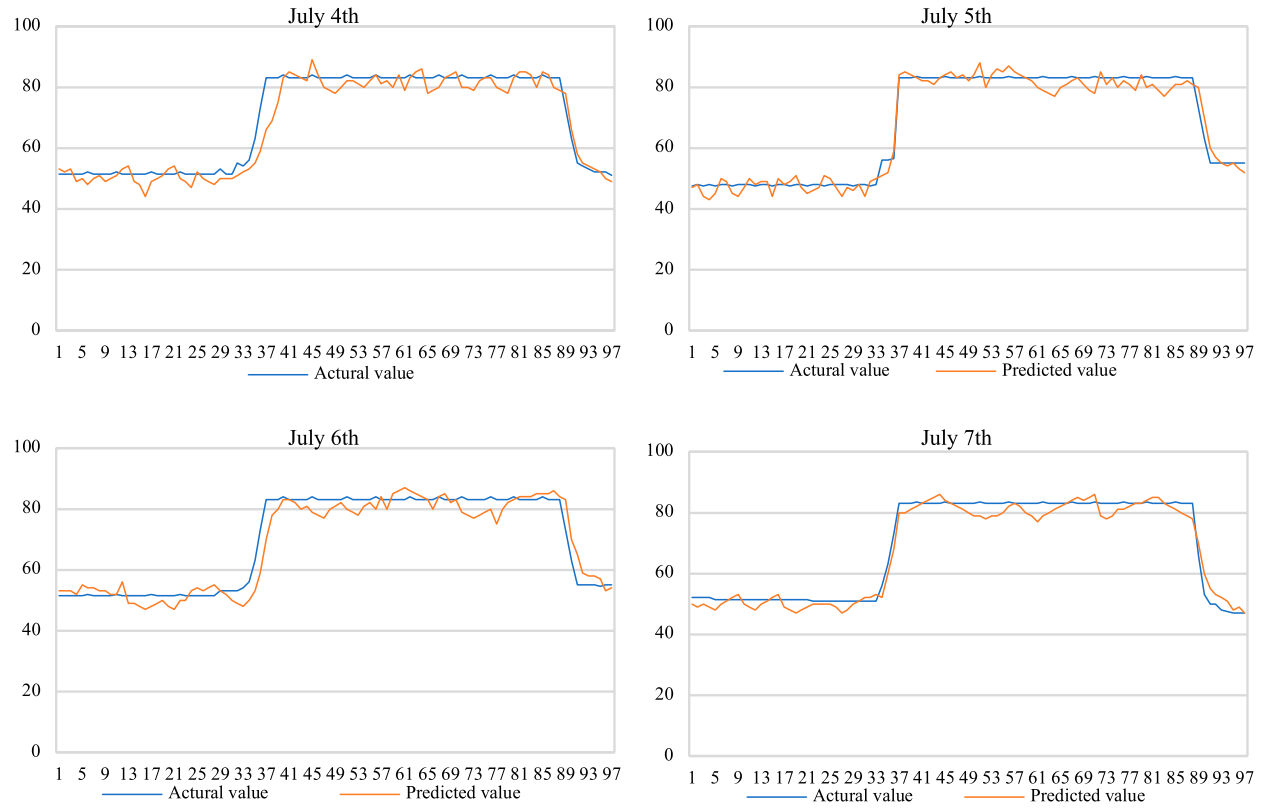

FIGURE 3
GM result prediction.

where Ω is the complexity of the decision tree; n is the total number of samples; l is the loss function; and y_i is the true value of the i-th sample.

The complexity is defined by the regular term:

$$\Omega(f_t) = \kappa T + \frac{1}{2}\lambda\sum_{j=1}^{T}\omega_j^2, \tag{3}$$

where T is the number of nodes of the leaf; ω_j is the vector value corresponding to the leaf node; κ is the minimum loss reduction required for leaf node splitting of the tree; and λ is the penalty term coefficient.

3) According to the addition structure of the GBDT algorithm, we obtain

$$\hat{y}_i^{\,t} = \hat{y}_i^{\,t-1} + f_t(x_i), \tag{4}$$

where $\hat{y}_i^{\,t}$ is the sum of the outputs of the first t trees of the i-th sample; $\hat{y}_i^{\,t-1}$ is the sum of the outputs of the first i trees of the $(t-1)$-th sample; and $f_t(x_i)$ is the output value of the tth tree of the ith sample.

Substituting Eq. 4 into the objective function and carrying out the Taylor expansion, we obtain

$$\begin{aligned} Obj^t &= \sum_{i=1}^{n}\left[g_i f_t(x_i) + \frac{1}{2}h_i f_t^{\,2}(x_i) + \kappa T + \frac{1}{2}\lambda\sum_{j=1}^{T}\omega_j^2\right] \\ &= \sum_{j=1}^{T}\left[G_i\omega_j + \frac{1}{2}(H_i+\lambda)\omega_j^{\,2}\right] + \kappa T, \end{aligned} \tag{5}$$

where $G_i = \sum g_i, H_i = \sum h_i$ and g_i and h_i are the first and second derivatives of the loss function, respectively.

Let the first derivative of Obj^t be 0. Then the optimal value of leaf node $\omega_j{}^*$ can be obtained as follows:

$$\omega_j{}^* = -\frac{G_j}{H_j+\lambda}. \tag{6}$$

At this time, the objective function value is

$$Obj^t = -\frac{1}{2}\sum_{j=1}^{T}\frac{G_j^{\,2}}{H_j+\lambda} + \kappa T. \tag{7}$$

4) Generate a new decision tree through the greedy strategy to minimize the value of the objective function (Friedman et al., 2001), and obtain the optimal predictive value $\omega_j{}^*$ corresponding to the leaf node. Add the newly generated decision tree $f_t(x)$ to the model to obtain

$$\hat{y}_i^{\,t} = \hat{y}_i^{\,t-1} + f_t(x_i). \tag{8}$$

5) Continue to iterate until the end of N iterations, and output the GBDT algorithm composed of N decision trees.

The GBDT algorithm has many effective implementations, such as the XGBoost algorithm and LightGBM algorithm, which are integrated learning algorithms of GBDT (Shi et al., 2018; Bentéjac et al., 2021).

XGBoost is an improved algorithm based on GBDT that uses multithreading parallelism to improve the accuracy and is suitable for classification and regression problems (Chen et al., 2016). The basic principle of XGBoost is the same as that of GBDT. The difference is that GBDT uses the first derivative of the loss function, while XGBoost uses the first and second derivatives to perform the second-order Taylor expansion of the loss function.

Experimentally, XGBoost is relatively faster than many other integrated classifiers, such as AdaBoost. The impact of the XGBoost algorithm has been widely recognized in many machine learning and data mining challenges, and it has become a more commonly used and popular tool among Kaggle's competitors and industry data scientists. In addition to using different boosting algorithms, MART and XGBoost also provide different regularization parameters. In particular, XGBoost can provide additional parameters that are not available in GBDT. In addition, it provides the penalty for a single tree in the additive tree model. These parameters will affect the tree structure and the weighting of the leaves to reduce variance in each tree. In addition, XGBoost provides an additional randomization parameter that can be used to disassociate individual trees, thereby reducing the overall variance of the additive tree model (Nielsen, 2016).

The loss function of the XGBoost algorithm is

$$Obj(\phi) = l(y, f(x)) + \sum_m \Omega(f_m), \tag{9}$$

where y is the true value corresponding to the current sample y; $f(x)$ is the predicted value of sample x; $l(y, f(x))$ is the loss function; f_m is the mth classification tree model; $\Omega(f_m)$ is the regularization term, which reflects the complexity of the algorithm; and ϕ is the model parameter to be solved.

$$\begin{aligned} Obj^{(m)} &= \sum_{i=1}^{N} l\left(y_i, \hat{y}_i^{(m)}\right) + \sum_{i=1}^{m} \Omega(f_i) \\ &= \sum_{i=1}^{N} l\left(y_i, \hat{y}_i^{(m-1)} + f_m(x_i)\right) + \Omega(f_m), \end{aligned} \tag{10}$$

$$Obj^{(m)} \approx \sum_{i=1}^{N} \left[l\left(y_i, \hat{y}_i^{(m-1)}\right) + g_i f_m(x_i) + \frac{1}{2} h_i {f_m}^2(x_i) \right] + \Omega(f_m). \tag{11}$$

The Taylor expansion is used to approximate function $f_m(x_i)$. Substituting Eq. 10 into Eq. 11, we obtain

$$g_i = \partial_{\hat{y}_i^{(m-1)}} l\left(y_i, \hat{y}_i^{(m-1)}\right), \tag{12}$$

$$h_i = \partial^2_{\hat{y}_i^{(m-1)}} l\left(y_i, \hat{y}_i^{(m-1)}\right), \tag{13}$$

where $\partial_{\hat{y}_i^{(m-1)}}$ and $\partial^2_{\hat{y}_i^{(m-1)}}$ are the first and second derivatives of $\hat{y}_i^{(m-1)}$ on the loss function, respectively.

The regularization term in the objective function is

$$\Omega(f_m) = \gamma T + \frac{1}{2}\lambda \|\omega\|^2, \tag{14}$$

where γ is the minimum loss reduction required for further splitting at the leaf node of the tree, representing the complexity of each leaf, and ω is the value of the leaf node.

2.2 Runoff hydropower forecasting method based on XGBoost

The runoff hydropower prediction based on XGBoost is mainly divided into five steps: data collection, preprocessing, characteristic engineering, model training, and model validation (Li et al., 2019). We collect historical hydropower generation data, runoff data, and meteorological data related to hydropower generation. Among them, runoff data refer to the flow data of the river, which can be obtained through hydrological stations. After screening, de-duplication, and checking the collected data, the duplicate, invalid, and abnormal data are removed. Second, we process the missing data and filled the missing data using the interpolation method. Then, we use the method based on an isolated forest to detect and process the outliers of the data. In runoff hydropower prediction, feature engineering is a very important step. It can process the data reasonably and improve the prediction performance of the model. In this paper, we use a variety of feature engineering methods, including lag characteristics, time characteristics, and statistical characteristics. Table 1 lists the specific functions:

Considering that meteorological data, which include multiple factors such as precipitation and temperature, have a great impact on runoff hydropower prediction, this paper proposes an XGBoost runoff hydropower prediction method based on "meteorological similar days." Before model training, the meteorological data of the day to be predicted are first composed into a feature vector, and the similarity is then calculated by the feature vector composed of the feature vector of the forecast day and the historical meteorological data. This paper uses the reciprocal of Manhattan distance to measure the similarity between the two. The specific form is as follows:

$$similarity = \frac{1}{\sum_{i=1}^{N} |x_i - y_i|} \tag{15}$$

where N represents the length of the meteorological vector, y_i represents the ith element of the meteorological vector of the day to be predicted, and x_i represents the ith element of the historical meteorological vector of a day. According to the above similarity, the XGBoost algorithm model is weighted by the loss function to increase the impact of similar samples on the forecast date. Finally, the model is verified based on this scheme.

3 Example analysis

We select the output data of the hydropower cluster in Yunnan area, which contains multistage runoff hydropower stations, as the sample data to evaluate the proposed method.

Hydropower prediction is a complex task. The industry usually uses capacity accuracy instead of RMSPE accuracy for the assessment of new energy. The formula is as follows:

$$ACC_{new\_energy} = \left(1 - \sqrt{\frac{1}{N}\sum_{i=1}^{N}\left(\frac{y_i - \hat{y}_i}{Cap}\right)^2}\right) \times 100\%, \tag{16}$$

where N is the number of output points collected in a day, taken as $N = 96$, and y_i is the actual output value at the i-th time point in a day. $\hat{y}_i$ is the predicted output value at the i-th time point in a day, and Cap is the capacity of the station.

The gray theory model (GM) is considered a classic model in the field of hydropower prediction, which mainly solves the problems of lack of data and uncertainty. Therefore, the prediction experimental group in this paper adopts the similar-day weighted XGBoost, while the control experimental group selects the original XGBoost and GM, normalizes the historical data to the interval of [−1,1], and takes 80% of the data as the training data and the remaining 20% as the test data. The prediction results are shown in Table 2.

It can be seen from the above table that considering the same factors, the prediction accuracy of GM in the dry season is higher than that of the original XGBoost algorithm after sample screening according to our proposed similarity measure and allocating weights to the sample. The prediction accuracy of GM in the dry season is higher than that of the original XGBoost algorithm, but it is not ideal in the wet season. The effectiveness of the sample weight selection method based on similar days is demonstrated using the control experimental group. In addition, we found that the accuracy of the algorithm for winter data prediction is higher than that in the summer. This is because the summer weather changes violently, the unit output level fluctuates greatly, and the weather has an unbalanced effect. Therefore, it can be seen that the selection of meteorological data has a great impact on the prediction accuracy of small hydropower output.

An overall comparison shows that the similar-day weighted XGBoost has the highest prediction accuracy compared to original XGBoost and GM in both wet and dry periods.

The prediction results using the similar-day weighted XGBoost algorithm are shown in Figure 1. It can be seen that the hydropower cluster has higher output and stable cycle in the wet season, and the prediction accuracy of this algorithm is higher.

Figures 2, 3 show that the prediction accuracy of original XGBoost is higher than that of GM in the wet season. Through the comparison of Figures 1–3, it can be seen that similar-day weighted XGBoost has the best prediction effect in the wet season.

4 Summary

In this paper, a novel hydropower forecasting method combining meteorological similar days and XGBoost model is proposed. By analyzing the historical meteorological and runoff data, this paper selected the meteorological similar days with meteorological conditions similar to the current data, which provided a valuable reference for the prediction of hydropower output. The XGBoost model not only shows its effectiveness in learning meteorological similar day datasets but also produces accurate and stable hydropower prediction results. The results show that the combination of meteorological similar days and XGBoost model is a promising method to improve the accuracy of hydropower prediction. The high prediction accuracy and stability of this method are particularly beneficial to water resource management and power production, which is conducive to better planning and utilization of hydropower resources, while ensuring a reliable power supply.

The application of this method in the Yunnan hydropower cluster in China has successfully demonstrated its practicability and the potential for promotion in other regions and power systems. However, it is worth noting that the universality of this method in different geographical locations and different climatic conditions needs further research and verification. The method proposed in this paper has made a valuable contribution to the field of hydropower prediction, and its effectiveness in improving the accuracy and stability of prediction highlights its importance in solving the challenges encountered in water resource and energy management. With continuous attention to water resources and energy, we believe that this method will help strengthen the management of sustainable water resources and energy, reduce the impact of natural disasters, and promote the development of green and sustainable energy in the future.

Data availability statement

The raw data supporting the conclusion of this article will be made available by the authors without undue reservation.

Author contributions

YW: writing–review and editing. YX: writing–review and editing. FX: writing–original draft. XZ: conceptualization and writing–review and editing. SL: writing–review and editing.

Funding

The author(s) declare that no financial support was received for the research, authorship, and/or publication of this article.

Conflict of interest

Authors YW, YX, XZ, and SL were employed by Yunnan Power Grid Co., Ltd. Author FX was employed by Beijing Tsintergy Technology Co., Ltd.

Publisher's note

References

Bentéjac, C., Csörgő, A., and Martínez-Muñoz, G. (2021). A comparative analysis of gradient boosting algorithms. *Artif. Intell. Rev.* 54, 1937–1967. doi:10.1007/s10462-020-09896-5

Bernardes, J., Jr, Santos, M., Abreu, T., Prado, L., Jr, Miranda, D., Julio, R., et al. (2022). Hydropower operation optimization using machine learning: a systematic review. *AI* 3 (1), 78–99. doi:10.3390/ai3010006

Bilgili, M., Keiyinci, S., and Ekinci, F. (2022). One-day ahead forecasting of energy production from run-of-river hydroelectric power plants with a deep learning approach. *Sci. Iran.* 29 (4). doi:10.24200/sci.2022.58636.5825

BordinSkjelbredKong, C. H. I. J., and Yang, Z. (2020). Machine learning for hydropower scheduling: state of the art and future research directions. *Procedia Comput. Sci.* 176, 1659–1668. doi:10.1016/j.procs.2020.09.190

Charbuty, B., and Abdulazeez, A. (2021). Classification based on decision tree algorithm for machine learning. *Appl. Sci. Technol. Trends* 2 (01), 20–28. doi:10.38094/jastt20165

Chen, T., and Guestrin, C. (2016). "XGBoost: a scalable tree boosting system," in Proceedings of the 22nd acm sigkdd international conference on knowledge discovery and data mining, San Francisco, CA, USA, August 13-17, 2016, 785–794.

Dehghani, M., Riahi-Madvar, H., Hooshyaripor, F., Mosavi, A., Shamshirband, S., Zavadskas, E. K., et al. (2019). Prediction of hydropower generation using grey wolf optimization adaptive neuro-fuzzy inference system. *Energies* 289 (12).

Demir, S., and Sahin, E. K. (2023). An investigation of feature selection methods for soil liquefaction prediction based on tree-based ensemble algorithms using AdaBoost, gradient boosting, and XGBoost. *Neural Comput. Appl.* 35 (4), 3173–3190. doi:10.1007/s00521-022-07856-4

Friedman, J. H. (2001). Greedy function approximation: a gradient boosting machine. *Ann. Statistics* 29 (5), 1189–1232. doi:10.1214/aos/1013203451

Graciano-Uribe, J., Sierra, J., and Torres-Lopez, E. (2021). Instabilities and influence of geometric parameters on the efficiency of a pump operated as a turbine for micro hydro power generation: a review. *Water Environ. Syst.* 9 (4), 1–23. doi:10.13044/j.sdewes.d8.0321

Hanoon, M. S., Ahmed, A. N., Razzaq, A., Oudah, A. Y., Alkhayyat, A., Huang, Y. F., et al. (2023). Prediction of hydropower generation via machine learning algorithms at three Gorges Dam, China. *Ain Shams Eng. J.* 14 (4), 101919. doi:10.1016/j.asej.2022.101919

Jung, J., Han, H., Kim, K., and Kim, H. S. (2021). Machine learning-based small hydropower potential prediction under climate change. *Energies* 14 (12), 3643. doi:10.3390/en14123643

Ke, G., Meng, Q., Finley, T., Wang, T., Chen, W., Ma, W., et al. (2017). Lightgbm: a highly efficient gradient boosting decision tree. *Adv. neural Inf. Process. Syst.* 30.

Kougias, I., Aggidis, G., Avellan, F., Deniz, S., Lundin, U., Moro, A., et al. (2019). Analysis of emerging technologies in the hydropower sector. *Renew. Sustain. Energy Rev.* 113, 109257. doi:10.1016/j.rser.2019.109257

Kumar, K., Singh, R. P., Ranjan, P., and Kumar, N. (2021). "Daily plant load analysis of a hydropower plant using machine learning," in *Applications of artificial intelligence in engineering*, 819–826.

Lai, J. P., Chang, Y. M., Chen, C. H., and Pai, P. F. (2020). A survey of machine learning models in renewable energy predictions. *Appl. Sci.* 10 (17), 5975. doi:10.3390/app10175975

Li, A., Su, S., Han, T., Yin, C., Li, J., Chen, L., et al. (2021). "Energy demand forecast in yunnan province based on seq2seq model," in E3S Web of Conferences 293, 02063, Strasbourg, France, May 5-7, 2021.

Li, C., Zhu, L., He, Z., Gao, H., Yang, Y., Yao, D., et al. (2019). Runoff prediction method based on adaptive Elman neural network. *Water* 11 (6), 1113. doi:10.3390/w11061113

Natekin, A., and Knoll, A. (2013). Gradient boosting machines, a tutorial. *Front. Neurorobotics* 7, 21. doi:10.3389/fnbot.2013.00021

Nielsen, D. (2016). *Tree boosting with xgboost-why does xgboost win" every" machine learning competition?* Trondheim, Norway: NTNU.

Shi, Y., Li, J., and Li, Z. (2018). *Gradient boosting with piece-wise linear regression trees*. arXiv preprint arXiv:1802.05640 Available at: http://arxiv.org/abs/1802.05640.

Walpole, R. E., Myers, R. H., Myers, S. L., and Ye, K. (1993). *Probability and statistics for engineers and scientists*, 5.

Zhang, F., Zhang, Y., Qiu, Y., Wu, X., Tao, Y., and Ji, Q. (2022). Research review on hydropower-wind power-photovoltaic multi-energy coupling power prediction technology. *Conf. Ser.* 2354 (1), 012016. doi:10.1088/1742-6596/2354/1/012016

Zhang, Y., Ma, H., and Zhao, S. (2021). Assessment of hydropower sustainability: review and modeling. *Clean. Prod.* 321, 128898. doi:10.1016/j.jclepro.2021.128898

Zhou, F., Wang, Z., Zhong, T., Trajcevski, G., and Khokhar, A. (2022). HydroFlow: towards probabilistic electricity demand prediction using variational autoregressive models and normalizing flows. *Intell. Syst.* 37 (10), 6833–6856. doi:10.1002/int.22864

Frontiers in
Energy Research

Advances and innovation in sustainable, reliable and affordable energy

Explores sustainable and environmental developments in energy. It focuses on technological advances supporting Sustainable Development Goal 7: access to affordable, reliable, sustainable and modern energy for all.

Discover the latest Research Topics

See more →

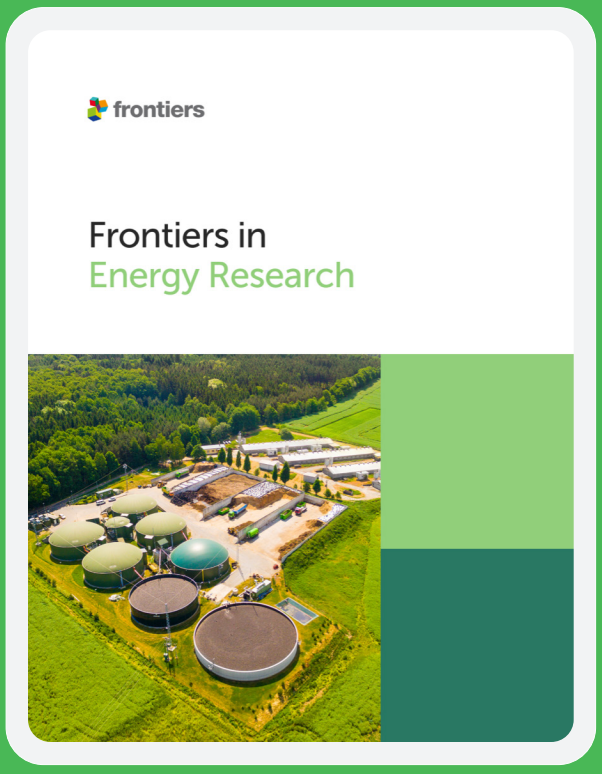

Frontiers

Avenue du Tribunal-Fédéral 34
1005 Lausanne, Switzerland
frontiersin.org

Contact us

+41 (0)21 510 17 00
frontiersin.org/about/contact